

UNIVERSITY OF
BIRMINGHAM

DRILLING OF Ti/CFRP/Al MULTILAYER STACK MATERIALS

by

CHUN-LIANG KUO

A thesis submitted to
The University of Birmingham
for the degree of
DOCTOR OF PHILOSOPHY

School of Mechanical Engineering
College of Engineering and Physical Sciences
University of Birmingham
May 2014

UNIVERSITY OF
BIRMINGHAM

University of Birmingham Research Archive

e-theses repository

This unpublished thesis/dissertation is copyright of the author and/or third parties. The intellectual property rights of the author or third parties in respect of this work are as defined by The Copyright Designs and Patents Act 1988 or as modified by any successor legislation.

Any use made of information contained in this thesis/dissertation must be in accordance with that legislation and must be properly acknowledged. Further distribution or reproduction in any format is prohibited without the permission of the copyright holder.

SYNOPSIS

The use of multilayer stack materials involving titanium, carbon fibre reinforced plastic (CFRP) composites and/or aluminium alloys is increasing as an alternative to traditional metallics, particularly for aerospace structures subject to extreme mechanical loads. Parts in the latest generation of commercial jet planes from Airbus and Boeing have already incorporated greater levels of composite based materials, which provide benefits in terms of superior strength to weight ratios leading to enhanced aircraft operational efficiency and associated fuel cost savings.

The joining of stacks used in aircraft wing and tail plane components remains largely mechanical based, thereby requiring the production of fastener holes etc. Current hole production strategies involve a multi-shot process whereby each layer of the stack is pre-drilled individually followed by a de-burring cycle where necessary. The holes in each material are subsequently 'lined up' and held together temporarily for reaming. The overall process is complicated, with low yields of ~50-60% (scrap rate of ~40-50%), depending on stack configuration/design and drilling parameters. This has led to considerable industrial interest in developing capability for single-shot drilling of multilayer stacks, which provides significant benefits not only in relation to productivity, but also potentially in terms of improved hole tolerance and joint integrity.

Following an extensive review of relevant literature, 3 main phases of experimental work was carried out to investigate the influence of various process conditions when single-shot drilling 3-layer Ti-6Al-4V/CFRP/A7050 stack materials. Phase 1 experiments were aimed at evaluating the effects of tool materials, operating parameters, drilling strategy, coatings and drill geometry on cutting forces, hole accuracy (diameter, out of roundness, cylindricity), surface integrity (roughness, 3D topography, subsurface alteration, microhardness, microstructure) and tool life. In Phase 1A, the use of TiAlN/TiN multilayer (5-6μm thick) coated carbide drills under a dual-level cutting speed of 30/120/120m/min (Ti-6Al-4V/CFRP/A7050) and a feed rate of 0.08mm/rev produced the best hole quality results (hole diameter: 6.320-6.360mm, hole cylindricity: 88.5μm), compared to uncoated drills. The use of a pecking strategy produced the lowest surface roughness of 1.8-7.5μm Ra in CFRP and similarly in the metallic layers where Ra was 0.35-1.74μm and 0.1-0.69μm in Ti and Al respectively. When employing triple margin TiAlN/TiN coated carbide drills in Phase 1B, both thrust force (Ti: ~44%, CFRP: ~16%, Al: ~54%) and torque (Ti: ~98%, CFRP: ~94%, Al:

~94%), were higher compared to corresponding single margin tools. However, overall hole diameter accuracy (6.315-6.335mm) and hole cylindricity (55.6-61.2μm) both improved with the triple margin drills. In Phase 1C, evaluation of diamond based coatings showed that despite their superior hardness, there was no significant benefit in terms of tool life over TiAlN/TiN hardmetal coated drills when drilling Ti/CFRP/Al stacks. The effect of tool point geometry was investigated in Phase 1D involving variation of drill point angle, helix angle and chisel diameter. Statistical analysis with respect to different response measures suggested a preferred combination of 140° point angle, 40° helix angle and 0.1mm chisel diameter.

Phase 2A research involved investigating the performance of a novel domed PCD material and the effect of feed rate when operating at elevated (20% increase) cutting speed. The results showed the domed PCD drills suffered premature failure after only 1 or 2 holes due to inappropriate point geometry, irrespective of the feed rate used (0.05-0.12mm/rev). However, lower thrust forces (Ti: ~25%, CFRP: ~41%) and torque (Ti: ~15.2%, CFRP: ~17.8%) were recorded when using domed PCD drills due to a smaller cutting edge radius (5.95μm) and rake face surface roughness (2.72μm Ra) when compared to CVD diamond coated drills. In Phase 2B research, a confirmation test to validate the performance of the preferred point design (140° point angle, a 40° helix angle and a 0.1mm chisel diameter) was undertaken. The results showed that the bespoke drill design generally outperformed the commercial drills evaluated in Phase 1 work. Phase 3 experiments assessed the influence of cutting fluid pressure/environment and feed rate on hole accuracy and surface integrity. When employing 10 bar external coolant, the maximum cutting temperatures in the Ti, CFRP and Al layers were ~351°C, ~244°C, and ~242°C respectively, which led to higher deviations in hole accuracy and poorer surface integrity compared to when operating with high pressure cutting fluid at 70 bar.

The key contributions of the research with respect to the single-shot drilling of Ti-6Al-4V/CFRP/A7050 stacks were: (i) improved understanding with regard to the influence of tool material/coatings on hole quality and surface integrity; (ii) identification of appropriate tool geometry and preferred cutting conditions and; (iii) correlation of the effect of cutting environment on resulting temperature and subsequent hole quality.

ACKNOWLEDGEMENTS

The author would like to express his appreciation to both Dr. Sein Leung Soo (Senior Lecturer and Head of the Machining Research Group) and Prof. David Keith Aspinwall in the School of Mechanical Engineering, University of Birmingham for their academic supervision and guidance over the period of the research.

Thanks are due to Andy Loat (Research and Development Technician) and Peter Thornton (Engine Research and Development Engineer), also from the School of Mechanical Engineering for their insightful discussions and assistance with the experimental work.

I am indebted to Will Thomas, Craig Carr and Sam Bradley (GKN Aerospace), David Pearson, Par Nordberg and Dr. Rachid M'Saoubi (Seco Tools), Dr. Peter Harden and Dr. Wayne Leahy (Element Six) for the provision of workpiece materials, tooling, funding as well as technical support for the research.

I would like to thank my fellow students and colleagues in the Machining Research Group for their valuable time, companionship and support during the course of the research.

Last but not least, I wish to express my deepest love and gratitude to my beloved parents, wife and daughters for their kind support, patience, love and understanding throughout this work.

TABLE OF CONTENTS

1 INTRODUCTION 1
1.1 Project background 1
1.2 Aims and objectives of the project 1
1.3 Structure of the thesis 2
2 LITERATURE REVIEW 3
2.1 Titanium alloys 3
2.1.1 Introduction 3
2.1.2 Classification of titanium alloys 3
2.1.2.1 Alpha (α) titanium alloys 3
2.1.2.2 Near α titanium alloys 4
2.1.2.3 Beta (β) titanium alloys 4
2.1.2.4 Alpha-beta (α+β) titanium alloys 4
2.1.3 Machinability of titanium alloys 5
2.1.3.1 Thermal conductivity 5
2.1.3.2 Chip contact length 6
2.1.3.3 Modulus of elasticity 6
2.1.3.4 Chemical reactivity 6
2.1.3.5 Chip formation in machining of titanium alloys 7
2.1.3.6 Titanium carbide layer formation 8
2.1.4 Industrial applications 8
2.2 Aluminium alloys 8
2.2.1 Introduction 8
2.2.2 Classification of aluminium alloys 9
2.2.3 Machinability of aluminium alloys 10
2.2.4 Industrial applications 10
2.3 Fibre reinforced plastic (FRP) composites 11
2.3.1 Introduction 11
2.3.2 Classification of fibre reinforced plastics 11
2.3.3 Matrix materials 12
2.3.4 Fibre reinforcement materials 13
2.3.5 Forms of FRPs and forming process 15
2.3.6 Prediction of properties in fibre systems 16
2.3.7 Machinability of fibre-reinforced composites 16
2.3.7.1 Influence of composite material 17

2.3.7.2 Influence of fibre orientation....17
2.3.7.3 Influence of cutting conditions....19
2.3.7.4 Effect of tool geometry/material....20
2.4 Drilling of multilayer composite/metallic stacks....20
2.4.1 Introduction....20
2.4.2 Cutting forces....21
2.4.2.1 Thrust force....21
2.4.2.2 Torque....22
2.4.3 Tool geometry....23
2.4.3.1 Chisel edge....23
2.4.3.2 Cutting edges....24
2.4.3.3 Rake angle....25
2.4.3.4 Point angle....26
2.4.4 Drilling of multilayer Ti/CFRP/Al stacks....26
2.5 Cutting tool materials....30
2.5.1 Introduction....30
2.5.2 Tool materials for drilling metallic-composite stacks....32
2.5.2.1 Cemented carbide (WC-Co)....32
2.5.2.2 Polycrystalline diamond (PCD)....33
2.5.3 Coatings....34
2.5.3.1 Chemical vapour deposition (CVD) diamond....35
2.5.3.2 Diamond-like carbon (DLC) coating....37
2.5.4 Tool wear....38
2.5.4.1 Wear of WC-Co tool material....40
2.5.4.2 Wear of PCD tool material....41
2.5.5 Cutting fluids and effects....42
2.6 Surface integrity in machining....44
2.6.1 Introduction....44
2.6.2 Surface texture parameters and characterisation....46
2.6.3 Diameter variation, out of roundness and cylindricity....48
2.6.4 Delamination....50
2.6.5 Burr formation....50
2.7 Temperature measurement and effects....53
2.7.1 Temperature effects in drilling of titanium alloys....54
2.7.2 Temperature effects in drilling of CFRP composite....55
2.7.3 Temperature effects in drilling aluminium alloys....55
2.8 Experimental design techniques and analysis....56

2.8.1 Full factorial experiments....56
2.8.2 Taguchi methods and factorial design....57
2.8.3 Analysing data from orthogonal arrays....57
2.8.3.1 Main effects plot....57
2.8.3.2 Analysis of variance (ANOVA)....58
2.8.3.3 Percentage contribution ratio (PCR)....58
2.8.3.4 Confirmation experiment....59
3 EXPERIMENTAL WORK....61
3.1 Workpiece materials....61
3.1.1 Titanium –Ti-6Al-4V alloy....62
3.1.2 CFRP composite laminates....63
3.1.3 Aluminium –A7050 alloy....65
3.2 Tool materials, geometries and coatings....65
3.2.1 Titanium-based coated carbide drills for Phase 1A....66
3.2.2 Multiple margin coated drills for Phase 1B....66
3.2.3 Diamond/diamond-coated drills in Phase 1C/Phase 2A....67
3.2.4 Bespoke geometry drills for Phase 1D/2B....69
3.2.5 Drills implanted with thermocouples for Phase 3....71
3.3 Equipment....72
3.3.1 Machine tool, cutting environment and fixturing....72
3.3.1.1 Matsuura FX-5 high speed machining centre....72
3.3.1.2 Cutting fluid supply....73
3.3.1.3 Fixturing of workpiece material....73
3.3.2 Cutting force measurement....74
3.3.3 Cutting temperature measurement....74
3.3.4 Tool wear measurement and microstructure analysis....75
3.3.5 Hole diameter, out of roundness and cylindricity measurement....76
3.3.6 Burr height measurement....76
3.3.7 Surface roughness and three-dimensional topography....77
3.3.8 Subsurface alteration analysis....78
3.3.8.1 Sample preparation....78
3.3.8.2 Microhardness measurement....79
3.3.8.3 Etching....79
3.3.8.4 Microstructure....79
3.3.8.5 SEM and EDX microscopy....80
3.4 Experimental design, procedures and test arrays....81
3.4.1 Phase 1A: Effect of tool material, feed rate and drilling strategy....82

3.4.2 Phase 1B: Influence of margin design, feed rate and drilling strategy.....83
3.4.3 Phase 1C: Hole quality and failure modes of diamond coated tools.....84
3.4.4 Phase 1D: Effect of drill point geometry.....84
3.4.5 Phase 2A: Evaluation of diamond coated/novel PCD drills and feed rate at elevated cutting speed.....86
3.4.6 Phase 2B: Confirmation test and benchmarking of bespoke drill geometry 87
3.4.7 Phase 3: Effect of cutting environment and feed rate.....87
4 RESULTS AND DISCUSSION.....89
4.1 Phase 1A: Effect of tool material, feed rate and drilling strategy.....89
4.1.1 Cutting force.....89
4.1.2 Tool wear and tool life.....91
4.1.3 Hole accuracy (diameter, out of roundness, cylindricity).....94
4.1.4 Burr formation.....96
4.1.5 Hole surface roughness.....98
4.1.6 Subsurface microhardness alteration.....100
4.1.7 Chip morphology.....103
4.2 Phase 1B: Influence of margin design, feed rate and drilling strategy.....104
4.2.1 Cutting force.....104
4.2.2 Tool wear.....106
4.2.3 Hole accuracy (diameter, out of roundness and cylindricity).....108
4.2.4 Burr formation.....110
4.2.5 Surface integrity.....112
4.3 Phase 1C: Hole quality and failure modes of diamond coated tools.....115
4.3.1 Cutting force.....115
4.3.2 Tool wear.....117
4.3.3 Hole accuracy.....120
4.3.4 Burr formation.....122
4.3.5 Hole surface roughness and topography.....124
4.3.6 Microhardness.....125
4.4 Phase 1D: Effect of drill point geometry.....127
4.4.1 Cutting force (thrust force and torque).....127
4.4.2 Tool wear and tool life.....129
4.4.3 Hole accuracy (diameter, out of roundness and cylindricity).....131
4.4.4 Burr formation.....134
4.4.5 Workpiece surface roughness and microhardness.....137
4.4.6 Subsurface alteration.....141

4.5 Phase 2A: Evaluation of diamond coated/novel PCD drills and feed rate at elevated cutting speed 145
4.5.1 Thrust force and torque 145
4.5.2 Tool wear and tool life 146
4.5.2.1 Fracture pattern in domed PCD drills 147
4.5.2.2 Failure pattern in CVD diamond coated drills 149
4.5.3 Hole accuracy (diameter, out of roundness, and cylindricity) 152
4.5.4 Burr formation 153
4.5.5 Surface integrity (roughness and microhardness) 154
4.6 Phase 2B: Confirmation test and benchmarking of bespoke drill geometry 157
4.6.1 Performance of preferred drill geometry 157
4.6.2 Comparison against uncoated, TiAlN/TiN coated and triple margin carbide drills 159
4.6.3 Comparison against diamond coated drills 160
4.7 Phase 3: Effect of cutting environment and feed rate 162
4.7.1 Cutting force 162
4.7.2 Tool wear and tool life 169
4.7.3 Hole accuracy (diameter, out of roundness, and cylindricity) 171
4.7.4 Burr formation 173
4.7.5 Hole surface roughness 175
4.7.6 Subsurface workpiece microstructure and microhardness 177
5 CONCLUSIONS 182
5.1 Literature review 182
5.2 Experimental work 182
5.2.1 Effect of tool material, feed rate and drilling strategy 182
5.2.2 Influence of margin design, feed rate and drilling strategy 183
5.2.3 Hole quality and failure modes of diamond coated tools 183
5.2.4 Effect of drill point geometry 184
5.2.5 Evaluation of diamond coated/novel PCD drills and feed rate at elevated cutting speed 185
5.2.6 Confirmation test and benchmarking of bespoke drill geometry 186
5.2.7 Effect of cutting environment and feed rate 186
5.3 Overall conclusions and recommended operating conditions 187
5.3.1 Tool material, coating and point geometry 187
5.3.2 Operating parameters 187
5.3.3 Cutting environment 187
6 RECOMMENDATIONS FOR FUTURE WORK 188
REFERENCES 189

APPENDIX 1 200
APPENDIX 2 201
APPENDIX 3 203
APPENDIX 4 206
APPENDIX 5 209
APPENDIX 6 212

LIST OF FIGURES

Figure 2.1 Cutting temperature of titanium alloys with carbide tool [9, 10]....6
Figure 2.2 Wear patterns of unsuitable tools for machining of titanium alloys [10] 7
Figure 2.3 Micrographs of (a) serrated-type chips from thermoplastic shear bands without fracture in the interior and (b) with fractures at the sides [13] 7
Figure 2.4 (a) Classification of composite material, (b) reinforcement phase [31]....12
Figure 2.5 (a) Atomic structure of carbon fibre [37], a schematic view of (b) high strength and (c) high modulus (PAN) carbon fibre [36] 14
Figure 2.6 Process flow of carbon fibre development for high strength/high modulus configurations [28]....14
Figure 2.7 Tensile strength and modulus map for utilities of carbon fibres [38]....15
Figure 2.8 (a) Lay-up configuration and woven fabrics in (b) plain weave, (c) three-harness satin weave and (d) five-harness satin weave [32] 15
Figure 2.9 Schematic of properties in transverse and longitudinal fibre systems [28] 16
Figure 2.10 Schematic of chip formation models in orthogonal cutting of CFRP [39] 18
Figure 2.11 Micrographs of fibre orientation of (a) 90 ˚and (b) 135˚ [41]....19
Figure 2.12 Surface textures in CFRP with DOCs of (a) 0.05mm and (b) 0.10mm [41]....19
Figure 2.13 Schematic of cutting system in composite: (a) geometry of cutting tool and fibre orientation, (b) spring-back effect [41]....20
Figure 2.14 Schematic of (a) triangle geometrical relationships in Merchant's force circle [75] and (b) cutting forces in drill [76]....22
Figure 2.15 Typical correlation of thrust force and torque over drilling tool radius [76]....23
Figure 2.16 Schematic view of chisel edge angle and chisel radius [72, 76]....24
Figure 2.17 Schematic of web angle, velocity angle and normal rake angle [72]....25
Figure 2.18 Influence of cutting lips over point angles [72] 26
Figure 2.19 Boeing 787 Dreamliner composite profile [80] 27
Figure 2.20 Schematic of single shot, two-shot and three-shot drilling operations 27
Figure 2.21 Range of mechanical/physical properties of various cutting tool materials [90]..31
Figure 2.22 (a) Ground surface with dislodged diamond grain in the matrix and; (b) laser machined surface with clean cut edge [100]....34
Figure 2.23 Morphology of multilayer coating (source: Sumitomo) [105]....35
Figure 2.24 (a) Columnar diamond coating, (b) nanocrystalline diamond film, (c) chisel edge of coated drill and (d) uncoated drill [106]....37
Figure 2.25 (a) Morphology of amorphous DLC coating [110], (b) diamond coating, ...38
Figure 2.26 Characteristics of typical wear patterns/features on cutting tools [105]....40
Figure 2.27 Schematic of flank wear (VB) in a single cutting point edge (ISO 3685) [115] ..40
Figure 2.28 (a) Solution wear and (b) fracture of WC in drilling of Ti-6Al-4V [119] 41
Figure 2.29 Chipping and fracture of PCD in machining of CFRP/Ti stacks [60] 42
Figure 2.30 Flow of HPC into chip-tool interface/cutting zones [128]....43
Figure 2.31 Effect of high pressure coolant on (a) surface roughness and (b) flank wear in machining titanium [123]....44
Figure 2.32 Schematic representation of a machined surface [136]....45
Figure 2.33 Typical defects/damage in drilling of metallic-composite stack materials [55] ...46
Figure 2.34 (a) Skewness and (b) kurtosis values corresponding to surface textures [145] 47
Figure 2.35 (a) Auto correlation function, and (b) power spectrum density plot [149] 48
Figure 2.36 (a) 'Walking effect' of chisel edge, (b) influence of depth of cut on harmonic effect and (c) multi-lobed roundness profile [145]....49

Figure 2.37(a) Computerised tomography scanning [139], (b) optical scanning [44] and (c) ultrasonic scanning [161] 50
Figure 2.38 Definition of burr according to ISO standard [166] 51
Figure 2.39 Classification of burrs according to Kim et al. [167] 51
Figure 2.40 Progression of burr formation [170] 52
Figure 2.41 Effect of surface exit angle on pivot point location [177] 53
Figure 2.42 Interlayer burr shapes in stack materials [172] 53
Figure 3.1 (a) Plate and (b) strip stack workpiece material 62
Figure 3.2 Micrograph of CFRP laminate sections [198] 64
Figure 3.3 (a) Specification [199], and coating configuration of (b) M type and (c) T type drills 66
Figure 3.4 (a) Specification [199] and (b) image of the triple margin drill 67
Figure 3.5 (a) Specification [199] and (b) image of DLC coated drill 68
Figure 3.6 (a) Specification [199] and micrographs of the (b) CVD diamond coated and (c) domed PCD drills 69
Figure 3.7 Schematic of web thinning and minimisation of obliquity 70
Figure 3.8 Schematic of normal rake angle 70
Figure 3.9 Bespoke drills used in Phase 1D 71
Figure 3.10 Drills with preferred combination of point geometry used in Phase 2B 71
Figure 3.11 TiAlN/TiN coated drills with implanted thermocouples 72
Figure 3.12 (a) Matsuura FX5 machining centre and (b) Dustomat 15 extraction system 72
Figure 3.13 Set up of (a) through-tool-coolant adoptor, (b) external nozzles and machining fixtures for plate and strip 73
Figure 3.14 Setup of Kistler (a) 9273 drilling dynamometer and (b) 5011 charge amplifiers 74
Figure 3.15 Setup of (a) rotary transmitter and (b) charge amplifier for temperature measurement 75
Figure 3.16 WILD M3Z toolmaker's microscope 75
Figure 3.17(a) Setup of Taylor Hobson Talyrond 300 and (b) schematic of measurement procedure for hole diameter 76
Figure 3.18 Surface roughness measurement using (a) Talysurf 120L, and (b) Surftest 77
Figure 3.19 Surface roughness and profile scanning using Alicona measurement system 77
Figure 3.20 (a) Mounting press and (b) grinding/polishing equipment 78
Figure 3.21 Mitutoyo MVK-G3 micro hardness testing 79
Figure 3.22 Leica DMLM microscope 80
Figure 3.23 (a) Emscope sputter coater and (b) JOEL 6060 SEM equipped with Inca EDX 80
Figure 3.24 Layout of the (a) plate and (b) strip machined workpieces 81
Figure 4.1 Cutting force plots at hole 90 using coated carbide tool at feed rate of 0.05mm/rev with (a) no pecking (Test 2) and (b) pecking (Test 6) 89
Figure 4.2 Cutting forces in drilling of Ti/CFRP/Al stacks at Hole 90 90
Figure 4.3 Progression of flank wear (VB) up to the end of test criterion in all tests 92
Figure 4.4 Cutting edge radius and substrate microhardness of (a) uncoated and (b) coated WC drills 93
Figure 4.5 Optical and SEM micrographs of worn drills in (a) Test 6 and (b) Test 5 93
Figure 4.6 Average hole diameters at test cessation 94
Figure 4.7 Out of roundness measurements of the (a) Ti, (b) CFRP and (c) Al layers at hole 90 in Test 3 95
Figure 4.8 Cylindricity form profile of last hole drilled in Test 5 and Test 6 96
Figure 4.9 (a) Optical images of burrs formed at the entrance of Ti and exit of Al layers in each experiment; and SEM of (b) entrance burr and (c) exit burr in Test 1 at test cessation 96

Figure 4.10 Progression of entrance burrs in the Ti layer 97
Figure 4.11 Progression of exit burrs in the Al layer 98
Figure 4.12 Average surface roughness (Ra) measurements over the test duration in all tests 98
Figure 4.13 Peak to valley surface roughness (Rt) measurements over the test duration in all tests 99
Figure 4.14 3-D surface topography in (a) Ti with pecking (Test 8), and (b) Ti, (c) CFRP, (d) Al without pecking (Test 4) using TiAlN coated WC at a feed rate of 0.08mm/rev 100
Figure 4.15 Microhardness depth profile at the last hole in Ti layer when drilling (a) without pecking and (b) with pecking for all tests 101
Figure 4.16 Subsurface microstructure of the last hole in Ti layer when drilling (a) without pecking, and (b) with pecking 101
Figure 4.17 Microhardness depth profile at the last hole in Al layers 102
Figure 4.18 Microstructure at the last hole in Al layer from Test 2 102
Figure 4.19 Chip morphology against cutting conditions and tool material recorded at the 30^{th}, 90^{th}, and 120^{th} holes 103
Figure 4.20 Main effect plots of thrust force and torque 104
Figure 4.21 Measurement of (a) thrust force and (b) torque in Ti, CFRP, Al layers 106
Figure 4.22 Main effect plot and ANOVA table for observation of tool wear 107
Figure 4.23 Tool flank wear at test cessation 107
Figure 4.24 Micrographs of (a) BUE (b) abrasion wear and (c) adhesion of Al alloy on the drill surface 108
Figure 4.25 Measurement of the hole diameter in all test 109
Figure 4.26 Measurement of hole out of roundness 110
Figure 4.27 Measurement of average hole cylindricity and out of roundness 110
Figure 4.28 Burr formation at hole entry and exit in the Ti and Al layers at the last hole produced using a triple margin drill and feed rate of 0.08mm/rev under pecking (Test 7) 111
Figure 4.29 Burr height measurement at the last hole in all tests 112
Figure 4.30 Hole surface roughness for each material layer in Tests 5 and 6 112
Figure 4.31 SEM micrograph of CFRP surface in (a) Test 5, (b) Test 6 113
Figure 4.32 Microstructure in (a) Ti and (b) Al layers of Hole 90 in Test 5 113
Figure 4.33 Microhardness measurements of Ti layers in hole 90 for all tests 114
Figure 4.34 Microhardness measurements of Al layers in hole 90 for all tests 115
Figure 4.35 Thrust for each material layer in all tests 116
Figure 4.36 Torque results for each material layer in all tests 116
Figure 4.37 Micrographs of drill wear progression in Test 1 118
Figure 4.38 EDX examination of adhered material on drill in Test 1 118
Figure 4.39 Micrographs of drill wear progression in Test 3 119
Figure 4.40 Micrographs of drill wear progression in Test 2 120
Figure 4.41 Average (a) hole cylindricity, (b) out of roundness over test duration 121
Figure 4.42 Hole cylindricity and profile at hole 70 in (a) Test 1, (b) Test 2 and (c) Test 3 . 122
Figure 4.43 Maximum entrance and exit burr height in Ti and Al layers in all test 123
Figure 4.44 Micrographs of entrance and exit burrs in Ti and Al layers at hole 70 in Test 1 123
Figure 4.45 Hole surface roughness of Ra and Rt over test duration 124
Figure 4.46 Micrographs of workpiece surfaces in Ti, CFRP and Al layers at hole 70 125
Figure 4.47 Microhardness depth profile measurement in the Ti and Al layers at the cessation of tests 126
Figure 4.48 Thrust force and torque in L9 test array 127
Figure 4.49 Main effect plots for thrust force and torque 128

Figure 4.50 Progression of tool wear in L9 test array 129
Figure 4.51 Main effects plot for tool wear 130
Figure 4.52 Micrographs of drill wear progression in Test 4 131
Figure 4.53 Average hole diameter over test duration 132
Figure 4.54 Average hole cylindricity and out of roundness over test duration 133
Figure 4.55 Maximum entrance and exit burr heights in Ti and Al layers 135
Figure 4.56 Exit burr form for hole 50, 70, 90 in Al layers 135
Figure 4.57 Main effects plot for burr height 136
Figure 4.58 Average roughness in Ti, CFRP and Al layers 137
Figure 4.59 Micrographs of hole surface texture in Ti layers 139
Figure 4.60 Micrographs of hole surface texture in CFRP layers 140
Figure 4.61 Micrographs of hole surface texture in Al layers 141
Figure 4.62 Micrographs of subsurface microstructure in Ti layers for all tests 142
Figure 4.63 Microhardness depth profile measurement for all tests in Ti layer 143
Figure 4.64 Micrographs of subsurface microstructure in Al layer for all tests 144
Figure 4.65 Microhardness depth profile measurement for all tests in Al layer 144
Figure 4.66 Thrust force and torque in the first hole for all tests 145
Figure 4.67 Scanning and measurement of cutting edge radius of new domed PCD and CVD diamond coated drills 146
Figure 4.68 Progression of tool wear to fracture in all tests 146
Figure 4.69 Micrographs of tool wear/fracture at the last hole for all tests 147
Figure 4.70 Micrograph of tool fractures at the cessation of Test 1 148
Figure 4.71 Micrograph of tool fractures at the cessation of Test 2 149
Figure 4.72 Micrograph of tool wear modes at the cessation of Test 4 150
Figure 4.73 Micrograph of tool fractures at the cessation of Test 5 151
Figure 4.74 Micrograph of tool fracture at the cessation of the Test 6 151
Figure 4.75 Average hole diameter over test duration 152
Figure 4.76 Average hole cylindricity and out of roundness over test duration 153
Figure 4.77 Burr height at the last hole in all tests 153
Figure 4.78 Burr at hole entry and exit in the Ti and Al layers at hole 10 in Test 6 154
Figure 4.79 Hole surface roughness in each material layer at test cessation 154
Figure 4.80 SEM micrographs and 3D topographic maps of CFRP hole surfaces in Test 1 and Test 4 155
Figure 4.81 Cross-sectional micrograph and microhardness depth profile in Ti layers 156
Figure 4.82 (a) Micrograph and (b) microhardness depth profile in Al layers 157
Figure 4.83 Thrust force, torque and temperature progression in Ti layer for last hole in Test 1 162
Figure 4.84 Thrust force, torque and temperature progression in Ti layer for last hole in Test 3 163
Figure 4.85 Thrust force, torque and temperature progression in Ti section for first hole in Test 6 164
Figure 4.86 Thrust force, torque and temperature progression in CFRP layer for last hole in Test 1 164
Figure 4.87 Thrust force, torque and temperature progression in Al layer for last hole in Test 1 165
Figure 4.88 Progression of cutting force and temperature in the Ti layer for all tests 166
Figure 4.89 Progression of cutting forces and temperature in the CFRP layer for all tests 167
Figure 4.90 Progression of cutting force and temperature in Al layer for all tests 168
Figure 4.91 Progression of tool flank wear in all tests 169
Figure 4.92 Micrographs of drill wear scar progression in Test 1 170

Figure 4.93 Optical and SEM micrographs of tool wear patterns after the last hole drilled in Tests 4, 5 and 6 171
Figure 4.94 Average hole diameter over test duration in all experiments..... 172
Figure 4.95 Average hole cylindricity and out of roundness over test duration in all experiments..... 173
Figure 4.96 Progression of entrance burr height in the Ti layer for all tests..... 173
Figure 4.97 Progression of exit burr height in Al layer for all tests..... 175
Figure 4.98 Average hole surface roughness (Ra) in Ti, CFRP and Al layers..... 176
Figure 4.99 Three dimensional surface topography scan of hole surface in CFRP layer from (a) Test 1 and (b) Test 3..... 176
Figure 4.100 Micrographs of microstructure alteration in Ti layer at the last hole..... 177
Figure 4.101 Micrographs of surface texture in CFRP layer at the last hole 178
Figure 4.102 Micrographs of subsurface microstructure in Al layer at the last hole 179
Figure 4.103 Microhardness depth profile measurement for the last hole drilled in the Ti layer for all tests..... 180
Figure 4.104 Microhardness depth profile measurement for the last hole drilled in the Al layer for all tests..... 181
Figure A5-1 Plate and strip stack workpiece material…….……..…….211
Figure A5-2 Micrograph of new and failed tools using E geometry design…….……..211
Figure A5-3 Micrograph of tool wear using D geometry of modified drills…...…….…….212
Figure A5-4 Micrograph the tool wear using F geometry of modified drills……..…212

LIST OF TABLES

Table 2.1 A list of commercial titanium alloys [1, 4]....3
Table 2.2 Classification of wrought aluminium [18] 9
Table 2.3 Designation of the first suffixed digit [20]....10
Table 2.4 Application of aluminium alloys in A380 airplane [18, 25] 11
Table 2.5 Properties of epoxy polymers compared with Al alloy and carbon steel alloy [32] 13
Table 2.6 Classification of carbon fibre via typical precursors [33] 13
Table 2.7 Key research publications on the drilling of metallic-composite stacks 21
Table 2.8 Properties of selected cutting tool materials/coatings and workpiece materials 31
Table 2.9 Properties of WC with varying grain size and Co content [14] 32
Table 2.10 Major PCD blank manufacturers, products and related properties [14]....34
Table 2.11 Surface integrity data set [132]....45
Table 2.12 Confounding process in an L8 array 57
Table 2.13 Results table for Taguchi L8 test....58
Table 2.14 Effects table for Taguchi L8 test 58
Table 2.15 Example of main effects plot....58
Table 3.1 Properties of annealed Ti-6Al-4V alloy [4] 63
Table 3.2 Specification and properties of CFRP laminate after curing [198] 64
Table 3.3 Properties of Al7050-T7651 alloy [20]....65
Table 3.4 Various point geometry combinations of the bespoke drill 70
Table 3.5 Grinding/polishing procedure and parameters for Ti and Al specimens....78
Table 3.6 Factors and their corresponding levels in Phase 1A....82
Table 3.7 Full factorial (2^3) test array in Phase 1A 82
Table 3.8 Factors and their corresponding levels in Phase 1B....83
Table 3.9 Full factorial (2^3) test array in Phase 1B 83
Table 3.10 Factors and their corresponding levels in Phase 1C....84
Table 3.11 Full factorial (2×2) test array in Phase 1C 84
Table 3.12 Phase 1D operating factors and their corresponding levels....85
Table 3.13 Taguchi (L9) test array in Phase 1D....85
Table 3.14 Phase 2A operating factors and their corresponding levels....86
Table 3.15 Phase 2A test matrix....86
Table 3.16 Phase 2B operating factors and preferred drill geometry....87
Table 3.17 Phase 3 operating factors and their corresponding levels 88
Table 3.18 Phase 3 test array....88
Table 4.1 ANOVA table for the thrust force and torque in each material layer 91
Table 4.2 ANOVA table for thrust force and torque....105
Table 4.3 ANOVA table for thrust force and torque....128
Table 4.4 ANOVA table for tool wear 130
Table 4.5 ANOVA table for hole diameter 132
Table 4.6 ANOVA table for average hole cylindricity and out of roundness....134
Table 4.7 ANOVA table of burr height in Ti and Al layers....136
Table 4.8 ANOVA table of hole surface roughness (Ra) in Ti and Al layers....138
Table 4.9 Validation of results produced using the bespoke design drill in Phase 1D 158
Table 4.10 Comparison of bespoke drill performance to results from Phase 1A/1B/1D....159
Table 4.11 Comparison of bespoke drill performance to results from Phase 1C/1D....161
Table A3-1 ANOVA table for tool wear in Phase 1A experiment..……...204

Table A3-2 ANOVA table for diameter in Phase 1A experiment.……204
Table A3-3 ANOVA table for burr height in Phase 1A experiment…….205
Table A3-4 ANOVA table for peak-to-valley roughness (Rt) in Phase 1A experiment…...205
Table A4-1 ANOVA table for diameter in Phase 1B experiment…….207
Table A4-2 ANOVA table for cylindricity/out of roundness in Phase 1B experiment……208
Table A4-3 ANOVA table for burr height in Phase 1B experiment……209

NOMENCLATURE

ACF	:	Autocorrelation function
Al	:	Aluminium
AMZ	:	Altered material zone
ANOVA	:	Analysis of variance
BCC	:	Body centred cubic
BUE	:	Built-up edge
BUL	:	Built-up layer
CCD	:	Charge-couple device
CFRP	:	Carbon fibre reinforced plastic
Co	:	Cobalt
cp	:	Commercially pure
Cr	:	Chromium
CR	:	Edge recession parallel to clearance face
CTE	:	Coefficient of thermal expansion
Cu	:	Copper
CVD	:	Chemical vapour deposition
DLC	:	Diamond-like carbon
DOC	:	Depth of cut
DOE	:	Design of experiment
E_1	:	Elastic modulus in longitudinal direction
E_2	:	Elastic modulus in transverse direction
EDG	:	Electrical discharge grinding
EDM	:	Electrical discharge machining
EDWM	:	Electrical discharge wire machining
F_{ad}	:	Adjusted delamination factor
F_d	:	Delamination factor
Fe	:	Iron
FRPs	:	Fibre reinforced plastics
H	:	Hydrogen
HCP	:	Hexagonal closed pack
HK	:	Knoop microhardness
HPC	:	High pressure coolant

HV	:	Vickers hardness
K_{IC}	:	Fracture toughness (Type I)
LN_2	:	Liquid nitrogen
LR	:	Wear land on rake face
Mn	:	Manganese
Mo	:	Molybdenum
MoS_2	;	Molybdenum disulfide
MQL	:	Minimum quantity lubricant
O	:	Oxygen
PAN	:	Polyacrylonitrile base carbon
PCD	:	Polycrystalline diamond
PCR	:	Percentage contribution ratio
PSDF	:	Power spectrum density function
PVD	:	Physical vapour deposition
Ra	:	Average roughness
Rq	:	Root mean square roughness
RR	:	Edge recession parallel to the rake face
Rt	:	Total peak-to-valley roughness
Rz	:	Mean roughness depth (5 sampling lengths)
SEM	:	Scanning electronic metrology
Sa	:	Average surface roughness (3D parameter)
St	:	Total peak-to-valley roughness (3D parameter)
Si	:	Silicon
SI	:	Surface integrity
Sn	:	Tin
sp^2	:	Hexagonal graphite lattice
sp^3	:	Tetrahedral diamond lattice
t	:	Web thickness
Ta(Nb)C	:	Tantalum niobium carbide
Tg	:	Glass transition temperature
Ti	:	Titanium
TiAlN	:	Titanium aluminium nitride
TiC	:	Titanium carbide
TiN	:	Titanium nitride
V	:	Vanadium

V_B	:	Flank wear
V_f	:	Volume of fibre
V_m	:	Volume of matrix
WC	:	Tungsten carbide
Zr	:	Zirconium
α	:	Rake angle
α_1	:	Coefficient of thermal expansion in longitudinal direction
α_2	:	Coefficient of thermal expansion in transverse direction
δc	:	Chisel edge angle
ρ_c	:	Density of composite
ρ_f	:	Density of fibre
ρ_m	:	Density of matrix
χ	:	Point angle
Ψ	:	Velocity angle
ω	:	Web angle
r	:	Drill radius
Ω_1	:	Primary relief angle
Ω_2	:	Secondary relief angle
ω_c	:	Weight of composite
ω_f	:	Weight of fibre
ω_m	:	Weight of matrix

1 INTRODUCTION

1.1 Project background

Owing to the increasing use of polymer based composites coupled with metallic alloys in aircraft structures, recent research activities have concentrated on understanding the effect of operating conditions as well as the behaviour of carbon fibre reinforced plastic (CFRP) and associated stack arrangements when drilling, with the principal aim of enhancing productivity and component integrity. The process of hole making in hybrid stack materials is currently carried out by drilling each layer separately followed by deburring prior to assembly for final reaming in order to meet part tolerance and surface roughness requirements. Published information on the drilling of metallic-composite stacks is limited, with available data indicating poor tool life and low productivity when employing hardmetal coated carbide drills. Difficulties associated with single-shot drilling of metallic-composite stacks stem primarily from the dissimilar properties of the different material layers, while research challenges include the identification of appropriate process conditions (cutting parameters, tool geometry/material, machining strategy etc.) to achieve the required hole quality and integrity at acceptable tool life.

The research detailed in the thesis was carried out in the Machining Research Group at the University of Birmingham as part of a Doctor of Philosophy (PhD) degree programme to investigate the single-shot drilling of 3-layer metallic-composite stacks. The project was undertaken in collaboration with a consortium of three industrial partners involving GKN Aerospace, Seco Tools, and Element Six, who provided financial as well as in-kind contributions and technical support. Details of the contact persons at each organisation together with their respective input are provided in Appendix 1.

1.2 Aims and objectives of the project

The overall aim of the project was to investigate the feasibility of single-shot drilling of 3-layer Ti/CFRP/Al stack materials and develop appropriate process capability as a potential alternative/replacement of the current multi-shot procedure employed in industrial production. The hole diameter selected for the work was in the main 6.35mm, with corresponding target specifications and tolerances detailed below:

- Hole diameter: 6.35 ±0.035mm

- Hole cylindricity: ≤150μm
- Hole out of roundness: ≤50μm
- External burr height: ≤0.2mm and inter-layer burr height ≤0.1mm
- Surface roughness: ≤1.6μm Ra in the metallic layers and ≤5.6μm Ra in the composite layer
- Hardened or neutral subsurface microhardness

More specifically, the key objectives of the work were to:

- Undertake an in-depth literature review on the drilling of multilayer metallic-composite stacks together with related topics including the effect of workpiece material properties, cutting parameters, and tool materials/geometry on machining performance.
- Establish the influence of drill geometries, coatings and tool materials when single-shot drilling Ti/CFRP/Al stacks.
- Identify tool wear mechanisms and its effects on workpiece surface/component quality.
- Evaluate the effect of operating parameters (cutting speed, feed rate and drilling strategy) and cutting environment on tool life, cutting temperature, hole accuracy/quality and surface integrity when drilling 3-layer stacks in a single-shot operation.
- Determine preferred point geometry together with associated operating parameters appropriate for single-shot drilling of Ti/CFRP/Al stacks at acceptable productivity rates and hole quality.

1.3 Structure of the thesis

The thesis comprises 6 main chapters. Following the introduction detailed here, a comprehensive literature review is presented in Chapter 2 covering the machinability of titanium alloys, CFRP composites, aluminium alloys and associated stacks together with the influence of key process factors including cutting parameters and tool materials on resulting hole accuracy and surface integrity. Chapter 3 outlines the equipment, workpiece materials and test procedures utilised together with the experimental arrays employed in each of the phases. The results from the experimental work are presented and discussed in Chapter 4 with the corresponding conclusions drawn from the research detailed in Chapter 5. Finally, suggestions for future research are highlighted in Chapter 6.

2 LITERATURE REVIEW

2.1 Titanium alloys

2.1.1 Introduction

Titanium alloys have been increasingly used from the 1950's for components in the aerospace industry, chemical processing/petroleum refining equipment and medical implants [1], due to their high strength-to-weight and modulus-to-weight ratios, high fracture strength and corrosion resistance. Owing to their inherent mechanical, chemical and thermal properties, the machining of titanium alloys is less straightforward compared with 'conventional' alloys particularly when precision assembly and workpiece surface integrity are key requirements. Research has been undertaken in respect of a range of manufacturing process as well as cost effective solutions for volume production [2].

2.1.2 Classification of titanium alloys

Titanium alloys have been formulated to various specifications, with elements such as aluminium, oxygen, nitrogen, molybdenum, vanadium as well as niobium [3], and classified as alpha (α), near α, alpha-beta (α+β) and beta (β) titanium alloys depending on their overall chemical composition and structure, see Table 2.1 [1, 4].

α/near α titanium alloys	β titanium alloys	α+β titanium alloys
Grade 1 (cp-Ti:0.2Fe,0.18O)	Beta C Ti-3Al-8V-6Cr-4Mo-4Zr	Ti-6-4 (Ti-6Al-4V)
Grade 4 (cp-Ti:0.5Fe,0.40O)	Ti-10-2-3 (Ti-10V-2Fe-3Al)	Ti-6-6-2 (Ti-6Al-6V-2Sn)
Grade 6 (Ti-5Al-2.5Sn)	Ti-15-3 (Ti-15V-3Cr-3Al-3Sn)	Ti-6-2-2-2-2 (Ti-6Al-2Sn-2Zr-2Mo-2Cr)
Ti-6Al-2Sn-4Zr-2Mo		Ti-6-2-4-6 (Ti-6Al-2Sn-4Zr-6Mo)

Table 2.1 A list of commercial titanium alloys [1, 4]

2.1.2.1 Alpha (α) titanium alloys

These alloys have excellent corrosion resistance and deformability. The commercially pure grades (cp1-4) of titanium with hexagonal closed-pack (HCP) α phase, are used in the annealed condition with limited secondary phase retained in the matrix and exhibit tensile

strength in the range of 240-740MPa [4]. Their major applications benefit from α titanium's cold formability, corrosion resistance and good weldability [3, 5]. Aluminium, carbon, oxygen and nitrogen are α-stabilisers, which are added to improve physical properties and mechanical properties, whilst palladium is alloyed to enhance corrosion resistance for extreme requirements. In general, yield strengths range from 170-480MPa due in part to the interstitial alloying element, oxygen [6], although ductility decreases.

2.1.2.2 Near α titanium alloys

Near α titanium alloys are highly α-stabilised. They contain α elements which provide excellent creep resistance with small quantities of β-stabilisers, such as vanadium, molybdenum, chromium, copper, magnesium and tantalum, which offers increased strength up to 1050MPa [1, 3]. Aluminium is added to increase the creep and oxidation resistance, but is limited to a maximum of 6% due to stress corrosion problems [4]. In addition, the ultimate service temperature is typically within the range of 500-550°C.

2.1.2.3 Beta (β) titanium alloys

This group of titanium alloys mainly incorporate β-stabilisers' such as molybdenum, vanadium, iron, chromium and niobium, in order to reduce the β-transus temperature for the phase transformation to a body centred cubic (BCC) phase as well as enhanced ductility. They are characterised by superior forging capability and cold formability [1, 3]. The β-stabilisers retained in the microstructure during heat treatment provides control of the β grain size and the volume fraction of α precipitation to meet various metallurgical and mechanical performance [5]. Solution treated β titanium alloys may have a yield strength of 900-1400MPa and appreciable fracture toughness (K_{IC}) of 70MPa-$m^{½}$. They are used in applications such as structural components and gas turbine discs [4].

2.1.2.4 Alpha-beta (α+β) titanium alloys

Alpha-beta (α+β) alloys contain a high percentage of α-stabilising and β-stabilising elements, providing a mixture of the characteristics of α and β alloys. As previously detailed, the α-stabilising elements are interstitial oxygen, nitrogen and carbon, resulting in improved strength at high temperatures; whereas the β-stabilising elements are subdivided into β-isomorphous alloying elements (Mo, V, Ta, Nb) and β-eutectoid alloying elements (Fe, Mn, Cr, Co, Ni, Cu, Si, H), which form inter-metallic compounds to strengthen the α matrix.

Generally, high α content provides high creep resistance and elevated temperature strength whereas high β content results in higher density and room temperature strength [3, 7]. Heat treatments are employed to obtain fully lamellar structures, fully equiaxed structures and bi-modal microstructures, by adjusting the volumes of the α-phase and β-phase in the microstructure, thereby leading to better mechanical and metallurgical properties for various applications [1, 8].

The most widely used α+β alloys have a β volume fraction of 5 - 40%. The alloy Ti-6Al-4V has 4wt% of vanadium (V) added to pure Ti to stabilise the β-phase and reduce the transformation temperature while the 6wt% of aluminium (Al) is added to increases the β transformation temperature. As a result, the β transformation temperature of Ti-6Al-4V increases to 980˚C and provides greater flexibility for a wide range of solution hardening treatments. The Ti-6Al-4V alloy is the most common α+β titanium with a yield strength of 880MPa at elevated temperatures of 350-400°C [5]. The alloy accounts for ~ 60% of the total volume of titanium products. The use of titanium in an airframe is 80-90% [5].

2.1.3 Machinability of titanium alloys

Titanium alloys are classified as difficult-to-cut materials due to their high temperature strength (880MPa at 350-400˚C) [9], low thermal conductivity (7.5w/mK), high chemical reactivity [10] and relatively low modulus of elasticity (114GPa). The material is also prone to strain hardening due to the formation of a harder second phase in the matrix at elevated temperatures during machining [8]. Research work has focused on overcoming problems related to their properties, as discussed in the following sections.

2.1.3.1 Thermal conductivity

Low thermal conductivity induces high cutting temperature [1]. Narutaki et al. [10] highlighted that the thermal conductivity of titanium alloys was about 7.5w/mK (1/6 of steel), resulting in heat being retained at the tip of the cutting edge. This has been shown to reach 1000K, even at low cutting speeds of 60m/min; whereas the same cutting speed in the machining of carbon steel produced a cutting temperature that was ~ 250K lower [10]. Figure 2.1 shows the variation in cutting temperature with respect to cutting speed when machining Ti alloys compared to carbon steel. Zoya et al.[9] found that when machining titanium alloys, temperature reached 800-850˚C, the HCP phase transformed to BCC and thereby increased

the chip strain and reduced chip-tool contact length. However, Karpat [11] proposed a revised model based on the relationship between strain and flow stress by considering the dynamic strain aging effect which led to thermoplastic instability. He reported that machining Ti-6Al-4V at cutting speeds of 30-120m/min and a feed rate of 0.1mm/rev, the corresponding temperature was lowered to ~ 350˚C.

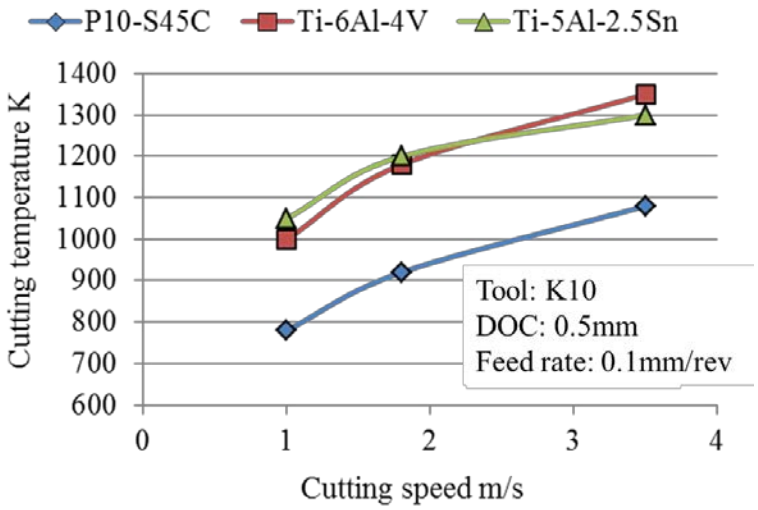


Figure 2.1 Cutting temperature of titanium alloys with carbide tool [9, 10]

2.1.3.2 Chip contact length

Small chip contact length causes high cutting pressure. Zoya et al. [9] concluded that the shorter contact length (about 30% of steel) caused a higher cutting pressure, which was three to four times higher than in the machining of steel, leading to compression rupture at the contact surface.

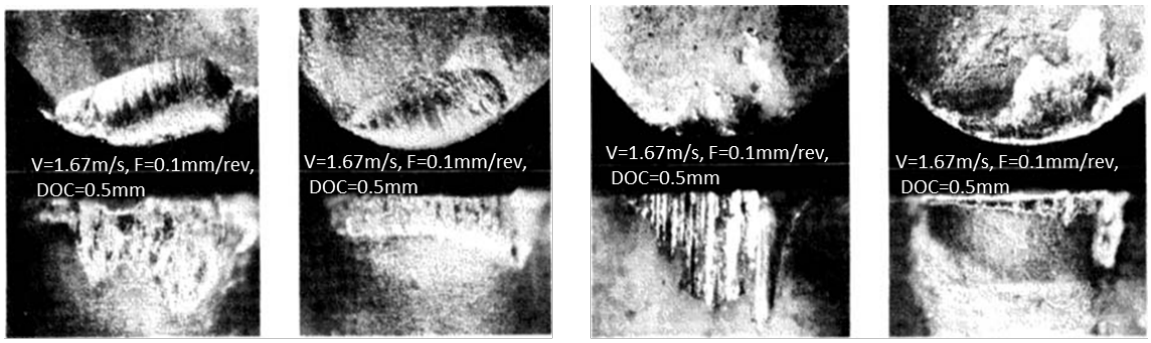
2.1.3.3 Modulus of elasticity

The low modulus of elasticity of titanium alloys can produce chatter. Ezugwu et al. [1, 8] suggested that when cutting titanium alloys, the cyclic movement of chip formation caused by deflection exerted vibration effects on the cutting tool, which introduced chatter. The high frequency vibration presented a cyclic loading on the cutting tool and initiated fatigue failure.

2.1.3.4 Chemical reactivity

High chemical reactivity dissolves elements from cutting tools or produces a build-up of compounds on the cutting edge. In the work by Hartung et al. [12] , it was found that titanium

alloys reacted with all cutting materials when the operating temperature was ~ 500°C. In the early stage, any strain hardened layer was dissolved or compounds were welded to the cutting tool. Figure 2.2 indicates the typical tool wear patterns resulting from solution wear [10].



(a) Cermet tool, dry cutting at 3 mins. (b) TiC coated tool, dry cutting at 2 mins. (c) Ceramic tool, dry cutting at 0.5 min. (d) CBN tool, wet cutting at 20 min.

Figure 2.2 Wear patterns of unsuitable tools for machining of titanium alloys [10]

2.1.3.5 Chip formation in machining of titanium alloys

Titanium chips can be continuous and periodically serrated, due to adiabatic shear band formation [13, 14] and fracture initiation theory [15]. In Komanduri and Von Turkovich's work [13], thermoplastic deformation occurred without fracture along the rake surface of the cutting tool, as seen in Figure 2.3(a) [13]. The thermoplastic deformation competed with strain hardening due to dislocation movements producing the serrated chip forms. Conversely, Shaw [15] and Shaw and Vyas [16] suggested that periodic shear fracture was introduced from the free surface of the workpiece to the tool tip with no plastic flow observed, as shown in Figure 2.3(b) [13].

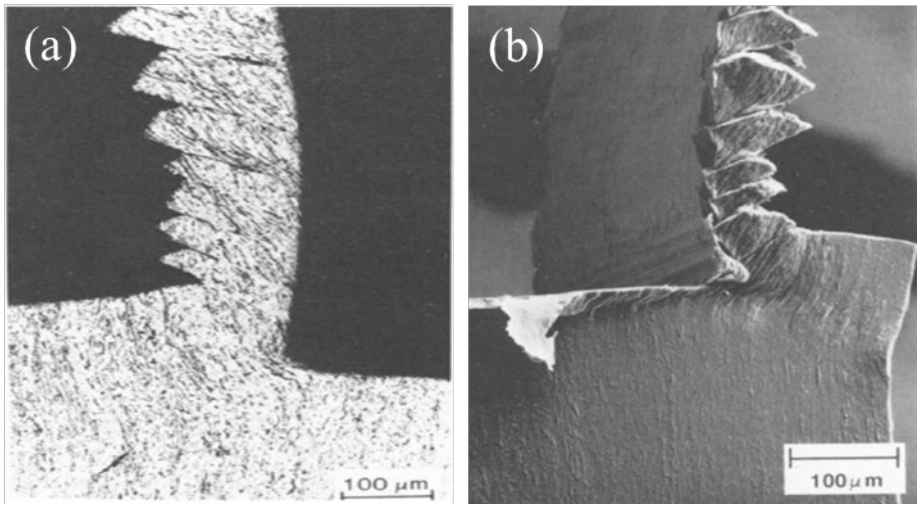


Figure 2.3 Micrographs of (a) serrated-type chips from thermoplastic shear bands without fracture in the interior and (b) with fractures at the sides [13]

2.1.3.6 Titanium carbide layer formation

It was observed that the formation of a thin layer of titanium carbide on the contact surface of cutting tools could hinder the dissolution and diffusion of the elements/compounds released from the cutters and maintain the hardness of the tool during operation. Hartung et al. [12] demonstrated that the thickness of the built-up layer (TiC) was determined by the balance of the diffusion flux of the tool constituents, the removal of tool constituents through chemical dissolution and the migration from titanium chips through the tool/chip interface. However, when the "protective layer" of TiC was generated by coating carbide tools using CVD technology, it did not provide the expected advantage. The coated layer rapidly flaked and deteriorated. Nabhani et al. [6] reported that PCD tools provided better wear resistance due to the existence of the TiC layer.

2.1.4 Industrial applications

Titanium alloys are primarily used in the aerospace industry for fans, compressor blades and discs, housings of the engines as well as structural components like wings and frames. Titanium alloys are also employed in other areas, such as:

- Process engineering for corrosion resistant parts made from commercially pure titanium alloys (G1-G7) [1].
- Marine engineering and power supply. Components include structural frames and steam turbine blades made of Ti-6Al-4V alloy for the advantage of corrosion resistance and high temperature strength [5].
- Automotive industry. Cold deformable titanium alloys and forgeable β alloys, Ti-22V-4Al and Ti-20V-4Al-1Sn, are utilised in order to reduce component weight particularly in automotive engine assembly [1].

2.2 Aluminium alloys

2.2.1 Introduction

Material selection in structural applications includes considerations such as weight to strength properties, fabrication capability and machinability; with aluminium alloys generally presenting the best-in-class solutions. Aluminium alloys are typically ~ 33% the weight of

steels, can be alloyed to provide high yield strength (455MPa)/tensile strength (515MPa) for A7050 T736, have low electrical resistance (28nΩ•m) and high thermal conductivity (231W/mK) for A1050 O together with high corrosion resistance, weldability and recycling capability [17, 18]. This makes it suitable for a broad range of applications in the aerospace [19], automotive and construction industries as well as for consumer electronics and mechanical equipment [17]. The shaping processes available for aluminium alloys are extensive, which includes casting, extrusion, forging, stamping, forming, powder metallurgy together with nearly all machining operations (generally not grinding).

2.2.2 Classification of aluminium alloys

According to the applications of aluminium alloys, fabrication processes are grouped according to: wrought and casting alloys [17]. The specifications for each group are categorised by the major alloying elements. Wrought aluminium alloys are specified with four-digit designation codes, initiated by the International Alloy Designation System (IADS). The alloys are identified with their principal alloy elements and applications [18], see Table 2.2.

Series	Principal alloying element	Applications
1xxx	99% are aluminium	chemical equipment and electrical conductors
2xxx	copper	aircraft structure and machine products
3xxx	manganese	sheet metal works
4xxx	silicon	welding electrodes and pistons
5xxx	magnesium	welded pressure vessel, salted water service
6xxx	magnesium and silicon	high strength structures
7xxx	zinc	aircraft, heavy duty/high strength
8xxx	other elements	N/A

Table 2.2 Classification of wrought aluminium [18]

The temper designations are denoted as F for as fabricated, H for strain-hardened, O for annealed, T for heat treatment and W for solution-heat-treated only [17]. Amongst these treatments or conditions, heat treatment T is followed with one to four suffixed digits, as seen in Table 2.3 [20], indicating the secondary treatment to adjust the properties, for instance, A2024-T8 and A7075-T6 used in upper fuselage panels [19].

First suffixed digit	Definition
1	Partial solution plus natural ageing
2	Annealed cast product only
3	Solution plus cold work
4	Solution plus natural ageing
5	Artificially aged only
6	Solution plus artificial ageing
7	Solution plus stabilising
8	Solution plus cold work then artificial ageing
9	Solution plus artificial ageing then cold work

Table 2.3 Designation of the first suffixed digit [20]

2.2.3 Machinability of aluminium alloys

The machining of aluminium alloys, has been extensively reviewed in the last two decades, with the paper by Konig and Erinski [21] detailing the machinability of cast alloys. Aluminium alloys can be machined by a wide range of cutting tool materials such as high speed steel, straight grade carbide, diamond and diamond coated tools [15]. Alumina based ceramic tools are not suitable due to chemical reactivity problems leading to diffusion/solution wear [14]. In the machining of aluminium alloys, the wear patterns are cutting edge rounding and abrasion wear on the flank face due to friction and mechanical force induced plastic deformation [21, 22]. Sánchez et al. [23] concluded that adhesion wear due to a built-up layer (BUL) and built-up edge (BUE) initiated by metallurgical fusion and mechanical adhesion, were prevalent at low cutting speeds (< 60m/min), leading to degradation of cutting tool performance. The vast majority of aluminium drilling operations are performed wet with a lubricant, however the recent development of dry machining using diamond/diamond coated tools, provides improved machined surface roughness and lower cutting forces as well as longer tool life and hole accuracy [22, 24].

2.2.4 Industrial applications

In terms of aluminium alloy consumption, 50% is accounted for by construction and transportation [20]. The recently launched Airbus A380 aircraft is comprised of 61% aluminium alloys used in the wing structure and fuselage [25, 26]. Table 2.4 details the specific aluminium alloys used in high load and heavy duty sections in the wing and fuselage components along with their mechanical and functional requirements.

Alloy-temper condition	Application	Mechanical/functional requirement
7056-T7951	Upper wing panels	Fracture toughness, fatigue strength
7010-T7651	Upper outer wing panel, heavier gauge wing ribs	Compression yield strength and modulus
7040-T7651	Fuselage main frames, cockpit window frame, beam, fittings	Static strength and toughness properties
7449-T7651	Lower gauge wing ribs	Static strength and modulus
7040-T7651	Wing spars	Static and fracture toughness
7449-T79511	Upper wing stringers	Static strength and modulus

Table 2.4 Application of aluminium alloys in A380 airplane [18, 25]

2.3 Fibre reinforced plastic (FRP) composites

2.3.1 Introduction

Over the past 30 years, fibre reinforced polymer (FRP) composites have developed to the stage where their strength (CFRP~4.3GPa) and modulus (CFRP~562GPa) are such that they are replacing metallic alloys for a large number of applications in the aerospace industry [27, 28]. The use of FRP composites, which were previously restricted to secondary structural designs (fuselage sections, spars and tail wings), can now been found in a greater number of Class 1 structures such as fans and airframes. For example, the new Boeing 787 Dreamliner and Airbus A380 were constructed with CFRP in their fuselage, instead of using aluminium alloys, providing a weight reduction advantage and high fatigue strength benefits [27, 29, 30].

2.3.2 Classification of fibre reinforced plastics

The classification of composites is detailed in Figure 2.4(a) indicating the various combinations of the matrix and reinforcement materials, with examples of the different shape/arrangements illustrated in Figure 2.4(b) [31].

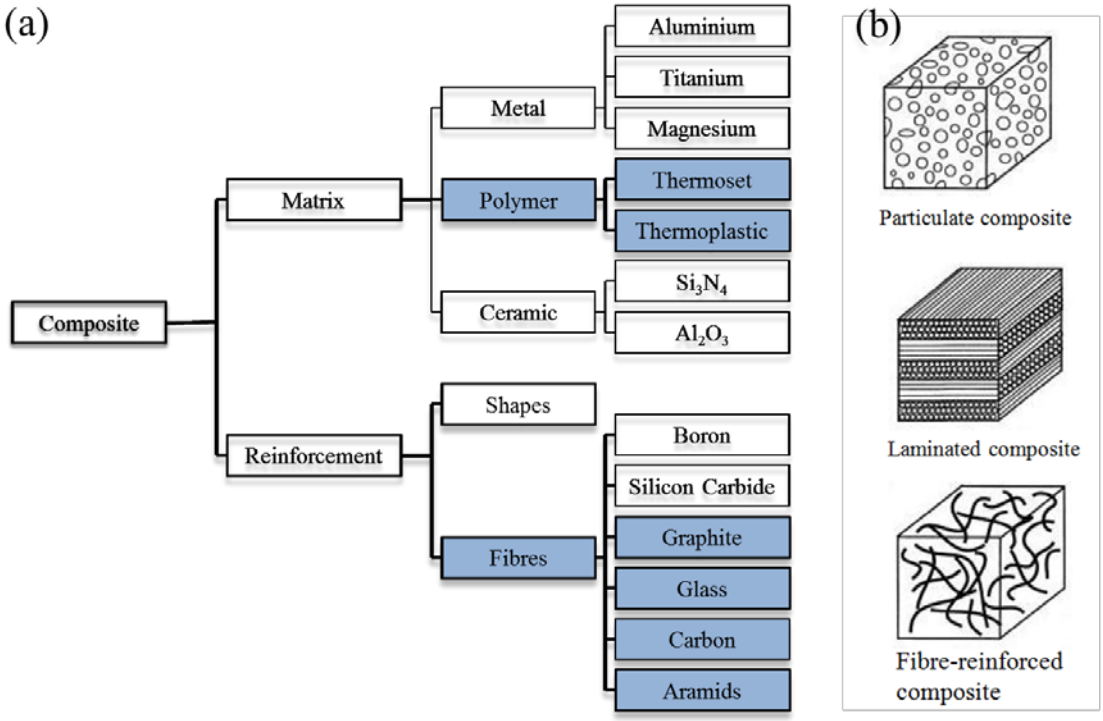


Figure 2.4 (a) Classification of composite material, (b) reinforcement phase [31]

2.3.3 Matrix materials

The matrix phase (thermoset or thermoplastic polymers) function as a binder to retain fibres in the preferred arrangement, transferring/distributing loads to the fibre axis and transmitting shear forces across the fibres [31]. They also act to protect the fibres from environmental attack and enhance their electrical and chemical properties [32]. Thermoset polymers are amorphous in both solid and liquid phases and cannot be melted by heating, due to the strong intermolecular/intramolecular covalent bonds, leading to stiffer, tougher and harder properties [33]. Conventional thermoset resin (epoxy) can be used in temperatures up to 250°C with a recorded glass transition temperature (Tg) of 180°C [28]. Principally, epoxy used as a matrix material has advantages such as excellent adhesion and bonding strength, inertness to chemicals and thermal resistance, appreciable mechanical properties and electrical insulation [27]. Table 2.5 [32] details the properties of epoxy compared to polyester resins and metallic alloys.

Polymers	Density (g/cm³)	Young's modulus (GPa)	Tensile strength (MPa)	Strain to failure (%)	Thermal conductivity (W/m°C)	Tg (°C)	Tm (°C)
Epoxy	1.10-1.20	2.6-3.8	60-85	1.5-8.0	0.17-0.20	65-175	-
Al. alloy 7075 T6	2.8	71	572	11	130	-	660
Steel 1020 cold drawn	7.85	207	420	15	51.9	-	1535

Table 2.5 Properties of epoxy polymers compared with Al alloy and carbon steel alloy [32]

2.3.4 Fibre reinforcement materials

The reinforcement fibre specified for high strength/high modulus applications is carbon fibre; its strength depending on its molecular structure, bonding mechanism and fibre orientation. Carbon fibres are extracted through a spinning process from three major precursors [34]; Rayon, PAN and pitch, followed by serial heat treatment processes [35] to produce the final product which is the filament, ranging from 5 to 8μm in diameter. The mechanical properties are detailed in Table 2.6. Figure 2.5(a) shows the atomic structure of the carbon fibre with its layered hexagonal lattice, which is parallel to each other and connected via intermolecular forces, resulting in different characteristics (soft or brittle). In Figure 2.5(b), the high tensile strength carbon fibre extracted from the PAN precursor is characterised with a turbostratic structure reflecting folded and crimped carbon layers after heat treatment. In Figure 2.5(c), the high modulus carbon is shown to be homogeneously graphitised with a hexagonal graphite structure after heat treatment [36, 37]. The process flow of the heat treatment is detailed in Figure 2.6. Figure 2.7 shows the service range of the high strength carbon fibre and high modulus carbon fibre [38].

Types by fibre precursors	Ultimate tensile strength (MPa)	Tensile modulus (GPa)	Density (g/cm³)	Diameter (μm)
Rayon-based carbon (Thronel 25)	1200-1400	166-193	1.47	5-9
Rayon-based carbon (Thronel 50)	1900-2100	303-379	1.66	8-11
PAN-based carbon (high modulus)	1600-1900	379-414	1.99	5-8
PAN-based carbon (high strength)	2200-2600	221-262	1.75	6-8
Pitch-based carbon (low-temperature heat-treated)	5000	350	2.1	9-11

Table 2.6 Classification of carbon fibre via typical precursors [33]

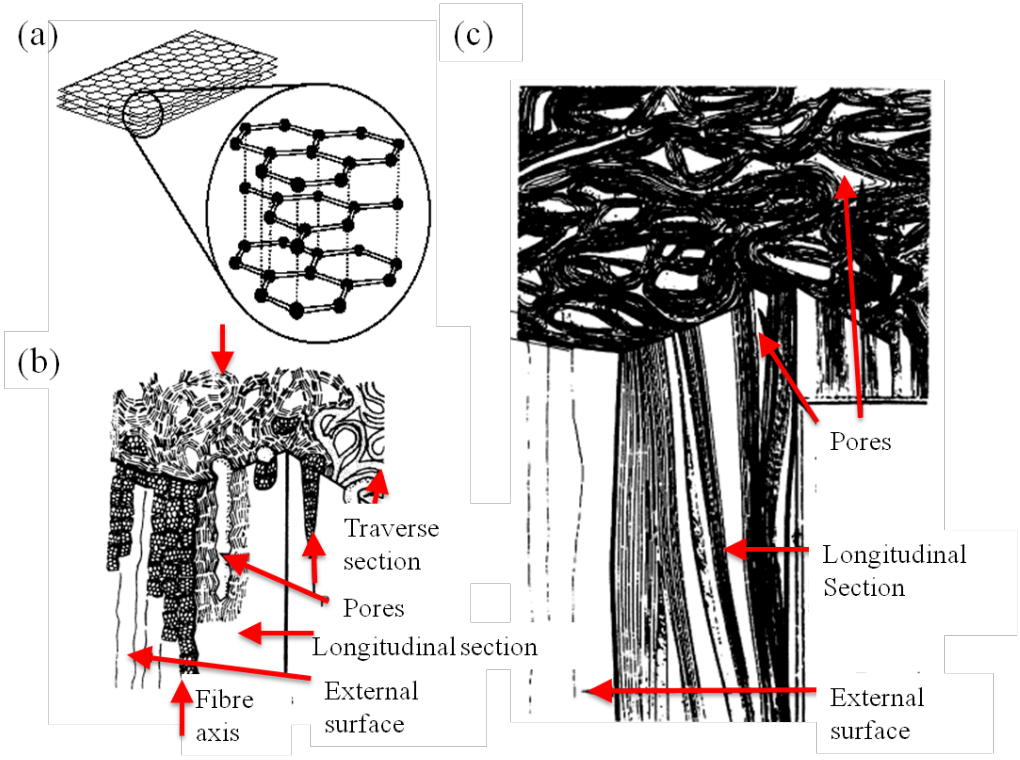


Figure 2.5 (a) Atomic structure of carbon fibre [37], a schematic view of (b) high strength and (c) high modulus (PAN) carbon fibre [36]

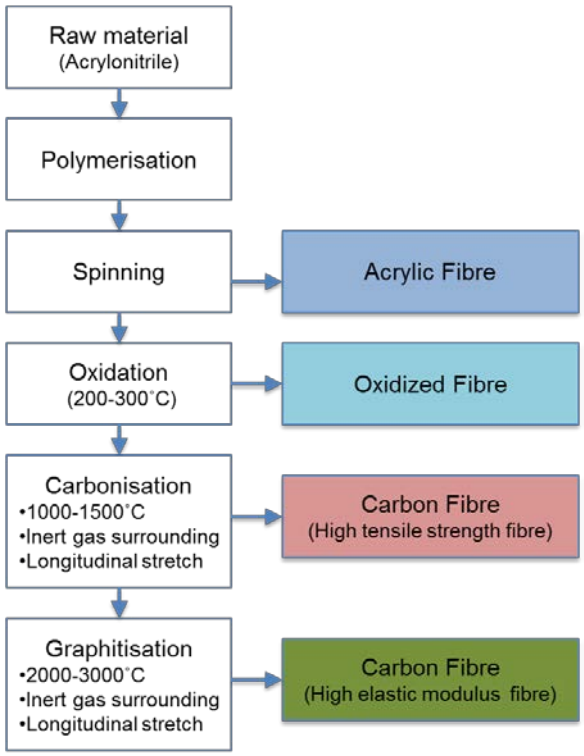


Figure 2.6 Process flow of carbon fibre development for high strength/high modulus configurations [28]

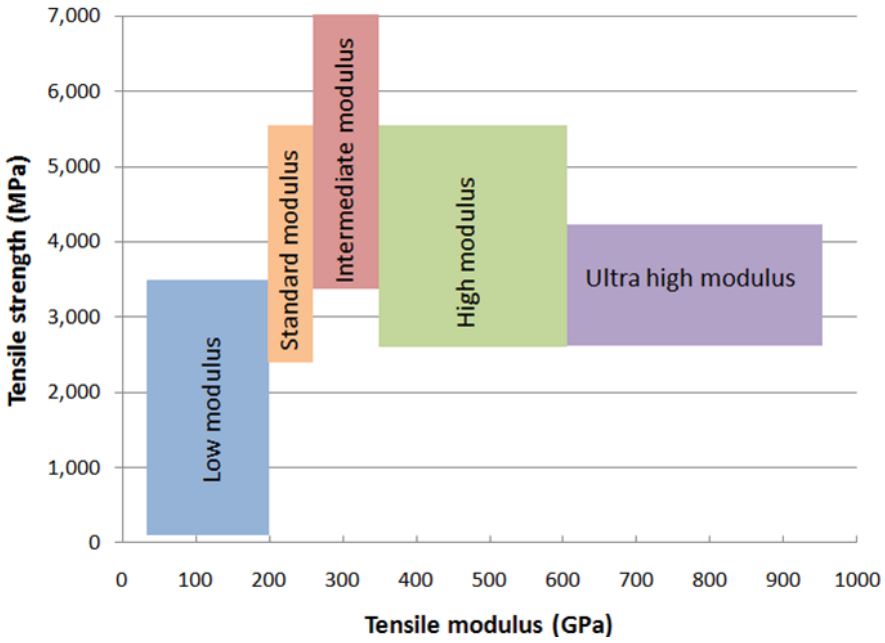


Figure 2.7 Tensile strength and modulus map for utilities of carbon fibres [38]

2.3.5 Forms of FRPs and forming process

Continuous fibres are often integrated into composite configurations by means of textile processing methods such as weaving, knitting and stitching, which generate the final products in the from of prepregs following impregnation with resins. Prepregs can be used in unidirectional/multidirectional arrangements or in woven fabric configurations as illustrated in Figure 2.8 [30]. The forming process can be categorised as composite moulding (compression moulding, bladder moulding, autoclave/vacuum bagging) [33, 34] or wet moulding process (filament winding, pultrusion, resin transfer moulding, vacuum moulding) [27, 32], depending on the impregnation of the resin being applied before or during the moulding process [27, 32].

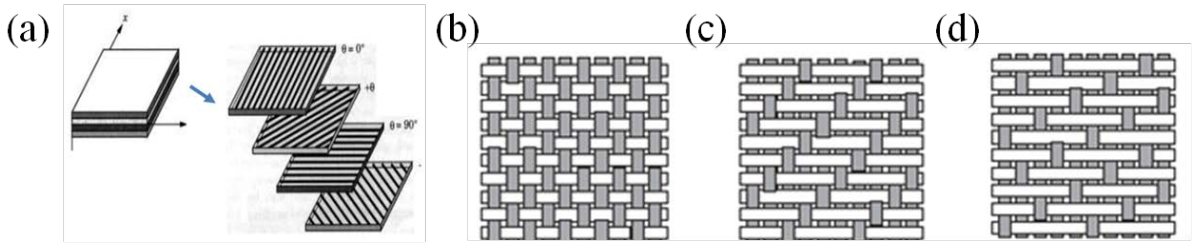


Figure 2.8 (a) Lay-up configuration and woven fabrics in (b) plain weave, (c) three-harness satin weave and (d) five-harness satin weave [32]

2.3.6 Prediction of properties in fibre systems

The properties of a carbon fibre composite laminate depend on the fibre orientation, stacked plies and the associated volume fractions. The final properties can be determined by superposition of each layer based on the law of serial or parallel arrangements of the fibre systems as seen in Figure 2.9 and Equations 1 to 6.

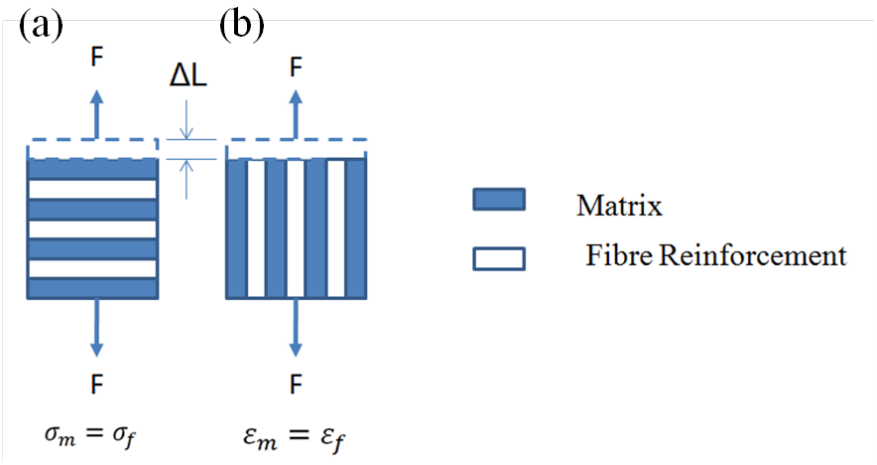


Figure 2.9 Schematic of properties in transverse and longitudinal fibre systems [28]

$\omega_c = \omega_f + \omega_m$, Weight conservation [34] (1)

$\rho_c = \rho_f V_f + \rho_m V_m$, The law of mixture [34] (2)

$E_1 = V_f E_{1f} + V_m E_m$, Longitudinal elastic modulus [34] (3)

$E_2 = \frac{E_{2f} E_m}{V_f E_m + V_m E_{2f}}$, Transverse elastic modulus [34] (4)

$\alpha_1 = \frac{\alpha_{1f} E_{1f} V_f + \alpha_m E_m V_m}{V_f E_{1f} + V_m E_m}$, Longitudinal CTE [28] (5)

$\alpha_2 = \left(1 + \nu_{12f} \frac{\alpha_{1f}}{\alpha_{2f}}\right) \alpha_{2f} v_f + (1 + v_m) \alpha_m v_m - \alpha_{1f} \nu_{12}$, Transverse CTE [28] (6)

2.3.7 Machinability of fibre-reinforced composites

Composite materials can be classified as difficult-to-cut [32] and do not conform to traditional metal cutting mechanics [39, 40] due to the heterogeneity and anisotropy of the fibre reinforced workpieces. The varying fibre orientations generally leads to discontinuous and interrupted machining [41, 42], while the reinforcement phase is usually highly rigid and very abrasive (~500HV), resulting in excessive tool wear and low productivity [43].

Additionally, the low specific thermal conductivity in the polymer matrix traps heat in the cutting zone, leading to a degradation of the machined surface quality [44, 45].

Koplev et al. [46] were the first to carry out orthogonal cutting experiments on CFRP to evaluate the influence of tool geometry on surface quality and cutting forces. It was found that workpiece surface roughness was highest when fibre orientation was perpendicular to the cutting edge; whilst the best surface was obtained with the fibre orientation parallel to the cutting direction. Konig and Graß [45] evaluated the influence of operating parameters on workpiece quality when drilling various FRP based composites (GFRP/CFRP/AFRP). The effects of cutting speed and feed rate when cutting FRP's were similar to trends observed when machining metallic materials; however the varying loads on the cutting edge (due to the different fibre orientations) resulted in inconsistent surface quality. Hocheng and co-workers [47-49] developed some of the earliest models to predict the thrust force threshold in order to achieve delamination-free drilling of CFRP. The model was able to determine the feed rate level where the threshold thrust force was not exceeded, thereby avoiding delamination at the ply interface and hole exit, which improved overall hole quality. In the following sections, the main factors governing FRP machining quality and performance are summarised and discussed.

2.3.7.1 Influence of composite material

The strength (>90%) of composite materials is mainly determined by the reinforcements and their volume fraction, see Section 2.3.6 which details the laws governing the prediction of the properties in fibre systems. The maximum fibre volume fraction is limited (~60% in the case of carbon fibre composites) due to the bonding strength being impaired by the incomplete impregnation of the matrix resins [31, 33]. When volume fraction is increased, material strength rises, but at the expense of higher tool wear [50]. Polymers (matrix material) generally have little effect on machinability however their relatively low thermal conductivities (~0.2W/mK) exacerbate heat related damage and deteriorates machined surface quality [33, 44, 45].

2.3.7.2 Influence of fibre orientation

Prepregs laid up within designed fibre orientations can influence strength in preferred directions but can be detrimental to machining performance. Unlike the cutting of

homogeneous and isotropic materials, different fibre orientations vary the cutting force as well as the chip forming process, which leads to discontinuous machining [39, 40, 51]. Wang et al. [39] classified the chip formation process in orthogonal cutting of FRP's into five typical models (Type I to V) with respect to fibre orientation and tool rake angle, as seen in Figure 2.10 [39] and detailed below; while Figure 2.11 shows examples of micrographs indicating the resulting surface textures [41].

- Type I model: When the feed direction is parallel to the fibre orientation with a positive tool rake angle, chip formation takes place via bending of the uncut material/plies.
- Type II model: When the feed direction is parallel to the fibre orientation with a negative tool rake angle, chip formation commences by compression and buckling of the material.
- Type III model: When the feed is in a 45˚ direction to the fibre orientation with positive/negative tool rake angle, chip formation occurs along a 'virtual' shear plane.
- Type IV model: When the feed is perpendicular (90˚) to the fibre orientation with positive tool rake angle, chip formation initiates by shearing across the fibre-matrix interface at the cutting edge.
- Type V model: When the feed is at a 135˚ angle to the fibre orientation with positive tool rake angle, chip formation occurs due to delamination and macro-fracture of the plies.

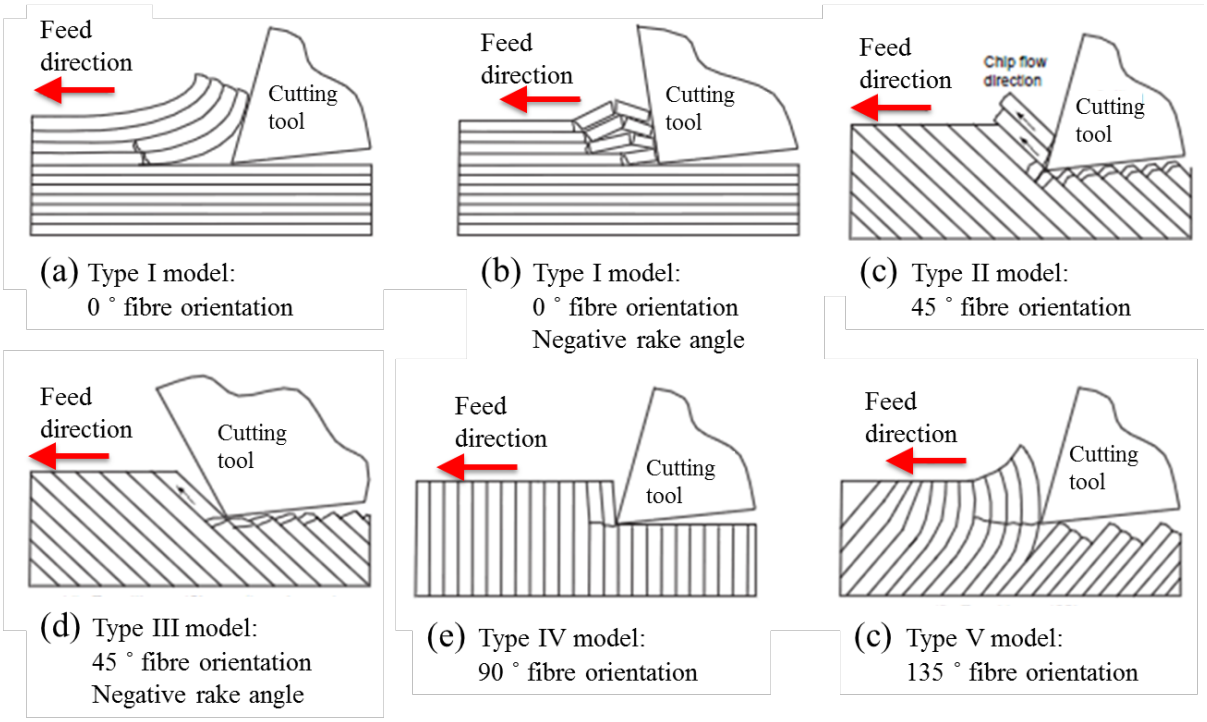


Figure 2.10 Schematic of chip formation models in orthogonal cutting of CFRP [39]

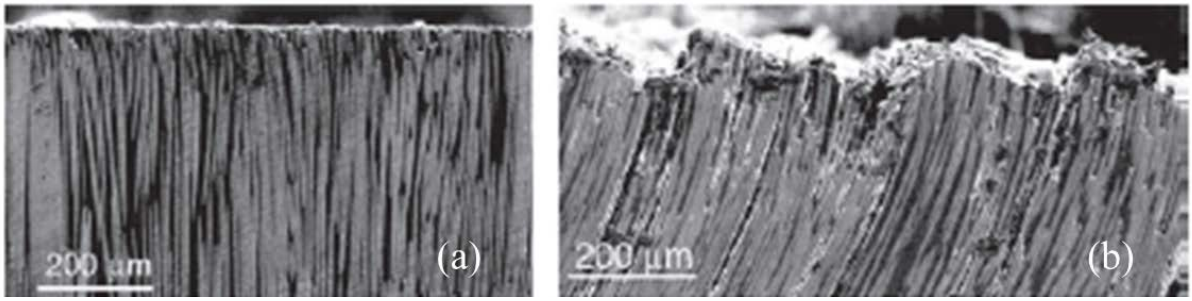


Figure 2.11 Micrographs of fibre orientation of (a) 90 ˚and (b) 135˚ [41]

2.3.7.3 Influence of cutting conditions

In the machining of fibre reinforced polymers where classical plastic deformation in the shear zone does not normally take place, empirical correlations are commonly used to investigate the influences of tool material, workpiece material, cutting speed, feed rate, depth of cut and fibre orientation on the cutting forces, tool wear and machined surface quality. Increased cutting speed when drilling has been shown to have minimal effect on thrust force when employing new tools [52], but can potentially accelerate tool wear, thereby leading to subsequent rises in thrust force [53, 54]. Campos Rubio et al. [55] concluded that high speed cutting increased machining temperatures due to the low thermal conductivity of the polymer matrix, resulting in softening of the material leading to a decrease in torque and degradation of surface integrity. However, when operating at high cutting speeds coupled with low feed rates, cutting temperature was lowered producing better surface finish with minimal delamination. Increased feed rate in drilling led to greater thrust forces and torque due to the larger uncut chip thickness, together with a rise in surface roughness due to a shorter contact cycle [56]. Wang et al. [41] reported that depth of cut (DOC) was the dominant factor influencing cutting force and surface roughness when machining unidirectional and multidirectional FRPs. Low DOC produced low roughness and better surface finish. Figure 2.12 [41] shows the CFRP surface texture when machining at two different DOC's.

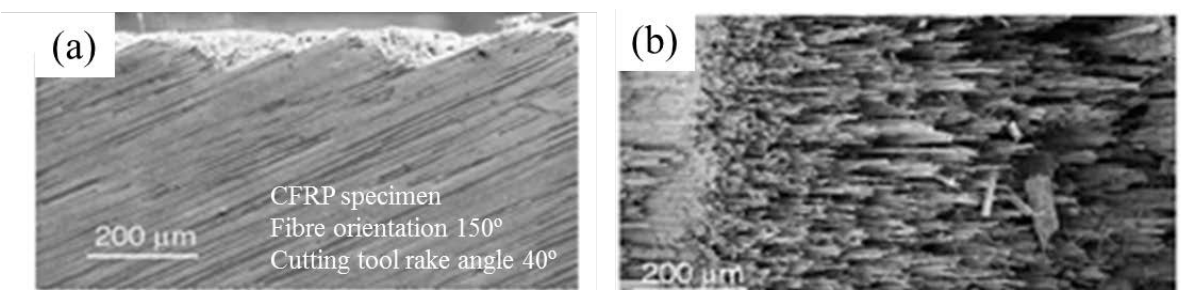


Figure 2.12 Surface textures in CFRP with DOCs of (a) 0.05mm and (b) 0.10mm [41]

2.3.7.4 Effect of tool geometry/material

The chip forming process in CFRP involves bending, compression, shearing and macro-fracture mechanisms, which vary in influence depending on fibre orientation as well as tool geometry [39, 40]. In the work by Wang and Zhang [41] and Durao et al. [57], cutting force and surface quality were found to be largely dependent on the rake and clearance angles of the cutting tool. Larger rake angles decreased the principal cutting force whilst increased clearance angles lowered the thrust force and reduced contact with the machined surface, leading to a reduction in tool wear and an improvement in surface quality [39-41]. In Figure 2.13, the larger cutting edge radius (depending on the ratio to the DOC) is shown to suppress the matrix instead of being sheared, resulting in a 'spring-back' effect [41] and delamination [58] of the machined surface leading to inconsistent surface quality. Tool materials recommended for machining FRPs are polycrystalline diamond (PCD) and diamond coated carbide [69, 77], as their higher hardness (8000-10000 HV) and thermal conductivity (~2000 W/mK) can provide greater resistance against the abrasive fibre reinforcement phase and more efficiently dissipate heat retained in the cutting zone [16].

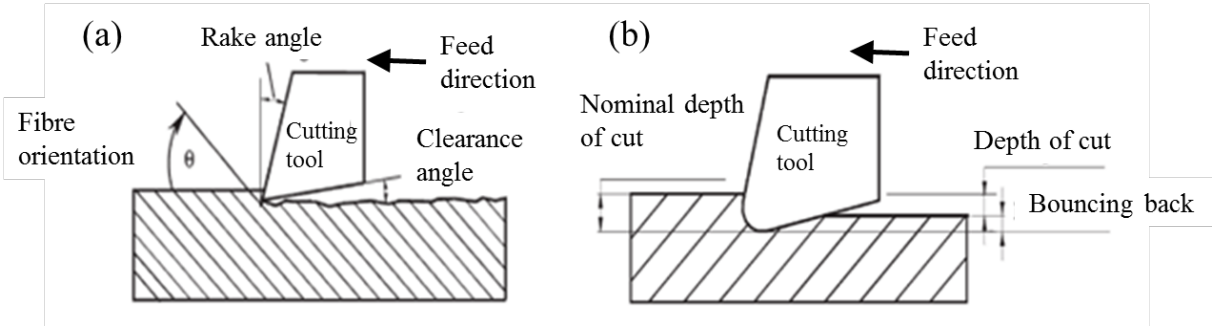


Figure 2.13 Schematic of cutting system in composite: (a) geometry of cutting tool and fibre orientation, (b) spring-back effect [41]

2.4 Drilling of multilayer composite/metallic stacks

2.4.1 Introduction

Aircraft structural components such as wings, tail wings and fuselage are typically constructed from metallic composites stacks of different configurations including CFRP/titanium [59-63], CFRP/aluminium [62, 64-66], graphite-bismaleimide/Ti [67, 68] and Ti/CFRP/Al [69, 70]. Multi-shot mechanical drilling operations are usually employed to generate holes for bolting and riveting of the material assemblies. The approach provides

sufficient strength/rigidity while also being convenient for maintenance [59, 60, 62, 64-71]. Research to date involving the single-shot drilling of composite/metallic stacks in particular however has been limited, with the key publications listed in Table 2.7.

	Kim/Ramulu et al. [67, 68]	**Brinksmeier et al. [75]**	**Zitoune et al. [70]**		**Shyha et al. [77]**
Workpiece material	Gr/Bi (7.62mm), Ti-6Al-4V (3.1mm)	A2024 (10mm), CFRP (10mm), Ti-6Al-4V (10mm)	CFRP (4.2mm), A2024 (3mm)		Ti-6Al-4V (10mm), CFRP (10mm), A7050 (10mm)
Tool specification	K20 point angle 118°	WC, 3 flutes, point angle 130°	K20, point angle 118°		K20, point angle 130°
Cutting environment	Wet	MQL	Dry		Flooding/dry
Drill diameter (mm)	6.35	16	4.6	8	6.35
Feed rate (mm/rev)	0.08-0.25	0.15	0.05-0.15	0.05-0.15	0.05-0.15
Cutting speed (m/min)	13.2-34.9	10, 20	15.2-39.7	26.4-69.1	20/40-60/120

Table 2.7 Key research publications on the drilling of metallic-composite stacks

2.4.2 Cutting forces

2.4.2.1 Thrust force

Watson [72] and Amarego and Cheng [73] reported that 50% of thrust force generated was due to the chisel edge with the rest produced by the cutting lips and friction acting on the rake surface. Equations 7-9 [74] establish the relationships between the total thrust force and process variables. As detailed in Figure 2.14 [75, 76], thrust force increases as effective rake angle decreases or shear angle increases [73], but decreases with smaller friction angle.

$$F_{\text{total thrust}} = 2\bullet (F_{\text{extrusion}} + F_{\text{cutting}} + F_{\text{friction}}) = 4\bullet (F_{\text{cutting}} + F_{\text{friction}}) \quad (7)$$

$$F_{\text{cutting}} = (r - r_{\text{chisel}}) \bullet \frac{S}{2} \bullet \frac{1}{\sin\phi} \bullet \tau_s \bullet \frac{\sin(\beta-\alpha_n)}{\cos(\phi+\beta-\alpha_n)} \quad (8)$$

where r is tool radius, r_{chisel} is the radius of chisel edge, s is the drill feed per revolution, ϕ is the shear angle, τ_s is the shear stress on shear plan, β is the friction angle, and α_n is the effective rake angle which is a function of radius, point and helix angles.

$$F_{\text{friction}} = \frac{(r - r_{\text{chisel}})}{\sin\chi} \bullet N_{\text{rake}} \bullet \sin\chi \quad (9)$$

where N_{rake} is the specific normal force $(\frac{N}{mm})$ acting on cutting lips, and χ is the half of point angle.

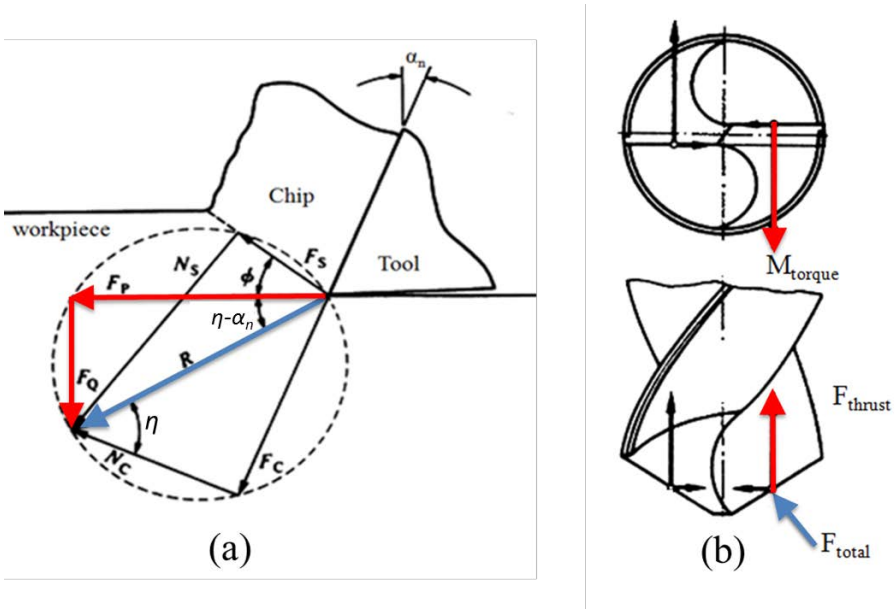


Figure 2.14 Schematic of (a) triangle geometrical relationships in Merchant's force circle [75] and (b) cutting forces in drill [76]

2.4.2.2 Torque

Equations 10 - 12 [74] calculates the total torque contributed by extrusion force at the chisel edge, cutting force at the cutting lips and friction on the rake face. The moment produced by the chisel edge is generally negligible due to the leverage approaching zero. Figure 2.15 shows the variation in thrust force and torque with respect to drill radius [76].

$$M_{\text{total torque}} = L\bullet (M_{\text{extrusion}} + M_{\text{cutting}} + M_{\text{friction}})$$

$$M_{\text{total torque}} = L\bullet (M_{\text{cutting}} + M_{\text{friction}}) \quad (10)$$

$$M_{\text{cutting}} = L\bullet (r - r_{\text{chisel}}) \bullet \frac{S}{2} \bullet \frac{1}{\sin\phi} \bullet \tau_s \bullet \frac{\cos(\eta-\alpha_n)}{\cos(\phi+\eta-\alpha_n)} \quad (11)$$

$$M_{\text{friction}} = \frac{(r-r_{\text{chisel}})}{\sin\chi} \bullet f_{\text{rake}} \quad (12)$$

where L is the mean moment arm, and f_{rake} is specific friction force $(\frac{N}{mm})$ acting on the flank surface.

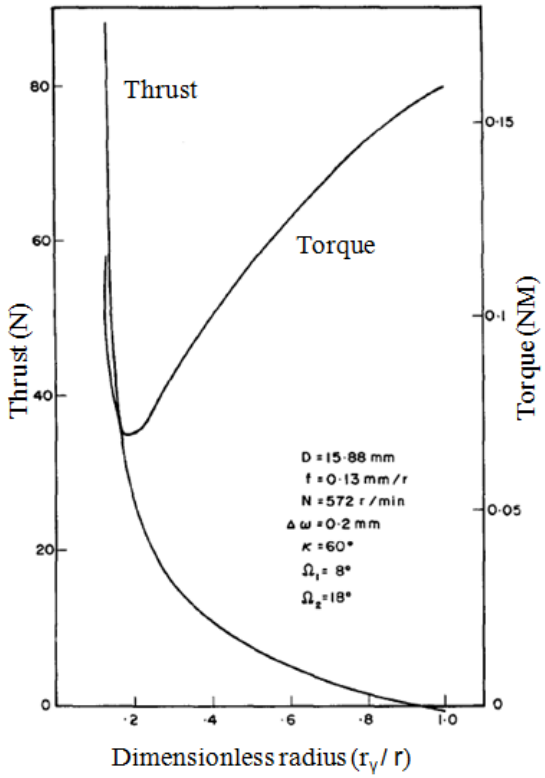


Figure 2.15 Typical correlation of thrust force and torque over drilling tool radius [76]

2.4.3 Tool geometry

According to the British Standard BS328 [77], a twist drill is characterised by two flutes and consists of a chisel edge and a pair of cutting lips. A detailed geometric analysis, both mathematically and empirically, is outlined in the following sections.

2.4.3.1 Chisel edge

The chisel edge is controlled by the primary and secondary (if any) clearance surface planes [72], which results in a negative rake during cutting. Consequently, the cutting action of the chisel is similar to an indentation, as the rotational speed approaches zero. The chisel edge therefore accounts for ~50% of the thrust force generated drilling [73]. The longer the chisel edge, the higher the drilling torque and thrust force. Conversely a thinned web can reduce the thrust force by 30-35% [78] compared to a conventional drill. Figure 2.16 shows a schematic of a chisel edge comprising the chisel edge angle (δ_c) and chisel radius (r_{chisel}), which determines the tool side rake and minimum pilot hole diameter respectively [72, 76]. Equations 13 and 14 can be used to calculate δ_c and r_{chisel} respectively.

$$\tan \delta_c = \frac{\tan \Omega_1 + \tan \Omega_2}{2 \cos \chi} \quad (13)$$

$$r_{chisel} = \frac{t}{\cos \delta_c} \quad (14)$$

where, Ω_1 is the primary relief angle, and Ω_2 the secondary relief angle.

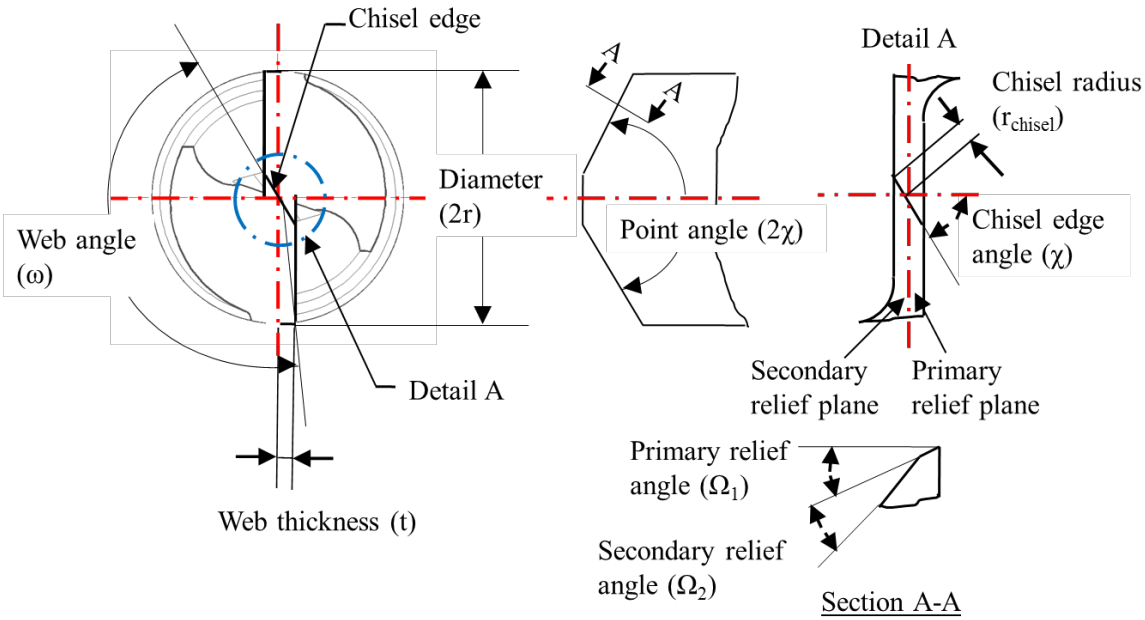


Figure 2.16 Schematic view of chisel edge angle and chisel radius [72, 76]

2.4.3.2 Cutting edges

Figure 2.17 details a schematic highlighting the web, velocity and normal rake angles of a twist drill [72]. A parameter known as the angle of obliquity (*i*), is a function of web angle (ω) and point angle (2χ), is detailed according to Equation 15 [73]. The web angle is calculated using Equation 16, with the shape of the cutting lips defined by the point angle, web thickness (2t) and drill radius (*r*) parameters.

$$\sin i = \sin \omega \bullet \sin \chi \quad (15)$$

$$\sin \omega = \frac{t}{r} \quad (16)$$

where t is half of the web thickness.

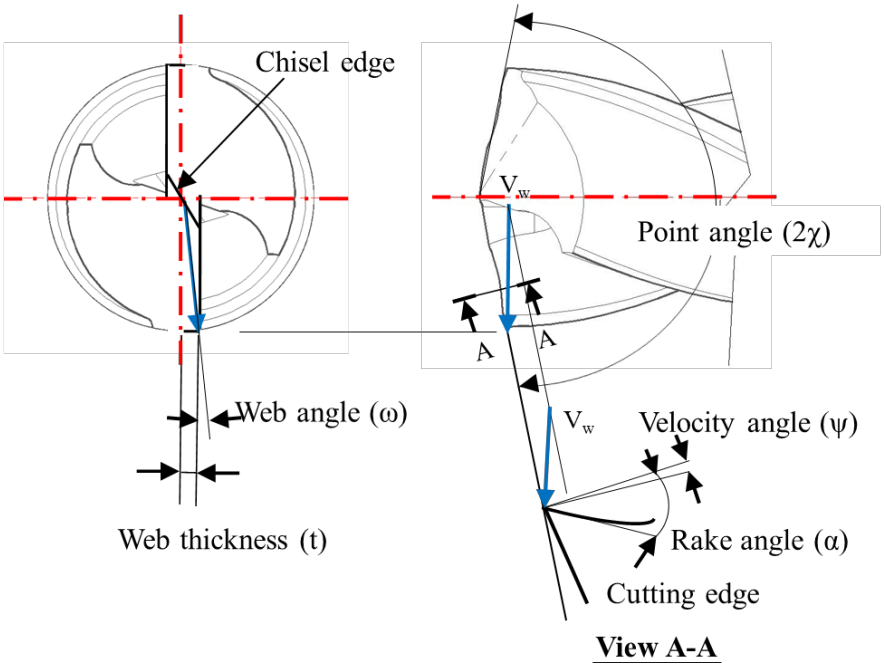


Figure 2.17 Schematic of web angle, velocity angle and normal rake angle [72]

2.4.3.3 Rake angle

The rake angle α on the cutting lips is determined by the helix angle and point angle, which varies with drill radius along the entire cutting edge from the centre to the periphery [72]. Figure 2.17 shows a schematic of each feature. The rake, normal rake [73] and feed angle are defined in Equations 17 [78], 18 and 19 respectively.

$$\tan \alpha = \frac{r\gamma}{r} \bullet \frac{\tan \lambda}{\tan \chi} \quad (17)$$

$$\alpha_n = \alpha - \psi = \alpha - \tan\omega \bullet \cos\chi \quad (18)$$

$$\theta = \frac{f}{(\pi \bullet D)} \quad (19)$$

where λ is the helix angle, 2χ is the point angle, $r\gamma$ is the radius at each point of the lip, r is the radius of the drill, α_n is the normal rake angle, ψ is the velocity angle (angle between the work velocity and normal to the drill axis containing the lip, projected in a plan to the lip), ω is the web angle and f is the half of web thickness.

2.4.3.4 Point angle

The ‘standard’ point angle of 120° was designed to fabricate twist drills with straight cutting lips. Angles less than 120° generally produces convex lips while angles exceeding 120° typically gives rise concave lips [72], as shown in Figure 2.18. The point angle has a direct influence on the thrust force, where increasing point angle reduces the rake angle, which subsequently increases the uncut thickness and hence thrust force. In contrast, larger point angles reduces the length of the cutting lip resulting in decreased torque levels [79].

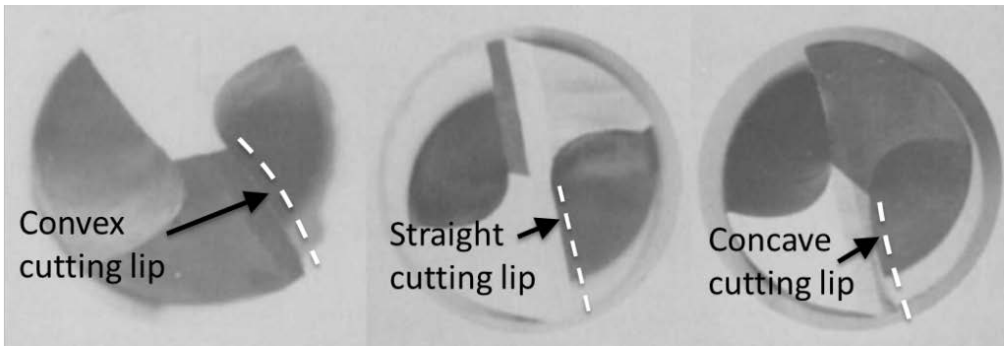


Figure 2.18 Influence of cutting lips over point angles [72]

2.4.4 Drilling of multilayer Ti/CFRP/Al stacks

Applications of multilayer metallic-composite stacks include aircraft wing sections and fuselage as highlighted in Figure 2.19 [80], with typical configurations involving two (Ti/CFRP and Al/CFRP) or three (Ti/CFRP/Al) layer arrangements. Such assemblies normally rely on mechanical joining and consequently, conventional hole drilling is a key processing technology. The capability for drilling of metallic-composite stacks in a single shot operation without further recourse to subsequent reaming (2-shot) and countersinking (3-shot) operations as detailed in the schematic in Figure 2.20, can potentially offer considerable advantages in terms of improved hole accuracy as well as the reduction of deburring costs. The contrasting mechanical/thermal properties of the metallic and composite layers however, leads to varying tool-workpiece material behaviour during drilling, which presents challenges in terms of identifying the preferred tool material and geometry as well as the appropriate cutting parameters.



Figure 2.19 Boeing 787 Dreamliner composite profile [80]

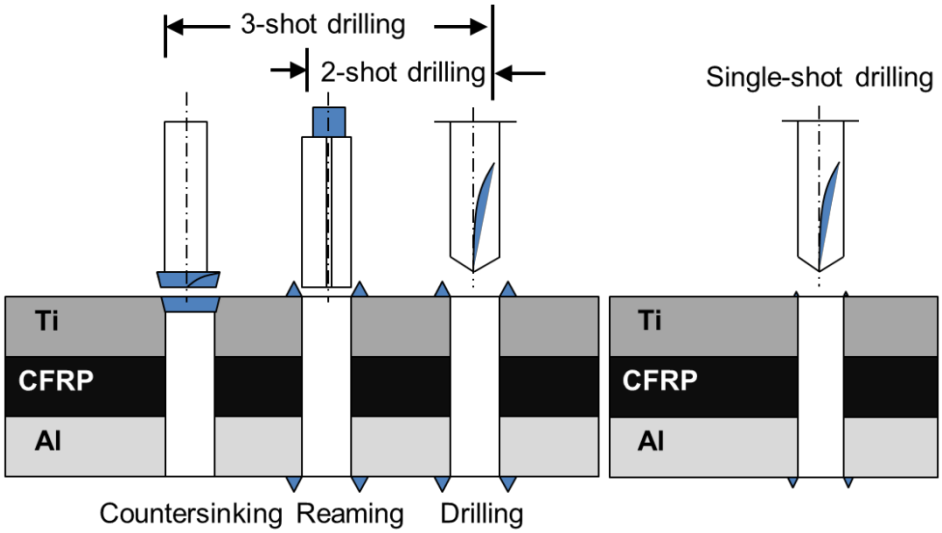


Figure 2.20 Schematic of single shot, two-shot and three-shot drilling operations

The choice of cutting tool material is one of the key factors that influences hole quality and productivity. Submicron (0.5-0.8μm) cemented carbide with high hardness (2000HV) and fracture strength (4300MPa) is generally the most widely utilised due to its relatively high tool life and comparatively low cost. The application of titanium-alloyed (TiAlN/TiN) coatings on WC substrates to increase hardness and/or reduce friction tends to improve wear resistance further, as well as providing better surface integrity without loss of toughness. In the work by Ramulu et al. [68] and Kim and Ramulu [67], experiments involving the drilling of graphite bismaleimide and Ti-6Al-4V stacks (Gr-Bi/Ti-6Al-4V) using HSS, HSS-Co and C2 carbide drills were performed under cutting speeds of 13.2-34.9m/min and feed rates of

0.03-0.25mm/rev. It was shown that carbide tools produced the lowest cutting forces, exit burrs and surface roughness with negligible workpiece damage, irrespective of the feed and speed levels tested. Zitoune et al. [65] evaluated the drilling performance of CFRP/A2024 stacks using nano-coated (nano-crystalline CrAlN/amorphous-Si_3N_4) WC drills with a diameter of 6mm under cutting speeds of 1050-2750rpm and feed rates of 0.05-0.15mm/rev. Thrust forces were up to 47% and 20~25% lower over the range of feed rates employed (0.06-0.14mm/rev) in the aluminium and CFRP layers respectively; in addition to a 30% lower workpiece surface roughness (Ra) in comparison to uncoated drills. The use of advanced diamond based coatings such as physical vapour deposited (PVD) diamond-like carbon (DLC) [81] and chemical vapour deposited (CVD) [82] diamond products have also been proposed as a potential solution for single-shot drilling of metallic-composite stacks, due to their superior mechanical and physical properties. Kuo et al. [83] carried out experimental work using CVD diamond and diamond like carbon (DLC) coated tools under dual-cutting speed (30m/min in Ti layer, 120m/min in CFRP/Al layers) conditions and varying feed rates of 0.08 and 0.15mm/rev. It was shown that the CVD diamond coated drills produced superior hole quality in terms of hole diameter (6.38±0.04mm) and cylindricity (<80μm) compared to the DLC coated tools due to the lower wear level at the drill periphery in the former. Experiments involving 9.525mm diameter tungsten carbide (ultra-fine grade) and polycrystalline diamond (bimodal grade) tools utilising dual-level cutting speeds of 300-800/2000-6000rpm when drilling 2 layer Ti/CFRP stacks were undertaken by Park et al. [60]. It found that the tool wear patterns in WC drills typically involved uniform edge rounding whilst micro-chipping or micro-fracture was prevalent at the cutting edge of the PCD tools due to the relatively brittle nature of the material. Nevertheless, the PCD drills outperformed the WC tools in terms of tool life.

In order to increase the rigidity of twist drills, tools with multiple cutting edges or multiple margin designs have been considered and evaluated. Ema et al. [84] conducted experiments using multiple cutting edge/flute drills, which suggested improvements in hole accuracy, but at the expense of an increase of torque and thrust force. It was recommended that thinning of the chisel edge web was a potential solution to reduce the rise in thrust force and torque. Piquet et al. [85] evaluated the performance of twist drills with three cutting edges having multiple facets when drilling thin carbon fibre composites. The special tool design was shown to improve hole accuracy compared to conventional twist drills and significantly reduced out of roundness and diameter errors. The performance of a bespoke triple margin design was

compared against standard twist drills when single-shot drilling 3 layer Ti/CFRP/Al stacks at a cutting speed of 30/120/120m/min and feed rates of 0.05 - 0.08mm/rev [86]. The former was observed to produce superior hole accuracy in terms of diameter, out of roundness, and cylindricity. However, subsurface analysis of the machined surfaces revealed a considerable increase of up to ~15% in workpiece microhardness within the Ti layer (~440$HK_{0.025}$) when employing the triple margin drills, which was most likely due to higher strain hardening as a result of the greater tool-material contact area.

Feed rate and cutting speed coupled with tool material are principal factors governing hole quality, tool life and associated workpiece surface integrity and power consumption when drilling. While operating at a high feed rate reduces the machining cycle, machining with a low feed rate generally produces better surface roughness. Similarly, the use of high cutting speeds increases cutting temperature, but leads to smaller chip thicknesses and lower cutting forces. The trade-off between productivity and hole quality is therefore related to the selection of feed and cutting speed combinations together with tool materials, via the associated interactions of the different constituent stack materials in terms of mechanical, thermal and chemical mechanisms. Carvajal et al. [62] carried out comprehensive statistical analysis on industry data/records in order to determine the influence of drill diameter, cutting speed and feed rate on hole diameter accuracy, when drilling various metallic-composite stack materials. They found that high feed rate levels generally produced lower hole diameter variations in both the metal and composite layers, whilst cutting speed showed limited influence. Brinksmeier and Janssen [69] studied the drilling of $AlCuMg_2$/CFRP/Ti-6Al-4V stacks using 16mm diameter conventional uncoated carbide twist drills as well as TiB_2 and diamond coated step drills under a cutting speed of 10-20m/min, feed rate of 0.15mm/rev and tool retraction/pecking strategy for improved chip removal. They reported that while coatings had minimal effect with regard to tool life, the TiB_2 coated step drill produced the lowest diameter variations. Operating at the low cutting speed level was also seen to reduce material adhesion at the cutting edge when drilling the titanium layer. Severe damage of the CFRP layer however was observed during evacuation of the Ti chips from the bottom of the stack. More recently, Shyha et al. [70] conducted experimental investigations to evaluate the influence of varying operating parameters (cutting speed, feed rate, environment) and coatings (uncoated, CVD diamond and a nano-grained AlTiN coated WC) when drilling 6.35mm diameter holes in Ti-6Al-4V/CFRP/A-7050 stacks. They concluded that the use of high pressure cutting fluid (70 bar) was critical in maintaining acceptable hole quality (diametrical accuracy, out of

roundness and cylindricity) and workpiece integrity, and that tool coatings had only a marginal effect. A hole diameter tolerance of ±0.02 mm was achieved even after drilling up to ~310 holes with out of roundness not exceeding ~ 20μm when operating under a two-stage cutting speed of 20/40/40m/min (for Ti/CFRP/Al) and feed rate of 0.05mm/rev.

2.5 Cutting tool materials

2.5.1 Introduction

In drilling, the mechanical/physical properties of the workpiece and tool materials such as hardness, fracture toughness, yield strength, elastic modulus and thermal related properties as well as respective cost, are key factors in determining application and overall performance. The majority of cutting tools currently employed in industry for machining advanced materials such as nickel based superalloys, Ti alloys and CFRP composites are predominantly WC-Co, which is generally coated (hardmetal, diamond based etc.) due to their relatively good balance of properties (high hardness/strength, fracture roughness, good thermal conductivity, good chemical resistance) and reasonable cost [15, 87]. More recently, the use of advanced PCD tools have been shown to provide substantial benefits (despite the relatively higher cost), particularly for machining Ti-alloys and CFRP composites. Table 2.8 details the key mechanical/physical properties of commonly employed tool materials and coatings for drilling metallic-composite stacks (corresponding data on Ti-6Al-4V, CFRP and A7050 workpiece material are also included).

In general, tool materials with high strength/hardness (PCBN, PCD etc.) have relatively low fracture toughness/bending strength and are susceptible to brittle fracture or impact loads [15], as described in Figure 2.21. As a result, coated tungsten carbide tooling with optimised geometry can potentially provide comparable performance to superhard materials [88] when machining certain materials, even under severe cutting conditions. The development of cutting tool technology over the past 25 years has primarily focused on aspects such as substrate material grades, coatings and geometries. While progress has been incremental rather than ground breaking, improvements [89] in terms of higher tool hardness and wear resistance [90], increased fracture toughness with lower binder content, more versatile/advanced coating technologies (CVD, PVD) and greater range of tool geometry/

designs have been realised. Nonetheless, the advances have translated to enhanced performance with respect to better surface quality, longer tool life and lower costs.

	Tool material					**Workpiece material**		
Properties	WC (K30-40)	TiAlN/ TiN coating	DLC Coating	CVD diamond coating	PCD	Ti-6Al-4V	A7050 T7651	CRFP
Density (g/cm³)	14.5	4.81	N/A	3.515	3.4	4.43	2.83	1.6
Hardness	1600HV	3000-3500 HV	4000-6000 HV	10000 HV	8000-10000 HV	340HV	171HV	60-67 Barcol
Fracture toughness (MPa·m ½)	13	N/A	N/A	3.4	7.9	66	24	1.8-3.3
Young's Modulus (GPa)	580	515	180	1000	841	115	72	150
Thermal conductivity (W/mK)	85	29	N/A	560	560	~6.7	154	1 ⊥, 70 // to fibre direction
Coeff. of thermal expansion (µm/K)	5.3-5.8	6.5	2-6	1.0	3.8	8.6-9.7	25	10 ⊥, -0.6 // to fibre direction
Approximate cost per drill (£)	75	80	90	250	750	N/A	N/A	N/A

Table 2.8 Properties of selected cutting tool materials/coatings and workpiece materials

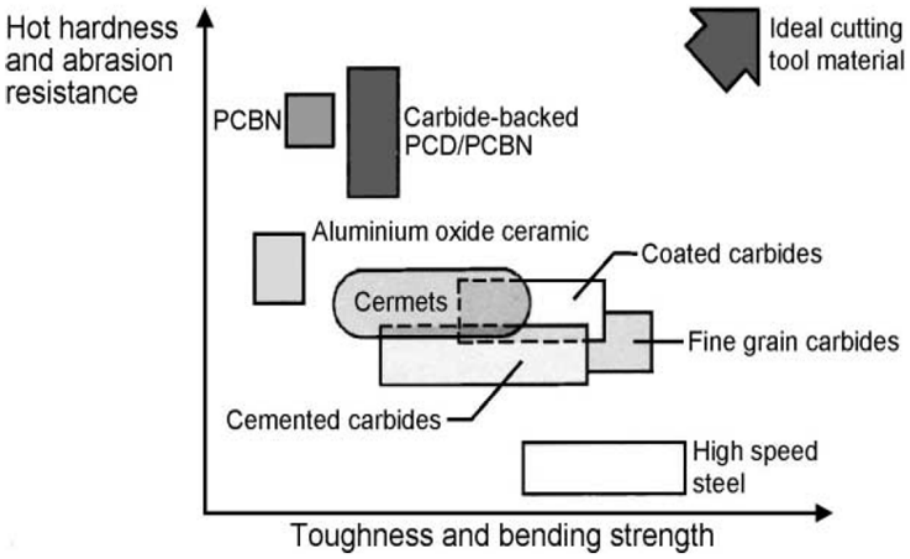


Figure 2.21 Range of mechanical/physical properties of various cutting tool materials [90]

2.5.2 Tool materials for drilling metallic-composite stacks

2.5.2.1 Cemented carbide (WC-Co)

Tungsten carbide blanks are manufactured through the process of mixing and sintering tungsten carbide particles with cobalt above 1300˚C, the latter acting as a binder phase that increases the toughness of the resulting material. During the sintering process, the WC particles disperses into a molten cobalt solution phase until solidification occurs to retain continuity/consistency of the mechanical properties [14]. Developments over the years relating to the synthesis of WC materials include modifying the cobalt content (3-12%) and tungsten carbide particle size (1-10μm) as well as additions of TiC, Ta(Nb)C compounds in place WC up to a maximum volume of 42%. This has led to the formulation of various WC grades with different levels of strength, hardness and diffusion resistance suitable for a wide range of machining applications [89].

One of the most widely employed WC grades is the K30-40 group, which are typically formulated with 10% Co and a submicron grain size (0.5-0.8μm). It is characterised by comparatively high hardness (1600HV at 20˚C) and fracture toughness (10 MPa $m^{1/2}$) levels together with relatively low cost [91], and is generally recommended for heavy duty cutting of titanium alloys. Other alternatives for machining Ti-6Al-4V include the C2/ISO K20 grade, which consists of 6% Co and a grain size of 0.8 - 1.4μm [1]. However when employing coatings, the K20 grades are generally utilised as the substrate due to the lower Co binder content which reduces diffusion/mitigation of carbon atoms and prevents adverse effects such as poor coating adhesion or graphitisation of the bonding layers [92, 93]. The influence of mean grain size and binder content on WC material properties is similarly critical; with fine grain size and low cobalt content providing higher strength and hardness [94]. Table 2.9 details mechanical properties of the WC with respect to grain size and Co binder content.

Co %	Mean WC grain size (μm)	Hardness (HV30)	Transverse rupture strength (MPa)	Compressive strength (MPa)	Young's modulus (GPa)	Fracture toughness (GPa)
6	0.7	1800	1750	4550	-	-
	1.4	1575	2300	4250	630	10
10	0.7	1670	2300	-	-	-
	1.4	1420	2400	4000	588	13

Table 2.9 Properties of WC with varying grain size and Co content [14]

2.5.2.2 Polycrystalline diamond (PCD)

Synthetic diamonds were initially produced in the early 1950's through heating graphitic carbon at temperatures over 1500°C and at high pressures of ~8GPa, with nickel added as a solvent to trigger a catalytic reaction of the carbon transforming to diamond crystals [15]. The synthetic diamond crystals were then ground to average grain sizes ranging from ~ 2 to 30μm having random orientations, which were subsequently compacted and sintered in a similar high temperature-high pressure process onto a cemented carbide substrate/base. Typical copper alloys (α-bronze, 90% Cu and 10% Sn) are used as the filling phase to fill the porous sites during sintering; whereas cobalt (nickel, manganese, iron, or their combinations) acts as a binder that diffuses from the WC-Co platform/substrate to wet the diamond grains and transport the particles into the matrix [95, 96]. In comparison with other tool materials such as WC-Co and ceramics, PCD has superior hardness (8000-10000HV), intermediate fracture toughness (7.9MPa.$m^{1/2}$) and shock resistance, excellent thermal conductivity (560W/mK), low coefficient of thermal expansion (3.8μm/K) and low coefficient of friction [97].

The mechanical properties of PCD are in part determined by the material grain size, as seen in Table 2.10. Larger grained PCD with lower metallic binder content results in higher fracture toughness and hardness [95] suitable for roughing and heavy duty cutting; whereas grades with fine grain sizes are generally used for finishing operations [32, 97]. The development of mixed/multimodal products having diamond grains ranging from 2 to 30μm have been shown to improve both tool strength and machined surface quality. Use of PCD for the machining of advanced aerospace materials such as fibre reinforced composites [98] and titanium alloys [1] has grown in recent years, due to its outstanding abrasion/wear resistance as well as elevated thermal conductivity. This generally allows tool life to be extended together with better preservation of cutting edge geometry that results in more consistent workpiece surface quality. The fabrication of PCD tools however are distinctly more complex and expensive [15, 99] compared to WC, with a variety of non-conventional machining processes such as electrical discharge machining (EDM), electrical discharge wire machining (EDWM) and electrical discharge grinding (EDG) [99] employed for rough cutting and shaping of blanks, with diamond grinding for final finishing where necessary [97]. Recent research involving five-axis laser machining of PCD cutting inserts has shown similar results when compared to grinding in terms of rake and flank face surface quality [100], see Figure 2.22.

Company	PCD product name	Co binder (%vol.)	Grain size (µm)	Transverse rupture strength (MPa)	Density (g/cm³)	Hardness (GPa/HV)
Element Six	Syndite CTM302	(2-8)	2-30	1437	3.99	50 GPa
	Syndite CTB002		2		4.24	50 GPa
	Syndite CTB010		10	1150	4.12	50 GPa
	Syndite CTB025		25	1100	3.86	50 GPa
GE Super Abrasives	Compax 1500		25-50		(3.82-4.2)	(63.76-78.48) GPa
	Compax 1300		10-15			
	Compax 1600		≤10			
	Stratapax 2500		25-125	1190		
Sumitomo Electric Industry Ltd.	DA 90	N/A	20-0.5	1100	N/A	11000HV
	DA 150		5	1500		11000HV
	DA 200		0.3	2000		9000HV

Table 2.10 Major PCD blank manufacturers, products and related properties [14]

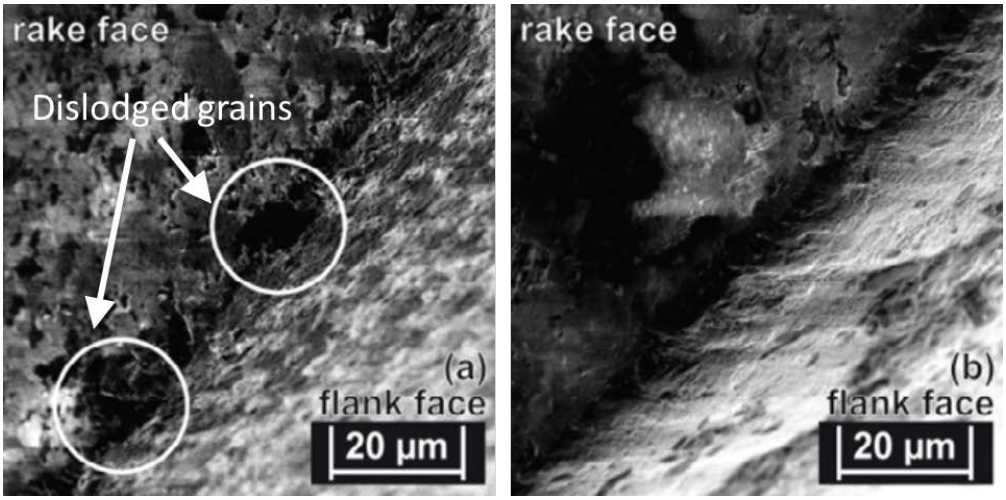


Figure 2.22 (a) Ground surface with dislodged diamond grain in the matrix and; (b) laser machined surface with clean cut edge [100]

2.5.3 Coatings

Hard coating technology was introduced in the early 1970's to improve the properties (higher hot hardness, reduced friction, increased diffusion and oxidation wear resistance etc.) and performance of cemented carbide tools by deposition of various single layer thin film coatings (e.g. TiC, TiN, TiCN, Al_2O_3) [101]. This was followed by the development of multi-layer coatings, which were formulated by depositing layers of different compositions to

provide a wider range of properties for specific applications [14], with an example of the morphology illustrated in Figure 2.23. Advances in coating techniques such as physical vapour deposition (PVD) were also seen to make major improvements to the adhesion and chipping resistance of coatings based on the introduction of a meta-stable phase [32]; whereas chemical vapour deposition (CVD) coatings involve the formulation of chemical-equivalent bonds to produce monolithic properties [101]. Other related developments aimed at enhancing the abrasive wear resistance, hot hardness and oxidation properties [89] of coatings include;

- PVD AlCrN monolayer hard coating [102] having high chemical stability and reduces solution wear rate under high service temperature (~1100˚C).
- Molybdenum disulphide (MoS_2) and graphite based soft coatings having low friction coefficient (0.03 to 0.07) and low hardness (1250-2500HV); diamond like carbon (DLC) hard coatings with low friction coefficient (<0.1) and high hardness (4000HV) [103].
- Thin and thick film CVD diamond with nano-crystalline and multilayer coatings having high hardness levels [92, 104].

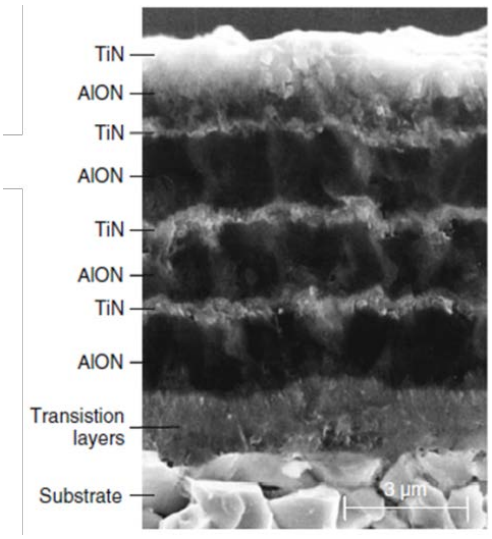


Figure 2.23 Morphology of multilayer coating (source: Sumitomo) [105]

2.5.3.1 Chemical vapour deposition (CVD) diamond

Diamond based coatings grown on tungsten carbide substrates using CVD techniques (CVD diamond) combines high hardness (~10000HV) and toughness (3.4MPa·$m^{1/2}$) characteristics, is a potential low cost alternative to PCD for the machining of Al alloys and FRPs composites. [81, 106]. The diamond films are grown via activating carbon-carrier gases (methane, aromatic hydrocarbons, etc.) with non-diamond carbon etchants and surface

preparation species (hydrogen, oxygen atoms) under temperatures of 1000-5000°C (which can be generated via different thermal sources) and vacuum pressure of 10torr-1atm [82, 101].

Substrate surface pre-treatments such as etching [107], intermediate layer coating heat-treatment [104] and seeding [82] are critical processes that are performed prior to growth of the CVD diamond layer as it influences the resulting adhesion strength of the coating. The etching process involves bead blasting [107] and Murakami acid etching [107] that roughens the substrate surfaces to provide interlocks and anchoring with the carbide matrix for enhancement of the adhesion strength as well as removes cobalt elements in order to prevent incomplete diamond nucleation or spontaneous graphitisation [92, 108]. Similarly, the intermediate layer coating acts as an interfacial barrier to hinder cobalt diffusion [108]. When seeding with a high density of diamond nuclei, the growth of the diamond is uniform and supresses the formation of small voids through cobalt diffusion and thereby enhances coating adhesion, whilst low levels of seeded nuclei results in the generation of large voids [108]. In the deposition process, the hydrogen atom released by carbon-carriers during the activation process either ‘abstracts’ the surface for insertion of a hydrocarbon atom or be ‘terminated’ by another hydrogen atom. The degree of competition between the H-abstraction and H-termination mechanisms determines the rate of coating growth [82].

Figure 2.24 depicts the morphologies of a thick film columnar and thin film nanocrystalline CVD diamond coating together with corresponding chisel edges of coated and uncoated drills. In thin film coatings (<50μm) [81, 92], the CVD diamond grows on cemented carbide inserts with randomly orientated fine crystals [82, 109] that exhibit good hardness properties (85GPa) [81] and relatively low roughness values. For thick film blanks, the CVD diamond layers extend to a thickness of ~ 2.3mm with a columnar structure, which are subsequently brazed onto cemented carbide tools [81, 104]. However, as the columnar structures are stacked in a matrix, voids and dislocations can form over time and therefore vulnerable to plastic deformation under heavy loading conditions, resulting in a reduction in strength [81, 104]. Unlike PCD inserts where fabrication and surface finishing is comparatively difficult using grinding/polishing operations [97]; thin film diamond coatings or nano-crystalline diamond films can be easily deposited even on tools with complex geometry as well as providing very smooth surface finish without the need for post polishing [106]. Furthermore, the absence of cobalt in CVD diamond films means that its thermal conductivity (~ 2000W/mK) is superior to PCD [32].

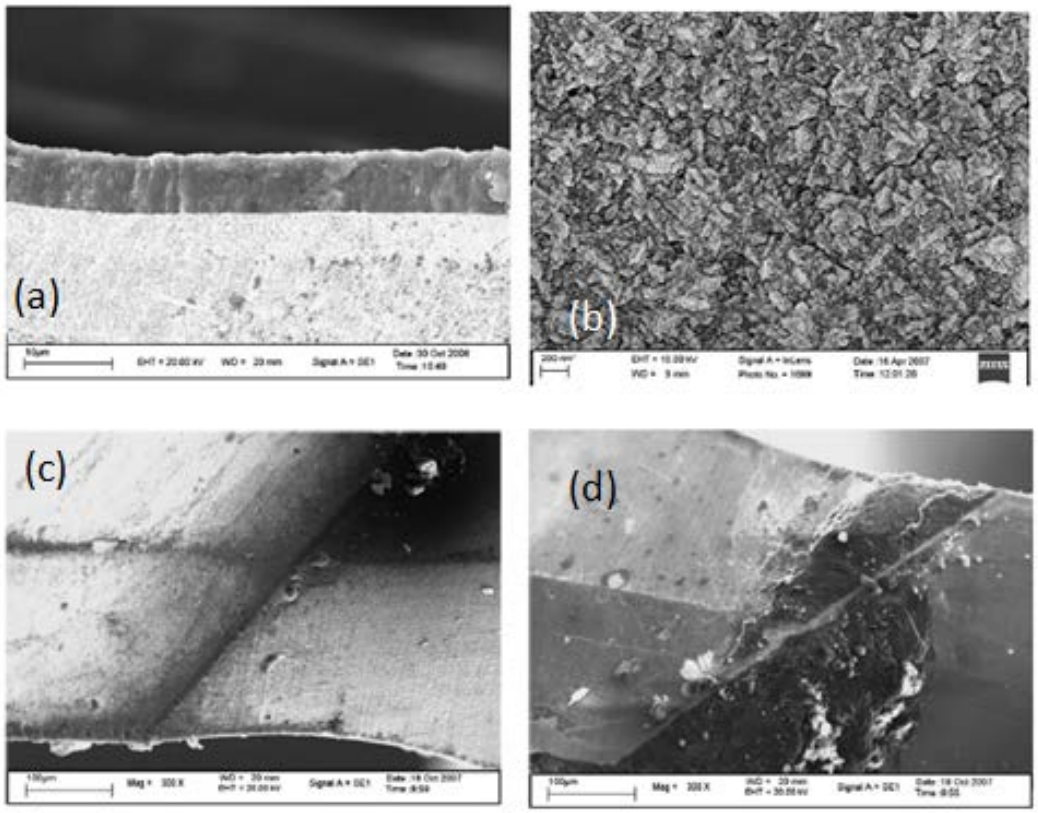


Figure 2.24 (a) Columnar diamond coating, (b) nanocrystalline diamond film, (c) chisel edge of coated drill and (d) uncoated drill [106]

2.5.3.2 Diamond-like carbon (DLC) coating

The principal mechanical properties of diamond-like carbon (DLC) coatings are elevated hardness (~4500HV), high elastic modulus (~180GPa) [110] together with a low friction coefficient (0.1) and a relatively thin film thickness (0.1-1µm); resulting in improved wear resistance and prolonged tool life [24, 111]. The main groups of DLC compounds are classified as non-hydrogenated amorphous carbon (a-C), hydrogenated amorphous carbon (a-C:H), and highly hydrogenated amorphous carbon (polymeric a-C:H), which varies according to the hydrogen concentration. This influences the growth rate of the cubic diamond (sp^3) and graphite (sp^2) bonds, which subsequently determines the hardness levels [82]. With full formation of the cubic lattice, the coating hardness approaches that of natural diamonds at 8000 to 9000HV [111]. Figure 2.25 depicts the surface morphology [110] and cross sections of typical DLC coatings [111].

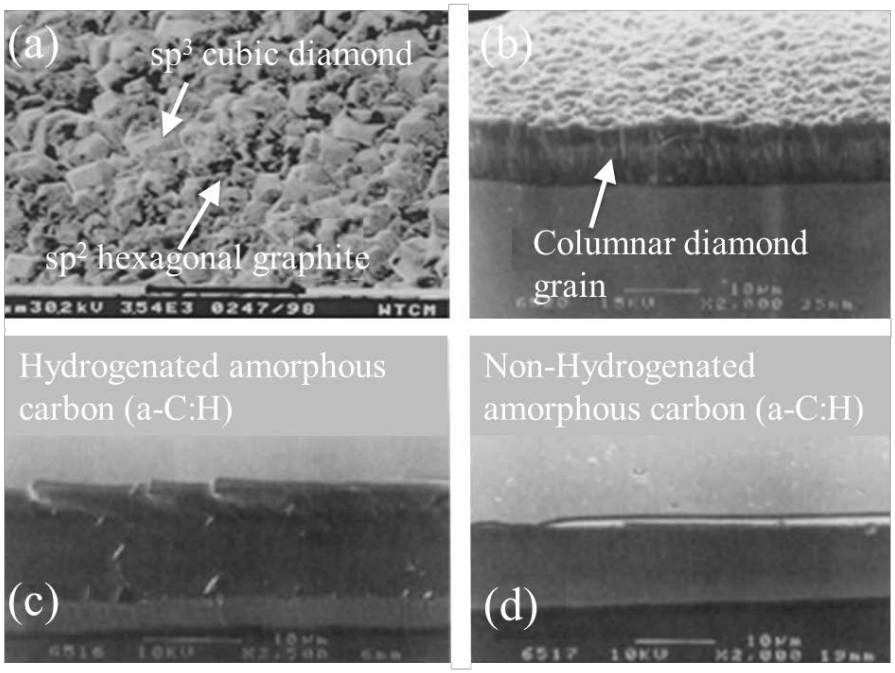


Figure 2.25 (a) Morphology of amorphous DLC coating [110], (b) diamond coating, (c) diamond-like hydrogenated and (d) hydrogenated free coating [111]

The friction of a DLC coating is determined by the ratio of the hard sp^3 and relatively soft sp^2 diamond bonds as well as the surface finish of the tool substrates [112]. Liu and Dandy [82] concluded that a graphitised tribo-layer (sp^2) formed in ambient air led to very low friction of DLC within the 10^{-2} range. In contrast, Jiang and Arnell [110] evaluated the influence of substrate (M42 steel) surface roughness on the wear behaviour of a DLC coating with sp^3 bonds. While frictional behaviour was generally not affected, coating wear rate increased with substrate surface roughness. The comparatively low friction coefficient (<0.1) of DLC coated carbide tools was observed to reduce adhesion wear and eliminate built-up edge when machining aluminium alloys under dry conditions [24]. This was in contrast to uncoated cemented carbide and finely crystallised CVD diamond coatings, which revealed a friction coefficient exceeding 0.8 and 0.4 respectively [112].

2.5.4 Tool wear

The degree of wear on a cutting tool can be used as an indication of resulting surface quality as well as a measure of tool life in machining. Taylor [113] was the first to establish an empirical model ($V \bullet T^n = C$) to estimate tool life based on the cutting speed and machining time to a predefined flank wear level (normally 0.3mm). Although an easy and

straightforward method for predicting tool life, key factors such as wear mechanisms, tool/workpiece material properties and their interactions with other operating conditions (feed rate, depth of cut, cutting environment etc.) were not considered in the Taylor equation. This therefore diminished the validity and accuracy of the model, particularly when applied to a wide range of workpiece materials and cutting operations. The principal tool wear mechanisms include abrasive wear, adhesion/built up edge, diffusion wear, micro chipping, gross fracture and plastic deformation, some of which are briefly outlined below:

- Abrasion wear: Masuda et al. [114] concluded that when machining CFRP using WC-Co under cutting speeds of 40-200 m/min, the dislodgement of hard particles from the flank face was due to the removal of the binder phase via an extrusion action under mechanical loading at low cutting speed (<45m/min) conditions.
- Built-up layer/built-up edge: Sánchez et al. [23] reported that when machining aluminium alloys at cutting speeds of 40-200m/min, temperature-induced oxidation of debris adheres onto the tool surface that initially results in a chemical-induced built-up layer, which is followed by a mechanical-induced built-up edge.
- Diffusion/solution wear: This wear mechanism is attributed to the chemical reaction and atomic migrations [14] of the tool material to the chip, which is particularly prominent under high cutting speed /high temperature conditions.
- Chipping/gross fracture and fatigue: This is generally due to shock/sudden mechanical impacts and thermal stresses especially under cyclic loading conditions [14].
- Plastic deformation: This usually occurs when the cutting nose/edge is subjected to high cutting temperatures and localised stress concentrations, which leads to deformation and sudden failure of the tool [14]. The condition is more pronounced in carbides with higher Co binder content [105].

Tool wear is typically quantified in terms of the length/width/height of material removed/lost from the tool sections. Some of the conventional notation used to describe/indicate the characteristics and location of the wear scar on the tool includes; LR - width of wear land on rake face; RR - edge recession parallel to the rake face; VB - flank wear; CR - edge recession parallel to clearance face and r_n - nose radius. Figure 2.26 depicts the schematic view of the typically wear patterns on an insert together with their key features [105] while Figure 2.27 shows the standard measures of a flank wear (VB) scar on a single point cutting edge [115].

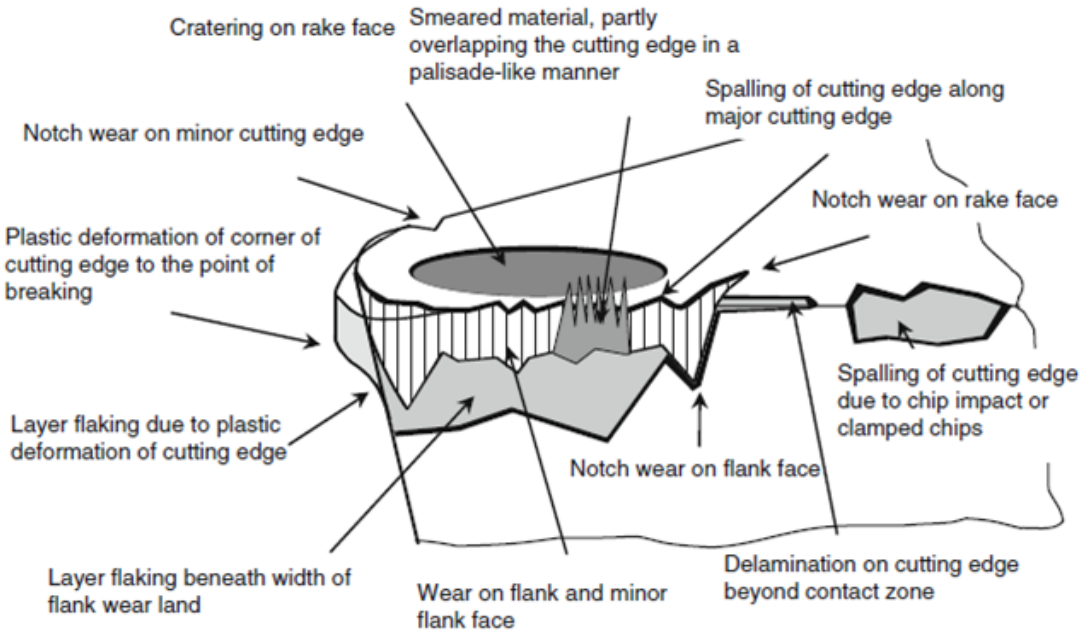


Figure 2.26 Characteristics of typical wear patterns/features on cutting tools [105]

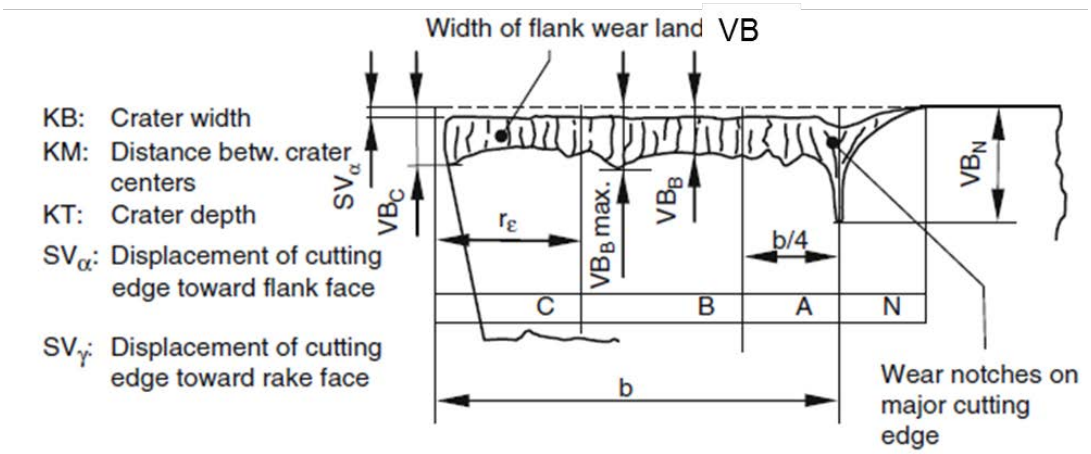


Figure 2.27 Schematic of flank wear (VB) in a single cutting point edge (ISO 3685) [115]

2.5.4.1 Wear of WC-Co tool material

Flank and crater wear are arguably the most common tool wear modes/patterns in metal cutting, which are normally caused by abrasion and diffusion mechanisms respectively. The degree of abrasion in cemented carbide tools is influenced in part by the cobalt content, grit size and distribution [116]; whilst the volume of wear was shown to be dependent on tool hardness and toughness [94]. Diffusion wear is initially triggered by the migration of the cobalt binder together with diffusion of tungsten and carbon atoms under working temperatures, which softens the carbide matrix [14]. The softened structure is then swept

away and removed during contact with the workpiece material [14]. Work undertaken by Saito et al. [94], Gee et al. [117] and Hartung et al. [12] concluded that abrasion wear decreased with lower cobalt content and smaller WC grain size [94, 117], which was explained by a mean free path equation; whereas diffusion wear decreased with reducing cutting temperature [12]. Diffusion however was found to be a dominant wear mechanism for WC-Co tools under certain conditions [118]. Figure 2.28 shows examples of diffusion and fracture wear patterns on carbide tools (K40, WC-10Co) used in the drilling of Ti-6Al-4V under a cutting speed of 50m/min and a feed rate of 0.07mm/rev.

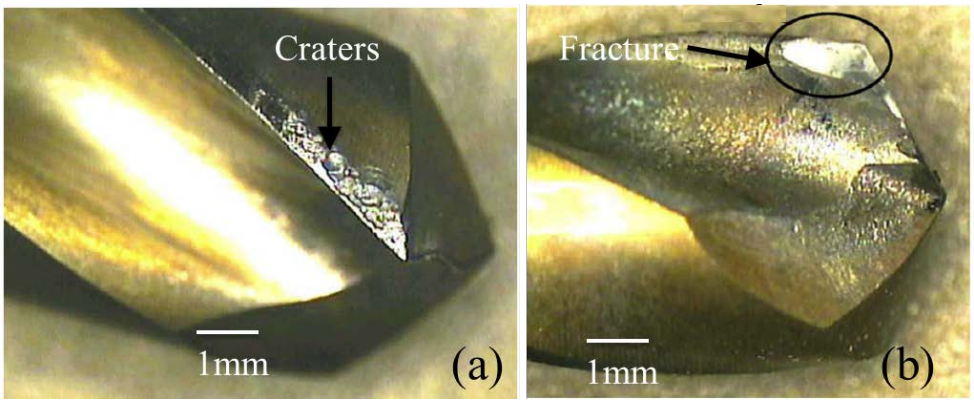


Figure 2.28 (a) Solution wear and (b) fracture of WC in drilling of Ti-6Al-4V [119]

2.5.4.2 Wear of PCD tool material

Abrasion, chipping and fracture are the most common wear modes observed in PCD tools when machining. As with WC materials, the wear rates are influenced by the PCD grain size [120], cobalt content and operating temperatures [121]. In abrasion wear, the binder particles are removed from the sintered matrix during cutting, which results in dislodgement of the diamond grains. With increasing operating temperature, the different thermal expansion rates between the diamond grains and binder phase (cobalt) generates internal stresses leading to chipping and crack initiation at the grain boundaries. Schouwenaars et al. [122] suggested that higher Co content increased the internal stresses due to unbalanced thermal expansion rates with respect to the diamond grains and accelerated reversion of the cubic diamond structure to hexagonal graphite at elevated temperatures (>700°C), thereby weakening the microstructure and promoted cracking. In contrast, when cutting temperatures exceeded 500°C during machining of titanium alloys, the formation of a TiC layer at the tool-workpiece interface restricts diffusion wear leading to extended tool life [1]. Konig and Neises [120] concluded

that increased diamond grain size hinders both the thermal damage and diamond graphitisation at elevated temperatures; therefore providing greater resistance to cracking/wear and improved thermal stability. Figure 2.29 shows typical chipping and fracture wear of a PCD drill following machining of a CFRP/Ti stack [60].

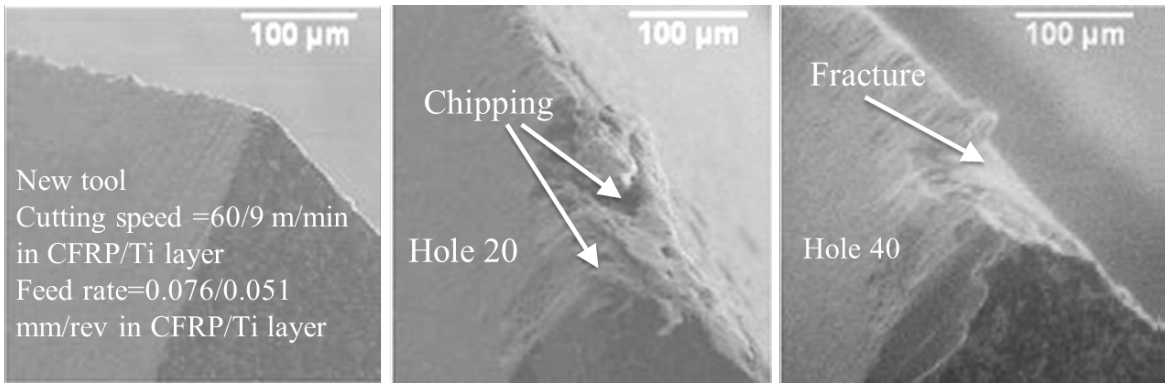


Figure 2.29 Chipping and fracture of PCD in machining of CFRP/Ti stacks [60]

2.5.5 Cutting fluids and effects

The application of cutting fluid in machining operations are principally to remove heat/thermal energy generated by material plastic deformation and friction at the secondary shear zone [123]. This serves to prolong tool life, reduce energy consumption and minimises thermally induced damage in the workpiece, cutting tool and machine tool system [14]. The composition of metalworking cutting fluids is primarily either water or oil-based with a mixture of chemical agents and additives such as emulsifiers, inhibitors and surfactants that enhances the lubrication and/or cooling properties of the fluid [105]. Research involving alternative mediums of cutting environment including minimum quantity lubrication (MQL) [124, 125], dry machining with compressed air [119, 125] or carbon dioxide (CO_2) gas [14] and liquid nitrogen (LN_2) [126] for cryogenic cooling have been increasingly reported in the literature due to their environmentally friendly and sustainable characteristics.

In addition to cooling and lubrication, cutting fluids also assist with chip evacuation from the cutting zone [127]. Work undertaken by Palanisamy et al. [128] showed that using high pressure coolant (HPC) above 7MPa and high flow rate delivery between 12 to 25l/min exhibited superior capacity for heat removal compared to conventional flood coolant. Kovacevic et al. [123] recommended that the cutting fluid should ideally be transported/aimed directly to the vicinity of the cutting zones (primary shear zone, tool-chip interface and

clearance surface adjacent to the machined surface) to increase the efficiency of heat removal. Ezugwu [8] reported that use of an external nozzle with a narrow, high pressure jet aimed at the chip-tool interface creates a 'hydraulic wedge', see Figure 2.30; which reduces seizure and temperature gradient at the secondary shear zone. However, where cutting edges are rotated or obscured, penetration of the fluid jet is diminished; hence Trent and Wright [14] recommends the use of over-flooding at high pressure/ flow rate to improve the cooling effect.

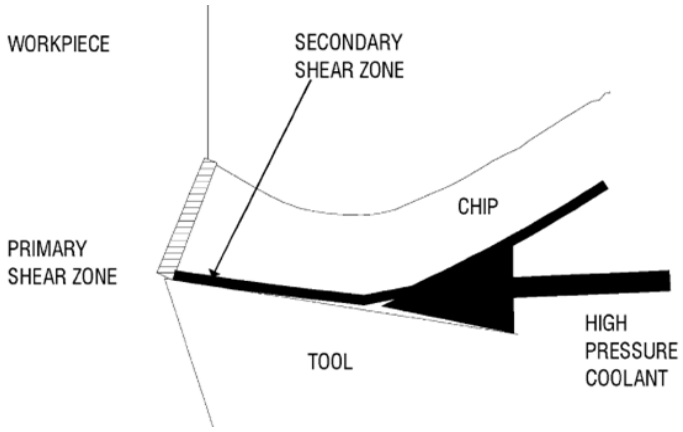


Figure 2.30 Flow of HPC into chip-tool interface/cutting zones [128]

Research involving the influence of cutting fluid when single-shot drilling Ti/CFRP/Al stacks is limited [64, 67-70], although there is substantial literature on the effect of cutting environment when machining titanium alloys [123, 124, 126, 128-131]. As detailed previously, the control and minimisation of temperature when machining titanium alloys is critical in order to maintain acceptable tool life and workpiece surface finish. Work carried out by Kovacevic et al. [123] showed that increasing cutting fluid pressure resulted in better penetration into the chip-tool interface zone when milling Ti-6Al-4V alloy, which reduced diffusion based wear. This was most likely due to a decrease in cutting temperature and suppression of the workpiece material's chemical reactivity. The reduction in tool wear rate also resulted in improved workpiece surface roughness [123], see Figure 2.31. Despite a shorter chip contact length when operating under a high pressure cutting fluid environment, cutting forces usually remain stable due to the lack of workpiece softening [131].

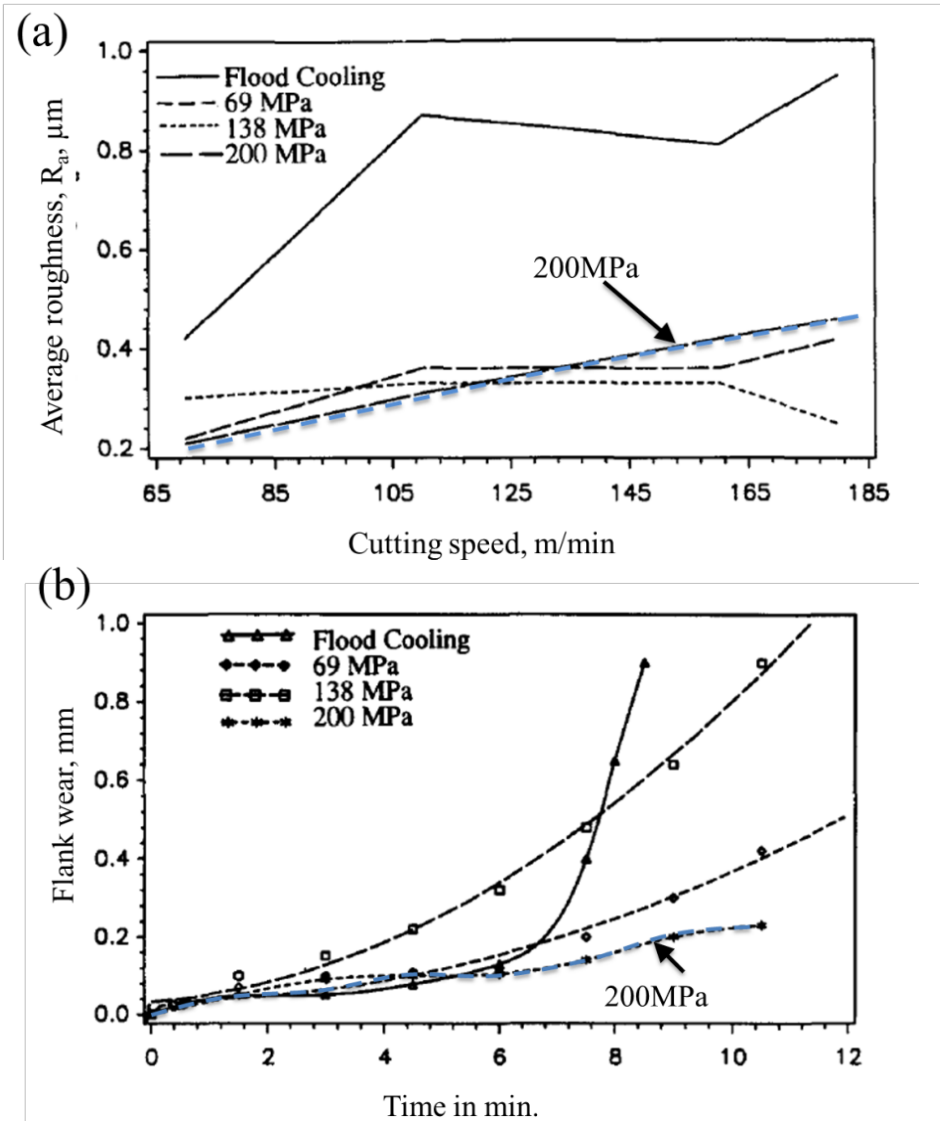


Figure 2.31 Effect of high pressure coolant on (a) surface roughness and (b) flank wear in machining titanium [123]

2.6 Surface integrity in machining

2.6.1 Introduction

Workpiece surface integrity can generally be characterised based on two principal measures: (i) surface texture, which is related to surface roughness/topography parameters [132], and (ii) subsurface metallurgical alterations in terms of mechanical, chemical, metallurgical and topographical factors, which are affected by the cutting process [133, 134]. Variations in workpiece integrity can have significant effects on material properties such as strength, fatigue life etc. which ultimately affects component functionality and performance. Work by Field and Kahles [132] and Field et al. [135] led to the development of a

methodology for defining workpiece surface integrity (SI) based on 3 key experimental data sets with different degrees of complexity and information as detailed in Table 2.11 [132]. The minimum SI data set is suggested as a baseline analysis while the standard SI data set involves additional screening fatigue, stress corrosion and residual stress/distortion evaluation. Figure 2.32 shows a schematic of a machined surface together with the typical scale/depth of subsurface alteration for the various workpiece material features [134, 136, 137].

Minimum SI data set	**Standard SI data set**	**Extended SI data set**
Surface finish Microstructure (<10×) • Microcracks • Plastic deformation • Phase transformation • Intergranular attack • Pits/tears/laps/protrusions • Built-up edge • Melted and re-deposited layers • Selective etching Micro hardness	Minimum SI data set + Fatigue (screening) Stress corrosion test Residual stress and distortion	Standard SI data set Fatigue test (obtain design data) + Additional mechanical tests • Tensile test • Stress rupture • Creep Other specific tests • Bearing performance • Sliding friction evaluation • Sealing properties of surface

Table 2.11 Surface integrity data set [132]

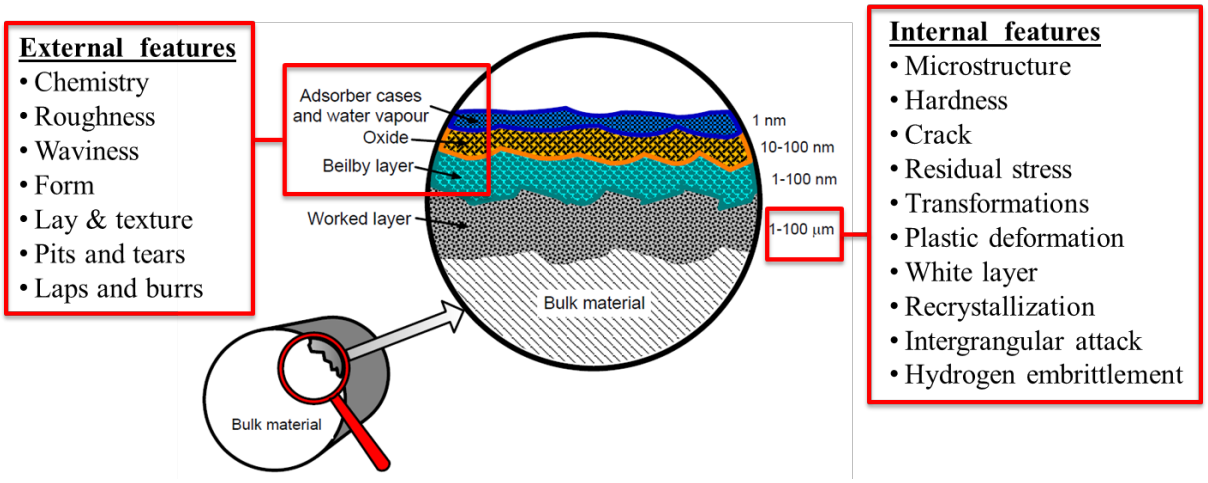


Figure 2.32 Schematic representation of a machined surface [136]

In the drilling of metallic-composite alloys, hole surface integrity based on the minimum data set is generally evaluated for the titanium, CFRP and aluminium layers. In addition to overall hole dimensional considerations (roundness/cylindricity, diameter etc.), the damage assessed in the fibre-reinforced composite section include delamination, fibre pull out, swelling, shrinkage, and matrix burn [45, 47, 138-141]; whilst in the metallic layers, hole surface roughness, microhardness variations and microstructural alterations were considered. Figure 2.33 details a schematic of the typical defects encountered following drilling of a 2 layer metallic-composite stack [67].

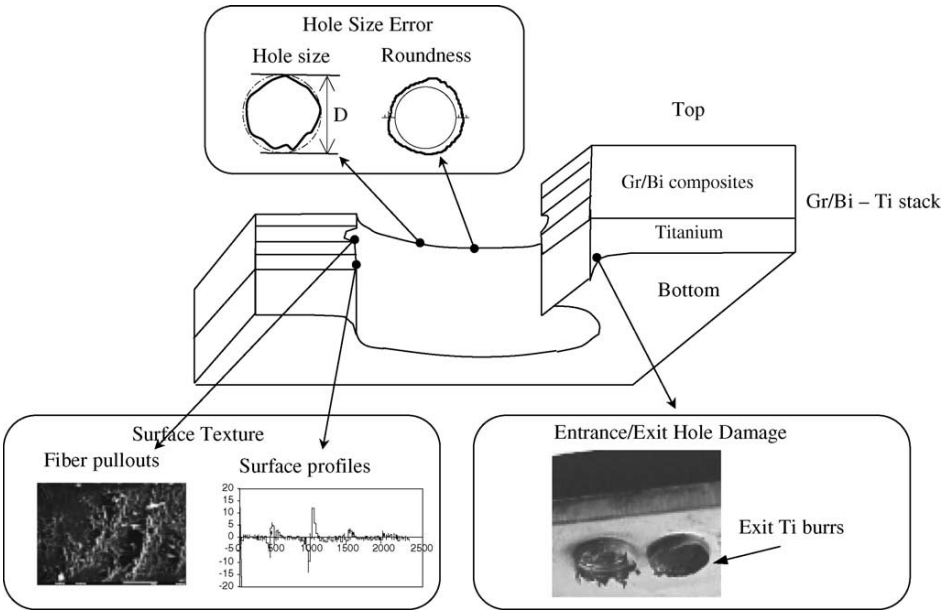


Figure 2.33 Typical defects/damage in drilling of metallic-composite stack materials [55]

2.6.2 Surface texture parameters and characterisation

Surface texture is typically characterised by roughness and waviness [142]. The roughness of a surface includes irregularities caused by individual manufacturing processes that imprint its pattern on the surface [142, 143] and is consequently superimposed over the form waviness, which is generally caused by vibration and chatter of the machine tool. The properties of surface texture are usually quantified using two (line) and three-dimensional (area/space) parameters. Whitehouse [144] and Smith [145] discussed the requirements for filtering/incorporating cut-off lengths to profiles measurements in order to describe the macro- and micro-geometrical aspects of surfaces, while the application of 2RC and Gaussian filters were considered for dealing with form deviations on waviness and roughness.

Surface roughness parameters are organised into three groups [142, 146, 147], which are defined and specified in ISO 13565-2:1997 [148]. The first group involves amplitude parameters of roughness (Ra, Rz, Rt, Rq etc.), which are characterised by the statistical distribution of height obtained from the amplitude probability density function of the profile. The second group relates to the shape of the ordinate distribution, described as the cumulative height distribution through skewness (Rsk=ζ) and kurtosis (Rku=ξ), which represents the asymmetry and the sharpness distribution a profile respectively [145, 147]. In practical terms, skewness describes the shape of a profile while kurtosis measures the sharpness of peaks in a profile [147]. Figure 2.34(a) shows examples of profiles with positive and negative skewness values, with the former suitable as a locking surface where adhesive-bonding properties are required. Conversely, a profile with negative skewness are preferred as load bearing surfaces [145]. A schematic description of kurtosis is illustrated in Figure 2.34(b), where a value > 3 generally indicates a profile with a high degree of sharp peaks while a value of < 3 implies a surface with a greater number of 'flat' peaks [145].

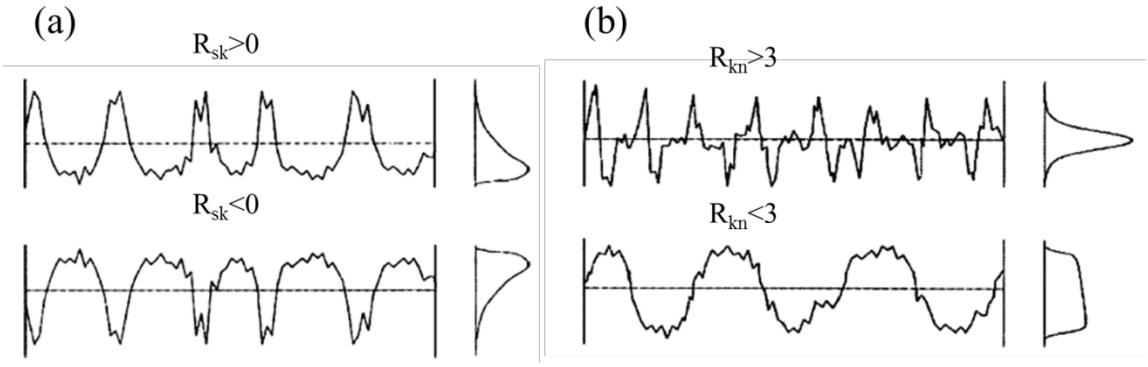


Figure 2.34 (a) Skewness and (b) kurtosis values corresponding to surface textures [145]

The third group of surface parameters are used to define the waviness (Wa, Wt), which are obtained from the autocorrelation function (ACF) or power spectrum density function (PSDF) [142, 146]. These measures are typically used to analyse and classify surface patterns in order to optimise manufacturing processes. Zipin [143, 146] concluded that each manufacturing process produces the unique surface pattern and therefore can be distinguished by the power spectrum density function. Ramulu et al. [149] reported that when drilling CFRP, the roughness pattern on the hole surface varied with fibre orientation and could therefore be detected from a power spectrum density plot. Figure 2.35 shows the periodic pattern produced by 60° plies that resulted in the highest spectrum density through the autocorrelation (τ=130μm) and power spectrum function (w/2π=0.0143) [149].

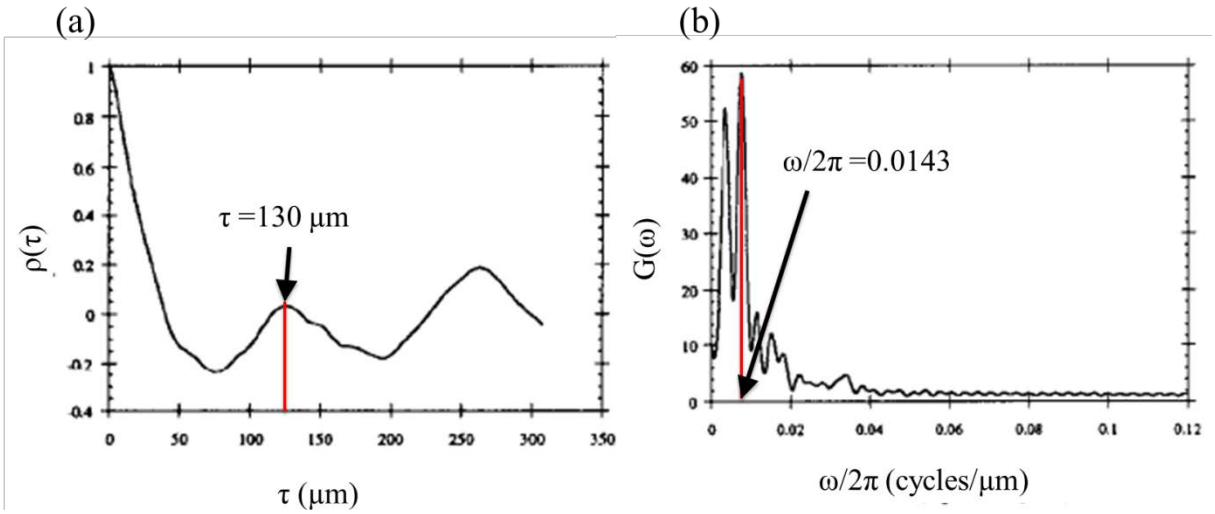


Figure 2.35 (a) Auto correlation function, and (b) power spectrum density plot [149]

2.6.3 Diameter variation, out of roundness and cylindricity

Diameter variation, out of roundness and cylindricity denotes the measure of hole radius deviation in one, two and three dimensions respectively. Out of roundness and cylindricity tolerances in engineering components are normally specified to ensure appropriate fitting during assembly and to distribute bearing stresses evenly across the hole circumference. Discrepancies in hole roundness and cylindricity are caused by various factors including process induced rotational imperfections, release of stored strain energy in workpiece [150], radial vibrations from tool displacement [151], thermal loads [152] and machine calibration errors [153]. Hole diameter accuracy, roundness and cylindricity are generally analysed both statically and dynamically as functions of drill geometry and mechanics of the drilling operation [145]. The main sources of hole dimensional variation are detailed below:

- Chisel edges with large point angles (relatively blunt) are prone to ‘walking’ [145] upon commencement of drilling which is then constrained at an angle following full engagement of the drill margins, resulting in a ‘bell-mouth’ effect as illustrated in Figure 2.36(a).
- Dissimilar lengths between cutting lips generate unbalanced thrust forces and torque, leading to ‘helical wandering’. This effect is exacerbated with increasing drilling length/depth and poor process rigidity, which results in drill deflection [154].
- High thrust force and torque acting on the cutting lips causes ‘unwinding’ of the twist drill, which induces dynamic instability in the form of vibrations and harmonic out-of-roundness effects, with degradation of surface topography [155]. Figure 2.36(b) shows the influence of depth of cut on harmonic effects [145].

Typical roundness errors due to unbalanced asymmetric cutting include severe variations in cross-sectional shape/profile when progressing from the top to the bottom of the hole, as shown in Figure 2.36(c) [145]. Franke [156] reported that deviation from nomimal hole diameter increased with fibre volume fraction and tool edge corner radius when drilling FRP materials. However, higher fibre volume fractions did not appear to affect the out of roundness levels as the fibres were elastically deformed/protruded according to the hole circumference, which did not vary with run-out of the drill feed axis.

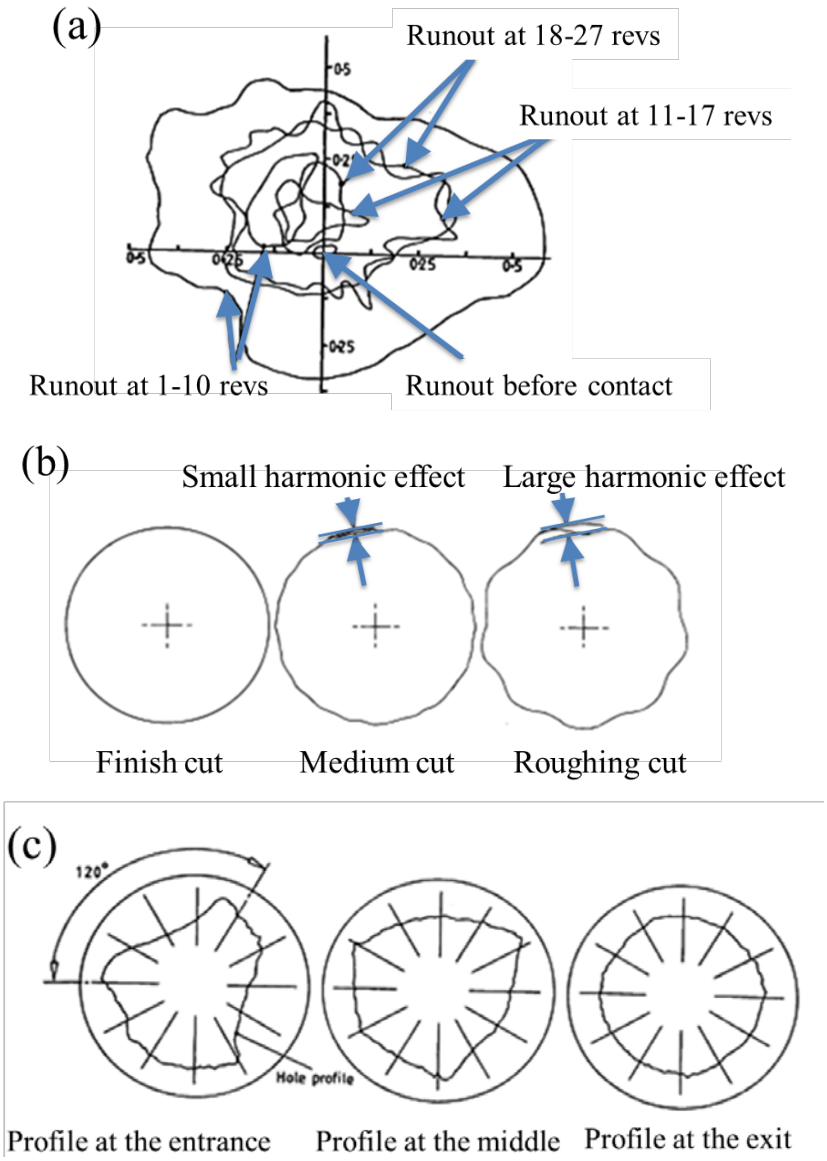


Figure 2.36 (a) 'Walking effect' of chisel edge, (b) influence of depth of cut on harmonic effect and (c) multi-lobed roundness profile [145]

2.6.4 Delamination

Delamination typically occurs in laminated composites according to a mode I fracture mechanism (tensile fracture) [49, 157], which exacerbates crack propagation and is recognised as a major factor in the degradation of component strength and in-service life. Such defects are normally prevalent at three zones of a hole, which are the entrance and exit locations as well as between individual plies [67, 157-159]. A measure that can be used to quantify the level of delamination is the 'delamination factor' (F_d), as defined by Equation 20 [44, 160]. An alternative parameter, which considers the area of visible damage, is the 'adjusted delamination factor' (F_{ad}), as expressed in Equation 21 [44, 160]. Various measurement techniques can be employed to determine the delamination size or area including computerised tomography scanning (C-scan) [139], optical scanning with image processing [44] and ultrasonic scanning [161], see Figure 2.37.

$$F_d = \frac{D_{max}}{D_o} \tag{20}$$

$$F_{ad} = \alpha \bullet \frac{D_{max}}{D_o} + \beta \bullet \frac{A_{max}}{A_o}, \qquad \alpha + \beta = 1 \tag{21}$$

where D_{max} was the maximum diameter measured, D_o the original drill diameter, A_{max} the maximum measured area of delamination, A_o the nominal drilled area, with α and β weighting constants, the sum of which are equal to one.

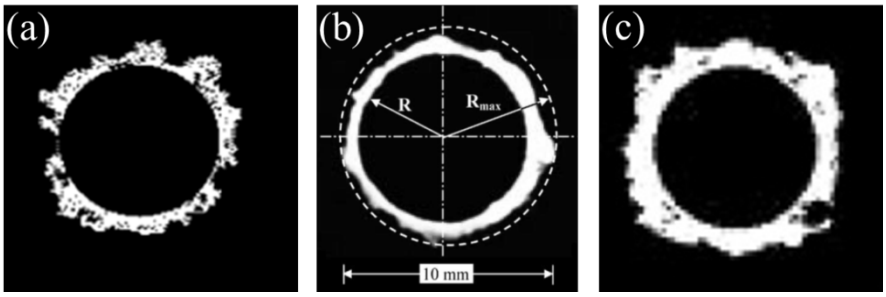


Figure 2.37(a) Computerised tomography scanning [139], (b) optical scanning [44] and (c) ultrasonic scanning [161]

2.6.5 Burr formation

Most drilling processes generate burrs, which is due to plastic deformation of the workpiece material in the form a tear, bent, lateral extrusion or rub-hardened residual material

at the entrance or exit of a hole [162-164]. The formation of burrs can lead to deterioration of hole integrity and damage to mating parts [162]. The cost of removing burrs is estimated at up to 30% [164] of the total manufacturing cost of a component. With multilayer materials, burr removal is preceded by dismantling of the stack arrangement with subsequent reassembly of the structure, which further escalates the outlay. Therefore, control of burr formation, minimisation of burr propagation and development of more efficient deburring technologies were proposed as major research goals in a CIRP keynote paper in 2003 [125] although as yet, results have not sufficiently satisfied the requirements of industrial applications.

Gillespie and Blotter [165] defined four categories of burrs; (i) Poison burr, (ii) rollover-burr, (iii) tear burr and (iv) cut-off burr, which were based on their respective forming mechanisms involving lateral deformation, longitudinal deformation, material tearing loose and over-stretched residual material. Aurich et al. [163] detailed in a review of the literature that burrs can be characterised geometrically using a burr value ‘g’ measured at its cross section, whilst the ISO standard [166] describes burrs as the length ‘a’ of edge protrusions, see Figure 2.38. More recently, Kim et al. [167] proposed that burrs can be classified into 5 groups based on a description of their shapes, as shown in Figure 2.39.

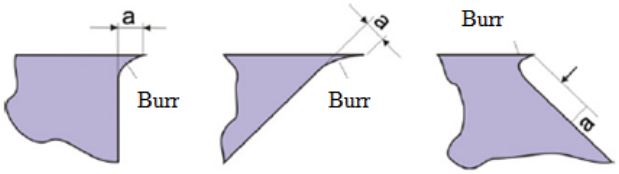


Figure 2.38 Definition of burr according to ISO standard [166]

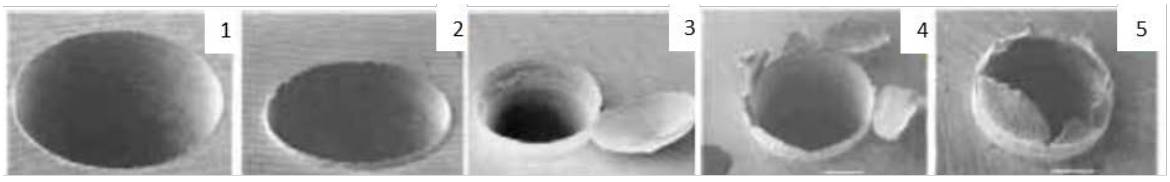


Figure 2.39 Classification of burrs according to Kim et al. [167]

Min and Dornfeld [168] reported that burrs can be measured precisely using a laser displacement sensor to an accuracy of 0.5μm, while Nakao and Watanabe [169] showed similar results were obtained when employing image processing technology together with a

CCD camera to evaluate burr height, thickness and profile. Hashimura et al. [170] highlighted that burr formation was generally more severe at hole exit in drilling, with the critical ratio of uncut chip thickness and radial support determining the pivot point for the initiation of material deformation / bending. Figure 2.40 shows schematically the development and progression of burr formation.

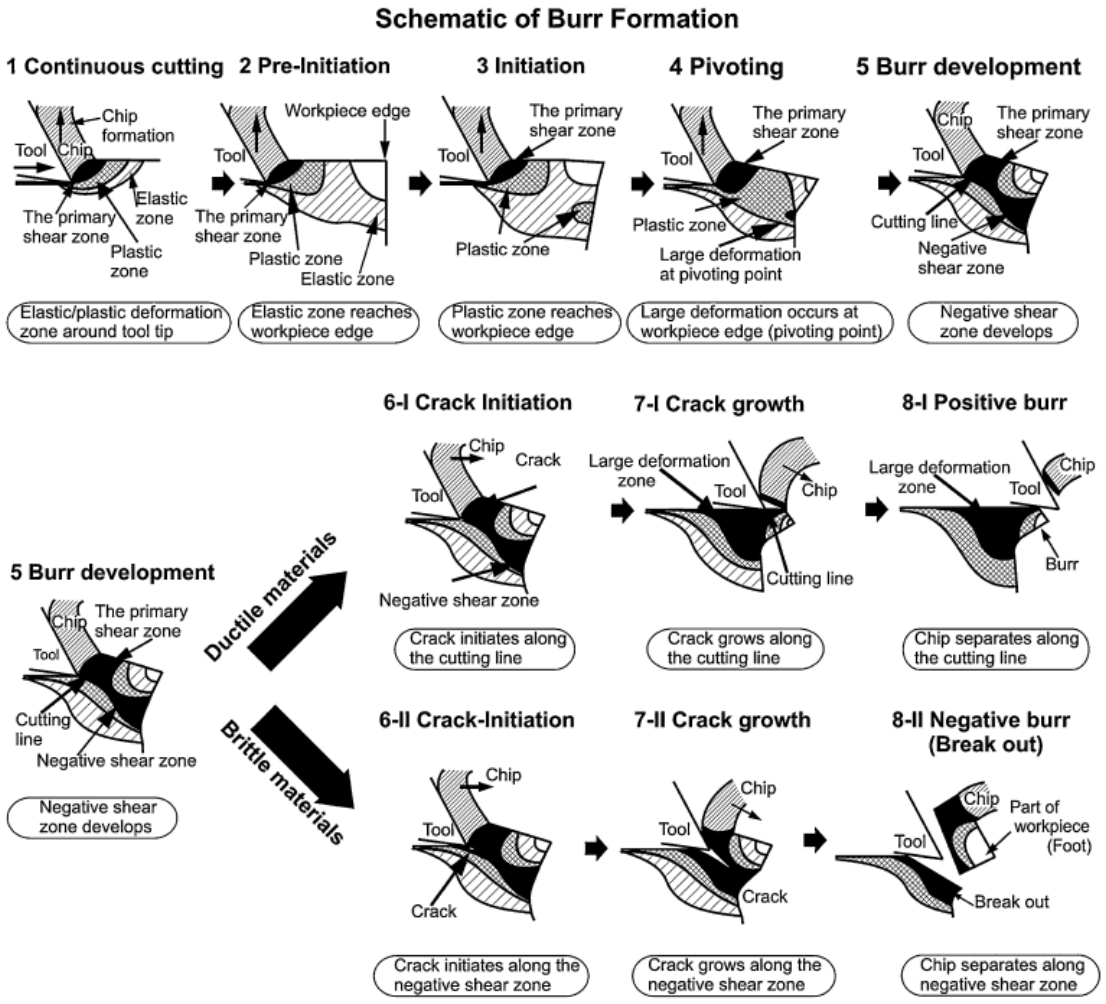


Figure 2.40 Progression of burr formation [170]

Various parameters can affect the formation and growth of burrs including cutting speed, feed rate, tool wear, tool geometry (point angle, helix angle, and releif angle), surface exit angle/pivot point and workpiece material properties [125, 162-165, 167, 168, 171-175]. Dornfeld et al. [164] and Stein and Dornfeld [176] concluded that higher cutting speed and greater tool wear increases burr height and thickness, while larger helix (35˚) and point angles (135˚) as well as feed rate reduces burr height and thickness. Ko et al. [162, 174] reported that

use of step drills generally minimised burr size due to a smaller second point angle (75˚) and larger depth of cut at the secondary cutting lips. Min et al. [177] found that increasing the surface exit angle shifted the pivot point towards the drill centre axis, thereby decreasing the bending moment on the material and suppressing burr formation. Figure 2.41 shows the influence of varying surface exit angles on pivot point location. The use of hybrid vibration-assisted drilling to reduce burr height was investigated when drilling titanium alloys, aluminium alloys and FRP by several researchers [178-180]. When drilling metallic-metallic and metallic-composite stacks, interlayer burrs were influenced by the sealant thickness / gap, which can cause irregular burr formation as shown in Figure 2.42.

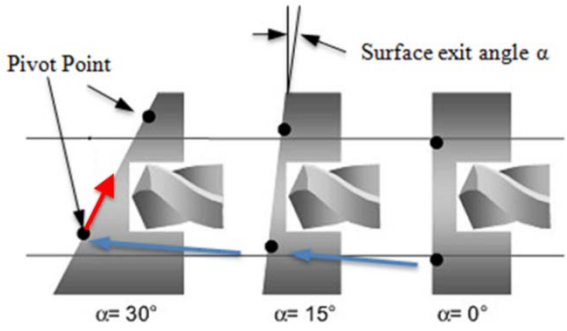


Figure 2.41 Effect of surface exit angle on pivot point location [177]

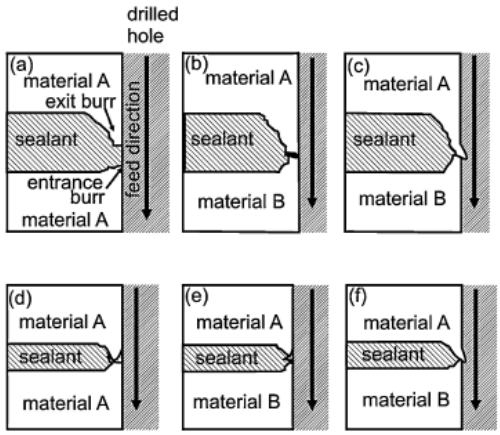


Figure 2.42 Interlayer burr shapes in stack materials [172]

2.7 Temperature measurement and effects

Heat is produced in practically all conventional metal removal processes due to plastic deformation of the workpiece material and friction between the chip and rake face of the tool. Higher cutting temperatures degrade the performance of the cutting tool, which reduces productivity as well as compromises the integrity of the machined surface. In a recent keynote

paper, Davies et al. [181] reviewed the range of techniques used for temperature measurement in machining operations as well as research into predictive methods for determining the effect of thermal variables on key process outputs. The evaluation of temperature in drilling operations is generally regarded to be relatively complicated. Agapiou and DeVries [182] established analytical equations to predict the temperature distribution along the cutting lips of a drill by incorporating a fundamental force model associated with chip thickness and tool-chip contact length. Bono and Ni [183] showed that the maximum temperature at the chisel zone was due to high frictional forces acting on the negative rake face. In contrast, Ueda et al. [184] reported that the highest temperature at the periphery of the cutting lips was due to maximum torque at high cutting speeds. High thermal loads at the chisel edge tends to damage the drill geometry leading to premature tool failure, while tool wear/fracture at the peripheral corner of a drill has detrimental effects on hole accuracy as well as workpiece surface integrity.

2.7.1 Temperature effects in drilling of titanium alloys

Le Coz et al. [185] reported that temperatures up to 600˚C were recorded when drilling Ti-6Al-4V alloy using a 10mm carbide drill at a cutting speed 35m/min and a feed rate of 0.16mm/rev under an internal MQL (minimal quantity lubrication) environment. Although operating at lower parameters (cutting speed of 30m/min and feed rate of 0.10mm/rev), Zeilmann and Weingaertner [186] showed that when drilling Ti-6Al-4V with 8.5mm diameter uncoated carbide tools, through-spindle application of MQL (P=3.5 bar, Q=50ml/h) reduced cutting temperatures to ~250˚C, compared to ~550˚C when the oil was supplied externally. Li and Shih [187] evaluated the influence of cutting environment when drilling Ti-6Al-4V using a 9.92mm diameter tool at a cutting speed of 183m/min and a feed rate of 0.051mm/rev. Maximum temperature was over 1210˚C when drilling dry, which decreased to ~651˚C under wet (internal coolant supply) conditions. The high temperatures generated (1210˚C) most likely caused annealing of the BCC β phase and triggered transformation to a HCP α phase, which resulted in a hardened subsurface layer (15-20μm) of over 10GPa. Conversely, workpiece microhardness was ~5.0 - 5.5GPa when drilling wet. In related work, diffusion wear of the cutting tool and subsurface microstructural alterations of the machined surface were also observed when drilling dry [188]. Hence, the use of high-pressure cutting fluids is generally recommended when machining titanium alloys due to their superior cooling rates.

2.7.2 Temperature effects in drilling of CFRP composite

The heat/temperature generated during machining of CFRP composites is a key factor affecting workpiece surface integrity, due to the dissimilar thermal properties of the matrix and reinforcement phases of the material. Konig and Graß [45] indicated that measured temperatures can exceed 300˚C when drilling CFRP, which is typically beyond the glass transition temperature of the polymer matrix and transforms the workpiece from a stiff, glassy material to a softer, rubber-like form. This can result in decomposition, melting and burning of the epoxy that adheres onto the cutting tool and reduces the sharpness of the cutting edge, subsequently causing a rise in thrust forces leading to interlayer delamination. Chen [44] carried out experimental investigations involving the drilling of CFRP composite laminates using 5mm diameter HSS drills at varying cutting speeds (35 – 200m/min) and feed rates (0.10 – 0.40mm/rev). The results showed that temperatures increased with increasing cutting speed and decreasing feed rate.

Konig and Graß [45] found that when drilling epoxy based CFRP composites (65% fibre content) at a feed rate of 0.02mm/rev and cutting speed of 50m/min under dry conditions, the ratio of heat distribution into the chip, workpiece material and cutting tool was 25%, 24% and 51% respectively. This was in contrast to metallic alloys where the breakdown is typically 37%, 5% and 58%, which suggests that heat absorption in CFRP was significantly higher in comparison to metallic based materials. Similarly, Weinert and Kempmann [189] reported that cutting temperatures ranged between ~ 200 - 350˚C when drilling CFRP composites at cutting speeds and feed rates of up to 180m/min and 0.18mm/rev respectively. Apart from thermally induced surface/sub-surface defects on the workpiece material (matrix burning, polymer decomposition etc.), increased machining temperatures generally results in enlarged hole diameters. Drilling in a wet environment was therefore suggested as a solution to minimise cutting temperature and extend tool life, but which could potentially trigger other workpiece related defects due to absorption of the fluid by the CFRP matrix.

2.7.3 Temperature effects in drilling aluminium alloys

Exposing aluminium alloys to elevated temperatures above 200°C for a sustained period when drilling can cause localised softening of the workpiece material, resulting in alterations of its metallurgical properties and associated influence on mechanical strength. Kalidas et al.

[190] evaluated the performance of three different coatings (TiAlN/TiN, TiAlN, MoS_2) against uncoated HSS tools in terms of hole diameter, workpiece surface roughness, cutting temperature and tendency for chip clogging, when drilling cast A356 alloy under dry and wet conditions. Maximum measured temperature over the range of experimental conditions was 51.2˚C when operating at a cutting speed of 45m/min and feed rate of 0.083mm/rev. The average radius (4.5535mm) of holes produced using TiAlN/TiN coated drills under a wet environment showed the least deviation from the nominal value (4.561mm) when measured along the axial direction. However, the relatively low thermal conductivity of the coating generated high temperature gradients at the drill-chip and drill-hole wall interfaces. As a result, chip clogging was prevalent due to the hot swarf adhering onto the drill flutes. Additionally, it was found that the cutting environment significantly influenced hole surface roughness, while coatings showed no appreciable effect. Bagci and Ozcelik [191] investigated the effects of drilling depth, cutting speed and feed rate on temperatures when dry drilling A7075-T651 using two different feed strategies. When employing the continuous feed strategy, cutting temperatures were observed to increase with drilling depth and cutting speed, but decreased with higher feed rates. In contrast, temperature was found to decrease with increasing spindle speed when utilising the step-by-step feed strategy.

2.8 Experimental design techniques and analysis

A key objective when analysing experimental results is to quantify and determine the influence of individual variables and levels as well as associated factor interactions on specified response measures/outputs. A further aim would be to identify the preferred combination of factor levels to achieve a required outcome based on the recorded experimental data. This can be performed by utilising statistical design of experiment (DOE) techniques [192].

2.8.1 Full factorial experiments

When a relatively low number of factors and levels are considered, a full factorial experimental design (levels of each factor tested against every level of other factors) can be realistically employed to assess all main factor effects and related interactions. However, when the quantity of factors/levels are large, the number of tests required to satisfy a full

factorial design would typically be impractical [193, 194]. An alternative solution involving fractional factorial designs were developed by G. Taguchi in the late 1970's [195].

2.8.2 Taguchi methods and factorial design

In Taguchi's method, the 'confounding' process was employed in fractional factorial designs to reduce the number experiments while maintaining the capability for calculating the significance of main factors and specific interactions with acceptable confidence. Taguchi introduced 'Orthogonal Arrays' that allows only a subset of factor levels to be combined with another subset of factor levels for the individual tests. The minimisation of interactions was accomplished by initially utilising a 'cause-and-effect' analysis to screen out any illogical assumptions followed by implementation of the 'confounding' process by replacing the main effects with interactions, as shown in Table 2.12 [195].

	A	B	G	C	F	E	D
Column NO.	1	2	3	4	5	6	7
Experiment							
1	1	1	1	1	1	1	1
2	1	1	1	2	2	2	2
3	1	2	2	1	1	2	2
4	1	2	2	2	2	1	1
5	2	1	2	1	2	1	2
6	2	1	2	2	1	2	1
7	2	2	1	1	2	2	1
8	2	2	1	2	1	1	2
Confounded	BG	AG	AB	AF	AC	AD	AE
2-factor	CF	CE	CD	BE	BD	BC	BF
interactions	DE	DF	EF	DG	EG	FG	CG

Table 2.12 Confounding process in an L8 array

2.8.3 Analysing data from orthogonal arrays

2.8.3.1 Main effects plot

The main effects plot shows the range of results obtained with respect to a given variable factor. Table 2.13 and Table 2.14 [196] illustrates a typical result and effects table for each factor while Table 2.15 an example main effects plot over the factor levels, with a steeper gradient suggesting a stronger influence/significance of the factor. Here, the preferred combination of factor levels according to the rule of 'larger is better' is $A_1B_2G_2C_1F_2E_2D_1$, while the combination of $A_2B_1G_1C_2F_1E_1D_2$ reflects the rule of 'smaller is better'.

	A	B	G	C	F	E	D	Result
Column NO.	1	2	3	4	5	6	7	
Experiment								
1	1	1	1	1	1	1	1	Result 1
2	1	1	1	2	2	2	2	Result 2
3	1	2	2	1	1	2	2	Result 3
4	1	2	2	2	2	1	1	Result 4
5	2	1	2	1	2	1	2	Result 5
6	2	1	2	2	1	2	1	Result 6
7	2	2	1	1	2	2	1	Result 7
8	2	2	1	2	1	1	2	Result 8

Table 2.13 Results table for Taguchi L8 test

	Factor	A	B	G	C	F	E	D
Average Response	Level 1	a1	b1	g1	c1	f1	e1	d1
	Level 2	a2	b2	g2	c2	f2	e2	d2
	Effect	a2-a1	b2-b1	g2-g1	c2-c1	f2-f1	e2-e1	d2-d1

Table 2.14 Effects table for Taguchi L8 test

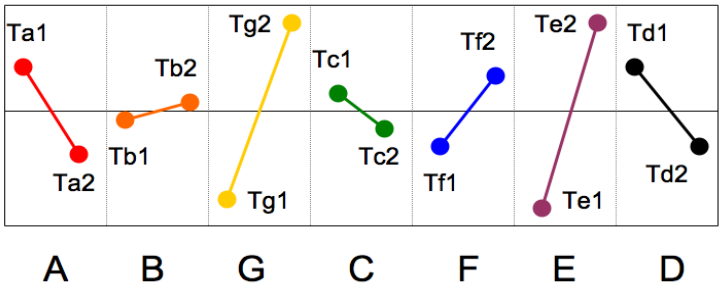


Table 2.15 Example of main effects plot

2.8.3.2 Analysis of variance (ANOVA)

In cases where the factors exceed two groups, a means t-test cannot be used by grouping the factors in pairs. Here, the method of 'Analysis of Variance' (ANOVA), which breaks down the total variability into its component parts and compares it to the experimental error, can be utilised. The initial hypothesis can be rejected or accepted by comparing the ratio of the mean sum of squares (F_{cal}) between a factor and the residual error to the appropriate significance level (usually 5%) value from the t-distribution chart [193, 196].

2.8.3.3 Percentage contribution ratio (PCR)

The amount of total variation calculated in an experiment attributed to each significant factor or interaction is known as the percentage contribution ratio (PCR) [196]. Factors that have a strong influence on a given response typically reflect high percentages of variance. If the strong factor/interaction can be properly controlled, the amount of variance is reduced,

thereby resulting in a lower value of percentage contribution. The percentage contribution ratio (PCR) can be calculated according to;

$$\text{PCR}=\frac{\text{Expected sum of squares for factor X}}{\text{Total sum of square}}\times 100\%$$

where the 'Expected sum of squares for factor x' = Sum of square X- (Residual variance M.S.S.) × (number of degrees of freedom for factor x).

The percentage contribution of the residual variance/error is an important measure to determine the effectiveness of the experiment. Where the percentage contribution of the residual variance/error is less than 15%, it is generally assumed that there were no significant factors ignored in the experiment. Conversely, a residual error PCR greater than 50% implies that significant factors were deleted or ignored from the experiment, conditions are not well-controlled or measurement errors were present [196].

2.8.3.4 Confirmation experiment

A confirmation experiment is used to verify whether the preferred factor levels match the predicted result [196]. The method of confirmation is to calculate the average of the result of the experiment and examine if the measured value is within the limit of the confidence interval (Equation 20) of the predicted value.

$$\text{Confidence interval} = \pm \sqrt{F_{\alpha}(1,\upsilon_e)V_e\left[\left(\frac{1}{n_{eff}}\right)+\left(\frac{1}{r}\right)\right]} \quad (20)$$

where : $F_{\alpha}(1,\upsilon_e)$ is the value from the T-distribution with the degree of freedom associated with the residual, V_e is the residual mean sum of square and;

$$n_{eff}=\frac{\text{Total number of observations}}{1+(\text{total degree of freedom associated with items used in estimated mean})}$$

Therefore, the confidence limit = Predicted value $\pm \sqrt{F_{\alpha}(1,\upsilon_e)V_e\left[\left(\frac{1}{n_{eff}}\right)+\left(\frac{1}{r}\right)\right]}$

In fractional factorial experiments, the preferred factor level combinations derived from the main effects plot can be a test that was run in the original set of experiments in the orthogonal array or otherwise; therefore the method of confirmation can take one of two different cases:

- Case 1: The best combination is within the orthogonal array experiments. In this case, the predicted value can be estimated by reading the average result from the particular experiment with the preferred factor/level combination.
- Case 2: The best combination is not within the orthogonal array experiments. In this case, the overall average is calculated to determine the change of each factor's influence on the combination. The sum of the effect will be the predicted value [194, 196].

3 EXPERIMENTAL WORK

The research was carried out over three main phases of experimental work. In Phase 1 experiments, the performance of various cutting tool materials (tungsten carbide/TiAlN multilayers, DLC and CVD diamond coatings) together with the effect of operating parameters and drilling strategy were evaluated with respect to forces, tool life, hole quality and workpiece surface integrity. A novel PCD format recently developed by Element Six (domed PCD) was evaluated for the single-shot drilling of Ti/CFRP/Al stacks in Phase 2 work together with confirmation trials to validate results of the bespoke drill geometry against recommended commercial products. Phase 3 involved an assessment of cutting environment (fluid pressure and dry) on machining temperature as well as the subsequent effect on workpiece integrity. The sub-phases associated with each phase of experiment are listed below:

- Phase 1A: Effect of tool material, feed rate and drilling strategy
- Phase 1B: Influence of margin design, feed rate and drilling strategy
- Phase 1C: Hole quality and failure modes of diamond coated tools
- Phase 1D: Effect of tool geometry and operating parameters
- Phase 2A: Evaluation of diamond coated/novel PCD drills and feed rate at elevated cutting speed
- Phase 2B: Confirmation test and benchmarking of bespoke drill geometry
- Phase 3: Effect of cutting environment and feed rate to cutting temperature

The following sections outline the workpiece materials, cutting tools, equipment and test procedures employed together with the experimental arrays.

3.1 Workpiece materials

The workpiece material used in all of the experiments was a 3-layer metallic-composite stack in the form of either a plate or strip as shown in Figure 3.1. The stacks comprised; (a) annealed Ti-6Al-4V titanium alloy with a yield strength and elastic modulus of 880MPa and 114GPa respectively; (b) carbon fibre reinforced plastic (CFRP) composite composed of pre-impregnated high tensile strength (HTS-268-12K) carbon fibres (6-8μm diameter) with an

epoxy matrix (prepreg), having a tensile strength of 1200MPa and stiffness modulus of 145GPa, with a 56.5% volume fraction of fibre content and; (c) A7050-T7651 aluminium alloy with a yield strength and elastic modulus of 455MPa and 72GPa respectively. Both the Ti and Al metallic plates were 10mm thick with square dimensions of 120mm×120mm, while the CFRP plates had thicknesses of either 10mm or 7mm. The stacks were arranged in the order of Ti/CFRP/Al and bonded together using a film adhesive (3M AF163-2X), which was cured for 60 minutes at 120˚C, resulting in a bond strength of 48.25MPa at the metallic-composite interfaces and a corresponding shear strength of 439.1GPa. While the plate workpieces were utilised for tool life testing, the thin strip measuring 120mm×17mm×30mm or 120mm×17mm×27mm, which were mechanically joined using two M6 button head screws without adhesives to enable easy disassembly were employed for force measurement, burr height evaluation and subsequent hole surface roughness, roundness and cylindricity analysis. All of the stack workpiece materials were prepared and supplied by the Composite Research Centre (CRC), GKN Aerospace at the Isle of Wight, UK.

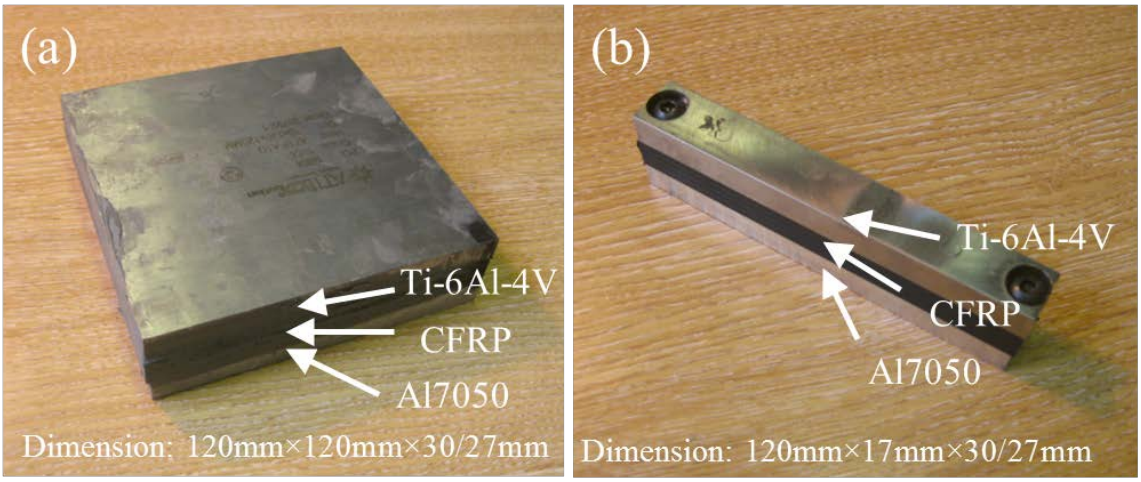


Figure 3.1 (a) Plate and (b) strip stack workpiece material

3.1.1 Titanium –Ti-6Al-4V alloy

The titanium alloy (Ti-6Al-4V) used in the present work was heat treated according to the procedure detailed in MIL-T-9046 (annealing temperature of 700-785°C, and holding time 5-15min) [197]. The resulting properties of the annealed Ti-6Al-4V are listed in Table 3.1 [4].

Physical property	**Metric unit**
Density	4.43g/cm^3
Mechanical Properties	**Metric unit**
Hardness, Knoop	363HK
Hardness, Vickers	349HV
Tensile strength, Ultimate	950MPa
Tensile strength, Yield	880MPa
Elongation at break	14%
Creep strength (400˚C, time≥540000s)	500MPa
Modulus of elasticity	113.8GPa
Fracture toughness	74.6MPa·m$^{1/2}$
Shear modulus	44GPa
Shear strength	550MPa
Thermal properties	**Metric unit**
Specific heat capacity	0.52J/g·°C
Thermal conductivity	6.7W/m·°C

Table 3.1 Properties of annealed Ti-6Al-4V alloy [4]

3.1.2 CFRP composite laminates

Unidirectional CFRP laminates employed in the stack materials consisted of 36 plies, and laid up in a sequence of $[45°/0°/135°/90°/45°/0°]_{3s}$ with each ply having a thickness of 0.25mm or 0.18mm, giving a total thickness of 10mm (used in Phase 1A/1B tests) and 7mm (used in Phase 1C/1D/2A/2B/3) respectively. The prepregs manufactured by the Advanced Composite Group (ACG) were cured with a step dwell of 80°C for 30 minutes followed by heating up to 135°C at a ramp rate of 1°C/min and subsequently held for 4 hours under a vacuum pressure of 0.9 bar. The specifications of the reinforcement and the matrix phase used in the prepregs and the associated mechanical/physical properties are detailed in Table 3.2, while Figure 3.2 shows a sample micrograph [198] of the laminate section.

Phase 1A/1B	
Prepreg specification	Description
Reinforcement	Toho Tenax HTS (High Tensile Strength) 12k, 268g, ply thickness =0.25mm, UD, 1.76g/cm^3 (ρ)
Matrix	ACG MTM44-1, 1.18 g/cm^3(ρ)
Fibre/resin code	ACG MTM44-1/HTS-268-12K (Vf=56.5%)
Fibre weave type	Unidirectional (UD) prepregs
Fibre orientation (laid-up)	$[45°/0°/135°/90°/45°/0°]_{3s}$
Phase 1C/1D/2A/2B/3	
Reinforcement	Toho Tenax HTS (High Tensile Strength) 12k, 268g, ply thickness=0.17mm, UD, 1.76g/cm^3 (ρ)
Matrix, fibre/resin code, fibre weave type, fibre orientation (laid-up)	As above
Physical property	Metric unit
Density	1.6g/cm^3
Mechanical properties	Metric unit
Hardness	60-65 Barcol (~35 Brinell hardness)
Tensile strength, ultimate	2000MPa
Shear strength (interlaminate)	14MPa
Modulus of elasticity	150GPa
Thermal properties	Metric unit
CTE	10µm/mK ⊥ and -0.6µm/mK // to fibre direction
Thermal conductivity	3W/mK ⊥and 70W/mK // to fibre direction

Table 3.2 Specification and properties of CFRP laminate after curing [198]

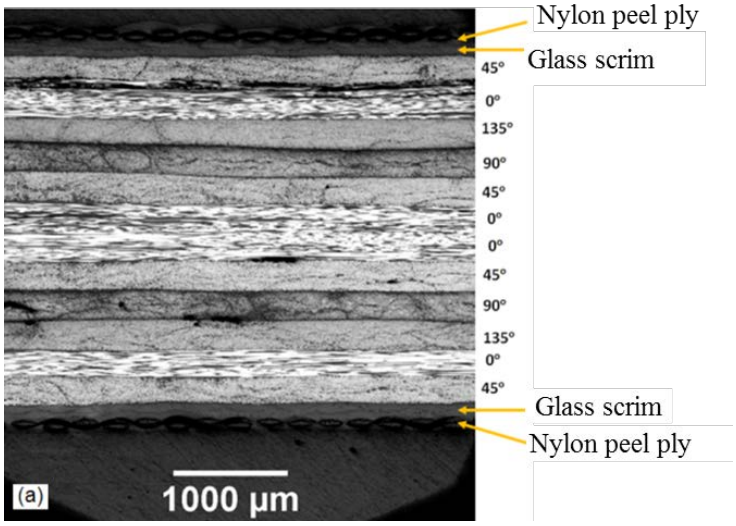


Figure 3.2 Micrograph of CFRP laminate sections [198]

3.1.3 Aluminium –A7050 alloy

The A7050-T7651 is a high strength aluminium alloy, containing 6% zinc and heat-treated via duplex aging, followed with stabilising treatments and stretching for stress relief. It is characterised by good fatigue crack resistance and higher fracture toughness, making it suitable for applications on wing panels, fuselage main frames and wing spars. Table 3.3 lists the properties of the A7050-T7651 alloy employed.

Physical properties	**Metric unit**
Density	2.83g/cm^3
Mechanical properties	**Metric unit**
Hardness, Knoop	187HK
Hardness, Vickers	171HV
Tensile strength, Ultimate	552MPa
Tensile strength, Yield	490MPa
Elongation at break	11%
Modulus of elasticity	71.7GPa
Fracture toughness (average, transverse-longitudinal direction)	30.8MPa·m$^{1/2}$
Shear modulus	26.9GPa
Shear strength	324MPa
Thermal property	**Metric unit**
Thermal conductivity	154W/mK
CTE	~25µm/mK

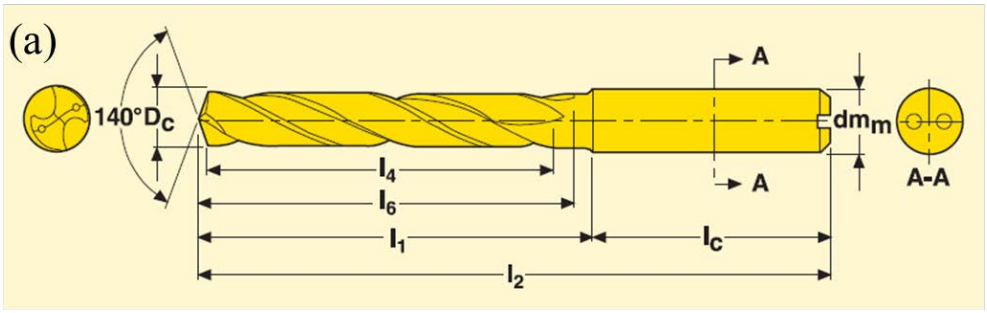
Table 3.3 Properties of Al7050-T7651 alloy [20]

3.2 Tool materials, geometries and coatings

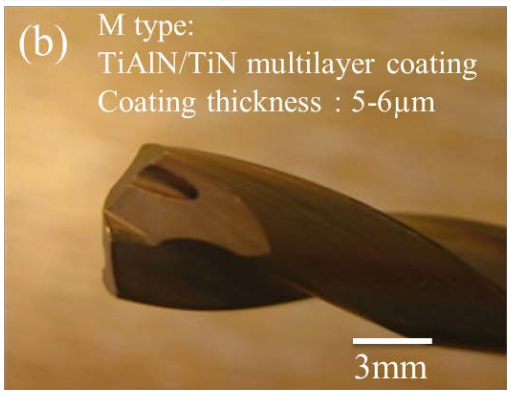
Various tungsten carbide based drills having different coatings (hard metal TiAlN, DLC, and CVD diamond) and geometry (margins, point angle/design, helix angle and web thickness) were utilised in Phase 1 experiments. Novel domed PCD drills were then evaluated in Phase 2 while coated WC drills implanted with thermocouples for temperature measurement were employed in Phase 3 experiments. All of the drills were fabricated and supplied by Seco Tools. Further details of the tool are outlined in the following sections.

3.2.1 Titanium-based coated carbide drills for Phase 1A

In Phase 1A, trials utilised 6.35mm diameter solid tungsten carbide twist drills having relief, helix and point angles of 14˚, 30˚ and 140˚ respectively; see Figure 3.3(a) showing a schematic and corresponding dimensions. The carbide material had a submicron grained (0.6µm) microstructure with 10% cobalt binder (K30-K40) providing a hardness and traverse rupture strength of 1610 HV_{30} and 3600N/m^2 respectively. Two different configurations were evaluated involving a multilayer coated (TiAlN+TiN) M type and uncoated T type drills, see Figure 3.3(b) and 3.3(c). All drills incorporated through tool coolant holes.



Drill Dia. Dc(mm)	Drill Geometry	Max drilling depth l4 (mm)	Part No. **	Dimensions in mm				
				l2	l1	lc	l6	dm_mh6
6.35	M	35	SD205AA-x.xx-35-8R1-M	91	55	36	53	8
6.35	T	35	SD205AA-02500-138-0315R1-T	91	55	36	53	8



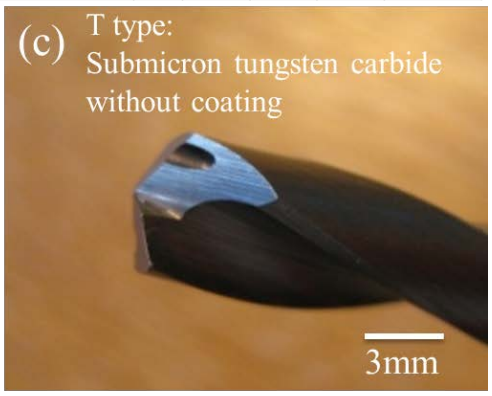
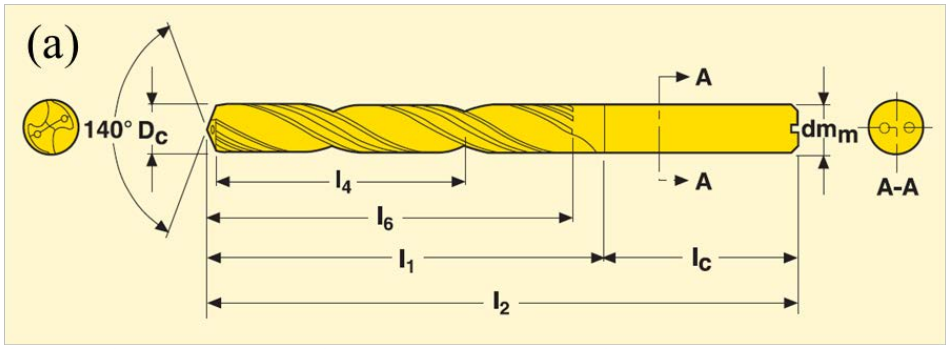


Figure 3.3 (a) Specification [199], and coating configuration of (b) M type and (c) T type drills

3.2.2 Multiple margin coated drills for Phase 1B

In Phase 1B, the performance of triple margin K30-K40 carbide drills having a TiAlN/TiN multilayer coating were investigated. Drills with higher/larger margins generally provide

greater stability during operation. Figure 3.4 details the specification and dimensions of the triple margin drill with point geometry equivalent to the tool used in Phase 1A.



Drill Dia. Dc(mm)	Drill Geometry	Max drilling depth l4 (mm)	Part No. **	Dimensions in mm				
				l2	l1	lc	l6	dm_mh6
6.35	6 Land margins	35	SD265A-02497-138-0315R1	91	55	36	53	8

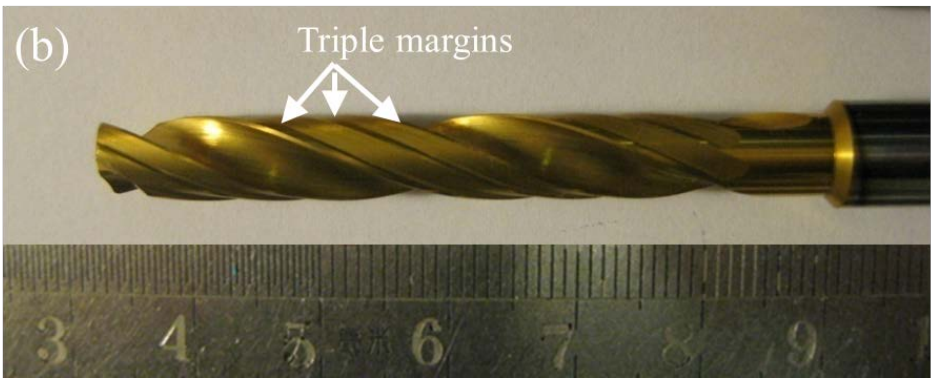
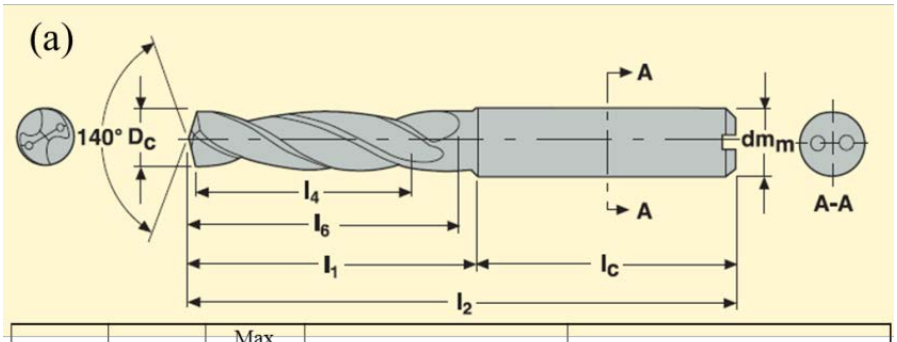


Figure 3.4 (a) Specification [199] and (b) image of the triple margin drill

3.2.3 Diamond/diamond-coated drills in Phase 1C/Phase 2A

Advanced diamond based coatings involving diamond like carbon (DLC) and chemical vapour deposition (CVD) diamond were assessed in Phase 1C. The former was applied on WC drills (point and helix angles of 140° and 30° respectively) via an unbalanced magnetron PVD sputtering process under a relatively low temperature (100-500°C) and high vacuum environment (10^{-4} mbar). The high ion bombardment produced a metastable sp^3 and sp^2 matrix structure giving a hardness of 4000-6000HV. The thickness of the DLC coating was 0.5µm coupled with a low friction coefficient of ~0.1 and maximum operating temperature of ~350°C. Figure 3.5 details the specification and dimensions of the DLC coated drill together with an image of the tool supplied.

(a)



Drill Dia. Dc(mm)	Drill Geometry	Max drilling depth l4 (mm)	Part No. **	Dimensions in mm				
				l2	l1	lc	l6	$dm_m h6$
6.35	2 Land margins	35	SD205AA-02500-091-0315R1-N	91	55	36	53	8

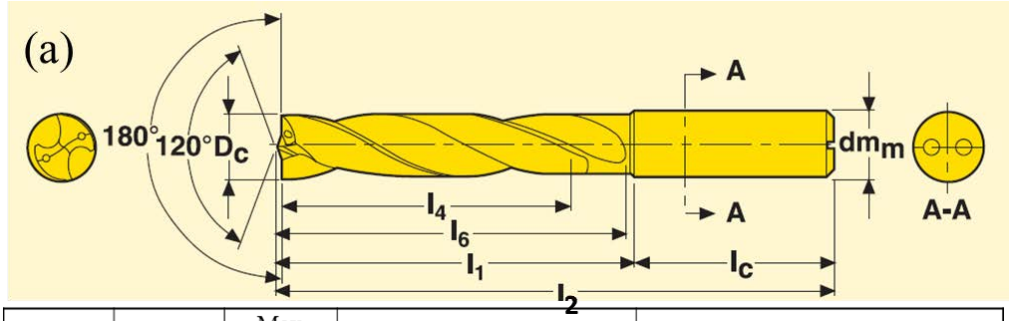
Triple margins

(b)



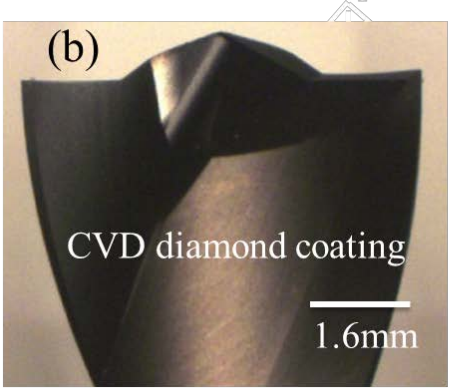
Figure 3.5 (a) Specification [199] and (b) image of DLC coated drill

In contrast, the CVD diamond coating operation was carried out under relatively high temperatures of 700-1000°C in a hot filament reactor at a low vacuum surrounding (1 bar). The coating thickness was ~ 5 to 6µm with a hardness of 8000-10000HV and operating temperature limit of 650°C, although the coefficient of friction was considerably higher at 0.4-0.6. The drill carbide substrate however was sintered with a lower (6%) cobalt content in order to reduce the extraction of carbon atoms from the WC matrix during the coating process and to improve layer adhesion. Figure 3.6(a) details the specification and dimensions of the CVD diamond coated drills, which incorporates a dual-stage point angle of 120°×180° as shown in Figure 3.6(b). Novel domed PCD drills employed in Phase 2A were manufactured with the same geometry as the CVD diamond coated drill. The PCD blanks fabricated by Element Six, comprises a multimodal grain size distribution (2-30µm), which were sintered under high temperature (1500°C) and high pressure (6GPa) and subsequently attached to a tungsten carbide shank by means of copper-brazing. The formulated PCD (CTM302) has a hardness of 50GPa, traverse rupture strength of 1437MPa, thermal conductivity of 560W/mK with a distribution of 91.7% diamond grains in the matrix leading to a high density of 3.99g/cm^3. Figure 3.6(c) shows a micrograph of the domed PCD drill used in the trials.



Drill Dia. Dc(mm)	Drill Geometry	Max drilling depth l4 (mm)	Part No. **	Dimensions in mm				
				l2	l1	lc	l6	$dm_m h6$
6.38	2 Land margins	35	SD205A-6.38-35-8R1-C2	91	55	36	53	8

Triple margins



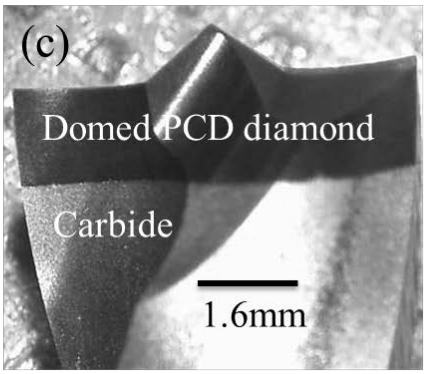


Figure 3.6 (a) Specification [199] and micrographs of the (b) CVD diamond coated and (c) domed PCD drills

3.2.4 Bespoke geometry drills for Phase 1D/2B

Several bespoke drills with variations in point angle, helix angle and web thickness were developed and tested in Phase 1D, to identify preferred point design for single-shot drilling of the 3 layer stacks. Figure 3.7 depicts the schematic of the designed geometry. In Figure 3.8, the proposed web thinning geometry was aimed at reducing the length of the chisel edge and minimising the obliquity of the cutting lips. This was expected to maximise the normal rake angle as the velocity angle approached zero. Table 3.4 details the 9 combinations of the bespoke drill geometry, which were fabricated with uncoated K30-K40 submicron WC and shown in Figure 3.9. Following results from Phase 1D, drills with the preferred point geometry combination were manufactured for confirmation runs in Phase 2B and is shown in Figure 3.10.

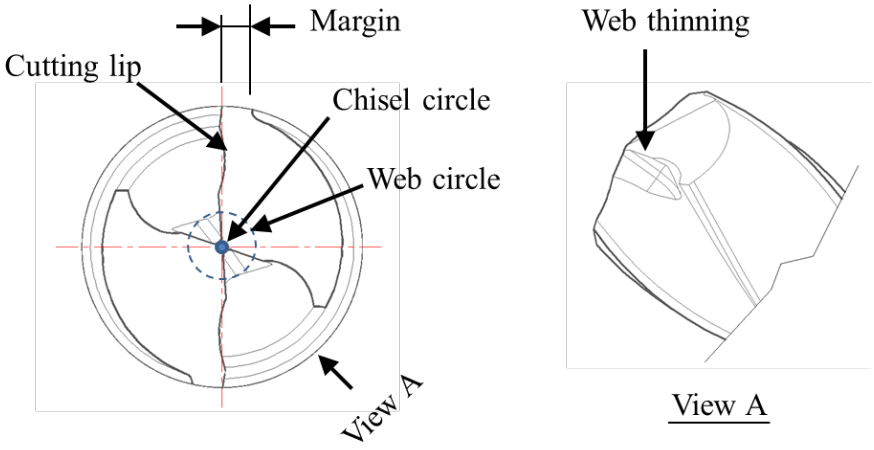


Figure 3.7 Schematic of web thinning and minimisation of obliquity

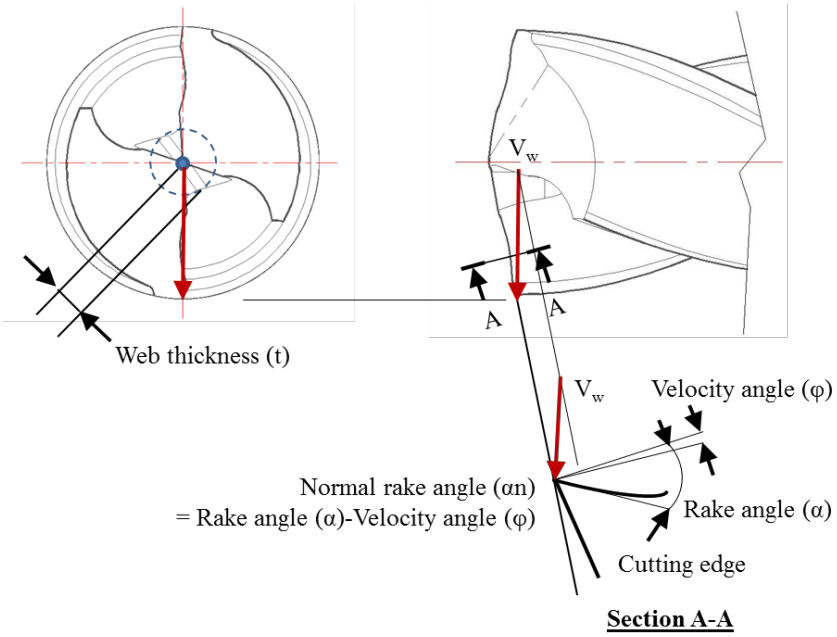


Figure 3.8 Schematic of normal rake angle

Tool No.	Chisel circle (mm)	Point angle (°)	Helix angle (°)
1	0.1	100	20
2	0.15	118	30
3	0.2	140	40
4	0.1	118	40
5	0.15	140	20
6	0.2	100	30
7	0.1	140	30
8	0.15	100	40
9	0.2	118	20

Table 3.4 Various point geometry combinations of the bespoke drill



Figure 3.9 Bespoke drills used in Phase 1D

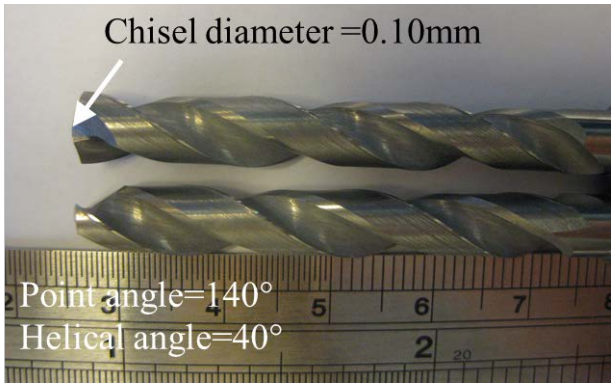


Figure 3.10 Drills with preferred combination of point geometry used in Phase 2B

3.2.5 Drills implanted with thermocouples for Phase 3

Several TiAlN/TiN coated carbide drills (M type) similar to those used in Phase 1A were implanted with K-type thermocouples via the through coolant holes at approximately 1.5mm from the cutting edge and margin for temperature measurement trials in Phase 3 experiments, see Figure 3.11. The implantaion procedure involved inserting the thermocouple having a sheath diameter of 0.65mm into the through coolant hole, followed by the use of thermal glue (silver/copper-based epoxy paste) to fill the gaps between the sheath and coolant hole prior to curing. The implantation and testing of thermocouples was carried out by Actarus SAS in France. Subsequent calibration of the thermocouples was undertaken at the University of Birmingham using a temperature bath prior to commencement of the experiments.

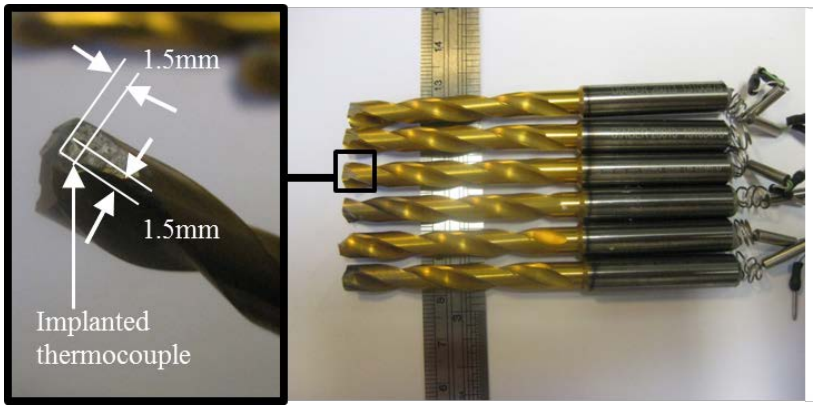


Figure 3.11 TiAlN/TiN coated drills with implanted thermocouples

3.3 Equipment

3.3.1 Machine tool, cutting environment and fixturing

3.3.1.1 Matsuura FX-5 high speed machining centre

The experiments were conducted on a Matsuura FX5 CNC vertical machining centre as shown in Figure 3.12(a) with a high speed spindle having a maximum rotation speed of 20000rpm and power rating of 15kW. The positional accuracy of the X and Y axes was ± 0.0015mm. The machining centre was integrated with a Renishaw tool setter (TS27R) for tool length detection and compensation via a built-in program. A Dustomat 15 vacuum extraction system (supplied by Filtermist Ltd) was also installed for evacuating CFRP debris particles down to 0.3µm from the cutting zone at a removal rate of 720m^3/hr, see Figure 3.12(b).



Figure 3.12 (a) Matsuura FX5 machining centre and (b) Dustomat 15 extraction system

3.3.1.2 Cutting fluid supply

All trials were performed wet (except for one trial in Phase 3), with the cutting fluid delivered either internally through the drill or externally via nozzles at various pressures and flow rates. A water based emulsion containing a 6-8% volume concentration of soluble mineral oil (Hocut 3380SE, produced by Houghton PLC) was used, which is generally recommended for the machining of aerospace materials (aluminium, titanium alloys, nickel based superalloys, etc.). In Phases 1A, 1B and 1C, the cutting fluid was applied via a retrofit through-tool coolant spindle adaptor system (6000 rpm maximum) incorporating a BT 40 tool holder capable of a maximum flow rate of 30l/min and corresponding pressure of 70 bar (7MPa). In Phases 1D, 2A, 2B and 3, cutting fluid was supplied through a pair of (1.5mm orifice diameters) at a pressure of up to 70 bar and flow rate of 58.8l/min. Figure 3.13 shows the setup of the through-tool-coolant spindle adaptor and external nozzles employed in the drilling trials.

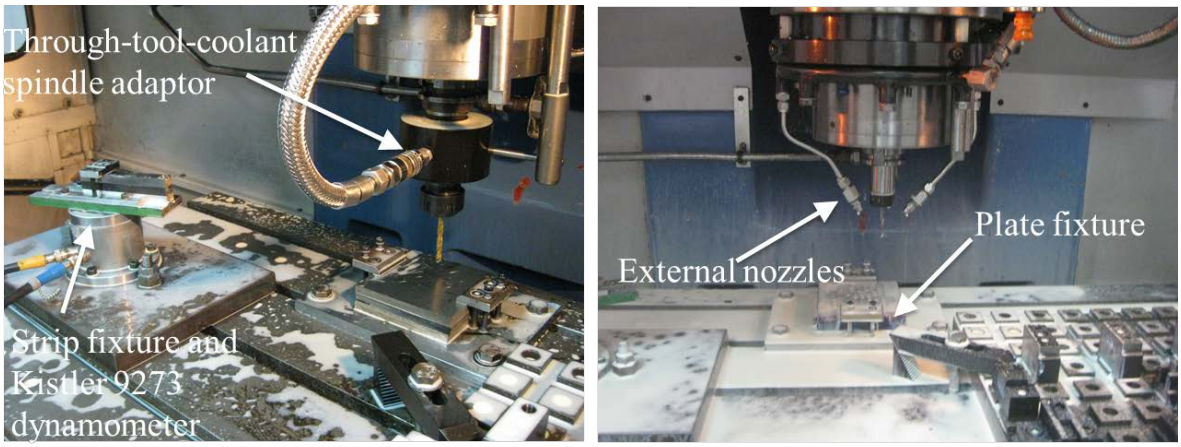


Figure 3.13 Set up of (a) through-tool-coolant adoptor, (b) external nozzles and machining fixtures for plate and strip

3.3.1.3 Fixturing of workpiece material

In all trials, strip specimens for surface integrity testing were held in a bespoke fixture, which was clamped onto a Kistler drilling dynamometer model 9273 (See Figure 3.13(a)). Similarly, plate workpiece stacks for tool life testing were clamped onto a base plate with an array of pre-drilled (9mm) holes to provide support and clearance during the exit of the drill from the material. The drilling sequence in the stack workpiece was set to enter from the titanium layer and exit from the aluminium layer.

3.3.2 Cutting force measurement

Drilling thrust force and torque was measured using a Kistler 9273 piezoelectric dynamometer connected to a series of 5011A charge amplifiers with Dynoware software employed for signal manipulation and analysis; see Figure 3.14. The measuring range of the unit for the Fx/Fy components was ±5kN with a sensitivity of -3.5pC/N for F_x/F_y, while for F_z, it was -5kN to 20kN with an associated sensitivity of approximately -1.9pC/N. In terms of moments (M_z), the measurement range was ±100Nm with a sensitivity of -1.5pC/N-cm. The natural frequency of the dynamometer was 1.5kHz for F_x, F_y and 3kHz for F_z.

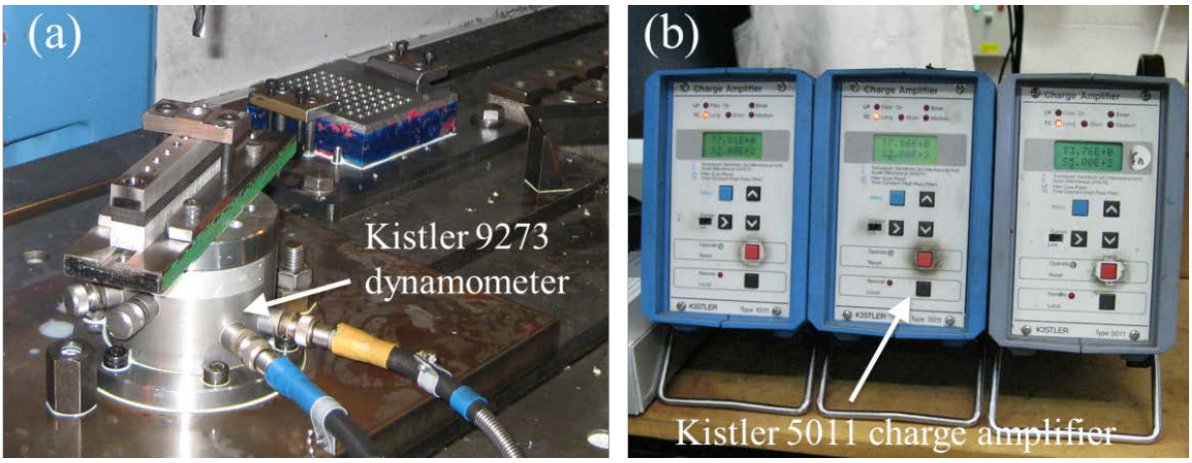


Figure 3.14 Setup of Kistler (a) 9273 drilling dynamometer and (b) 5011 charge amplifiers

3.3.3 Cutting temperature measurement

Temperature measurement was performed via the implanted thermocouples (K-type) in the WC drills, which were held in an Actarus rotary transmitter mounted on a BT40 tool holder as seen in Figure 3.15(a). The voltage signals were transferred to a Microtel K1 charge amplifier through an RF antenna and subsequently analysed using Dynoware software, see Figure 3.15(b). The system has a maximum operating rotational speed of 10000rpm, while the accuracy of temperature measurement was 1°C based on an acquisition frequency of 100Hz and a data capture time delay/response of 150µs. Calibration was carried out using a temperature bath ranging from 22°C to 80°C.

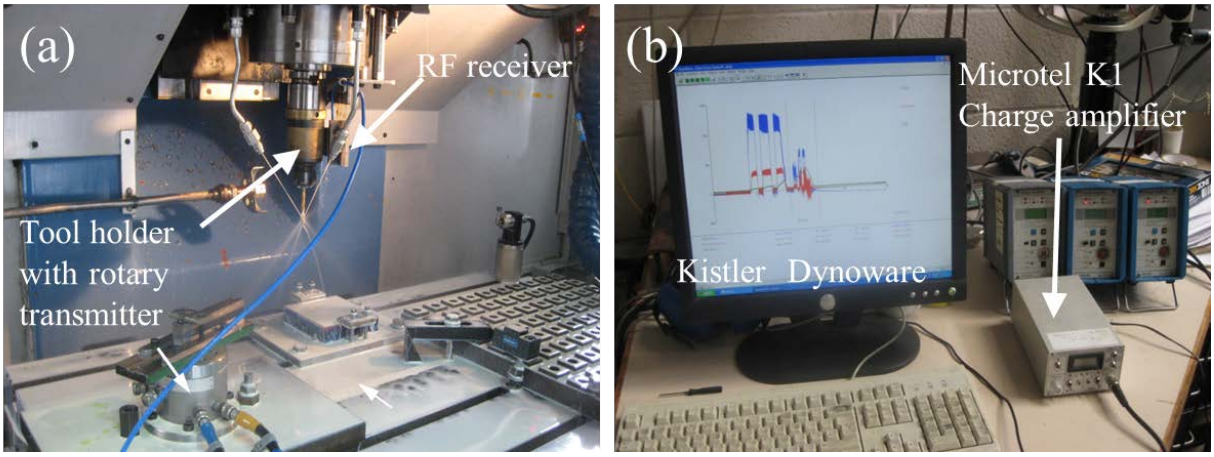


Figure 3.15 Setup of (a) rotary transmitter and (b) charge amplifier for temperature measurement

3.3.4 Tool wear measurement and microstructure analysis

Tool flank wear (VB), chipping and fracture of cutting lips were measured using a WILD M3Z toolmaker's microscope, which was equipped with a X-Y platform driven by digital micrometres having a resolution of 1µm. A 10 mega pixel digital camera (Canon EOS 400D) was installed on a special adaptor to capture micrographs of the drills, which were held in a modified rotary tilting table (0-45° angle) mounted on the measuring stage, see Figure 3.16. The maximum flank wear on each of the drill cutting lips were measured and analysed.



Figure 3.16 WILD M3Z toolmaker's microscope

3.3.5 Hole diameter, out of roundness and cylindricity measurement

Hole quality in terms diameter, out of roundness and cylindricity were assessed using a Taylor Hobson Talyrond 300 system, see in Figure 3.17(a). The measurement resolution for hole diameter is 1µm while for out of roundness and cylindricity parameters, the smaller division was 0.01µm. Diameter measurement was undertaken at 9 axial positions (3 in each material section) over the stack height as shown in Figure 3.17(b). Three hundred points around the hole circumference were probed of each height location with the diameter of each material layer calculated and a Gaussian filter applied for smoothing of the scanned profile. The out of roundness was determined by measuring the offset distance between the centres of the drilled holes and calibration ring gauge. In contrast, the evaluation of overall hole cylindricity involved a least square regression analysis of the data from the 9 measured axial positions. All measurements were replicated twice and the results averaged.

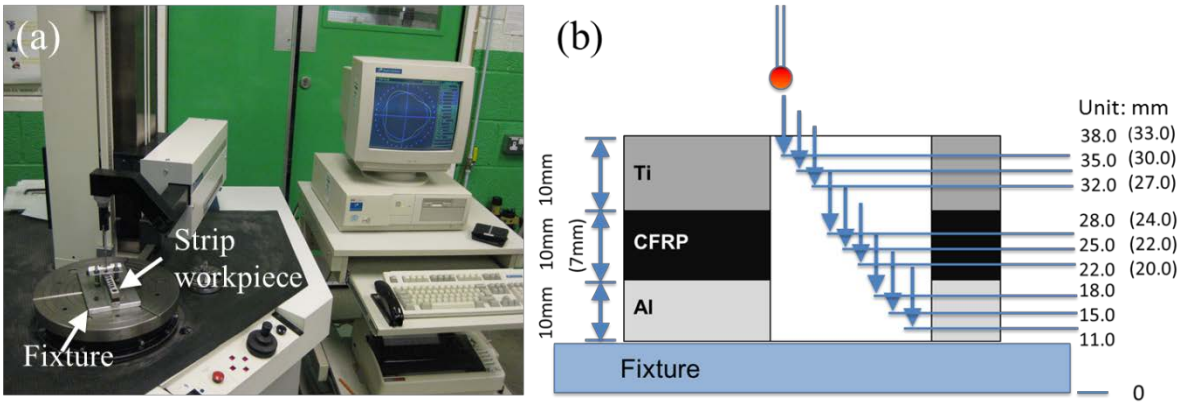


Figure 3.17(a) Setup of Taylor Hobson Talyrond 300 and (b) schematic of measurement procedure for hole diameter

3.3.6 Burr height measurement

Burr height assessment was conducted using a conventional height gauge, which was equipped with a level type dial gauge having a precision of 0.01mm. The mean of four quadrant points around the hole at the entrance and exit in each material layer were recorded with the measurements repeated twice and an average calculated.

3.3.7 Surface roughness and three-dimensional topography

In Phase 1 and 2, the evaluation of hole surface roughness in the Ti/CFRP/Al stacks was carried out utilising a Taylor Hobson Talysurf 120L, which was equipped with a laser interferometer for height measurement and an X-Y table driven by a servo motor for both 2D and 3D surface topography assessment, see Figure 3.18(a). For 2D line roughness measurement (Ra, Rt) a diamond tipped stylus (2µm radius) was drawn over 5 sampling cut-off length of 0.8mm giving a total evaluation length of 4mm, while for 3D parameters (Sa) an area of 2.7mm × 0.75mm was scanned. In Phase 3, 2D hole surface roughness was measured with a Mitutoyo Surftest 201/301, see Figure 3.18(b), over the same cut-off and evaluation distance. Limited surface roughness and edge geometry evaluation of selected drills were performed using an Alicona Infinite focus optical measurement system (Model No: IFMG4g), as shown in Figure 3.19. The scanning source was a white light interferometer which progressively adjusted the scanning depth to produce a three dimensional image of the measured surface or form, with the associated analysis software calculating roughness or dimensional parameters respectively.

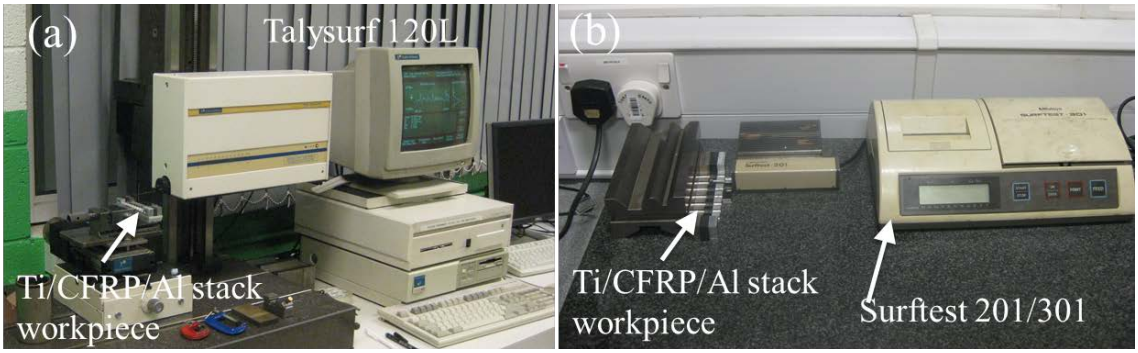


Figure 3.18 Surface roughness measurement using (a) Talysurf 120L, and (b) Surftest

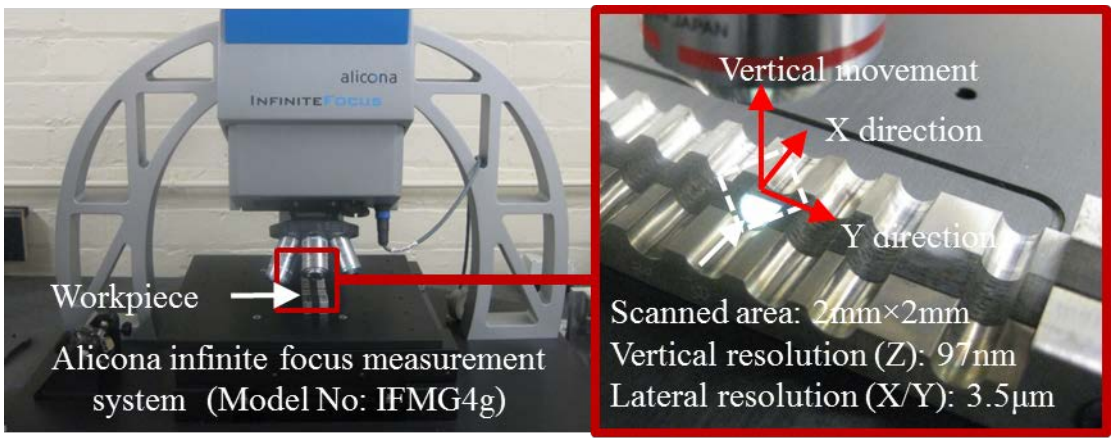


Figure 3.19 Surface roughness and profile scanning using Alicona measurement system

3.3.8 Subsurface alteration analysis

3.3.8.1 Sample preparation

Holes for microstructure and microhardness evaluation were sectioned using an Agie-Charmiles ROBOFIL FI 240ccs 5 axis wire electrical discharge machine (WEDM) and subsequently hot mounted in Bakelite via a mounting press under a curing condition of 150°C and 29MPa for 15 minutes, as shown in Figure 3.20(a). The mounted samples were then ground and polished by employing a Buehler Alpha 2 grinder-polisher, see Figure 3.20(b). The grinding procedure commenced with rough 400 mesh SiC abrasive papers to remove any heat affected zone (~300µm), followed by successive fine grinding using 600 mesh, 800 and 1000 mesh abrasive papers with dispensing water. The samples were then polished with 9, 6, and 3µm diamond grits suspensions on UltraPol cloths and finish lapped with colloidal silica on the micro cloth. Table 3.5 details the procedure and polishing parameters.

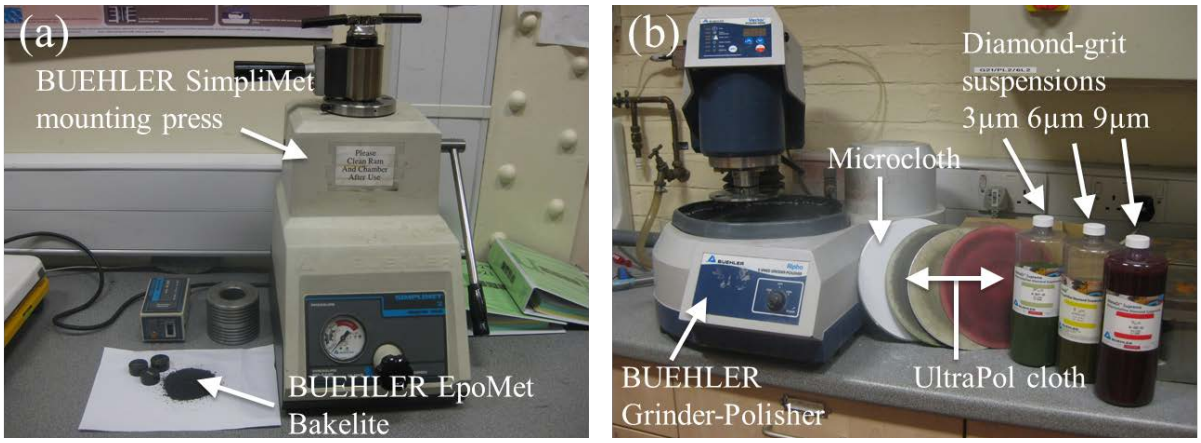


Figure 3.20 (a) Mounting press and (b) grinding/polishing equipment

Step	Abrasives	Rotational speed (RPM)		Rotational direction		Load (N)	Duration (min)	
		Ti	Al	Ti	Al		Ti	Al
1	#400 SiC paper	300	300	Comp.	Comp.	27	2	1
2	#600 SiC paper							2
3	#800 SiC paper							
4	#1000 SiC paper							
5	9µm diamond grit	150	150	Contra.			4	3
6	6µm diamond grit							
7	3µm diamond grit							
8	0.5µm colloidal silica				Contra.		3	
Comp.: Complementary (platen and specimen holder both rotate into same direction. Contra.: Platen and specimen holder rotate in opposite direction.								

Table 3.5 Grinding/polishing procedure and parameters for Ti and Al specimens

3.3.8.2 Microhardness measurement

Microhardness depth profile measurements of cross-sectioned hole surfaces from the aluminium and titanium layers were carried out using a Mitutoyo MVK-G3, with a Knoop indenter at a load of 25g over a 15s period, see Figure 3.21. Measurements were taken at various depth intervals (15 - 100µm) up to 815µm beneath the hole surface. Each reading was repeated twice and an average calculated.

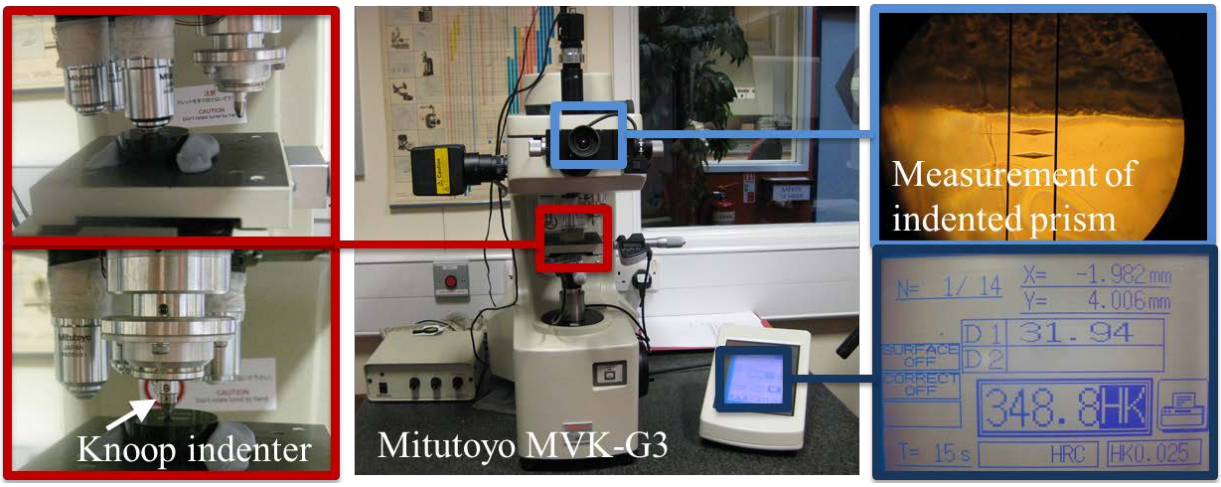


Figure 3.21 Mitutoyo MVK-G3 micro hardness testing

3.3.8.3 Etching

The aluminium samples were etched using Keller's reagent comprising 2ml hydrofluoric acid (HF), 3ml hydrochloric acid (HCL), and 5ml nitric acid in 190ml of water. The specimens were soaked in etchant for ~45s. Similarly, the titanium samples were etched in a volume solution of 2% HF (40% vol. concentration), 10% HNO_3 (70% vol. concentration) and 88% water for a duration of ~50s.

3.3.8.4 Microstructure

Cross-sectional hole microstructure and burr form analysis were carried out on a Leica DMLM optical microscope equipped with a digital camera and having a maximum magnification of 500X. Associated image processing software (Omnimet 8.7) was utilised for linear and angular dimensional evaluation of features on the micrographs, as detailed in Figure 3.22.

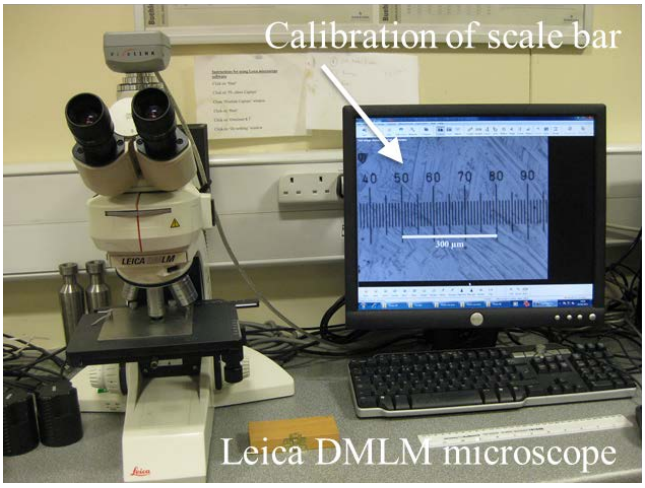


Figure 3.22 Leica DMLM microscope

3.3.8.5 SEM and EDX microscopy

A vacuum sputter coater was utilised for applying a thin gold coating of a few nanometre thickness on the mounted samples increase the electrical conductivity of the CFRP workpiece surfaces, see Figure 3.23(a). High resolution analysis of the cross-sectional subsurface microstructure in the aluminium, titanium and CFRP layers as well as tool substrate/coatings were carried out via a JEOL 6060 scanning electron microscope (SEM), see Figure 3.23(b), with magnification of up to 10,000X. Elemental analysis of the workpiece and cutting tool materials was conducted via an Inca energy-dispersive X-ray spectroscopy (EDX) unit.

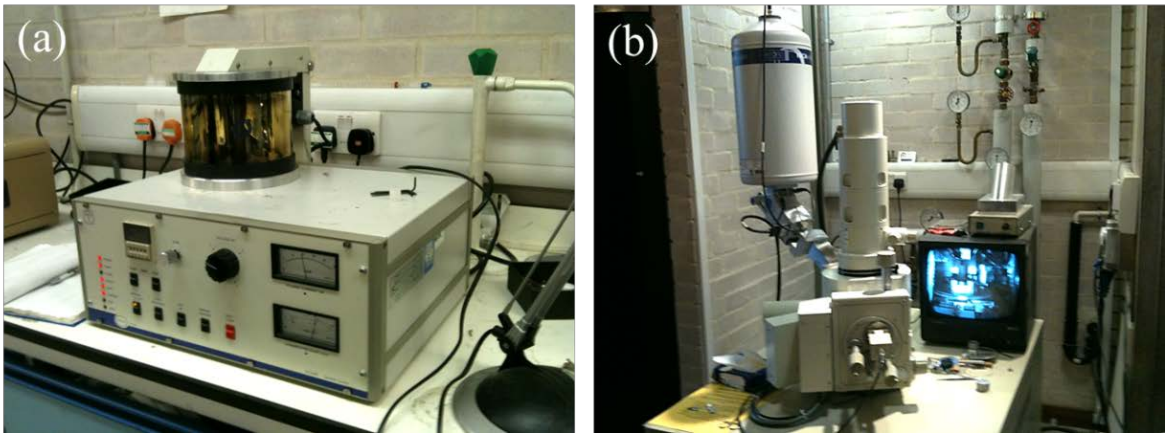


Figure 3.23 (a) Emscope sputter coater and (b) JOEL 6060 SEM equipped with Inca EDX

3.4 Experimental design, procedures and test arrays

In all trials, the drilling sequence in the stack workpiece was set to enter into the titanium layer and exit from the aluminium section. Figure 3.24 presents the layout of the machined workpieces (plate and strip), which was carried out according to the CNC program detailed in Appendix 2. Due to the limited availability of workpiece material, the end of test criteria was 180 holes for Phase 1A/B/D and 90 holes for Phase 1C/2B, or when any of the following criteria recommended by ISO3685:1993 [115] was met:

- Average non-uniform flank wear ≥ 0.3mm, or
- Maximum flank wear (VBmax) =0.6mm, or
- Fracture or catastrophic failure

The only exception was in Phase 2A experiments where drills were tested to failure (or a wear area of 1500μm×1500μm) in order to evaluate the progression of PCD and diamond coated tool wear modes/patterns. Response measures in terms cutting force, tool wear, burr formation, hole diameter, out of roundness, hole cylindricity and hole surface roughness were evaluated after Hole 1, 10, 20, and 30 followed by intervals of 20 holes thereafter. Analysis of microhardness and microstructure were undertaken at the last hole drilled.

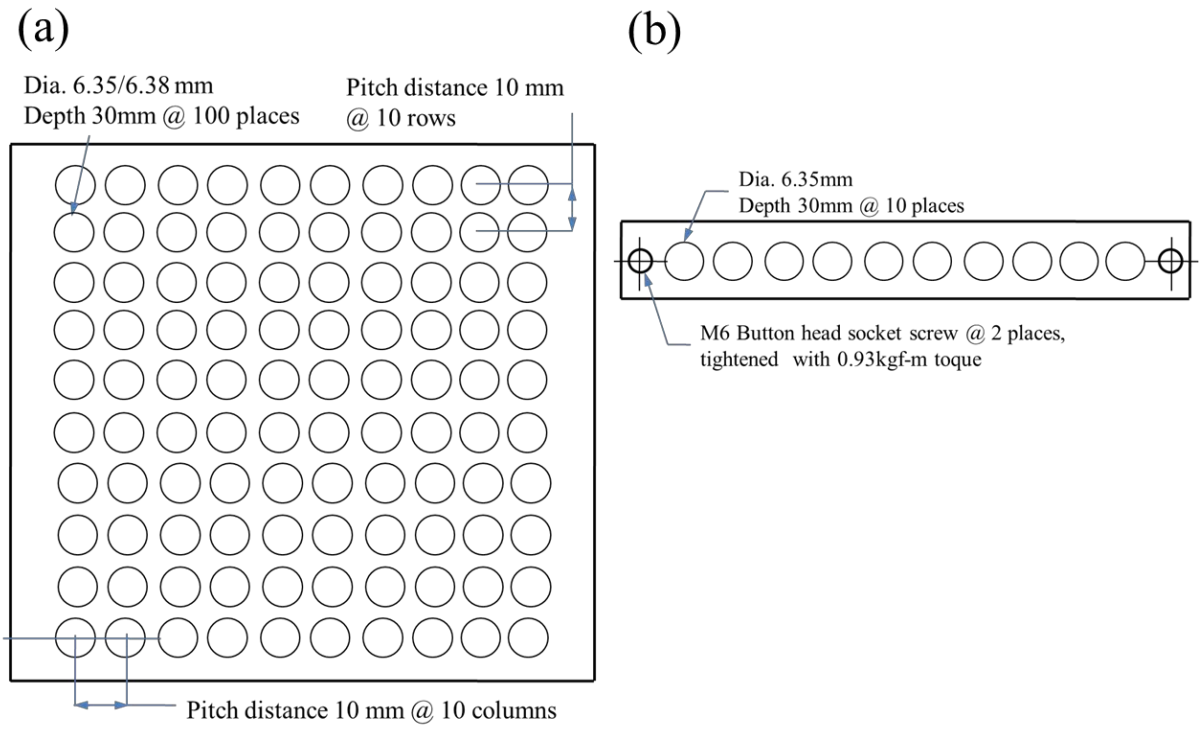


Figure 3.24 Layout of the (a) plate and (b) strip machined workpieces

3.4.1 Phase 1A: Effect of tool material, feed rate and drilling strategy

A full factorial experiment was performed to investigate the effect of drill coating, feed rate and drilling strategy (each at 2 levels) when single-shot drilling Ti/CFRP/Al stacks. A dual level cutting speed was utilised, which was fixed at 30/120/120m/min for the Ti/CFRP/Al layers respectively. Uncoated (T type) and TiAlN/TiN (M type) coated WC drills were used while feed rate was varied between 0.05 and 0.08mm/rev, with trials carried out with or without a peck cycle (involving a 2mm retraction of the tool at material boundary of the stack). Performance measures included cutting forces, tool life/wear, burr formation, chip morphology, hole quality and surface integrity, with main effect plots produced and ANOVA undertaken using Minitab software to identify significant factors. Table 3.6 details the fixed and variable factors together with their corresponding levels while the full test array is shown in Table 3.7.

<table>
<tr><th>Fixed factors</th><th>Description</th><th>Variable factors</th><th>Level 1</th><th>Level 2</th></tr>
<tr><td>Workpiece material</td><td>Ti-6Al-4V/ CFRP/A7050, t=30mm</td><td>Tool coating</td><td>Uncoated WC (T type)</td><td>TiAlN/TiN coated WC (T type)</td></tr>
<tr><td>Drill diameter</td><td>6.35mm</td><td>Feed rate</td><td>0.05mm/rev</td><td>0.08mm/rev</td></tr>
<tr><td>Cutting speed (Ti/CFRP/Al)</td><td>30/120/120m/min</td><td rowspan="2">Cutting strategy</td><td rowspan="2">No pecking</td><td rowspan="2">Pecking with 2mm retraction at material layer interface</td></tr>
<tr><td>Cutting environment</td><td>Internal through coolant, 70 bar cutting fluid pressure and 30l/min flow rate</td></tr>
</table>

Table 3.6 Factors and their corresponding levels in Phase 1A

Test No.	Tool coating	Feed (mm/rev)	Cutting strategy
1	Uncoated WC	0.05	No pecking
2	TiAlN/TiN coated WC	0.05	No pecking
3	Uncoated WC	0.08	No pecking
4	TiAlN/TiN coated WC	0.08	No pecking
5	Uncoated WC	0.05	Pecking
6	TiAlN/TiN coated WC	0.05	Pecking
7	Uncoated WC	0.08	Pecking
8	TiAlN/TiN coated WC	0.08	Pecking

Table 3.7 Full factorial (2^3) test array in Phase 1A

3.4.2 Phase 1B: Influence of margin design, feed rate and drilling strategy

Based on results from Phase 1A, the influence of TiAlN/TiN coated drills having a multiple-margin design, together with variations in feed rate and cutting strategy on cutting force, hole quality and surface integrity were evaluated when single-shot drilling of Ti/CFRP/Al in Phase 1B. This involved a full factorial experiment with the associated process factors and operating levels detailed in Table 3.8. Table 3.9 shows the test array with statistical analysis employed to identify main effects and interactions between factors.

<table>
<tr><th>Fixed factors</th><th>Description</th><th>Variable factors</th><th>Level 1</th><th>Level 2</th></tr>
<tr><td>Workpiece material</td><td>Ti-6Al-4V/ CFRP/A7050, t=30mm</td><td>Margin design</td><td>Single margin</td><td>Triple margin</td></tr>
<tr><td>Tool material</td><td>TiAlN/TiN coated WC</td><td>Feed rate</td><td>0.05mm/rev</td><td>0.08mm/rev</td></tr>
<tr><td>Drill diameter</td><td>6.35mm</td><td rowspan="3">Cutting strategy</td><td rowspan="3">No pecking</td><td rowspan="3">Pecking with 2mm retraction at material layer interface</td></tr>
<tr><td>Cutting speed, Ti/CFRP/Al</td><td>30/120/120m/min</td></tr>
<tr><td>Cutting environment</td><td>Internal through coolant, 70 bar cutting fluid pressure and 30l/min flow rate</td></tr>
</table>

Table 3.8 Factors and their corresponding levels in Phase 1B

Test No.	Tool material	Feed (mm/rev)	Cutting strategy
1	Triple margin	0.05	No pecking
2	Single margin	0.05	No pecking
3	Triple margin	0.08	No pecking
4	Single margin	0.08	No pecking
5	Triple margin	0.05	Pecking
6	Single margin	0.05	Pecking
7	Triple margin	0.08	Pecking
8	Single margin	0.08	Pecking

Table 3.9 Full factorial (2^3) test array in Phase 1B

3.4.3 Phase 1C: Hole quality and failure modes of diamond coated tools

Phase 1C aimed to investigate the performance of ultrahard diamond based coatings (DLC and CVD diamond) and influence of feed rate variation (0.08 and 0.15mm/rev) when single shot drilling Ti/CFRP/Al stacks. Cutting speed was kept constant at 30/120/120m/min, with a peck cycle involving a 2mm drill retraction after machining 5mm employed in all tests, see Table 3.10. Details of both the DLC and CVD diamond coated drills were outlined previously in Section 3.2.3 while the full factorial test array is shown in Table 3.11. Cutting forces and wear/failure characteristics of the drills were evaluated together with subsequent effects on hole quality and surface integrity. Each of the drills were tested to fracture/catastrophic failure or a maximum of 90 holes.

Fixed Factors	Description	Variable Factors	Level 1	level 2
Workpiece material	Ti-6Al-4V/ CFRP/A7050, t=27mm	Tool material	DLC	CVD diamond
Drill diameter	6.35mm (DLC), 6.38mm (CVD diamond)	Feed rate	0.08mm/rev	0.15mm/rev
Cutting speed (Ti/CFRP/Al)	30/120/120m/min			
Cutting strategy	Pecking with 2mm tool retraction every 5mm drilling			
Cutting environment	External coolant, 70 bar cutting fluid pressure and 58.8l/min flow rate			

Table 3.10 Factors and their corresponding levels in Phase 1C

Test No.	Tool material	Feed rate (mm/rev)
1	DLC	0.08
2	CVD diamond	0.08
3	DLC	0.15
4	CVD diamond	0.15

Table 3.11 Full factorial (2×2) test array in Phase 1C

3.4.4 Phase 1D: Effect of drill point geometry

Following results from Phases 1A, 1B and 1C, the influence of drill point geometry was investigated in Phase 1D in order to improve tool performance and hole quality when single-

shot drilling Ti/CFRP/Al stacks. While use of drills with smaller point angles (< 118°) are generally recommended for CFRP composites and Al alloys to decrease thrust forces; the drilling of Ti based materials typically requires larger point angles to reduce cutting lip length and hence torque as well as to provide a stronger chisel point. Similarly, the drill point web thickness can divert any ploughing/impact extrusion into cutting at the chisel zone. Therefore, the variable factors considered were drill point web thickness/chisel diameter, point angle and helix angle, each at 3 levels as detailed in Table 3.12 together with the constant parameters. A fractional factorial L9 Taguchi experimental design was utilised with statistical analysis employed to identify significant factors as well as the preferred factor levels with respect to the different response measures, see Table 3.13.

Fixed factors	**Description**	**Variable factors**	**Level 1**	**Level 2**	**Level 3**
Workpiece material	Ti-6Al-4V/ CFRP/A7050, t=27mm	Point angle (°)	100	118	140
Tool material/ diameter	WC-10Co/ Ø=6.35mm	Helix angle (°)	20	30	40
Cutting speed, Ti/CFRP/Al	30/120/120m/min	Chisel diameter (mm)	0.10	0.15	0.2
Feed rate	0.08mm/rev				
Cutting strategy	Pecking with 2mm tool retraction every 5mm drilling				
Cutting environment	External coolant, 70 bar cutting fluid pressure and 58.8l/min flow rate				

Table 3.12 Phase 1D operating factors and their corresponding levels

Test No.	**Chisel diameter (mm)**	**Point angle (°)**	**Helix angle (°)**
1	0.1	100	20
2	0.15	118	30
3	0.2	140	40
4	0.1	118	40
5	0.15	140	20
6	0.2	100	30
7	0.1	140	30
8	0.15	100	40
9	0.2	118	20

Table 3.13 Taguchi (L9) test array in Phase 1D

3.4.5 Phase 2A: Evaluation of diamond coated/novel PCD drills and feed rate at elevated cutting speed

In Phase 2A, the CVD diamond coated WC tool utilised previously in Phase 1C was benchmarked against a recently developed domed PCD product at an elevated cutting speed of 36/144/144m/min (20% higher then used in Phase 1). The geometry for both drills were equivalent to a two-stage point angle of 120° × 180° (see Section 3.2.3) and diameter of 6.38mm. Feed rate was varied over 3 levels (0.05, 0.08, and 0.12mm/min) while cutting fluid was delivered via external coolant nozzles at a constant pressure and flow rate of 70 bar and 58.8l/min respectively. The fixed and variable factors are detailed in Table 3.14 with the corresponding full factorial test matrix shown in Table 3.15. In order to assess the tool failure modes, tests were performed to the point of drill failure, with cutting force and hole quality measures recorded at intervals of 10 holes.

Fixed factors	Description	Variable factors	Level 1	Level 2	Level 3
Workpiece material	Ti-6Al-4V/ CFRP/A7050, t=27mm	Tool material	Domed PCD	CVD diamond coated WC	-
Drill diameter	6.38mm	Feed rate, mm/rev	0.05	0.08	0.12
Cutting speed, Ti/CFRP/Al	36/144/144m/min				
Cutting strategy	Pecking with 2mm tool retraction every 5mm drilling				
Cutting environment	External coolant, 70 bar cutting fluid pressure and 58.8l/min flow rate				

Table 3.14 Phase 2A operating factors and their corresponding levels

Test No.	Tool material	Feed rate (mm/rev)
1	Domed PCD	0.05
2	Domed PCD	0.08
3	Domed PCD	0.12
4	CVD diamond coated WC	0.05
5	CVD diamond coated WC	0.08
6	CVD diamond coated WC	0.12

Table 3.15 Phase 2A test matrix

3.4.6 Phase 2B: Confirmation test and benchmarking of bespoke drill geometry

Following analysis of the results from Phase 1D, uncoated WC drills with the preferred point combination geometry were fabricated for the confirmation trial in Phase 2B. The test conditions were similar to those used in Phase 1D and is shown in Table 3 16 together with the bespoke drill geometry. Response measures evaluated included the predicted intervals of tool life, cutting forces, hole quality (diameter, out of roundness, cylindricity), burr height and hole surface roughness. Results from the confirmation test were also compared against the performance of the other tool configurations in phase 1A, 1B, 1C in order to validate the bespoke point drill for single shot drilling of Ti/CRP/Al stacks.

Fixed factors	**Description**	**Confirmation Run**	Point angle (°)	Helix angle (°)	Chisel diameter (mm)
Workpiece material	Ti-6Al-4V/ CFRP/A7050, t=27mm	1	140	40	0.1
Drill material/ diameter	WC-10Co/ Ø=6.35mm				
Cutting speed, Ti/CFRP/Al	30/120/120m/min				
Feed rate	0.08mm/rev				
Cutting strategy	Pecking with 2mm tool retraction every 5mm drilling				
Cutting environment	External coolant, 70 bar cutting fluid pressure and 58.8l/min flow rate				

Table 3.16 Phase 2B operating factors and preferred drill geometry

3.4.7 Phase 3: Effect of cutting environment and feed rate

The objective of Phase 3 experiments was to analyse the influence of cutting fluid pressure and feed rate on cutting temperature and thrust force/torque when drilling Ti/CFRP/Al stacks using 6.35mm diameter TiAlN/TiN coated WC drills implanted with K-type thermocouples (see Section 3.2.5 for details). Subsequent effects on tool wear, hole quality (diameter, out of roundness, and cylindricity) and surface integrity (hole surface roughness and subsurface

microhardness alteration) were also assessed. Cutting fluid was supplied externally via coolant nozzles at varying pressures of 10, 35, 70 bar with corresponding flow rates of 38, 52.3, 58.8l/min respectively. Two levels of feed rate was employed (0.08 and 0.12mm/rev) while a constant cutting speed of 30/120/120m/min was used in all trials, see Table 3.17. Five tests were performed at different combinations of fluid pressure and feed rate (full factorial not under taken due to limited in tooling), which were compared against a further trial undertaken dry at 0.08mm/rev feed rate, see Table 3.18.

Fixed factors	**Description**	**Variable factors**	**Level 1**	**Level 2**	**Level 3**
Workpiece material	Ti-6Al-4V/ CFRP/A7050, t=27mm	Feed rate (mm/rev)	0.08	0.12	-
Drill material/ diameter	TiAlN/TiN coated tungsten carbide, ∅=6.35mm	Cutting fluid pressure, flow rate (bar, l/min)	10, 38	35, 52.3	70, 58.8
Cutting strategy	Pecking of 2mm tool retraction after advancing 4mm in Ti layer and after 5mm in Al layer. No pecking in CFRP layer Note: Drill starting position was at a 2mm offset from the Ti surface				
Cutting speed, Ti/CFRP/Al	30/120/120m/min				

Table 3.17 Phase 3 operating factors and their corresponding levels

Test No.	**Feed rate (mm/rev)**	**Cutting fluid pressure (bar)**
1	0.08	10
2	0.08	35
3	0.08	70
4	0.12	70
5	0.12	10
6	0.08	Dry

Table 3.18 Phase 3 test array

4 RESULTS AND DISCUSSION

4.1 Phase 1A: Effect of tool material, feed rate and drilling strategy

4.1.1 Cutting force

Figures 4.1(a) and (b) show typical force signals when drilling Ti/CFRP/Al stacks under a single-shot operation using TiAlN/TiN coated WC drills under a feed rate of 0.05mm/rev, without and with a pecking strategy respectively. Where the former was employed, a steep decrease in the force and torque traces was observed as the drill exits from the Ti layer and enters into the CFRP section. This was due to a 'dwell period' (where the tool does not advance) to accommodate the change in spindle rotational speed (increased in cutting speed). When a pecking strategy was utilised, the force traces show a steep drop to approximately zero as the drill was retracted to facilitate the change in spindle rotational speed.

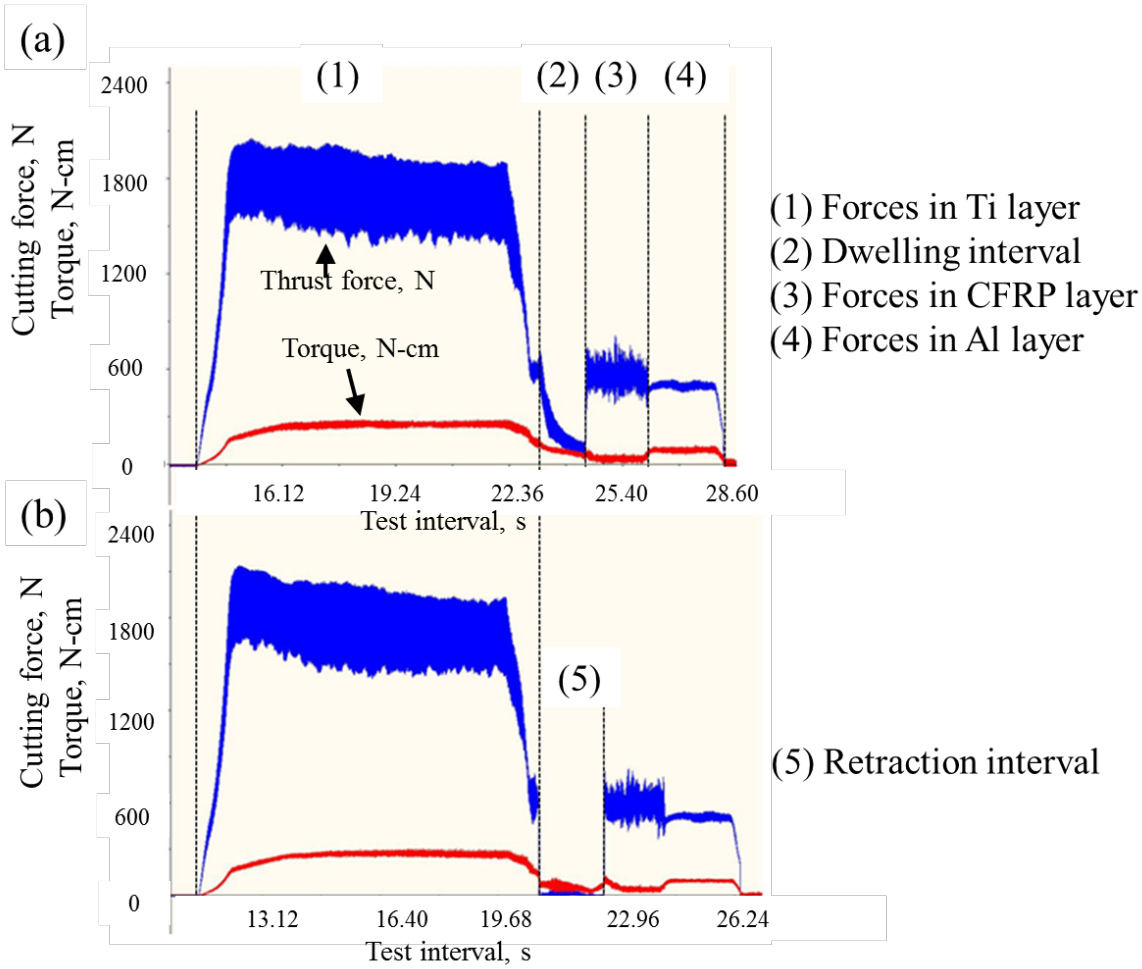


Figure 4.1 Cutting force plots at hole 90 using coated carbide tool at feed rate of 0.05mm/rev with (a) no pecking (Test 2) and (b) pecking (Test 6)

Figure 4.2 shows the thrust force and torque recorded in each layer of the stack after drilling 90 holes for all tests. Drilling with the higher feed rate of 0.08mm/rev generally resulted in an average reduction in thrust force of 12% when compared against trials at 0.05mm/rev. This was somewhat unusual, which could have been due to the increase in the effective rake angle (static rake angle and dynamic feed angle) [155]. In contrast, the use of coated drills led to ~12-18% higher thrust forces, which was most likely attributed to the increased radius of the cutting edge as a result of the coating layers (reduced sharpness). The coated drills however produced lower torque levels by up to ~10%, which was probably due to the improved wear resistance afforded by the coating layer at the peripheral corners.

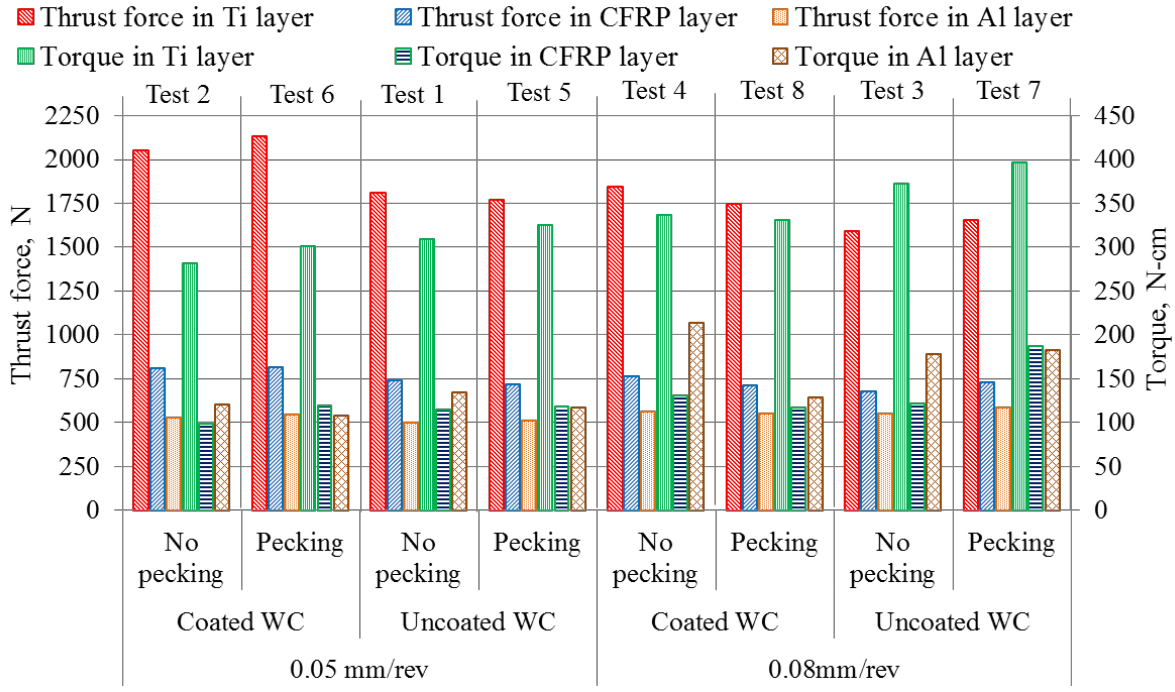


Figure 4.2 Cutting forces in drilling of Ti/CFRP/Al stacks at Hole 90

Application of the peck strategy did not appear to have any noticeable effect on thrust force or torque. This was corroborated by the ANOVA in Table 4.1, which indicated that tool coating and feed rate were significant factors affecting thrust force and torque in the Ti layer only, while feed rate also had a major influence on thrust force and torque in the Al layer, with PCR's of ~56 and 55% respectively.

Thrust force			Ti layer			
Source of variances	D.F.	Seq S.S.	M.S.	F	P	PCR
Tool material	1	112812	112812	23.16*	0.009	45.0%
Feed rate	1	107184	107184	22.01*	0.009	42.7%
Drilling strategy	1	24	24	0.01	0.01	0%
Residual	4	19482	4871			12.1%
Sum of square variances	7	239503				
Torque			Ti layer			
Source of variances	D.F.	Seq S.S.	M.S.	F	P	PCR
Tool material	1	2903.2	2903.2	19.97*	0.011	28.0%
Feed rate	1	5995.1	5995.1	41.23*	0.003	59.4%
Drilling strategy	1	353.8	353.8	2.43	0.194	2.1%
Residual	4	581.6	145.4			10.5%
Sum of square variances	7	9833.7				
Thrust force			CFRP layer			
Source of variances	D.F.	Seq S.S.	M.S.	F	P	PCR
Tool material	1	7503	7503	7.23	0.055	39.3%
Feed rate	1	4773	4773	4.6	0.099	22.7%
Drilling strategy	1	19	19	0.02	0.900	18.9%
Residual	4	4151	1038			19.1%
Sum of square variances	7	16445				
Torque			CFRP layer			
Source of variances	D.F.	Seq S.S.	M.S.	F	P	PCR
Tool material	1	730	730	1.45	0.295	4.6%
Feed rate	1	1389.2	1389.2	2.76	0.172	18.2%
Drilling strategy	1	726.2	726.2	1.44	0.296	4.5%
Residual	4	2013.9	503.5			72.7%
Sum of square variances	7	4859.2				
Thrust force			Al layer			
Source of variances	D.F.	Seq S.S.	M.S.	F	P	PCR
Tool material	1	169.3	169.3	0.44	0.545	0%
Feed rate	1	3461.1	3461.1	8.91*	0.041	56.3%
Drilling strategy	1	266.8	266.8	0.69	0.454	0%
Residual	4	1554	388.5			43.7%
Sum of square variances	7	5451.2				
Torque			Al layer			
Source of variances	D.F.	Seq S.S.	M.S.	F	P	PCR
Tool material	1	200.0	200.0	0.35	0.587	0.00%
Feed rate	1	6267.0	6267.0	10.92*	0.03	55.09%
Drilling strategy	1	1562.4	1562.4	2.72	2.72	9.5%
Residual	4	2298.2	574.6			35.41%
Sum of square variances	7	10332.6				

(* Significant at the 5% level, $F_{cal\ 1,4}$ =7.71)

Table 4.1 ANOVA table for the thrust force and torque in each material layer

4.1.2 Tool wear and tool life

Figure 4.3 details the progression of the tool flank wear against the number of holes drilled for all trials. It was observed that tests involving coated drills produced between 90-140 holes before reaching the tool life criterion of 0.3mm flank wear. Conversely, flank wear of the

uncoated drills did not exceed ~0.23mm even after machining 180 holes. The influence of feed rate was also apparent, with drill wear rate up to ~28% lower when operating at the higher feed of 0.08mm/rev, which was possibly due to the reduced contact time between the tool and workpiece. The result also substantiates the lower thrust forces observed when employing higher feed rates detailed previously in Section 4.1.1. The corresponding ANOVA calculations detailed in Appendix 3, showed that both tool coating and feed rate were statistically significant factors with respect to tool wear, with the former having an overwhelming PCR of ~78.4%. While the use of a pecking cycle generally reduced tool wear by up to ~10%, drilling strategy was not statistically significant at the 5% level.

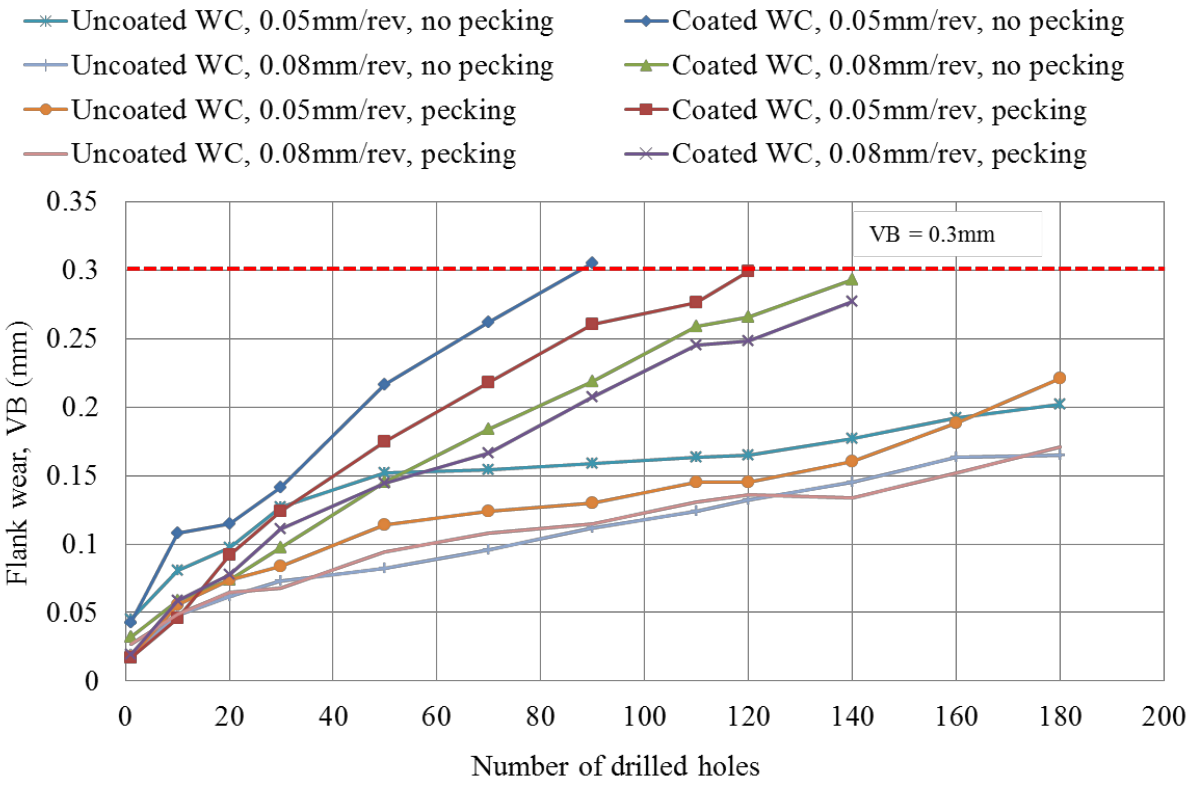


Figure 4.3 Progression of flank wear (VB) up to the end of test criterion in all tests

Figure 4.4 shows SEM micrographs of cross-sectioned cutting edges from uncoated and coated drills. In addition to the larger radius (~33µm), microhardness analysis revealed that the hardness of the WC substrate in the coated drill (1731$HK_{0.025}$) was 24% lower than the uncoated WC tool (2287$HK_{0.025}$), which could have been caused by the coating process. The relatively weaker WC substrate was a possible reason for the lower tool life obtained when employing the coated drills.

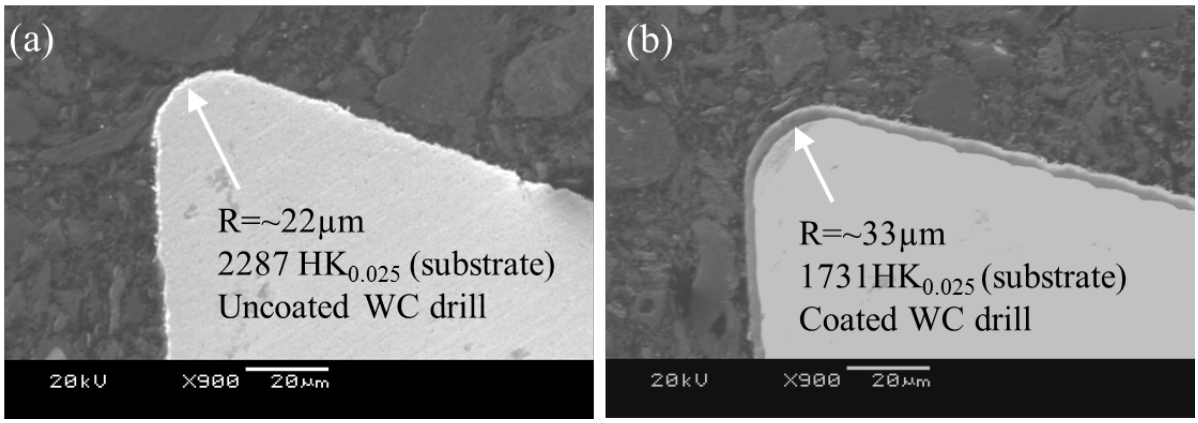


Figure 4.4 Cutting edge radius and substrate microhardness of (a) uncoated and (b) coated WC drills

Further examination of the worn drills showed the presence of extensive adhered material, built up edge (BUE) and abrasion wear on the flank face of the tool, with the wear patterns similar in all tests, see Figure 4.5. The adhered material and BUE, which was primarily Al from the workpiece stack (confirmed by EDX analysis) was observed to extend almost across the entire length of the cutting lips, irrespective of the machining conditions. However, the thickness of the BUE layer on the cutting edge was generally larger on the coated drills similar to the burn marks, which were evident beneath the abrasion wear scar on all tools. This was thought to be carbon deposits from vaporised cutting fluid [200], which were more prevalent towards the drill corners due to the likely higher cutting temperature.

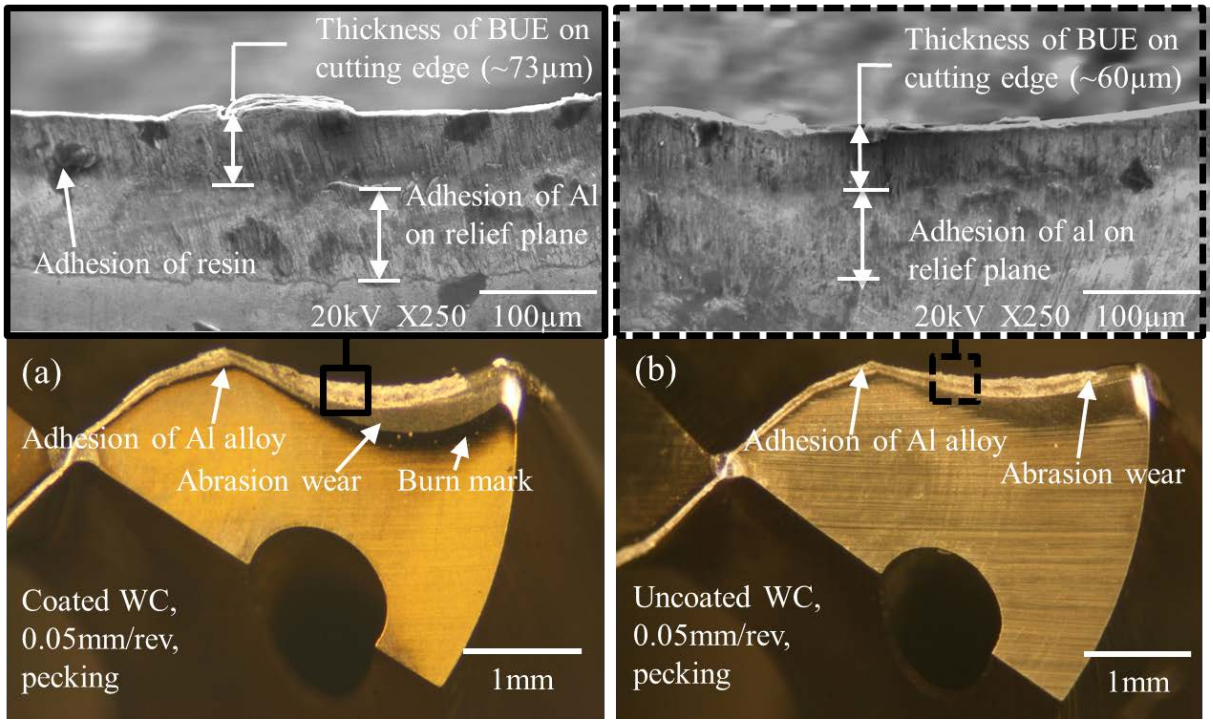


Figure 4.5 Optical and SEM micrographs of worn drills in (a) Test 6 and (b) Test 5

4.1.3 Hole accuracy (diameter, out of roundness, cylindricity)

The average hole diameters in each of the material sections as well as the overall diameters over the 3 layer stack at test cessation is shown in Figure 4.6. Although the range of hole diameter measurements varied between 6.30-6.395mm, the average values were all within 6.35±0.035mm. Despite the majority being undersized, holes produced by the coated drills at test cessation exhibited superior accuracy in terms of diameter with lower deviations (maximum of 0.02mm) from the nominal value (6.35mm) compared to the uncoated tools. This was attributed to the lower wear level (33%) at the peripheral corners of the coated drills. Tool coating was found to be the principal factor affecting hole diameter in both the Ti and CFRP layers with PCR's of 64.5% and 57.5% respectively, according to the ANOVA detailed in Appendix 3. Similarly, drilling strategy had a significant effect in the Ti layer while feed rate was only seen to influence hole diameter in the CFRP section.

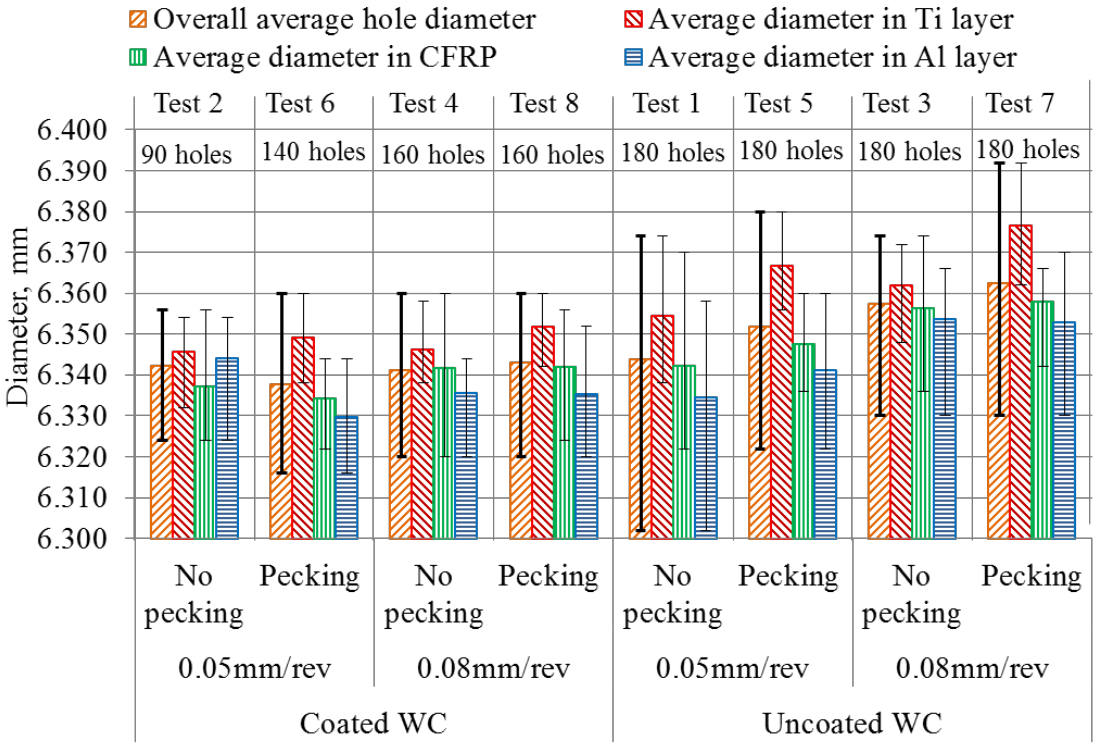


Figure 4.6 Average hole diameters at test cessation

Figure 4.7 details the typical hole roundness profile and corresponding out of roundness measurements in each material layer of the stack. None of the variables had a major effect on out of roundness in the CFRP and Al layers, while tool material/coating was found to be significant at the 5% level in Ti layer, see ANOVA in Appendix 3. All of the holes examined in the Ti layer showed a tri-lobed shape, which was either due to run out of the drill when entering the workpiece material or 'sliding' of the chisel edge away from the hole centreline

upon contact with the workpiece surface. The latter typically occurs when employing drills with larger chisel areas/thickness and is also known as ‘walking’, which causes bending of the tool resulting in asymmetric reaction forces on the cutting lips leading to the lobed profile as shown Figure 4.7(a). When moving deeper into the stack, support from the hole walls neutralised/reduced the initial eccentric forces acting on the drill, which not only restored the circularity of the hole but significantly decreased the out of roundness levels in the CFRP and Al layers of the stack, see Figure 4.7(b) and, Figure 4.7(c).

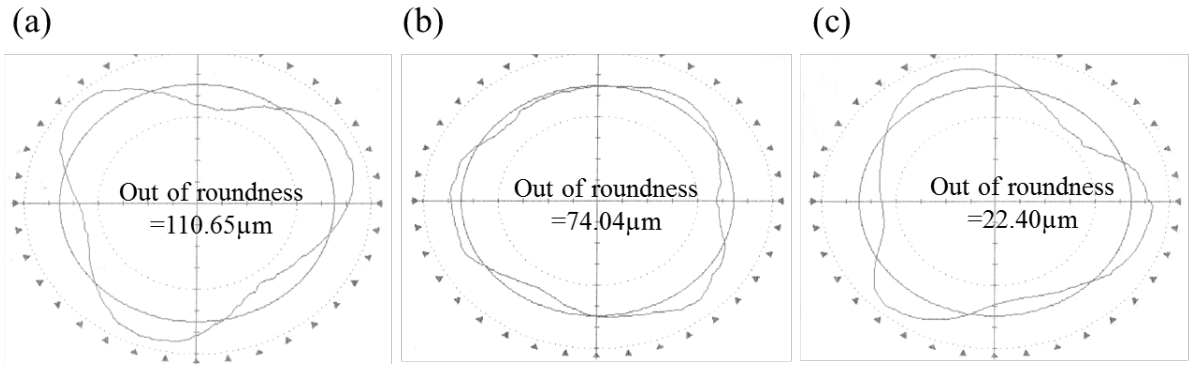


Figure 4.7 Out of roundness measurements of the (a) Ti, (b) CFRP and (c) Al layers at hole 90 in Test 3

Average hole cylindricity at test cessation were found to vary between 74-157µm whereas the average out of roundness in the Ti, CFRP and Al layers were in the range of 53-121µm, 33-109µm and 25-78µm respectively, depending on the operating conditions. Figure 4.8 details the 3D hole profile produced using an uncoated and coated drill in Test 5 and 6 respectively. In general, the uncoated tools displayed a greater tendency to produce holes with poorer hole cylindricity of 110.1µm over the 3 layer stack. This was possibly due to high levels of tool runout/deflection, with the relatively sharper chisel edge (uncoated) unable to counteract the unbalanced forces during drilling.

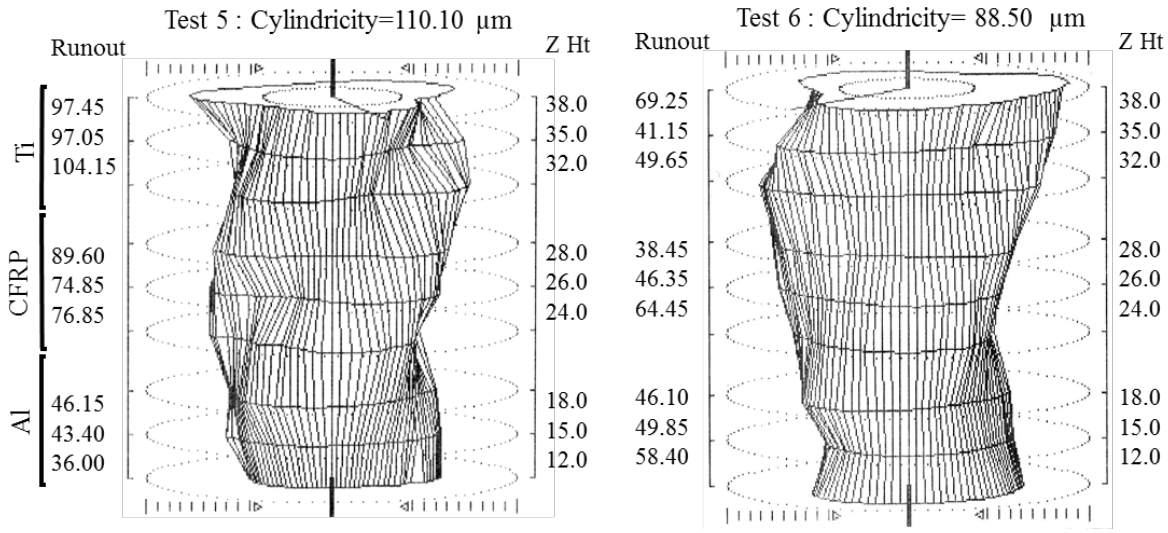


Figure 4.8 Cylindricity form profile of last hole drilled in Test 5 and Test 6

4.1.4 Burr formation

Images of the burrs formed at the entry (Ti) and exit (Al) of the stack for the last hole drilled in all tests are detailed in Figure 4.9(a). All of the burrs observed at the hole entrance were classified as Type II uniform burrs [167] while leaned-back burrs [164] were generally present at the exit location in the Al layer. Examples of the typical burr shape/form on the Ti and Al sections are shown in Figure 4.9(b) and Figure 4.9(c) respectively.

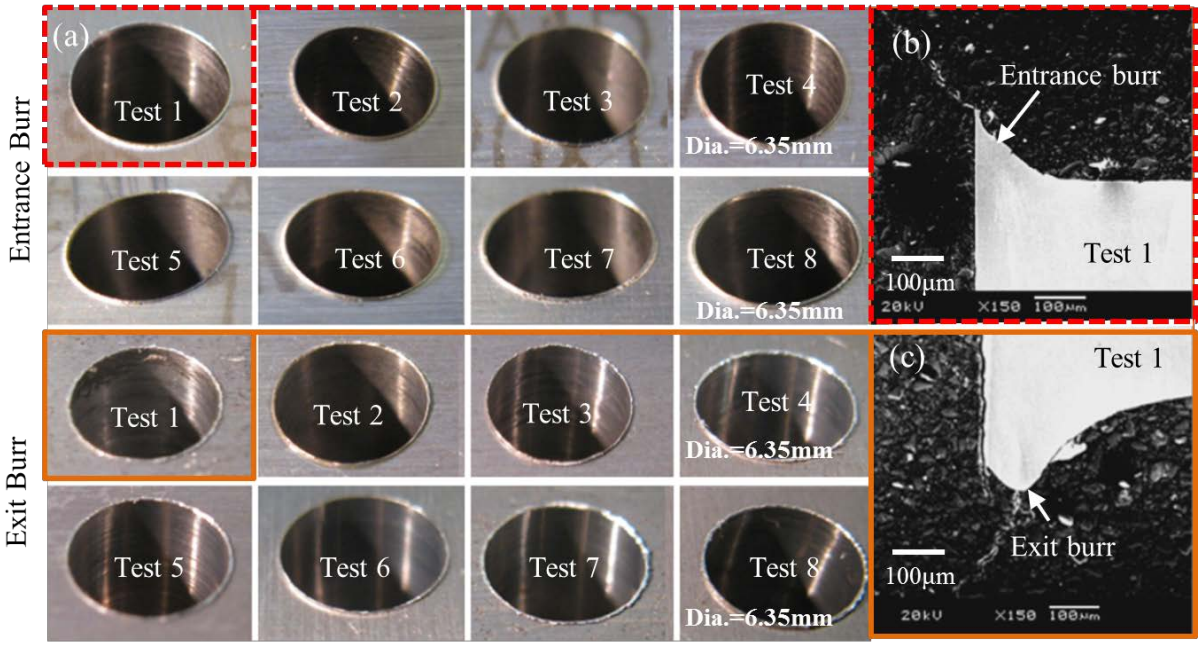


Figure 4.9 (a) Optical images of burrs formed at the entrance of Ti and exit of Al layers in each experiment; and SEM of (b) entrance burr and (c) exit burr in Test 1 at test cessation

Figure 4.10 shows the progression of entrance burr height in the Ti layer for all trials, which increased from ~0.03mm to a maximum of ~0.23mm over the test duration. The corresponding ANOVA (see Appendix 3) showed that only drilling strategy had a statistically significant effect on burr height in the Ti section with a PCR of ~56%. In contrast, burr size was typically larger at the exit location in the Al layer, which varied from 0.05mm when using a new tool to 0.34mm at the test cessation; see Figure 4.11. In general, drilling with the higher feed of 0.08mm/rev produced smaller burrs, possibly due to the shorter tool-workpiece contact duration. As a result, plastic deformation of the workpiece material at the hole exit was retarded, which reduced burr formation [162]. Despite this, none of the variables was found to be significant with respect to burr height at the exit location. Interlayer burr heights recorded at the exit of the Ti section ranged between 0.16-0.35mm (typically 0.35-0.50mm) whilst those at the entrance of the aluminium section were considerably smaller varying from 0.01 to 0.09mm. This was due to burr formation at the exit and entry of the Ti and Al sections being supressed by the CFRP layer.

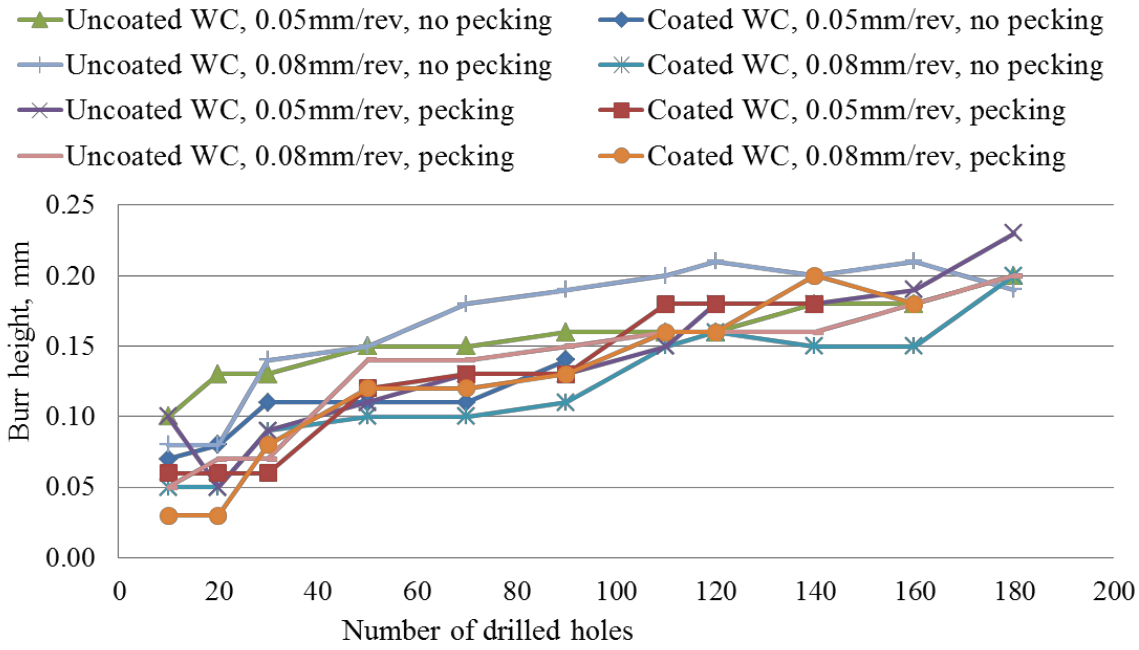


Figure 4.10 Progression of entrance burrs in the Ti layer

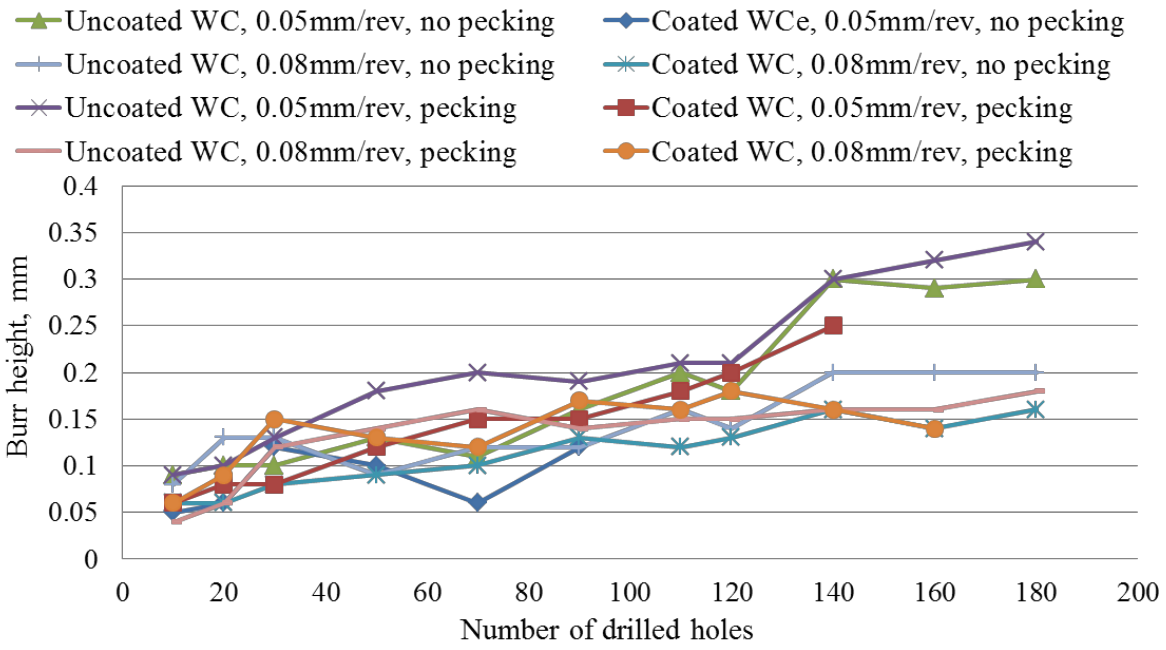


Figure 4.11 Progression of exit burrs in the Al layer

4.1.5 Hole surface roughness

Figure 4.12 shows the average surface roughness (Ra) results in each layer over the test duration for all tests. The Ra in the Ti, CFRP, and Al layer of the stack ranged between 0.35-1.74µm, 0.53-11.68µm, and 0.11-0.69µm respectively depending on cutting parameters. Trends in surface roughness (Ra) results of the Ti and Al layers showed no correlation with tool flank wear irrespective of the drills employed. In contrast, hole Ra in the CFRP layer typically deteriorated with increasing wear of the tools.

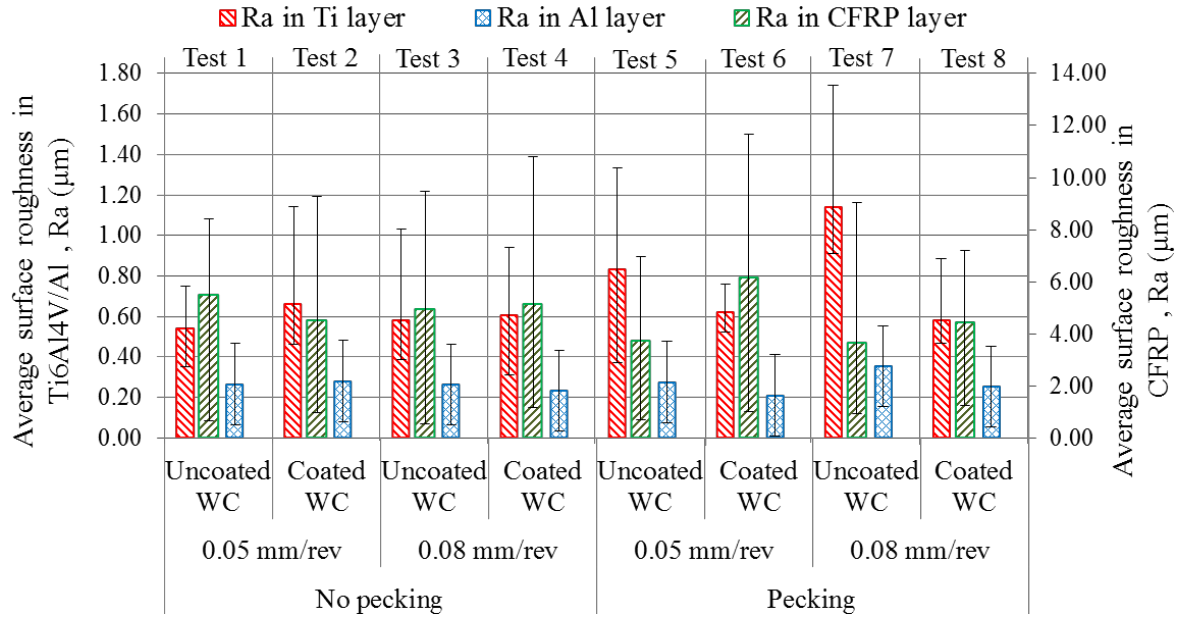


Figure 4.12 Average surface roughness (Ra) measurements over the test duration in all tests

Figure 4.13 shows the average peak-to-valley surface roughness (Rt) over the test duration, which provides a better indication of the actual variation in surface height profile in comparison to Ra data. The results showed that average Rt roughness in the CFRP layers when drilling with pecking were between 35.9-52.2µm but which ranged from 7.94 to 77.69µm over the test duration. Conversely, average Rt was up to 58% higher when operating without pecking, although corresponding ANOVA calculations revealed that drilling strategy was only significant at the 5% level with regard to Rt in the Ti layer and having a PCR of ~55%. None of the other variables was found to have a major influence on Rt in any of the stack layers, see Appendix 3.

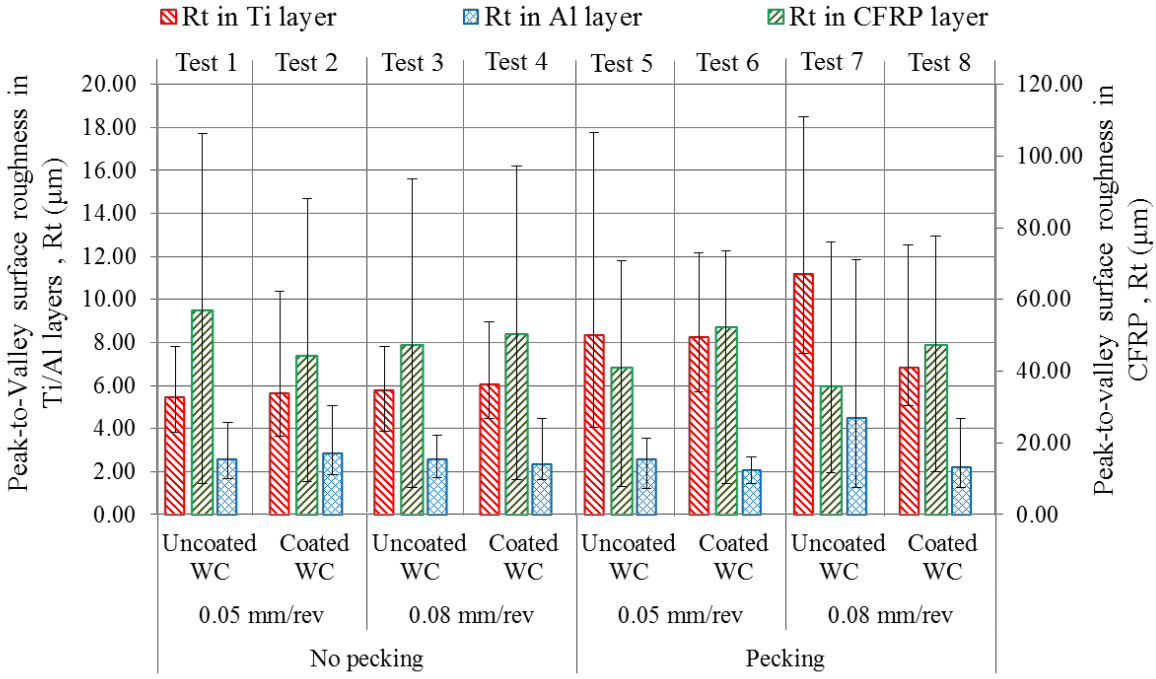


Figure 4.13 Peak to valley surface roughness (Rt) measurements over the test duration in all tests

Figure 4.14 shows the influence of peck cycle on 3D surface topography of the Ti layers (results for surface roughness significant at 5% level) for the last holes drilled together with the typical surface generated on the CFRP and Al sections. While the difference in Sa results was minor (0.382µm vs. 0.335µm), the Ti surface when machined under a pecking strategy exhibited a smoother profile (particularly towards the exit location), see Figure 4.14 (a), compared to tests undertaken without pecking as shown in Figure 4.14(b). This was most likely due to a reaming effect caused by the drill retraction during the pecking process. The Rt values however were significantly higher when utilising pecking, which was influenced by the presence of high peaks on the surface profile near the hole entry location. This was possibly due to chatter during entry of the drill into the workpiece, which was further exacerbated by

the tri-lobed shape of the hole in the Ti section. The surface on CFRP layers were generally characterised by deep grooves as a result of fibre/matrix pull out, which were especially prevalent at the 135° plies, leading to relatively high roughness values of 42.2µm St, see Figure 4.14(c). Conversely, the hole surface topography in the Al layer were largely consistent, similar to that shown in Figure 4.14(d), irrespective of the machining conditions.

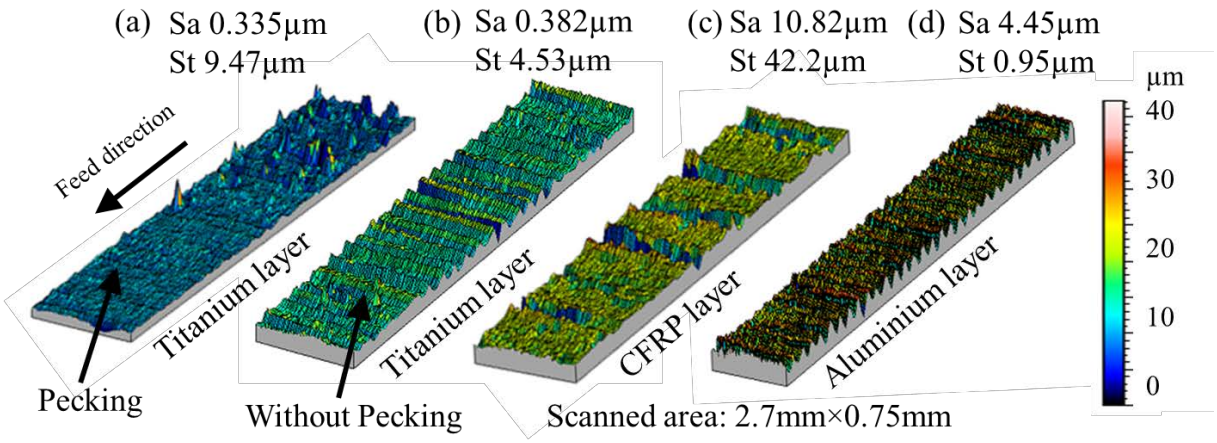


Figure 4.14 3-D surface topography in (a) Ti with pecking (Test 8), and (b) Ti, (c) CFRP, (d) Al without pecking (Test 4) using TiAlN coated WC at a feed rate of 0.08mm/rev

4.1.6 Subsurface microhardness alteration

When drilling without pecking, microhardness depth profile measurements revealed a hardened layer of up to ~420$HK_{0.025}$ (~12% increase over bulk hardness) to a depth of ~65µm, in the majority of the Ti samples evaluated, see Figure 4.15(a). Conversely, when operating with pecking, a reduction in workpiece microhardness of ~8 to ~12% was observed in two of the trials. Sample SEM micrographs of cross-sectioned hole substrate microstructure in the Ti section drilled without and with pecking are detailed in Figure 4.16. The former showed evidence of a plastically deformed layer below the machined surface while no sign of microstructure alteration was seen in the latter.

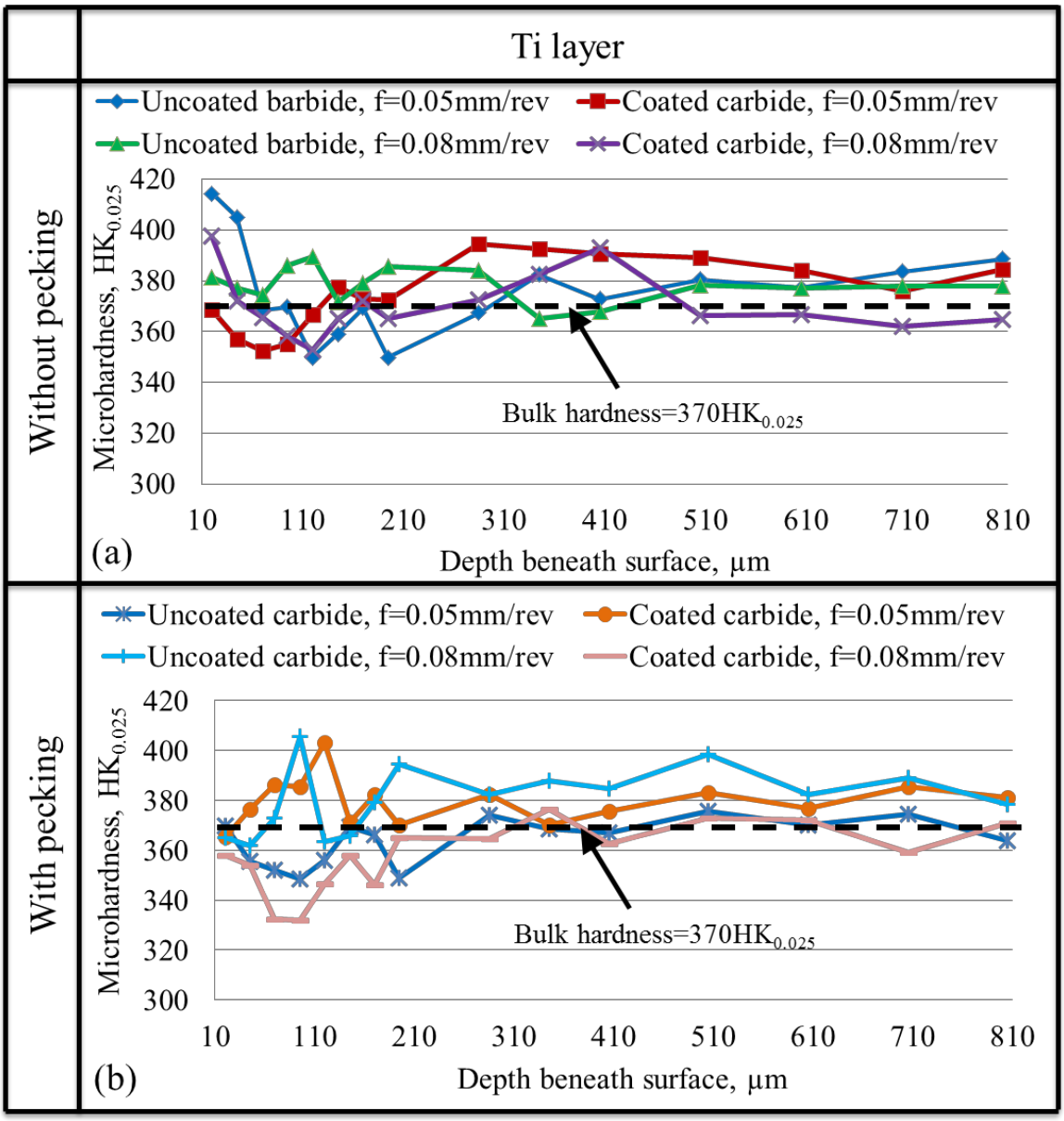


Figure 4.15 Microhardness depth profile at the last hole in Ti layer when drilling (a) without pecking and (b) with pecking for all tests

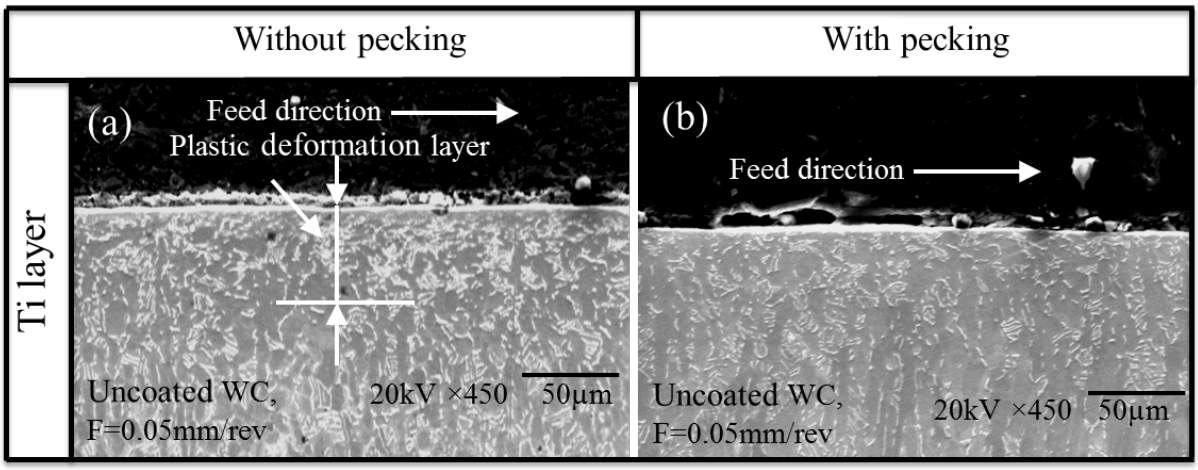


Figure 4.16 Subsurface microstructure of the last hole in Ti layer when drilling (a) without pecking, and (b) with pecking

The microhardness depth profile in the Al layer measured at the last hole for all tests is presented in Figure 4.17. All of the samples analysed showed marginal workpiece softening (2-10% below material bulk hardness) at the hole surface, which then increased to ~190$HK_{0.025}$ to a depth of ~200µm. Examination of the cross-sectioned holes however showed no indication of any subsurface microstructural alterations similar to that shown in Figure 4.18.

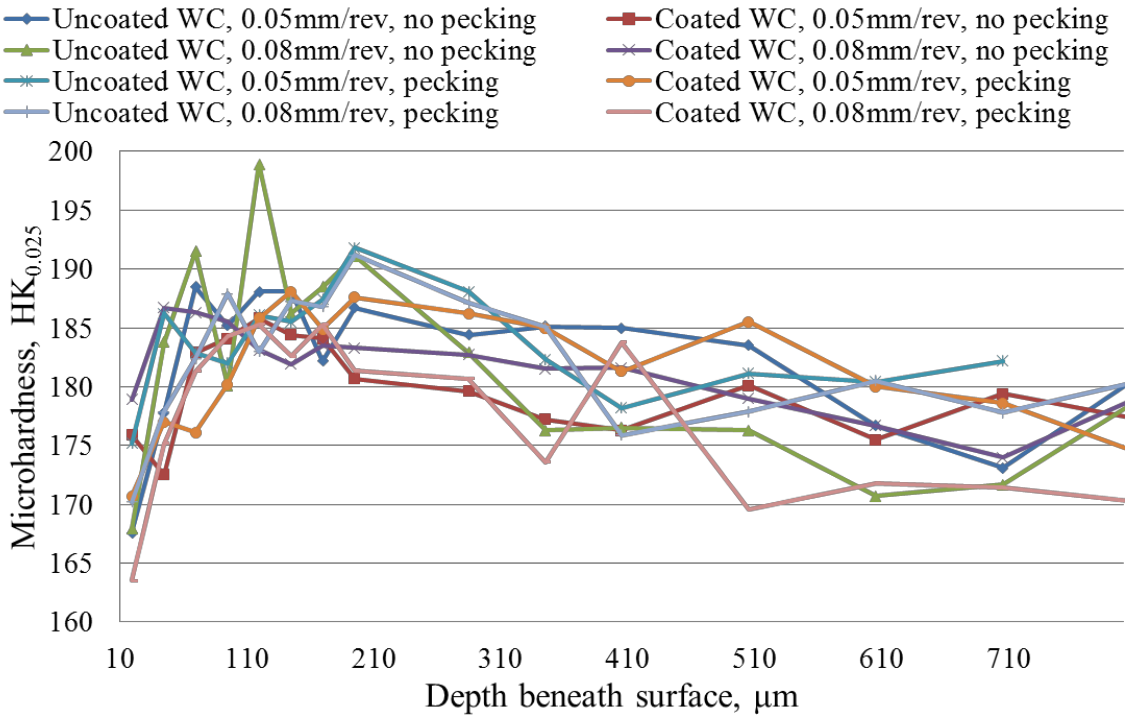


Figure 4.17 Microhardness depth profile at the last hole in Al layers

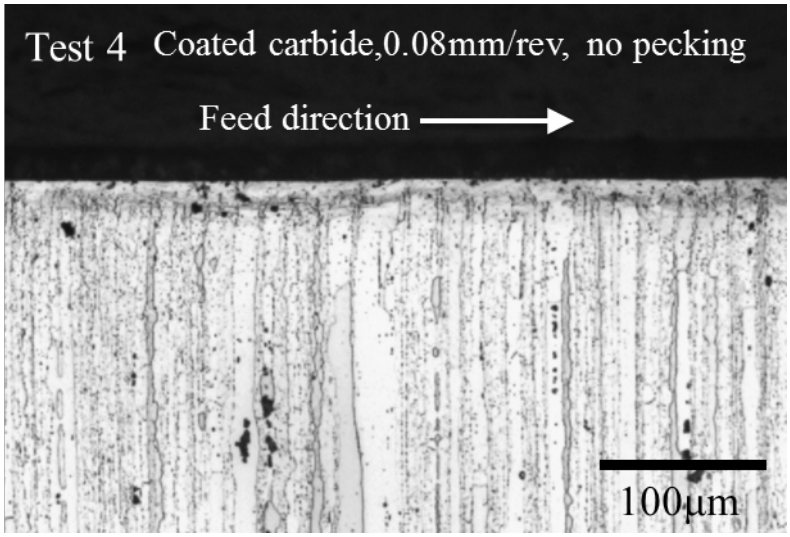


Figure 4.18 Microstructure at the last hole in Al layer from Test 2

4.1.7 Chip morphology

Figure 4.19 shows the types/form of Ti and Al chips produced at different operating conditions. The morphology of the swarf observed was broadly classified into 5 categories [201] as detailed below;

- Long (7-8 turns) continuous washer-type helical chips
- Short (3-4 turns) continuous washer-type helical chips
- Short (1-2 turns) conical helical chips
- Packed (3~4 layers) elemental chips
- Loose elemental chips

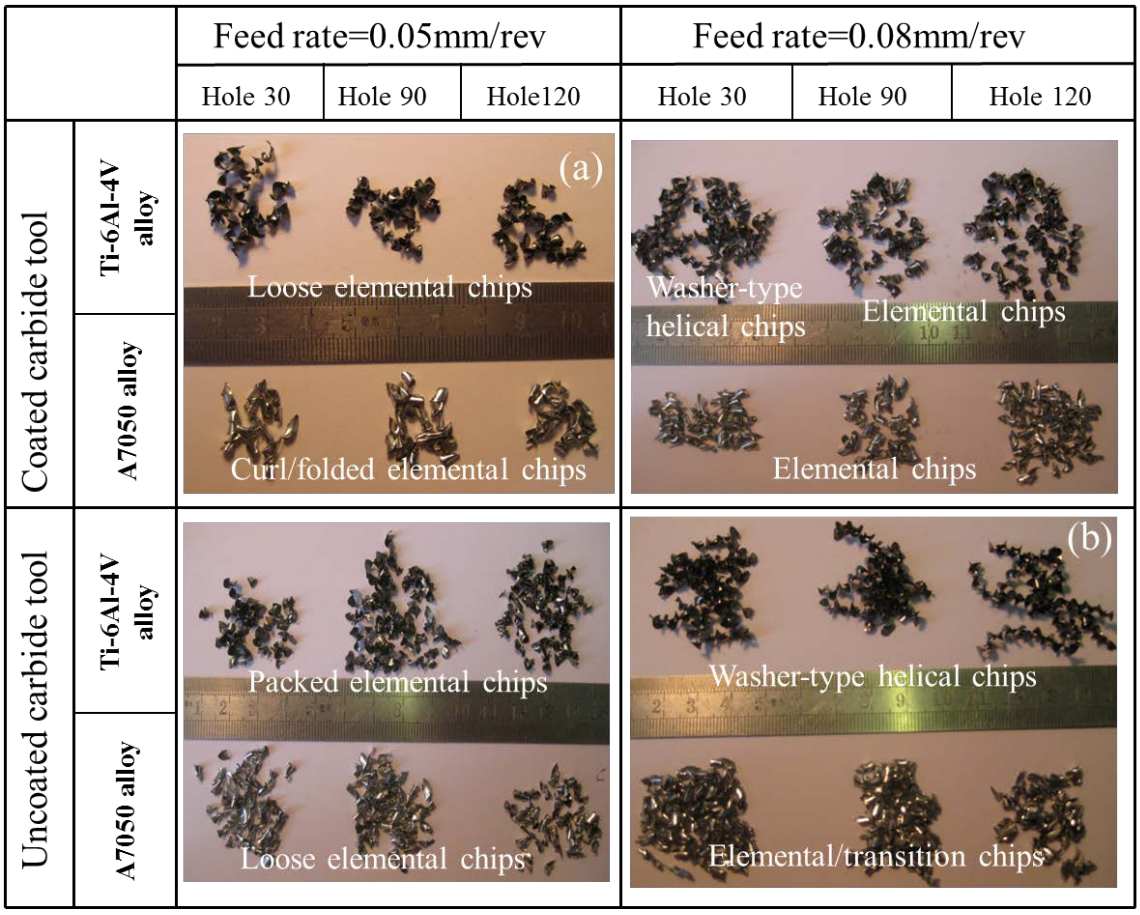


Figure 4.19 Chip morphology against cutting conditions and tool material recorded at the 30th, 90th, and 120th holes

Short washer-type helical chips were typically generated at the entrance of the Ti layer when drilling with coated carbide tools at the low feed rate (0.05mm/rev), but which then changed to lose elemental swarf as the drill moved further into the material, see Figure 4.19(a). This was due to relatively low shear zone temperatures at the start of cutting [202], with the increased thermal softening of the Ti material changing the chip morphology as cutting progressed, although no sign of serrated chips were seen in any of the tests. As the

drill penetrated into the CFRP layer, powder-like swarf was produced that mixed with the emulsion to form a slurry, but which was subsequently evacuated by the flow of the cutting fluid. Chips from the Al layer however were typically short curl/folded elemental chips throughout the test duration. When employing uncoated carbide drills at the higher feed rate of 0.08mm/rev through the Ti section, long/short continuous helical chips together with sporadic elemental swarf were prevalent, see Figure 4.19(b). The regular and stable chip formation was also a possible reason for the lower tool wear observed when operating at 0.08mm/rev, see Section 4.1.2. Elemental chips however were evident when drilling the aluminium layer at the higher feed rate, possibly due to strain hardening effects.

4.2 Phase 1B: Influence of margin design, feed rate and drilling strategy

4.2.1 Cutting force

Figure 4.20 presents the main effects plots for thrust force and torque in each of the material layers for the last hole drilled. Margin design appeared to have the strongest effect on both responses in all cases in comparison to feed rate and drilling strategy.

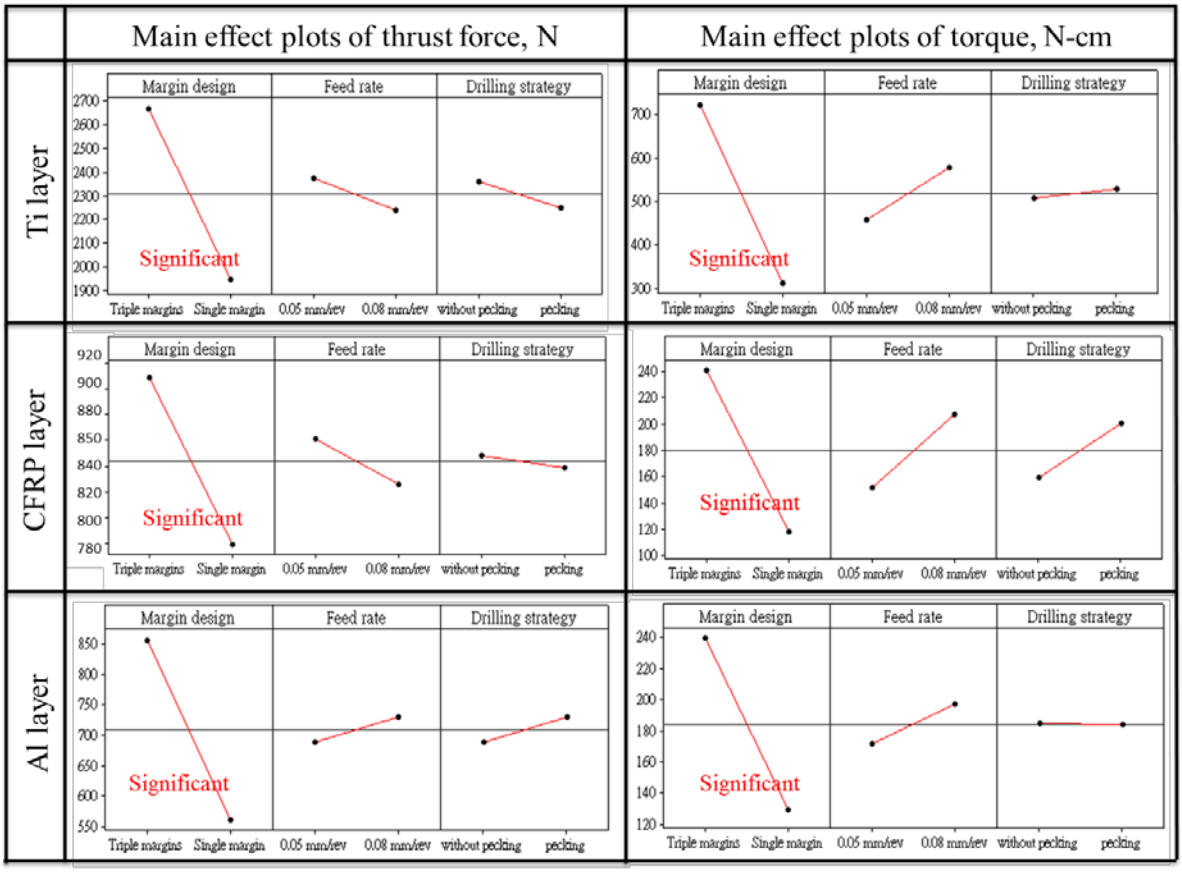


Figure 4.20 Main effect plots of thrust force and torque

The results from the ANOVA in Table 4.2 confirmed that the margin design was the only statistically significant factor affecting thrust force as well as torque when drilling through titanium, CFRP and aluminium layers, with corresponding PCR's varying from 51% to 89%. The increase in thrust force and torque was attributed to the greater friction from the increased tool-workpiece contact as a result of the larger area produced by the triple margin geometry. This was possibly further exacerbated by imperfections or deviations in the hole shape or geometry (e.g. tri-lobed profile, poor cylindricity or parallelism etc.), which can increase resistance to drill rotation. Figure 4.21 shows results of thrust forces measured at the last hole, which indicates that the use of triple margin tools generally increased the thrust force by ~44%, ~16% and ~54% in the Ti, CFRP, Al layers respectively when compared to the single margin drills. Similarly, torque in the Ti section increased by ~98%, 28% and 67% in the Ti, CFRP, Al layers respectively when utilising the triple-margin drill, whereas a rise in feed rate led to a minor increase (<5.3%) in torque in all layers.

	Thrust force					Torque			
	Ti layer					Ti layer			
Source of variances	D.F.	Seq S.S.	M.S.	F	PCR	Seq S.S.	M.S.	F	PCR
Margin design	1	1028895	1028895	46.1*	85.45%	336569.0	27954.0	61.09*	85.49%
Feed rate	1	32545	32545	1.58	0.87%	27954.0	336569.0	5.07	5.80%
Drilling strategy	1	24531	24531	1.1	0.00%	705.0	705.0	0.13	0.00%
Residual	4	89265	22316		13.68%	22039.0	5510.0		8.7%
Sums of Squares		1177937				387267.0			
	CFRP layer								
Source of variances	D.F.	Seq S.S.	M.S.	F	PCR	Seq S.S.	M.S.	F	PCR
Margin design	1	33528	33528	29.43*	79.50%	30334	30334	18.88*	50.93%
Feed rate	1	2482	2428	2.18	3.30%	6228	6228	4.20	0.00%
Drilling strategy	1	176	176	0.15	0.00%	3412	3412	2.34	0.00%
Residual	4	4557	1139		17.20%	6860	6860		49.07%
Sums of Squares		40742				46094			
	Al layer								
Source of variances	D.F.	Seq S.S.	M.S.	F	PCR	Seq S.S.	M.S.	F	PCR
Margin design	1	174316	174316	42.06*	85.89%	24156.0	24156.0	78.68*	89.46%
Feed rate	1	3617	3617	0.87	0.00%	1275.0	1275.1	4.15	3.63%
Drilling strategy	1	3625	3625	0.88	0.00%	0.5	0.5	0.00	0.00%
Residual	4	16568	4142		14.11%	1228.0	307.0		6.91%
Sums of Squares		198126				26659.7			

* Significant at the 5% level, $F_{cal\ 1,4}$ =7.71

Table 4.2 ANOVA table for thrust force and torque

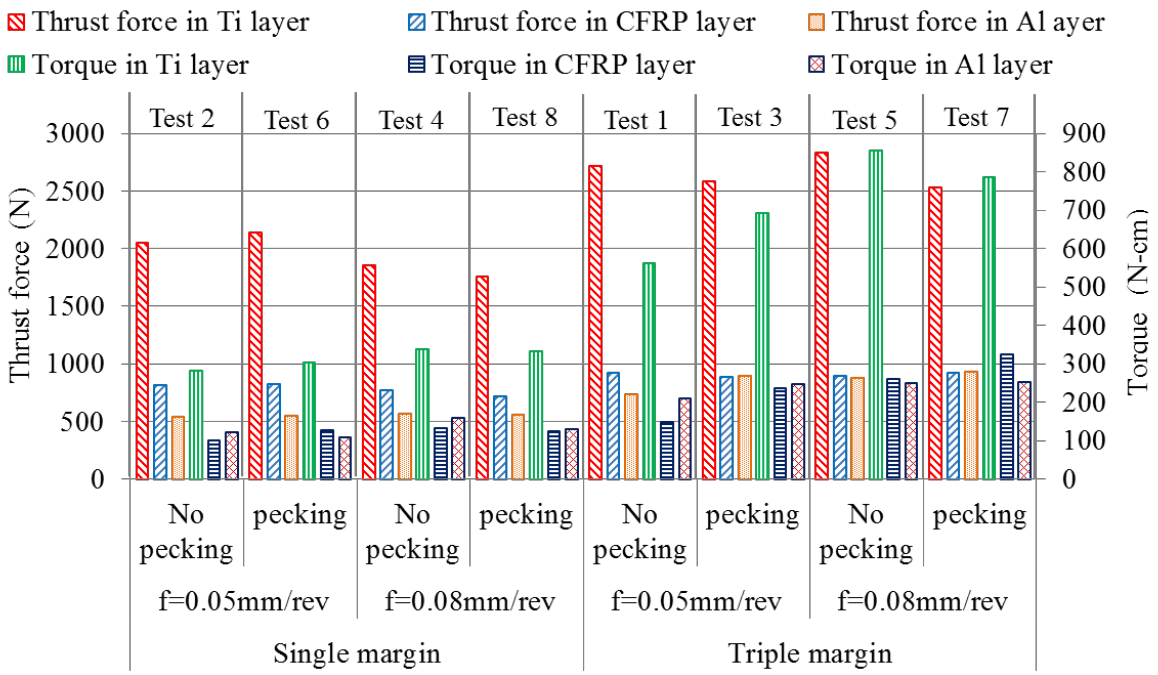
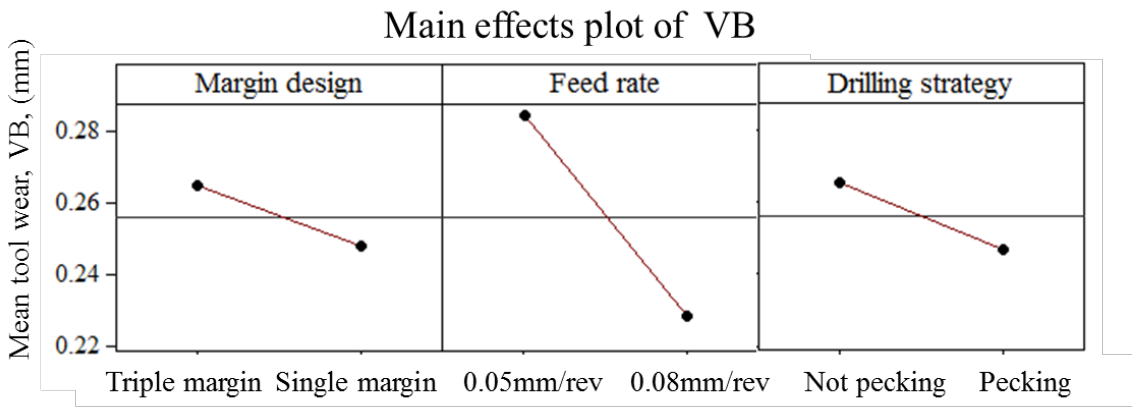


Figure 4.21 Measurement of (a) thrust force and (b) torque in Ti, CFRP, Al layers

4.2.2 Tool wear

Figure 4.22 presents the main effects plot for mean tool wear at the cessation of tests, which highlighted that feed rate had a significant effect with the corresponding ANOVA indicating a PCR of 72.4%. Tool flank wear data for each trial detailed in Figure 4.23 clearly showed lower wear rates when utilising the higher feed rate level of 0.08 mm/rev, which corresponded to the trends obtained in Phase 1A. Figure 4.24 shows micrographs of the typical wear modes observed when drilling with triple margin drills. Figure 4.24(a) reveals that the built-up edge increased moderately from the chisel edge to the peripheral corner for a triple margin drill. The build-up of material at the former location was due to the lower cutting speed at the chisel edge leading to a ploughing, whilst the higher wear land at the peripheral corner increased friction during machining. In Figure 4.24(b), the built-up edge was etched and removed. The micrograph shows that the abrasion extended from the inner to the outmost periphery due to the increased cutting speed and resultant force. On the drill margin, adhesion of material was observed due to excessive rubbing with the machined hole surface. Analysis of the drill flank surface using energy dispersive spectroscopy (EDX) verified that the adhered material was primarily aluminium alloy as shown in Figure 4.24(c).



Tool wear	Overall stack					
Source of variances	D.F.	Seq. S.S.	M.S.	F	P	PCR
Margin design	1	0.00058	0.00058	2.76	0.17	4.40%
Feed rate	1	0.00627	0.00627	29.2*	0.01	72.40%
Drilling strategy	1	0.00068	0.00068	3.26	0.15	5.67%
Residual	4	0.00084	0.00021			
Sum of square variance		0.00837				

* Significant at the 5% level ($F_{0.05}$ 1, 4=7.71)

Figure 4.22 Main effect plot and ANOVA table for observation of tool wear

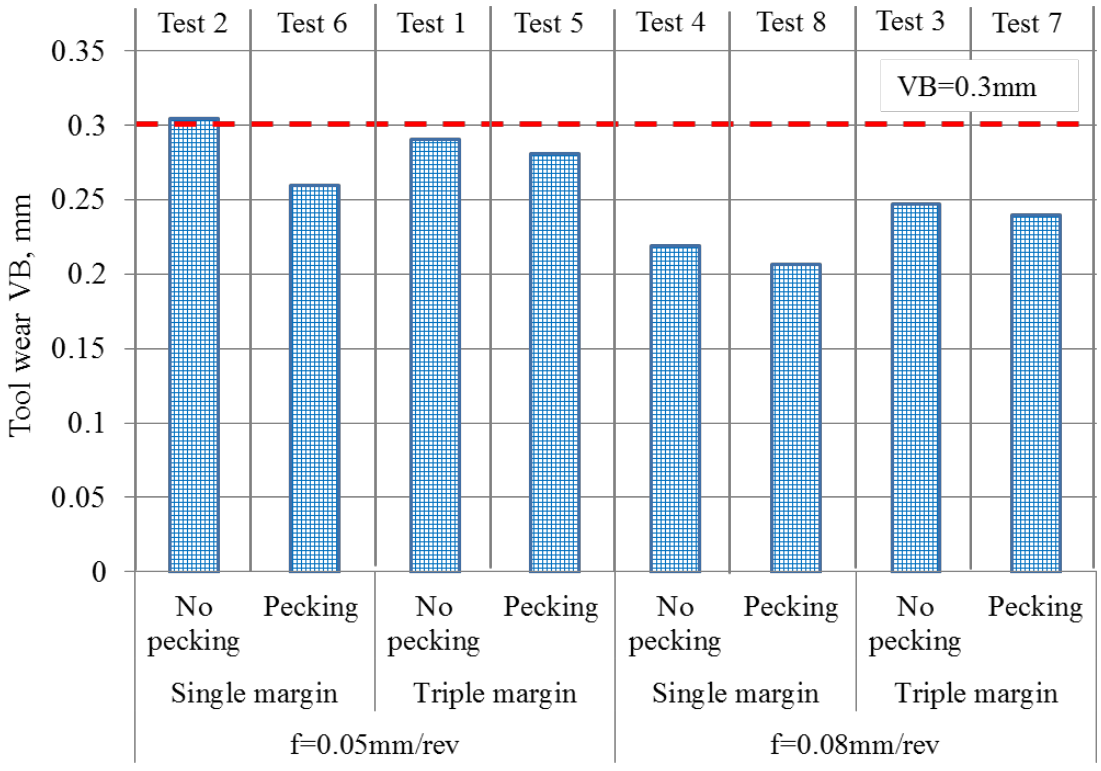
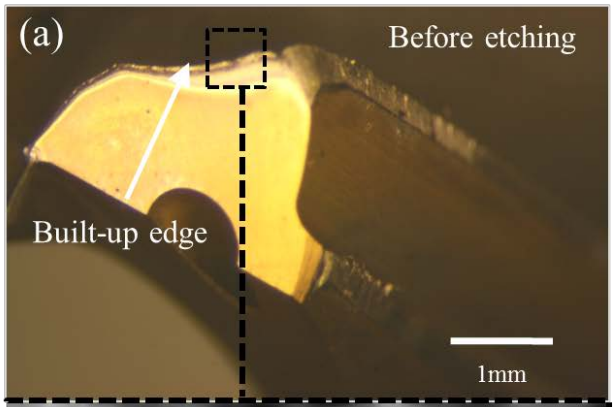
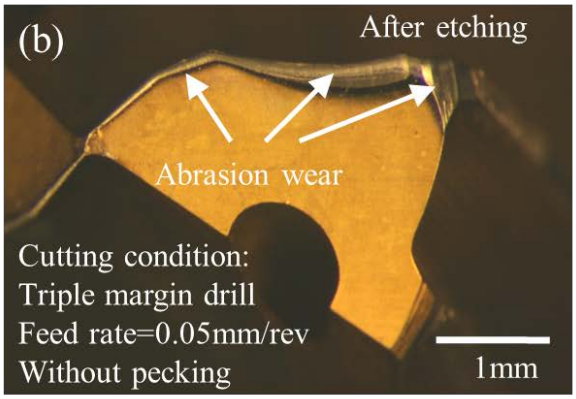
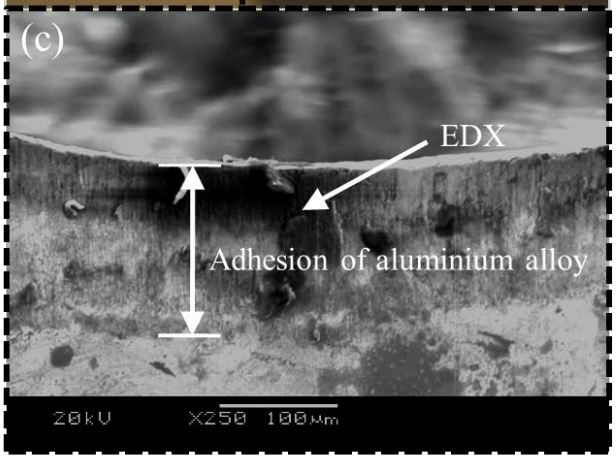


Figure 4.23 Tool flank wear at test cessation







Element	Weight%	Atomic%
C	15.9	30.72
O	1.29	1.87
Mg	1.17	1.12
Al	73.85	63.52
Si	0.13	0.1
K	0.14	0.08
Ti	0.1	0.05
Cu	1.69	0.62
Zn	4.96	1.76
Ag	0.56	0.12
Yb	0.2	0.03
Totals (%)	100	

Element detected in EDX analysis

Figure 4.24 Micrographs of (a) BUE (b) abrasion wear and (c) adhesion of Al alloy on the drill surface

4.2.3 Hole accuracy (diameter, out of roundness and cylindricity)

Figure 4.25 shows the evolution of hole diameter with respect to the number of holes drilled in all tests. The results clearly highlighted two distinct groups, where the single margin drills produced holes with superior hole diameter accuracy, which varied between 6.332-6.368mm over the test duration, irrespective of operating conditions. In contrast, all of the holes machined using the triple margin geometry were undersized, with the majority near or marginally below the lower tolerance limit of 6.315mm after exceeding ~50 holes drilled. The associated ANOVA showed that margin design was the principal significant factor affecting hole diameter in the Ti, CFRP and Al layers with PCRs of 71.68%, 88.09% and 89.33% respectively, whilst feed rate and drilling strategy had virtually no influence. Further inspection of the triple margin drill geometry revealed a considerably larger corner radius of 220µm as opposed to 85µm in the single margin drills. The extended radius essentially acts as a chamfer at the peripheral corners, which tends to reduce the cutting/shearing efficiency and increase the incidence of ploughing/plastic deformation. As a result, smaller hole diameters were produced.

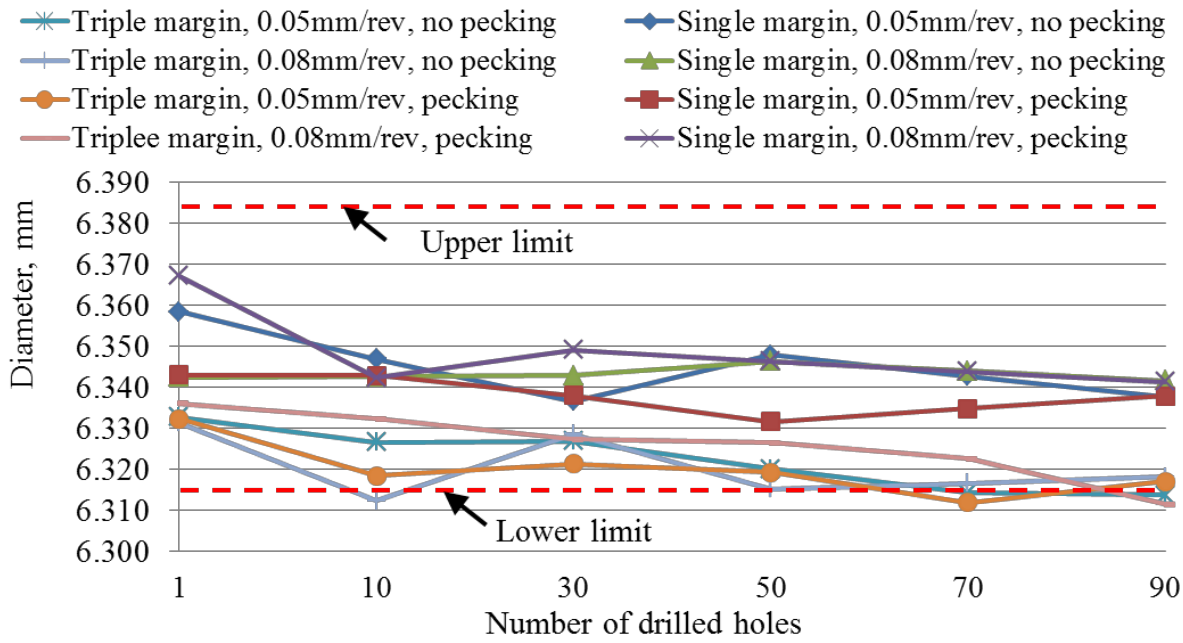
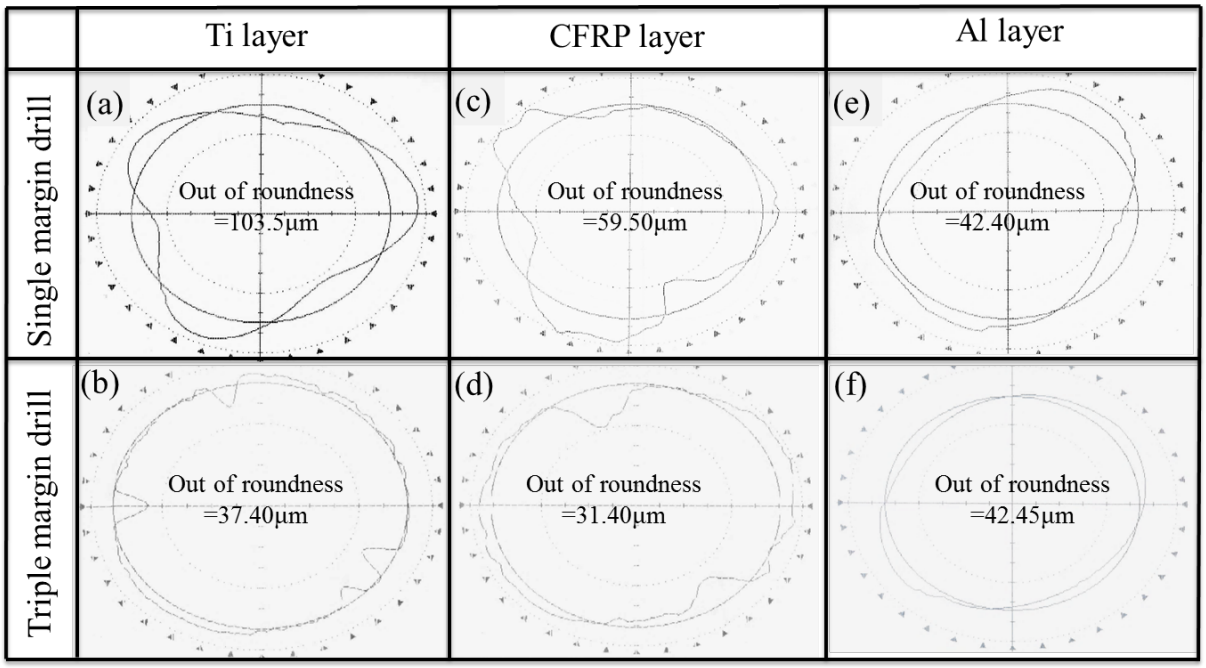


Figure 4.25 Measurement of the hole diameter in all test

Figure 4.26 shows examples of hole roundness plots in the Ti, CFRP and Al layers machined using single and triple margin drills. In general, the latter produced holes with lower out of roundness, most likely due to the larger chamfer land at the peripheral corner of the tools. This was seen to improve form deviations (e.g. tri-lobe) generated when employing the single margin drills, particularly in the Ti section, see Figure 4.26(a) and 4.26(b). Similarly in the CFRP layer, hole roundness improved with the use of the triple margin drill, see Figure 4.26(c) and 4.26(d), which possibly induced increased smearing of the matrix over the different directional plies as well as reducing the incidence of uncut fibres (tendency for greater bending or bulking of the fibres). While the difference in out of roundness values of the holes in the Al section was negligible, the hole profile was enhanced when employing the triple margin drills, as shown Figure 4.26(e) and 4.26(f).

Figure 4.27 shows that operating with triple margin drills together with pecking strategy produced comparatively low average out of roundness values in all 3 layers of the stack as well as the best overall hole cylindricity (55.6-61.2µm). While the ANOVA calculations detailed in Appendix 4 showed that drilling strategy had a moderate influence on hole cylindricity with a PCR of 31.28%, none of the variables were statistically significant at the 5% level. In contrast, margin design had a substantial effect on hole roundness in the Ti and CFRP sections, with corresponding PCR's of ~96% and 70% respectively.



Cutting condition: feed rate of 0.08mm/rev, no pecking

Figure 4.26 Measurement of hole out of roundness

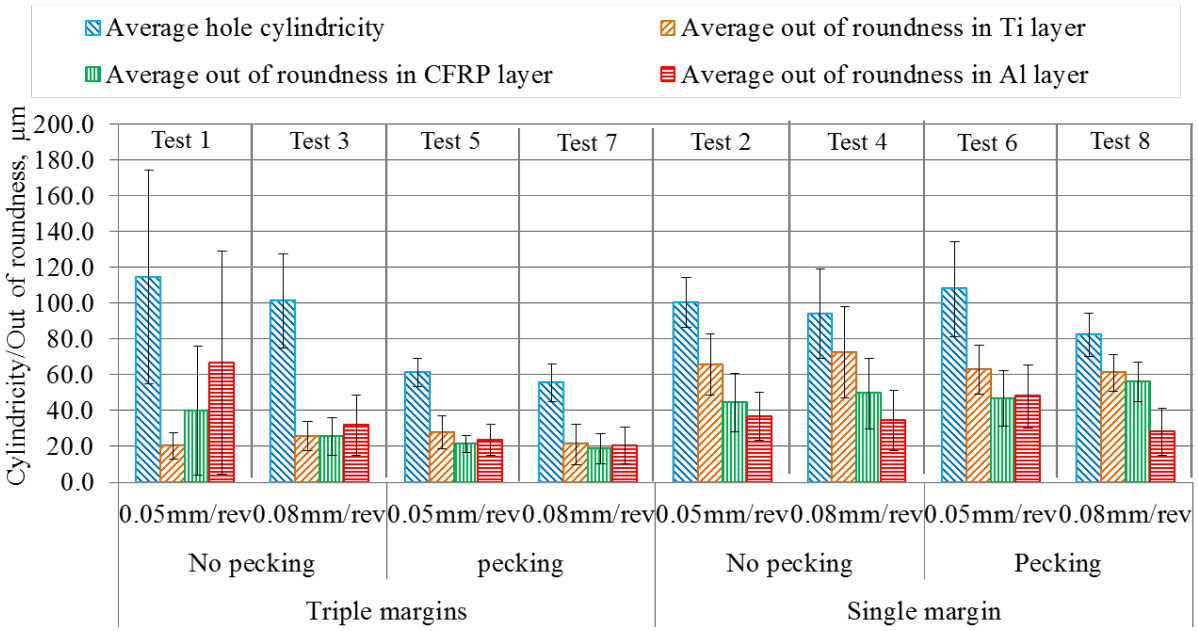


Figure 4.27 Measurement of average hole cylindricity and out of roundness

4.2.4 Burr formation

According to results from the ANOVA outlined in Appendix 4, margin design was the sole factor having a significant influence on hole entrance burrs in the Ti layer with a PCR of 90.12%. Conversely, none of the variables were statistically significant with respect to entrance burr size in the Al layers. In terms of exit burr height however, margin design was

significant at the 5% level in both the Ti and Al layers with PCR's of 49.9% and 80.5% respectively. Figure 4.28 shows the burrs generated at the entry and exit of the last hole drilled in the Ti and Al layers from Test 7. In general, when using triple margin drills, transient type burrs occurred at the entry location of both metallic layers whereas uniform burrs were generated at the hole exit. Tool geometry was found to be the dominant factor as burr size generally increased by 50-430% when machining with the triple margin drills. As shown in Figure 4.29, burr height at test cessation was typically larger at the exit position with a maximum of 0.32mm and 0.77mm compared to 0.30mm and 0.09mm at hole entry in the Ti and Al layers respectively. The smaller exit and entrance burrs on the Ti and Al layers respectively were similarly due to the presence of the CFRP laminate, which acted to suppress/resist material flow at the interface.

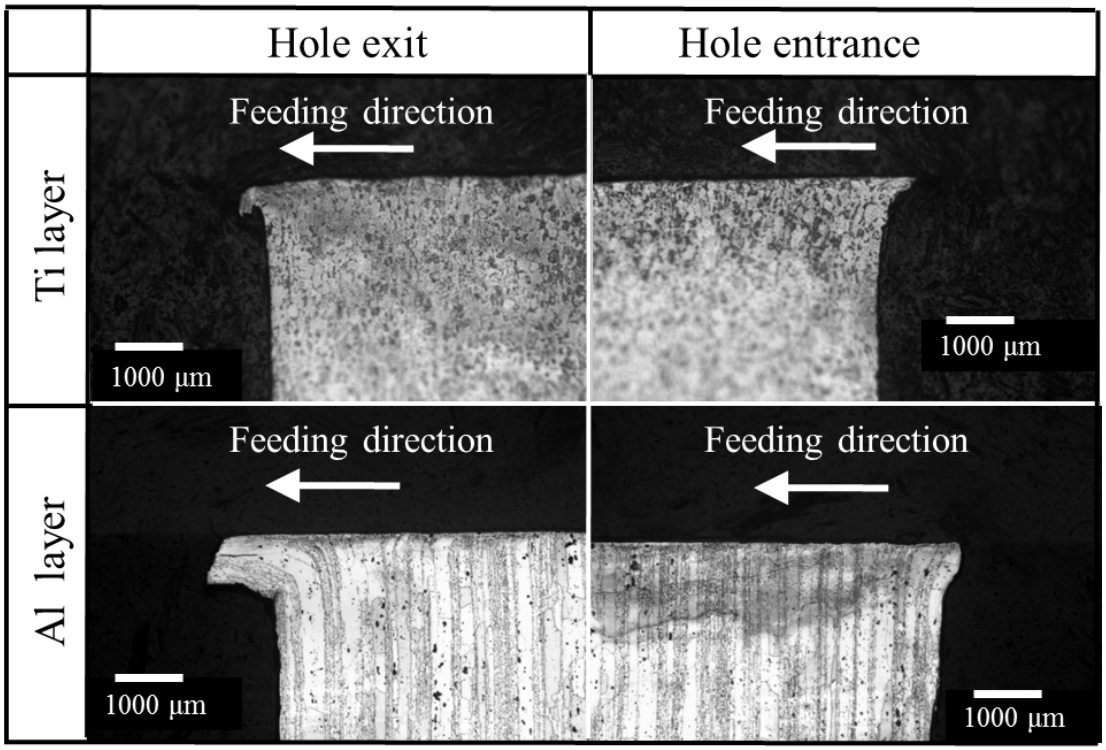


Figure 4.28 Burr formation at hole entry and exit in the Ti and Al layers at the last hole produced using a triple margin drill and feed rate of 0.08mm/rev under pecking (Test 7)

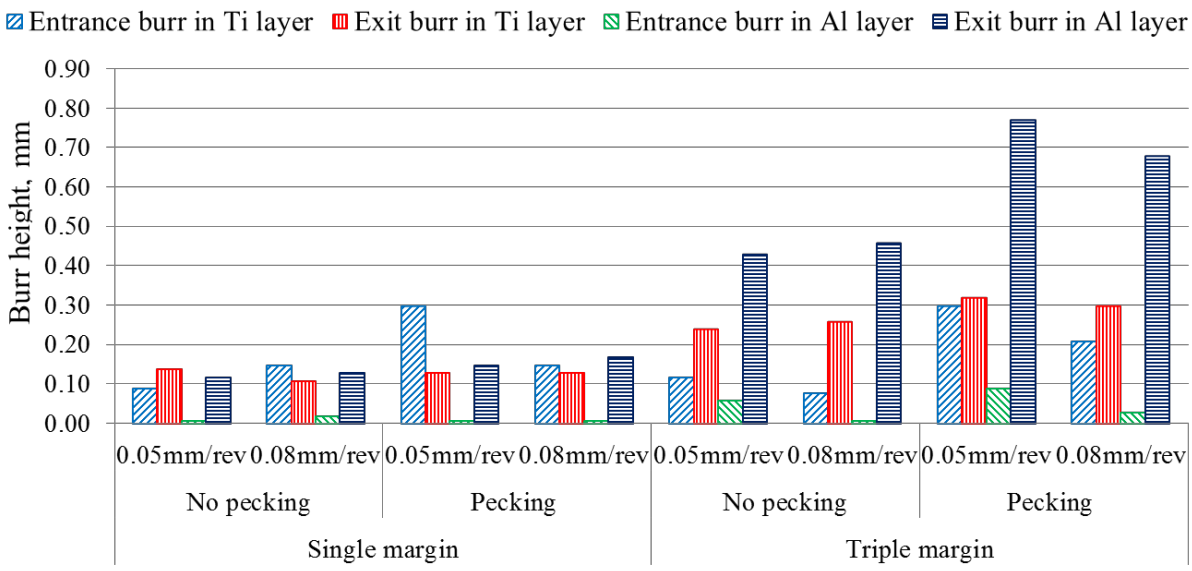


Figure 4.29 Burr height measurement at the last hole in all tests

4.2.5 Surface integrity

Hole surface roughness in the metallic layers of the stack was found to deteriorate when employing the triple margin geometry over the single margin drills, although this trend was reversed on the CFRP layer. Figure 4.30 shows the evolution of workpiece surface roughness (Ra) against the number of holes drilled in each material element for Test 5 (triple margin) and Test 6 (single margin) when operating under a feed rate of 0.05mm/rev with a pecking cycle. The maximum hole surface roughness on the Ti layer produced in Test 5 was 1.35µm Ra, which was approximately double that obtained when utilising the single margin drill. Similarly, for the aluminium layer, Ra was up to 3 times greater when using the triple margin drills.

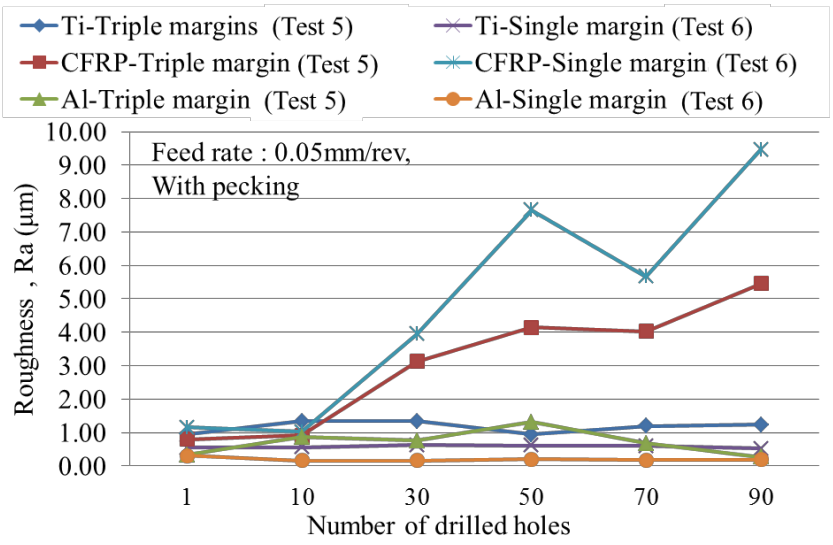


Figure 4.30 Hole surface roughness for each material layer in Tests 5 and 6

Hole surface roughness in the CFRP layer was generally observed to increase rapidly after ~10 holes, this was possibly due to the nature of the damage typically generated on the CFRP surfaces including material pull out, uncut fibres, resin melt, matrix cracking etc. In Figure 4.31(a), the increase in rubbing/contact between the triple margin drill and hole surface led to 'smearing' of the matrix material. Defects in the form of matrix cracking and fibre loss on the CFRP hole surfaces were however evident and more widespread on all plies when using single margin drills, see Figure 4.31(b).

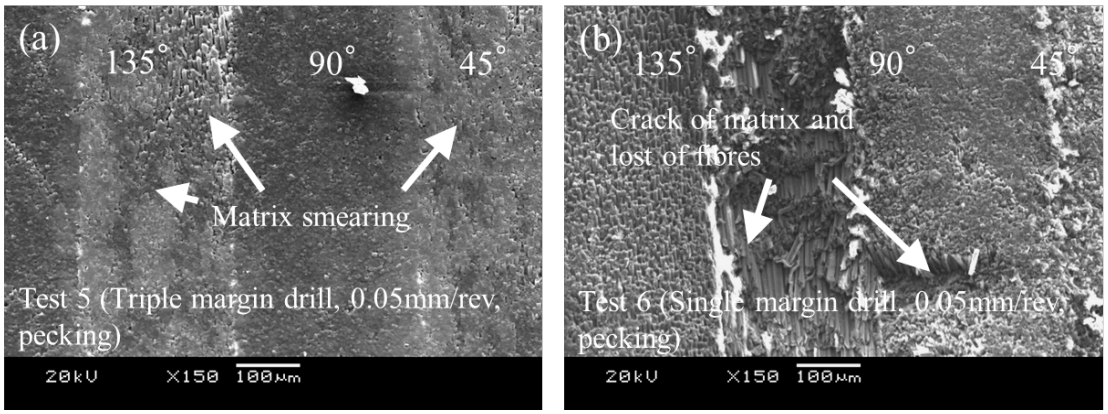


Figure 4.31 SEM micrograph of CFRP surface in (a) Test 5, (b) Test 6

Figure 4.32(a) and 4.32(b) show cross-sectional micrographs of the machined surfaces in the Ti and Al layers respectively for the last hole drilled in Test 5, which produced the highest levels of sub-surface alterations. Severe plastic deformation extending to a depth of ~184µm beneath the machined surface was recorded in the titanium layer while a ~75µm layer of elongated grains was similarly visible in the aluminium segment of the stack. This contrasted significantly with the depth of the microstructural deformation obtained when using the single margin drill in Test 6, which was only ~40 and 30µm in the Ti and Al layers respectively.

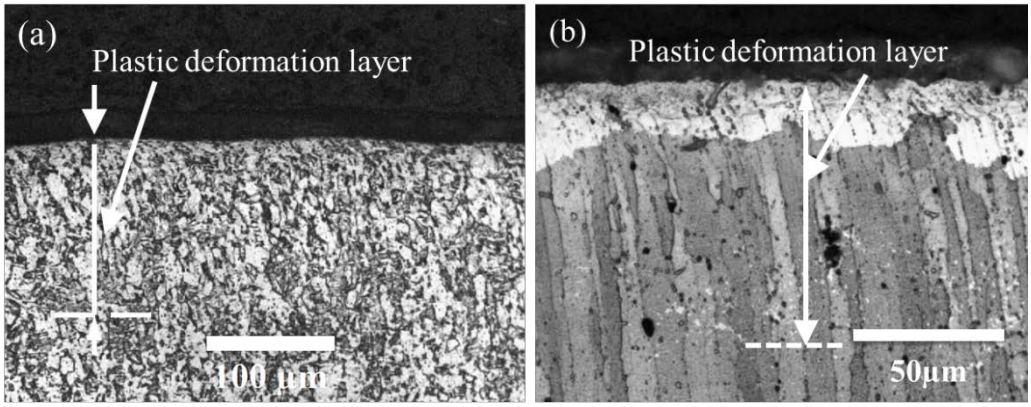


Figure 4.32 Microstructure in (a) Ti and (b) Al layers of Hole 90 in Test 5

Subsurface microhardness alterations commonly occur after machining due to thermal softening or strain hardening, depending on the process conditions and metallurgical nature of the workpiece material. Figure 4.33 shows microhardness depth profile plots for the last hole drilled in the titanium plates for all tests. When drilling with triple-margin tools, the hole surfaces in the Ti layer typically exhibited a strain-hardened layer extending to a depth of ~200µm, with a maximum level of 440$HK_{0.025}$ (15% above bulk material hardness) observed in Test 5. This corresponded with the increased thrust forces and torque recorded for the triple margin drills as shown previously in Figure 4.21. Conversely, the use of single margin drills generally resulted in softened sub-surface regions down to a minimum hardness of 330$HK_{0.025}$ (~13% below bulk hardness value), which was seen in Test 8. In Figure 4.34, no significant variation in workpiece microhardness was evident in the aluminium layer of the stacks machined with triple margin drills, despite the presence of a heavily deformed sub-surface microstructure similar to that detailed in Figure 4.32(b). An increase of up to 10% (~190$HK_{0.025}$) however was obtained in all trials employing the single margin tools.

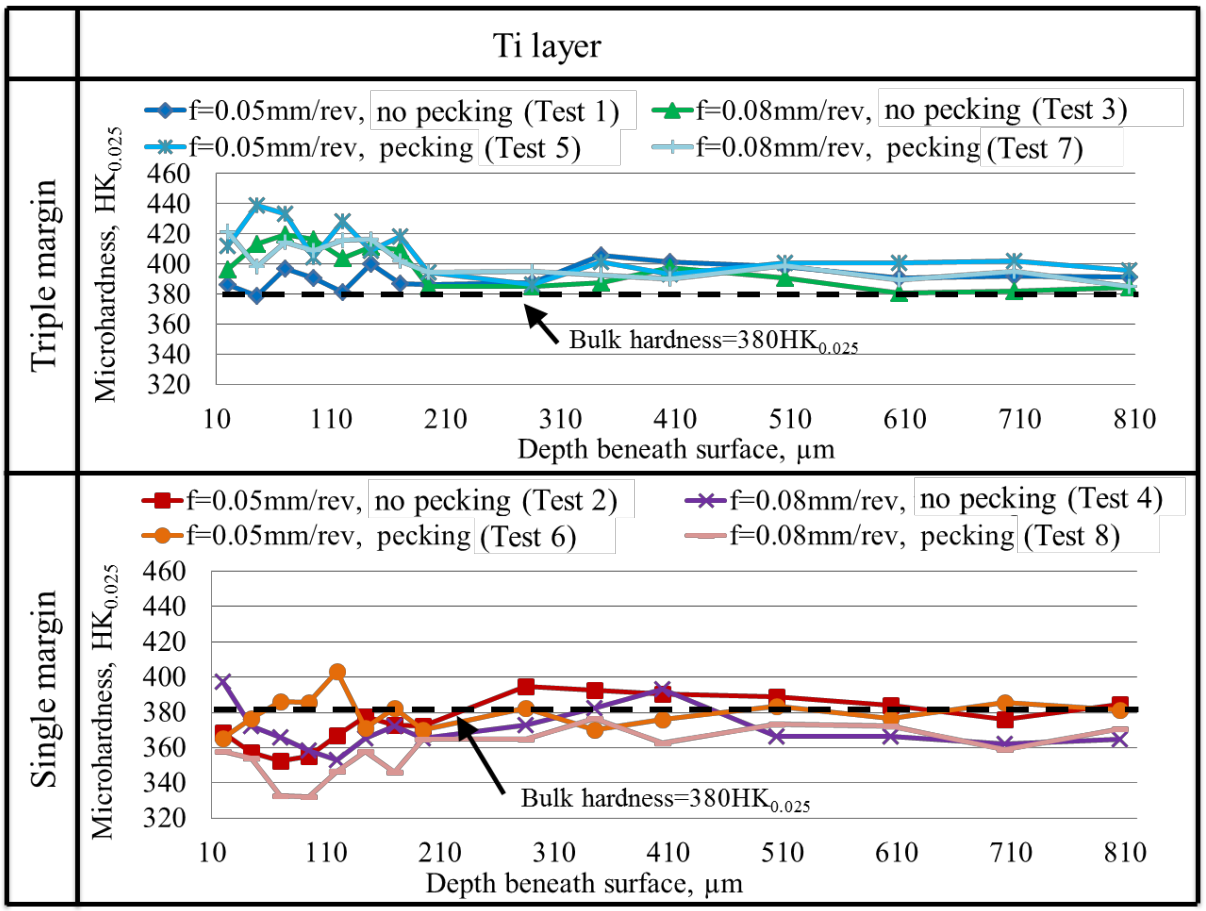


Figure 4.33 Microhardness measurements of Ti layers in hole 90 for all tests

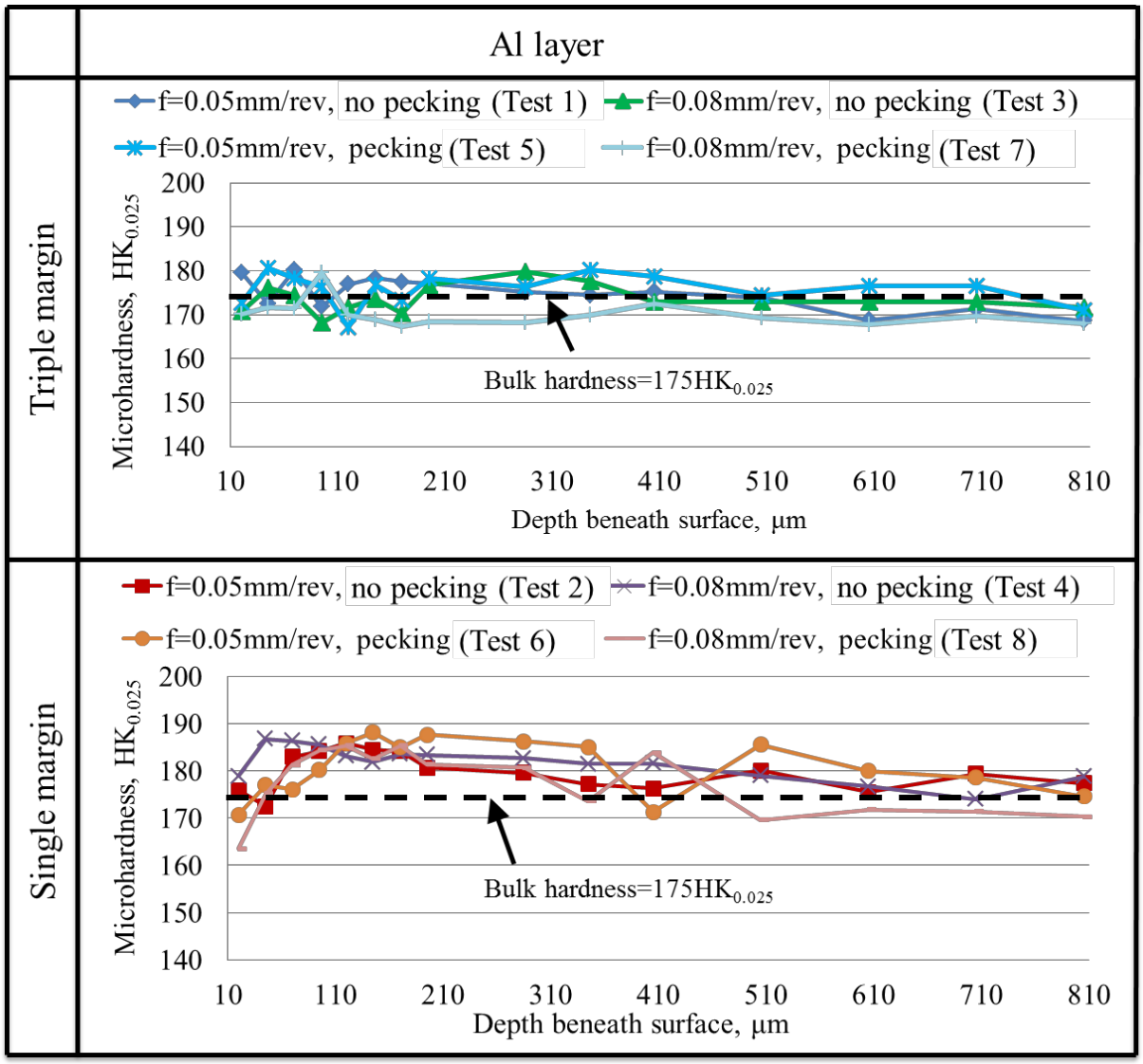


Figure 4.34 Microhardness measurements of Al layers in hole 90 for all tests

4.3 Phase 1C: Hole quality and failure modes of diamond coated tools

4.3.1 Cutting force

Figure 4.35 and Figure 4.36 detail the evolution of thrust force and torque respectively in each material section for all experiments. When employing the DLC coated drill at a feed rate of 0.08mm/rev in Test 1, thrust forces in the Ti, CFRP and Al layers increased from 526N, 222N and 265N in the first hole to 818N, 339N and 346N respectively after only 10 holes. The rapid rise (~56%) of thrust force in the Ti plate was attributed to the premature chipping and severe adhesion of workpiece material on the drill cutting edge. Similarly, torque increased by two to three-folds from initial values of 163N-cm, 59N-cm and 98N-cm in the Ti, CFRP and Al sections respectively after 10 holes. Subsequent rises in both thrust force and torque however was gradual until 70 holes when the test was halted due to fracture of the

drill corner, with values of ~1047N and 460N-cm recorded. This was in contrast to results from equivalent trials involving hardened coated drills in Phase 1A, where thrust forces were 80% higher (1881N) after 70 holes, see Section 4.1.1.

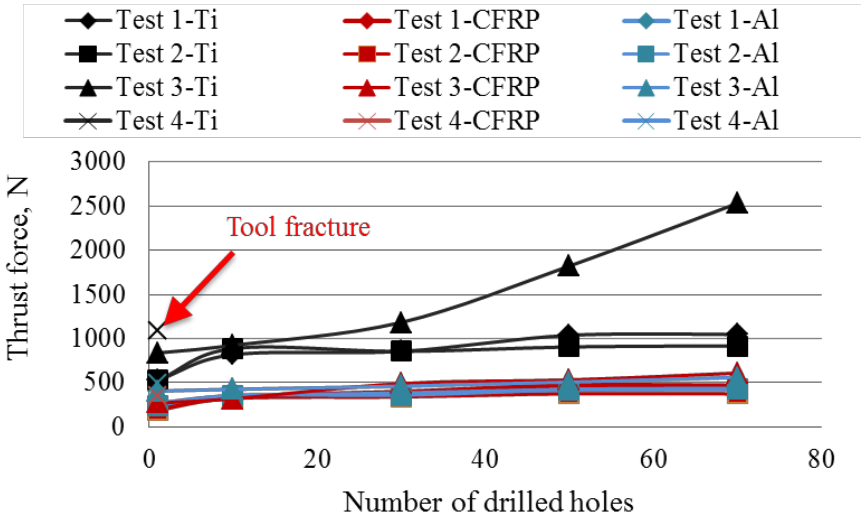


Figure 4.35 Thrust for each material layer in all tests

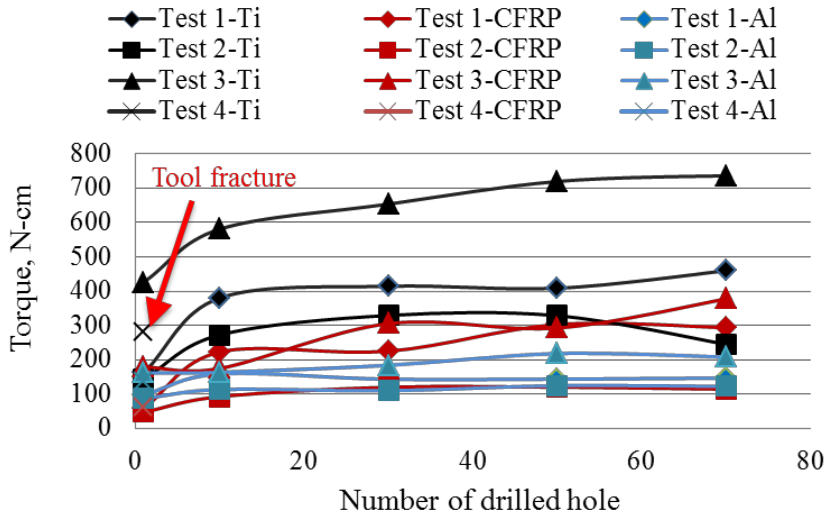


Figure 4.36 Torque results for each material layer in all tests

Considerably higher initial thrust forces in hole 1 were recorded in all 3 layers of the stack (Ti-837N; CFRP- 276N; Al- 406N) as the feed rate of the DLC coated drill was increased to 0.15mm/rev in Test 3. While forces in the Al workpiece remained fairly stable (462N) even after 30 holes, a steady increase of up to 41% (1184N) and 78% (492N) in the Ti and CFRP layers respectively was observed over the same interval following which complete delamination of the DLC coating occurred on the flank face. This subsequently led to a steep escalation of thrust force in the Ti layer, which more than doubled to ~ 2500N after 70 holes. Corresponding torque levels also increased from 427N-cm, 179N-cm and 161N-cm to 654N-

cm, 306N-cm and 184N-cm in the Ti, CFRP and Al layers respectively after 30 holes. As with Test 1, the experiment was discontinued after hole 70 due to severe fracture of the cutting lip corner radius.

Despite having a higher coefficient of friction (~0.4-0.6), marginally lower thrust forces of 524N, 187N, 243N and torque of 45N-cm, 48N-cm, 87N-cm in the Ti, CFRP, Al layers were obtained when drilling with a CVD diamond coated drill in the new condition at a feed rate of 0.08 mm/rev in Test 2, compared to the DLC coated product. This was most likely due to the geometry of the former, which involved a sharper primary point angle (120˚) that lowered thrust forces and a secondary angle of 180˚ that shortened the cutting lips and hence reduced torque. The progression of both thrust force and torque following the first hole was similar to the trend shown in Test 1, with both increasing by ~70 and 100% respectively in the Ti and CFRP sections after 10 holes. Subsequent values stabilised up to 70 holes. When utilising a feed rate of 0.15mm/rev in Test 4, the CVD diamond drill produced only 3 holes before catastrophic tool failure, thereby forcing premature termination of the experiment.

4.3.2 Tool wear

The average flank wear of the DLC coated drill after 70 holes in Test 1 was approximately 110µm, which was similar to the values (~108µm) produced by the uncoated carbide tools when machining at equivalent operating conditions, see Section 4.1.2. Figure 4.37 details corresponding micrographs of the drill at regular intervals over the test duration, which indicated that wear at the cutting edge was triggered by abrasion with signs of micro chipping after about 10 holes. The formation of a built-up edge (BUE) consisting principally of adhered aluminium alloy was initiated after ~20 holes, particularly near the corner edge, which was confirmed by energy dispersive X-ray (EDX) spectroscopy analysis detailed in Figure 4.38(a). The adhered layer/BUE continued to grow as machining progressed, which finally led to loss of the DLC coating as the BUE broke off from the drill surface. The repeated process of adhered material build up and removal eventually resulted in weakening and ultimately fracture of the drill corner. Subsequent SEM analysis of the worn drill showed chipping marks on the DLC coating and exposed carbide substrate at the corner together with evidence of epoxy matrix residue attached to the cutting edge, see Figure 4.38(b) for EDX examination.

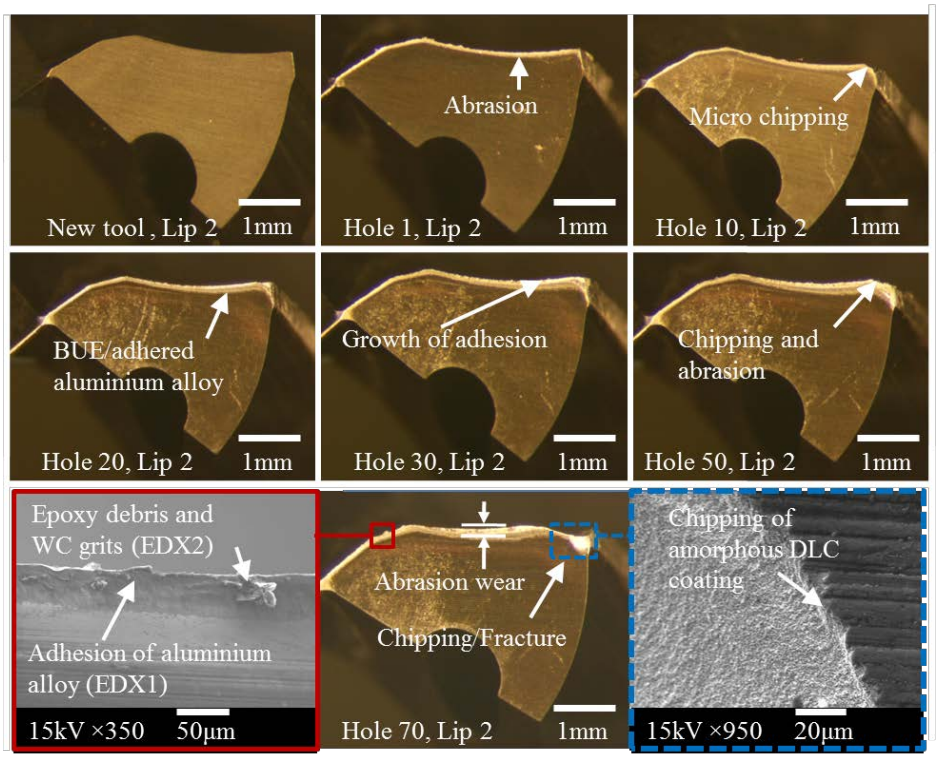


Figure 4.37 Micrographs of drill wear progression in Test 1

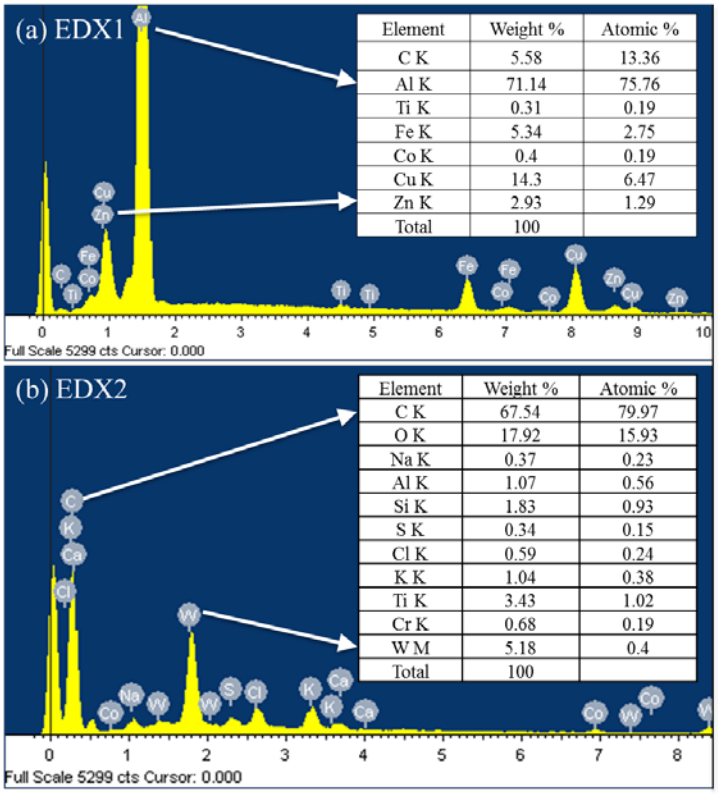


Figure 4.38 EDX examination of adhered material on drill in Test 1

When feed rate was increased to 0.15mm/rev, the wear rate of the DLC coated drill used in Test 3 accelerated considerably with an average flank wear after 70 holes measuring ~255µm. In contrast to Test 1, both abrasion and adhesive wear mechanisms were apparent

immediately after commencement of the experiment, see Figure 4.39. The build-up of Al workpiece material initially concentrated at the chisel edge region but subsequently extended over the cutting lips and peripheral corners as machining progressed. Wear on the drill flank face and adhered material increased steadily and corresponded with the rapid rise of thrust force and torque detailed previously in Figure 4.35 and 4.36 respectively. Signs of micro chipping on the cutting lips at the drill corner were prominent after 50 holes, which was partly due to the relatively high thrust force in the Ti section that reached ~1800N. Several reasons were thought to be responsible for the tool failure after 70 holes, not least the cyclic variation of thrust forces acting as the drill travelled through the stack (maximum of ~2500N in Ti and minimum of ~500N in CFRP layer over ~3 second duration), which may have induced a low cycle fatigue condition which triggered brittle fracture [203]. Subsequent SEM evaluation of the fractured area revealed the presence of coalescent voids near the rake surface together with striations indicative of fatigue failure from cyclic loading, see Figure 4.39. The fine band structure of the latter propagating through the tungsten carbide matrix is characteristic of a brittle fracture mechanism [203].

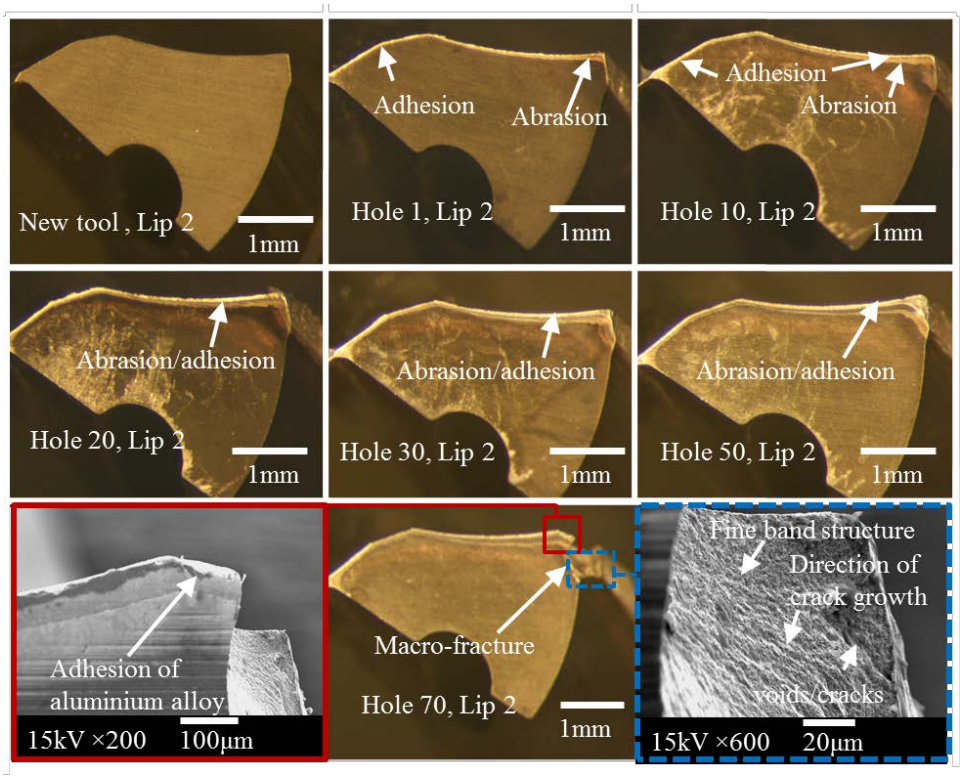


Figure 4.39 Micrographs of drill wear progression in Test 3

Figure 4.40 details wear progression of the CVD diamond coated drill utilised in Test 2. Adhesion of workpiece material on the cutting edge was visible after the first hole while flaking/peeling of the coating was observed after hole 20. Initial delamination of the diamond

coating was most acute at the chisel section due to the 120° point angle, which provided an area of stress concentration and was therefore subjected to a greater proportion of loading during machining. Subsequent failure of the CVD diamond layer was likely triggered by a critical accumulation of shear stress/strain at the bond interface caused by the dissimilar stiffness modulus between the coating (1000GPa) and drill substrate (580GPa) material. Despite extensive loss of the coating layer, there was no significant increase in thrust force and torque detected even after 50 holes. This suggests that successive wear of the drill from abrasion was gradual up until hole 70, where fracture of the chisel edge occurred. Further SEM analysis of the exposed carbide region highlighted the presence of micro-cracking at several locations on the worn cutting lips. However unlike experiments involving the DLC coated drills, the corners of the CVD diamond coated tool remained intact at test cessation, although traces of adhered Al material were prevalent.

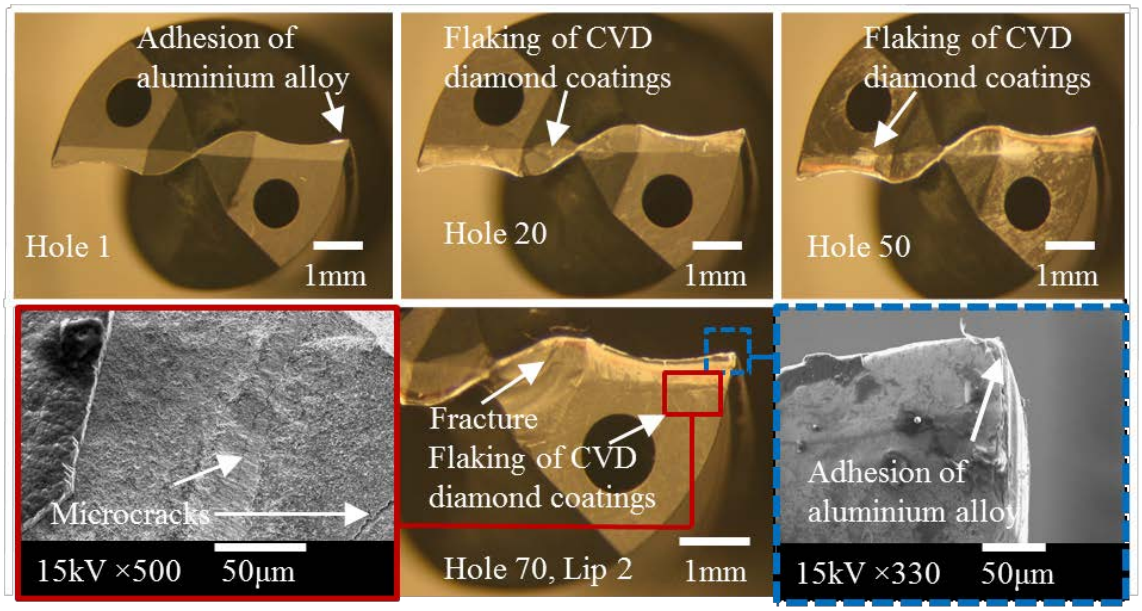


Figure 4.40 Micrographs of drill wear progression in Test 2

4.3.3 Hole accuracy

Figure 4.41(a) details the average diameter of the last hole drilled in each individual material layer and the overall stack for all tests. The CVD diamond coated drills produced the best results when operating at 0.08mm/rev feed rate, with measured diameters ranging from 6.34 to 6.40mm over the test duration of 70 holes. This was within the typical hole diameter tolerance of 6.38 ± 0.0375mm for aerospace applications. In contrast, holes machined with the DLC coated drills were marginally oversized particularly in the Ti section, with the overall diameter moving out of tolerance after 30 and 10 holes when employing feed rates of 0.08 and

0.15mm/rev respectively. The superior performance of the CVD coated drills was attributed to the two-stage point design, which provided the drill with improved 'self-centring' capability, thereby reducing tool deflection or run-out. Figure 4.41(b) shows average hole cylindricity over the entire stack together with corresponding out of roundness measurements for each of the individual Ti, CFRP and Al sections. The test undertaken with the DLC coated drill at 0.08mm/rev produced holes with an average cylindricity of 140.6µm while increasing the feed rate to 0.15mm/rev reduced this value to 77.4µm. Hole cylindricity further improved when utilising the CVD diamond coated tool at 0.08mm/rev, with an average recorded value of 65.7µm.

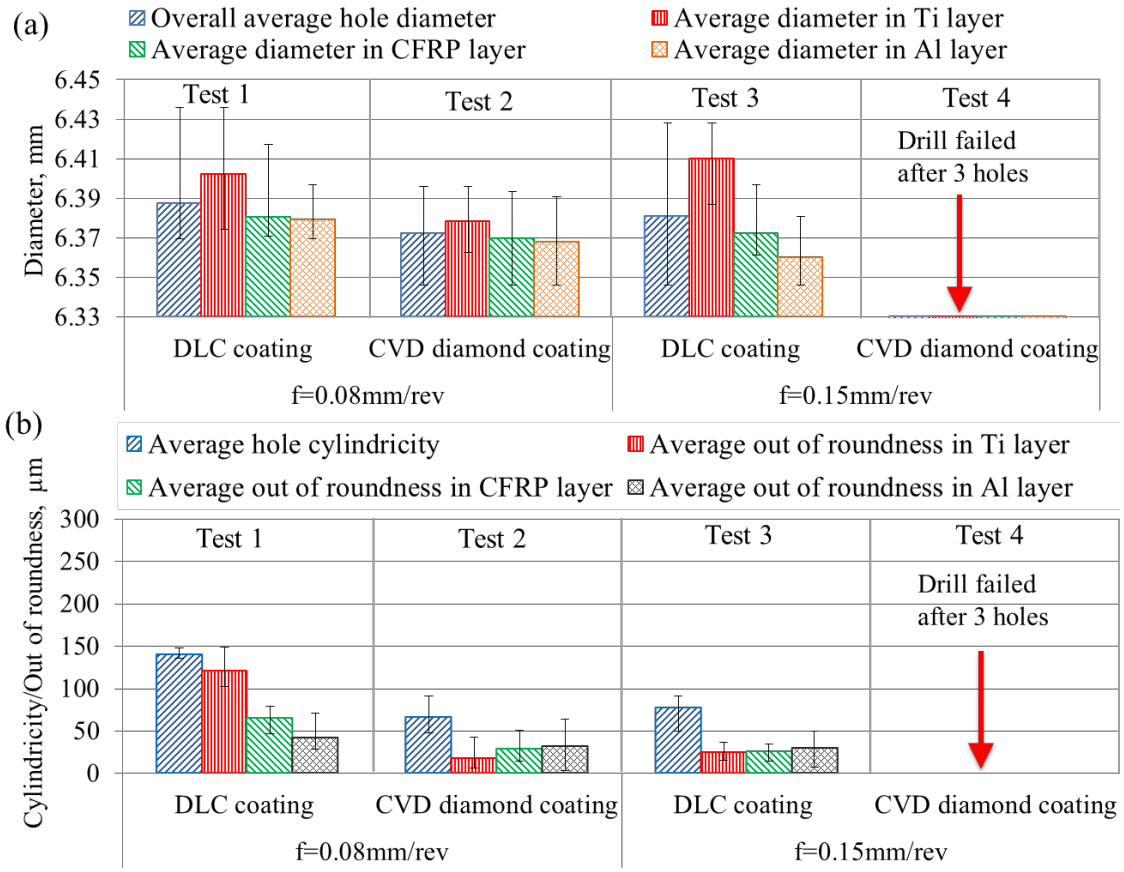


Figure 4.41 Average (a) hole cylindricity, (b) out of roundness over test duration

Figure 4.42 details the 3D hole profiles evaluated at hole 70 in Tests 1 to 3 respectively. The holes machined in Test 1 typically exhibited a 'tri-lobed' cross section, as shown in Figure 4.42(a). This suggests that low frequency vibration in the form of radial tool deflection previously discussed in Section 4.1.3 was probably induced when utilising the DLC coated drill under these conditions. This would also explain the comparatively high out of roundness levels (average of up to ~120µm in the Ti section) seen previously in Figure 4.41(b). When

employing the CVD diamond coated drill in Test 2, the average out of roundness did not exceed ~30µm in any of the material sections, which was reflected in the circular cross section of the hole illustrated in Figure 4.42(b). The hole profile however was tapered towards the exit location, as the tendency for drills to wander diminishes as it moves deeper into the stack [145]. Increasing the feed rate of the DLC coated drill to 0.15mm/rev in Test 3 resulted in similar hole roundness values as in Test 2, which were on average ~100% better compared to Test 1. In addition, the change in feed rate suppressed formation of the three-lobed profile; although a 'bell-mouth' shape at the top of the hole was prevalent, see Figure 4.42(c). This was possibly due to the greater wear/flattening of the chisel edge, which exacerbated 'wander' of the drill from the centre of the hole as it entered the stack.

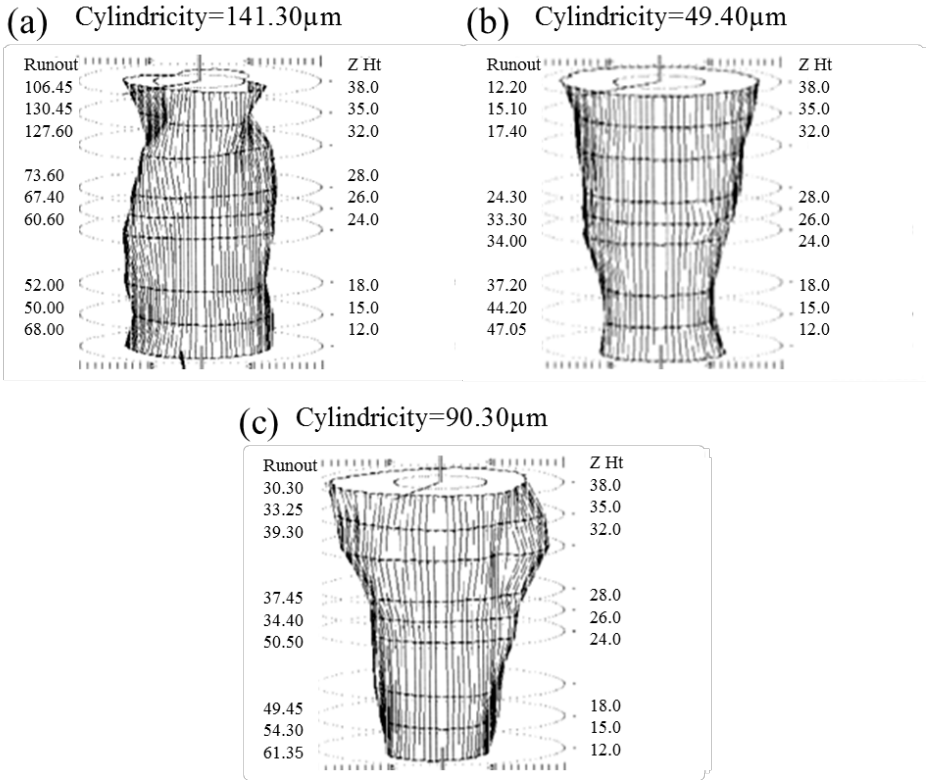


Figure 4.42 Hole cylindricity and profile at hole 70 in (a) Test 1, (b) Test 2 and (c) Test 3

4.3.4 Burr formation

The first holes produced using new drills were found to be virtually burr free in all tests irrespective of feed rate or point geometry/tool coating, with the onset of burr formation observed as machining progressed. Figure 4.43 details the maximum burr height measured at both the hole entry and exit locations in the Ti and Al layers over the duration of each trial. With the exception of hole exit on the Al sections in Test 1, burr height did not exceed ~0.11mm even at test cessation. In all cases, the burrs generated were classified as uniform

(Type II) [167], with cross sections similar to that shown in Figure 4.44. When operating at a feed rate of 0.08mm/rev, the maximum burr size at the exit position of the stack (Al layer) was over 4 times larger when using the DLC (0.38mm) compared to the CVD diamond coated drill (0.09mm). This was attributed to enlargement of the corner chamfers and greater wear of the cutting edge in the former due to chipping/fracture. The result was increased plastic deformation/ploughing of the aluminium workpiece material immediately prior to drill exit together with shifting of the pivot point away from the hole, leading to larger, elongated burrs [204]. Increasing feed rate to 0.15mm/rev in Test 3 significantly reduced burr height due to shorter contact time between the drill corner and workpiece material, which also promoted greater shearing/fracture of the chip. In contrast, relatively small burrs were observed at the hole exit and entry of the Ti and Al layers respectively in all of the holes evaluated. This was due to the CFRP plate acting to restrain the development and propagation of burrs [172].

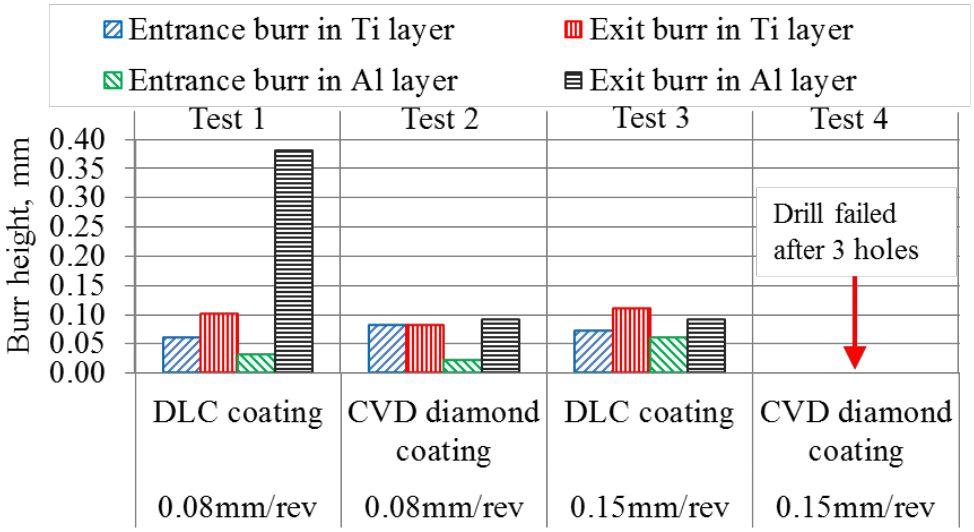


Figure 4.43 Maximum entrance and exit burr height in Ti and Al layers in all test

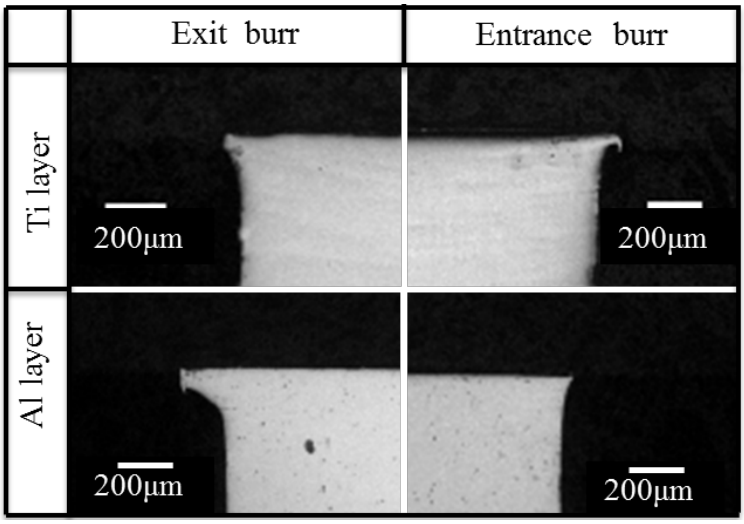


Figure 4.44 Micrographs of entrance and exit burrs in Ti and Al layers at hole 70 in Test 1

4.3.5 Hole surface roughness and topography

Figure 4.45 details the hole surface roughness (Ra and Rt) averaged over the trial duration for all tests. The mean surface roughness (Ra) ranged from 0.39-2.31µm, 0.50-3.67µm, 0.16-0.73µm in the Ti, CFRP and Al layers respectively, while the corresponding peak-to-valley roughness (Rt) were 7.40-23.58µm, 8.38-35.53µm, and 1.59-12.81µm. The maximum Rt recorded in the Ti and Al segments were found to be 4-6 times higher in comparison to hole surfaces produced using the TiAlN/TiN coated drills (~5.07µm and 2.05µm for the Ti and Al respectively) as detailed in Section 4.1.5. This was attributed to the more severe wear patterns of the diamond coated drills, which were characterised by chipping and fracture at the peripheral corners whilst the TiAlN/TiN drills generally failed by progressive abrasion wear. The trends however were reversed when considering the CFRP layer with surface roughness not exceeding 35.53µm Rt when utilising the diamond coated tools as opposed to surfaces produced using hardmetal coated drills having a maximum Rt of 77.69µm.

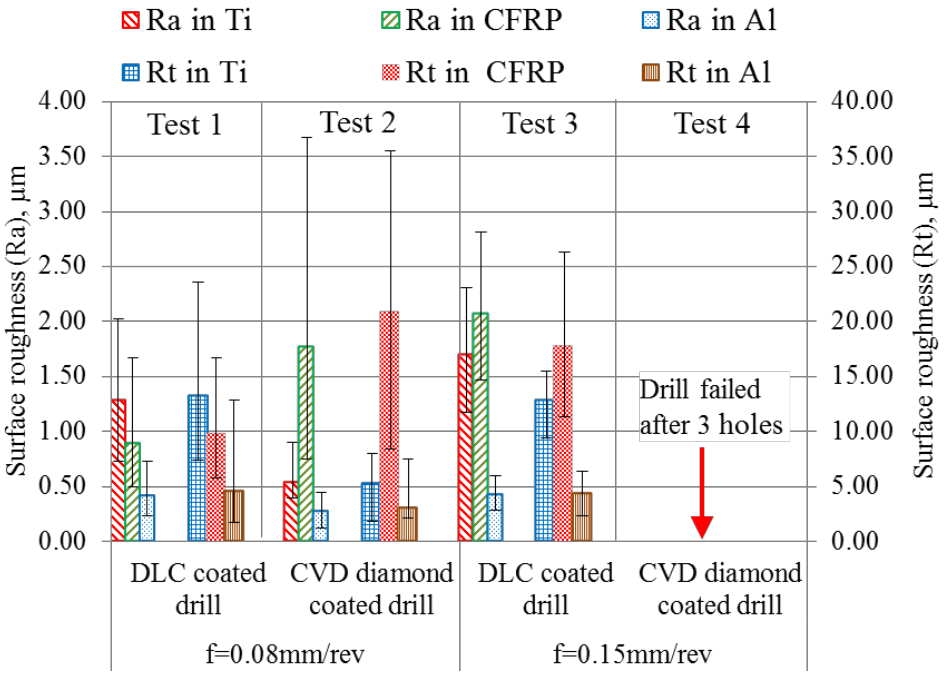


Figure 4.45 Hole surface roughness of Ra and Rt over test duration

Figure 4.46 shows the typical holes surfaces produced by the DLC and CVD coated drills in the Ti, CFRP and Al layers after 70 holes machined, at a feed rate of 0.05mm/rev in Test 1 and Test 2. High levels of material laps and scaling were prevalent on the Ti and Al surfaces generated using the DLC coated drill together with traces of resin matrix residue. This was not seen in the holes from Test 2 involving the CVD-diamond coted tools, with only scratches /feed marks and material side flow/chip rest visible, which reflects the lower surface

roughness measured as detailed in Figure 4.4.5. The CFRP surface however generally exhibited signs of matrix cracking irrespective of the drill wear modes.

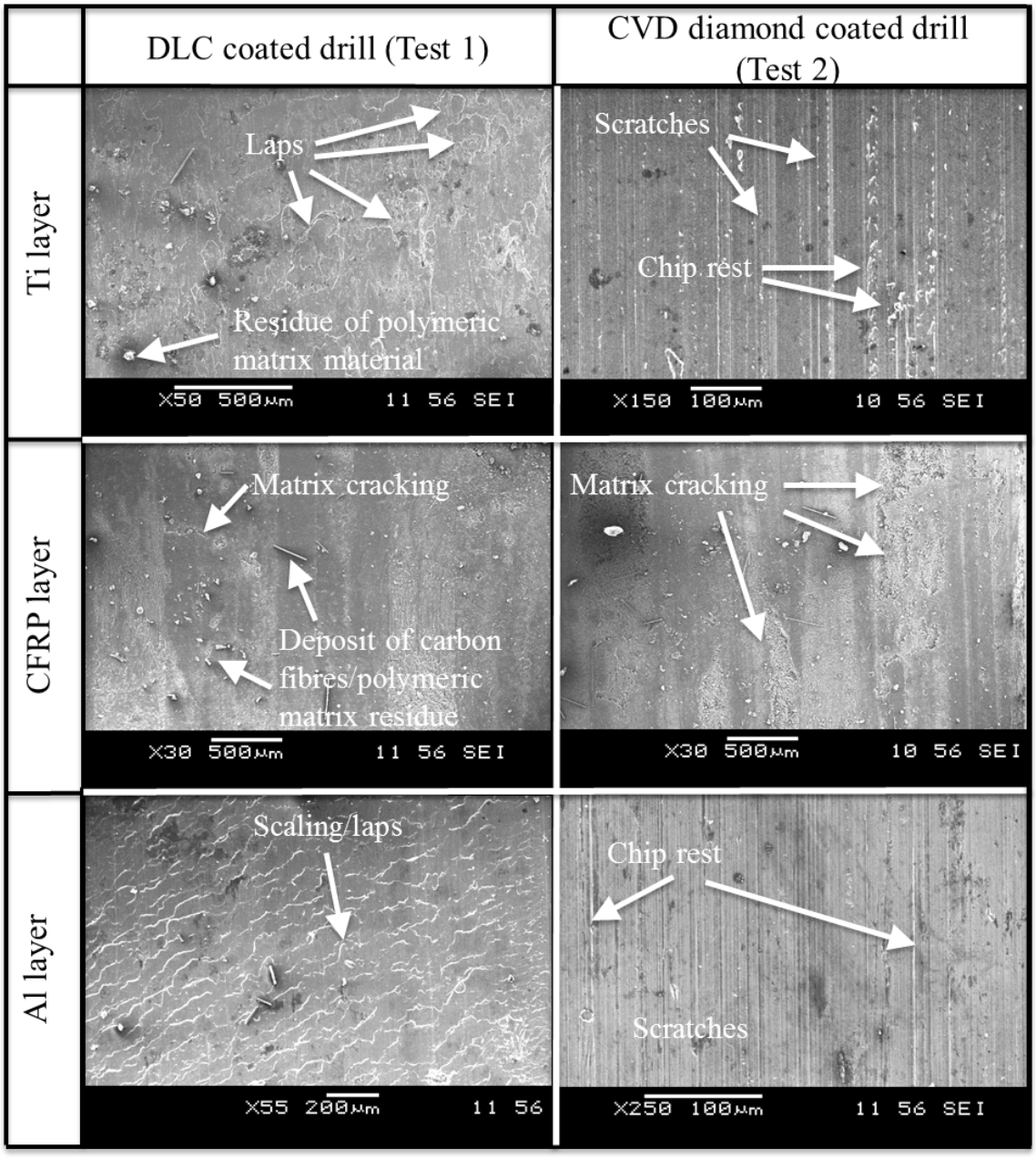


Figure 4.46 Micrographs of workpiece surfaces in Ti, CFRP and Al layers at hole 70

4.3.6 Microhardness

Figure 4.47 presents the microhardness depth profile plots in the titanium and aluminium layers for the last hole drilled in Tests 1-3. When using the DLC coated drill under a feed rate of 0.15mm/rev, mean microhardness in the Ti layer increased up to a maximum of $433HK_{0.025}$ at 20µm beneath the machined surface, which was ~18% higher than the bulk hardness value of the workpiece material. This was most likely due to strain hardening caused by the heavily

worn drills and high thrust forces of up to 2534N. The microhardness variations were similar when drilling at the lower feed rate of 0.08mm/rev with both the DLC and CVD diamond coated drills, although the degree of hardening was limited to ~8% above the bulk hardness. Conversely, there was negligible alteration in subsurface microhardness of the Al layers regardless of the tool coating or feed rate level employed.

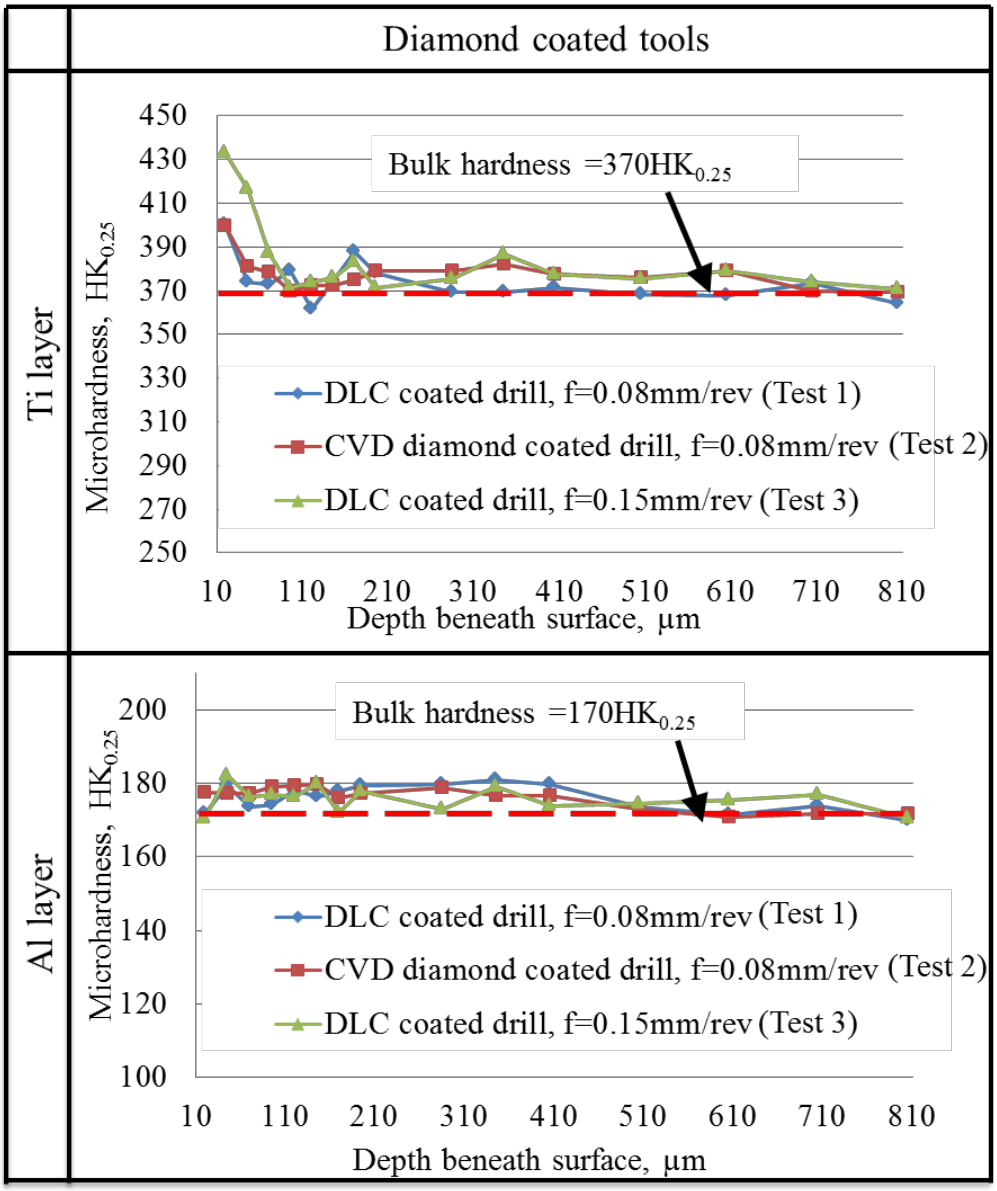


Figure 4.47 Microhardness depth profile measurement in the Ti and Al layers at the cessation of tests

4.4 Phase 1D: Effect of drill point geometry

4.4.1 Cutting force (thrust force and torque)

Figure 4.48 details the cutting forces measured at the 70th hole, which indicates that the thrust forces in the Ti, CFRP and Al sections varied between 964-1327N, 345-557N and 363-532N respectively depending on the drill geometry while corresponding torques were 266-387N-cm, 91-196N-cm and 112-295N-cm. Despite the main effects plot in Figure 4.49 suggesting a point angle of 140°, helix angle of 40° and chisel diameter of 0.10mm as the preferred combination for minimum thrust force in the Ti layer, none of the variables were found to have a significant effect (at the 5% level) on thrust force or torque in any of the material sections, as detailed by the ANOVA shown in Table 4.3. Nevertheless, helix angle was observed to have relatively high PCR's of 60-75% with respect to thrust force in all 3 segments of the stack.

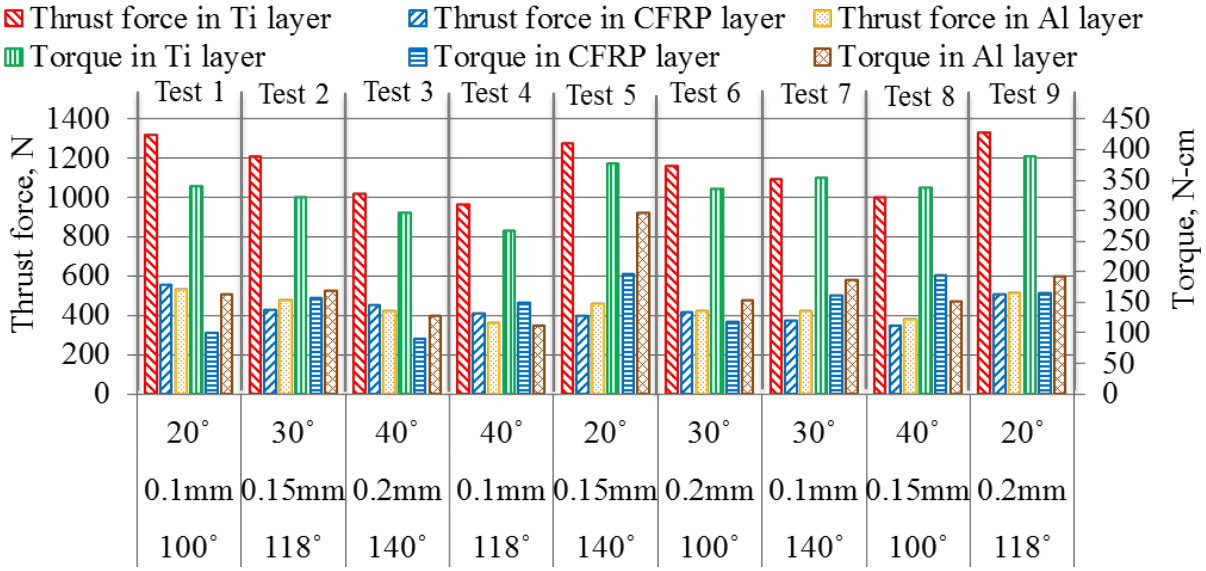


Figure 4.48 Thrust force and torque in L9 test array

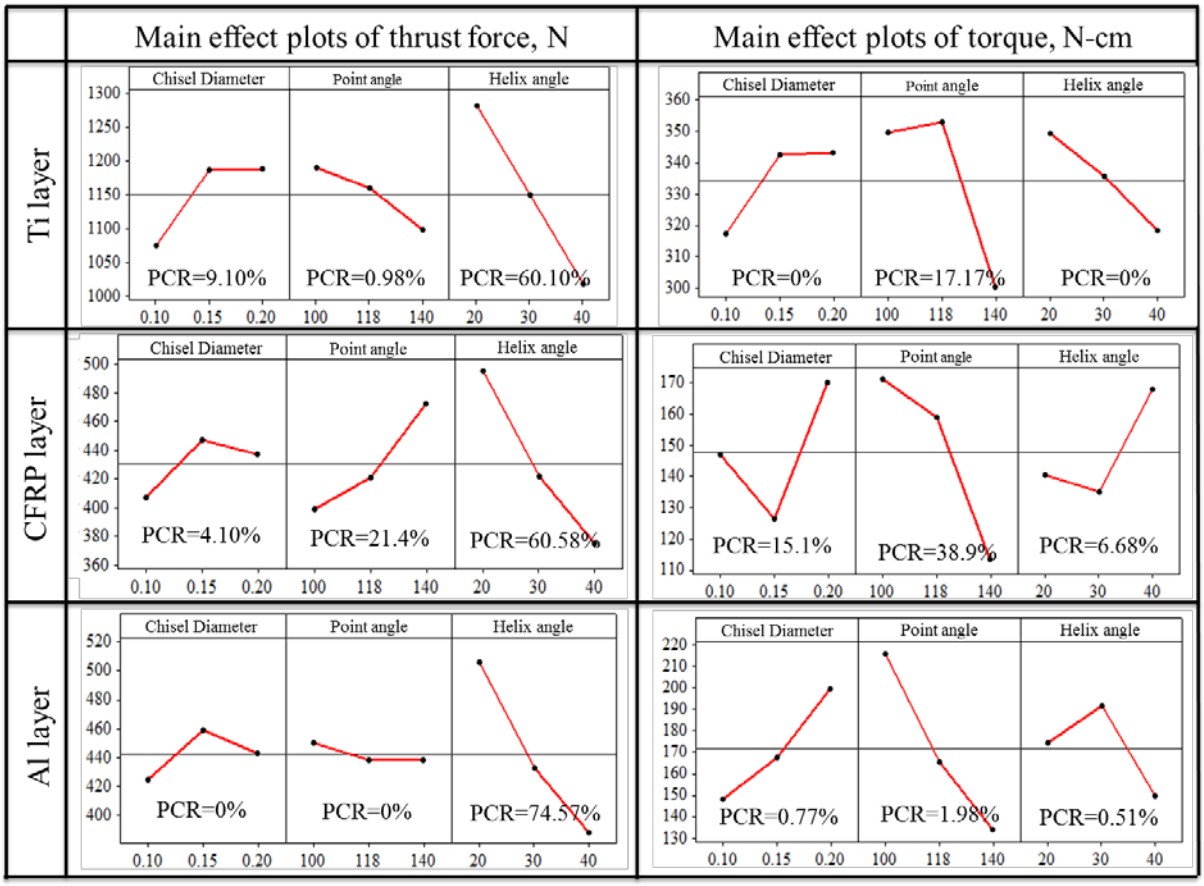


Figure 4.49 Main effect plots for thrust force and torque

	Thrust force					Torque			
	Ti layer					Ti layer			
Source of variances	D.F.	Seq S.S.	M.S.	P	PCR	Seq S.S.	M.S.	P	PCR
Chisel diameter	2	25552	12776	0.31	9.10%	1310.0	655.0	0.714	0.00%
Point angle	2	13014	6507	0.47	0.98%	5206.0	2603.0	0.386	17.17%
Helix angle	2	104254	52127	0.1	60.10%	1433.0	716.0	0.696	0.00%
Residual	2	11504	5752		29.82%	3278.0	1639.0		82.83%
Sums of squares		154325				11227.0			
	CFRP layer					CFRP layer			
Source of variances	D.F.	Seq S.S.	M.S.	P	PCR	Seq S.S.	M.S.	P	PCR
Chisel diameter	2	2603	1301.7	0.32	4.10%	2849	1424	0.283	15.10%
Point angle	2	8546	4273	0.12	21.40%	5564	2783	0.168	38.86%
Helix angle	2	22006	11003	0.05	60.58%	1887	943.7	0.373	6.68%
Residual	2	1194	597.4		13.92%	1124	562		39.36%
Sums of squares		34351				11425			
	Al layer					Al layer			
Source of variances	D.F.	Seq S.S.	M.S.	P	PCR	Seq S.S.	M.S.	P	PCR
Chisel diameter	2	1685.0	843.0	0.6	0.00%	4024.0	2012.0	0.6	0.00%
Point angle	2	271.0	135.0	0.9	0.00%	10309.0	5155.0	0.3	22.81%
Helix angle	2	20997.0	10499.0	0.1	74.57%	2681.0	1340.0	0.7	0.00%
Residual	2	2223.0	1112.0		25.43%	5234.0	2617.0		77.19%
Sums of squares		25176.0				22248.0			

(Significant at 5% level, Fcal 2,2=19)

Table 4.3 ANOVA table for thrust force and torque

When benchmarked against results (in Section 4.1.1) involving the commercial T-type uncoated carbide drill (point angle of 140˚, helix angle of 30˚, chisel edge of 0.35mm) operating at 0.08mm/rev, the bespoke design with a thinned web (chisel diameter of 0.1mm) in Test 7 showed a reduction in thrust forces of up to 28% (1156 vs. 1600N), 47% (390 vs. 791N) and 22% (410 vs. 529N) in the Ti, CFRP and Al layers respectively, see Figures 4.2 and 4.48. This was attributed to the higher positive rake angle and larger chip evacuation area of the latter.

4.4.2 Tool wear and tool life

Figure 4.50 details the progression of the tool flank wear against the number of holes drilled in all tests. All of the drills reached the end of test criterion of 90 holes with corresponding flank wear levels varying between 65-94µm. While the main effects plot in Figure 4.51 indicated that a point angle, helix angle and chisel diameter of 118°, 40° and 0.2mm respectively was recommended for minimising tool wear, none of the factors were statistically significant at the 5% level as detailed in the ANOVA in Table 4.4. Flank wear was seen to rise rapidly within the first 10 holes for all drills (VB of 32-55µm) with further increases relatively gradual until test cessation.

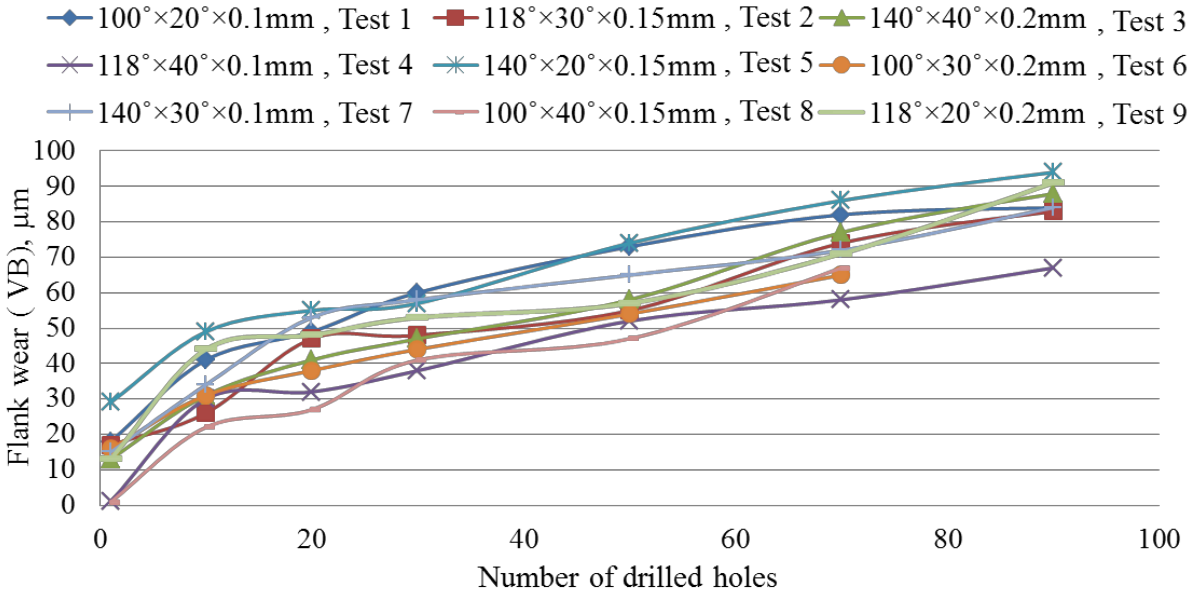


Figure 4.50 Progression of tool wear in L9 test array

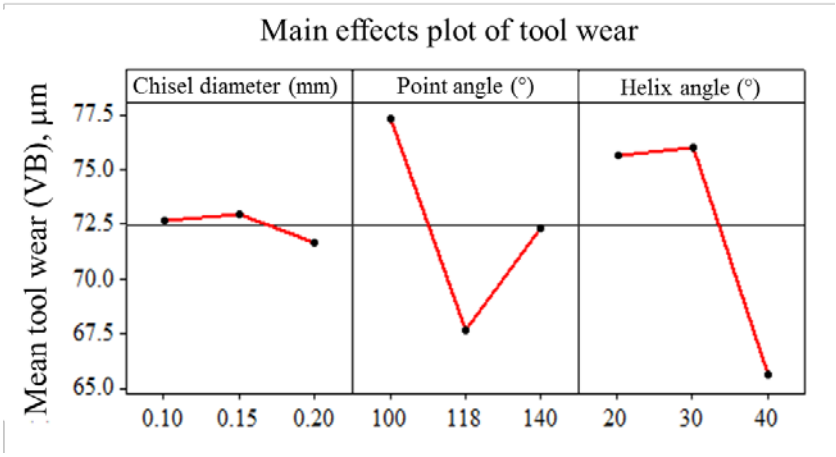


Figure 4.51 Main effects plot for tool wear

Tool wear	Average in overall stack					
Source of variances	D.F.	Seq S.S.	M.S.	F	P	PCR
Chisel diameter	2.0	2.9	1.4	0.01	0.988	0.0
Point angle	2.0	140.2	70.1	0.57	0.635	0.0
Helix angle	2.0	206.9	103.4	0.85	0.541	0.0
Residual	2.0	244.2	122.1			100.0
Sum of square variances		594.2				

(* Significant at the 5% level, $F_{cal\ 2,2}$ =19)

Table 4.4 ANOVA table for tool wear

Figure 4.52 shows optical micrographs of drill wear progression in Test 4 (point angle of 118˚, helix angle of 40˚ and chisel diameter of 0.1mm), which produced the lowest flank wear level after 90 holes. Adhesion of Al workpiece material together with BUE was predominant within the first 20-30 holes, particularly along the cutting edge closer to the chisel section due to the lower cutting speed nearer the centre of the drill. Growth of abrasion wear was prevalent towards the outer periphery of the tool, eventually leading to chipping/minor fracture at the drill corner. The maximum flank wear at test cessation was 46% less than the corresponding value observed on the tool in Test 5, which had a 140˚ point angle, 20˚ helix angle and 0.2mm chisel diameter. The variation in point geometry led to a difference in effective radial rake angle 26.7˚ and 7.5˚ for the drills in Test 4 and Test 5 respectively, which appeared to be a significant element for reducing thrust forces in the former by up to 30%.

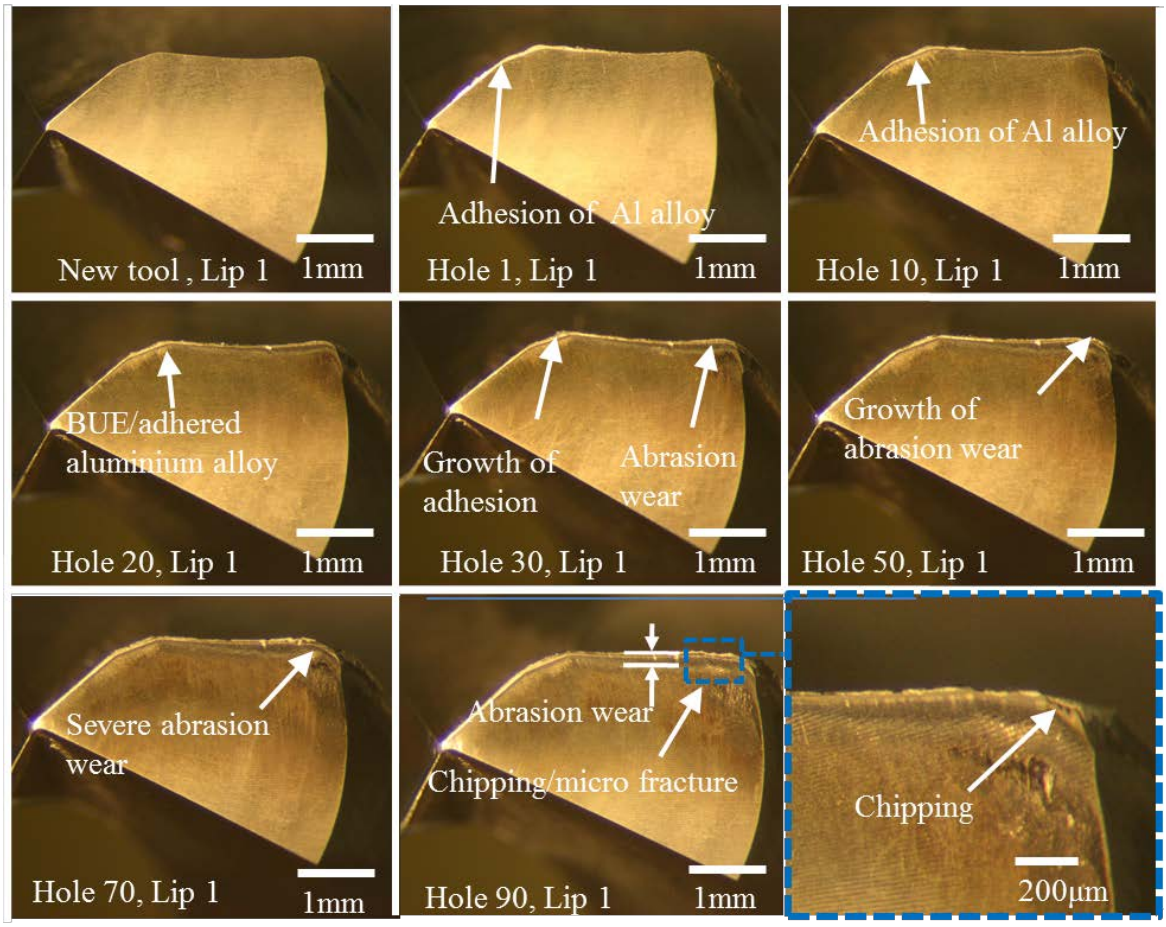


Figure 4.52 Micrographs of drill wear progression in Test 4

4.4.3 Hole accuracy (diameter, out of roundness and cylindricity)

Figure 4.53 details the average hole diameters produced over the duration of each test, which ranged from 6.302mm to 6.443mm. The drill with a 140° point angle, 40° helix angle and 0.2mm chisel diameter produced holes with the least deviation from the nominal diameter with average values of 6.362, 6.353 and 6.365mm in the Ti, CFRP and Al layers respectively. The relatively low standard variance of 0.00826, 0.00240 and 0.00983 suggests a very small spread/distribution of the data.

Table 4.5 shows the ANOVA for hole diameter, where helix angle and chisel diameter were statistically significant factors in the Ti layer with PCR's of 60.8% and 22.88% respectively. Drills with a higher helix angle (40˚) typically produced larger diameter holes, which corresponded to a longer spiral flute length and hence relatively lower drill rigidity during operation. Such drills were therefore more prone to vibrations/deflection and consequently enlarged hole diameters, as the applied thrust forces on the drill point acted to 'unwind' the spiral flutes [155]. Similarly for the CFRP layer, the helix angle had a significant influence on hole diameter with a PCR of 50.1%, albeit with diameters increasing

at the lower helix angle (20˚). This was due to higher axial forces between the drill peripheral margin and machined surface when utilising tools with larger helix angles, leading to fibre pullout resulting in smaller hole diameters compared to those produced using low helix angle drills. In contrast, none of the variable factors were significant with regard to hole diameter in the Al layer.

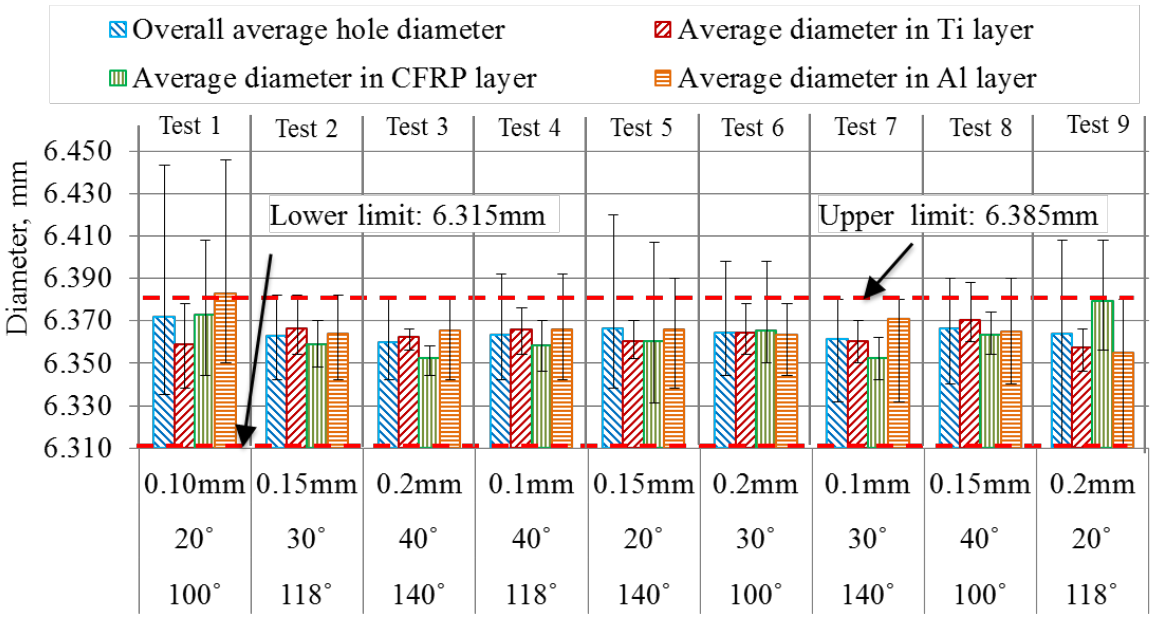


Figure 4.53 Average hole diameter over test duration

Diameter	Ti layer					
Source of variances	D.F.	Seq S.S.	M.S.	F	P	PCR
Chisel diameter	2	0.00003	0.00002	23.16*	0.041	22.88%
Point angle	2	0.00002	0.00001	12.85	0.072	12.23%
Helix angle	2	0.00008	0.00004	59.86*	0.016	60.77%
Residual	2	0.00000	0.00000			4.12%
Sum of square variances		0.00013				
Diameter	CFRP layer					
Source of variances	D.F.	Seq S.S.	M.S.	F	P	PCR
Chisel diameter	2	0.00004	0.00002	1.37	0.422	1.03%
Point angle	2	0.00038	0.00019	14.58	0.064	37.73%
Helix angle	2	0.00049	0.00025	19.04*	0.050	50.12%
Residual	2	0.00003	0.00001			11.12%
Sum of square variances		0.00094				
Diameter	Al layer					
Source of variances	D.F.	Seq S.S.	M.S.	F	P	PCR
Chisel diameter	2	0.00023	0.00011	2.67	0.272	31.87%
Point angle	2	0.00012	0.00006	1.43	0.411	8.31%
Helix angle	2	0.00001	0.00000	0.11	0.903	17.14%
Residual	2	0.00008	0.00004			42.68%
Sum of square variances		0.00044				

(* Significant at the 5% level, $F_{cal\ 2,2}$ =19)

Table 4.5 ANOVA table for hole diameter

Figure 4.54 details the average hole out of roundness in each material layer of the stack together with the overall cylindricity values for all trials over the entire test duration. The former were recorded of ~24µm, ~30µm and ~27µm in the Ti, CFRP and Al layers respectively whereas the latter ranged 52-138µm in average. An analysis of the data suggests that the drill in Test 3 with a 140° point angle, 40° helix angle and 0.2mm chisel diameter showed the best performance, which produced holes with the lowest out of roundness and cylindricity as well as the least variation from the recorded mean value. The corresponding ANOVA calculations for hole cylindricity and out of roundness shown in Table 4.6 however indicated that none of the factors were statistically significant with respect to both parameters. None of the operated drill geometries dominated the variation of roundness and hole cylindricity, yet the feed rate, cutting speed and drilling strategy might present a statistical significance.

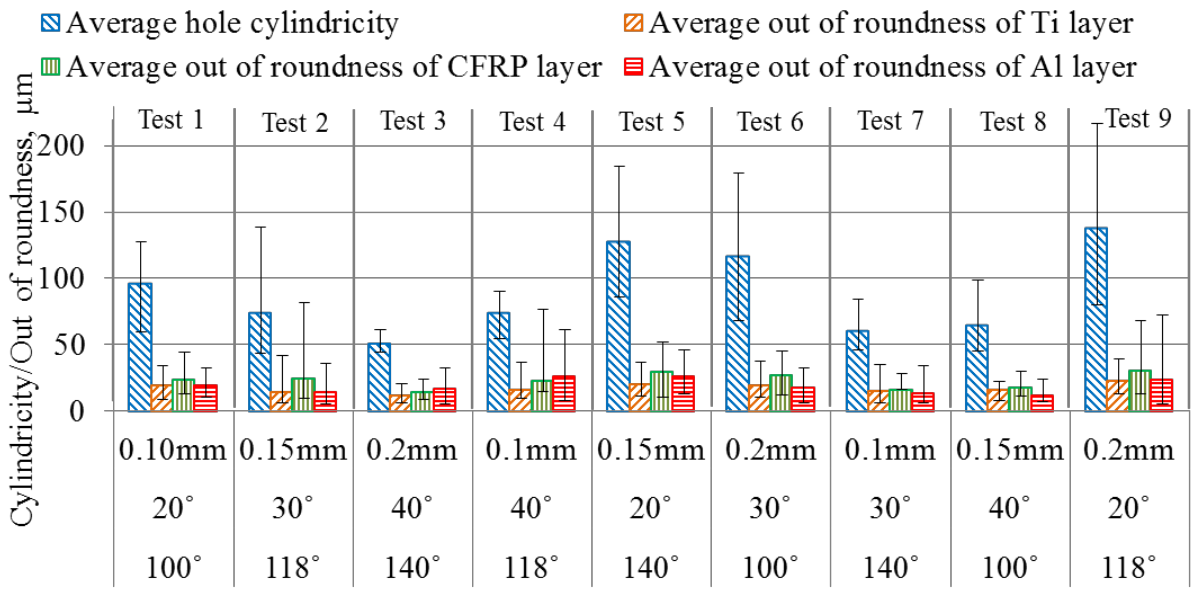


Figure 4.54 Average hole cylindricity and out of roundness over test duration

Hole cylindricity	Overall stack					
Source of variances	D.F.	Seq S.S.	M.S.	F	P	PCR
Chisel diameter	2	949.2	474.6	0.60	0.624	0.00%
Point angle	2	412.9	206.4	0.26	0.792	0.00%
Helix angle	2	5043.0	2521.5	3.21	0.238	43.50%
Residual	2	1572.6	786.3			56.5%
Sum of square variances		7977.6				
Out of roundness	Ti layer					
Source of variances	D.F.	Seq S.S.	M.S.	F	P	PCR
Chisel diameter	2	3.0	1.5	0.18	0.844	0.00%
Point angle	2	11.8	5.9	0.73	0.578	0.00%
Helix angle	2	62.3	31.1	3.83	0.207	49.31%
Residual	2	16.2	8.1			50.68%
Sum of square variances		93.3				
Out of roundness	CFRP layer					
Source of variances	D.F.	Seq S.S.	M.S.	F	P	PCR
Chisel diameter	2	20.74	10.37	0.33	0.753	0.00%
Point angle	2	54.96	27.48	0.87	0.535	0.00%
Helix angle	2	139.18	69.59	2.20	0.313	27.29%
Residual	2	63.27	31.64			72.71%
Sum of square variances		278.16				
Out of roundness	Al layer					
Source of variances	D.F.	Seq S.S.	M.S.	F	P	PCR
Chisel diameter	2	6.4	3.2	0.07	0.934	0.00%
Point angle	2	35.1	17.6	0.38	0.722	0.00%
Helix angle	2	106.7	53.3	1.17	0.461	6.39%
Residual	2	91.4	45.7			93.61%
Sum of square variances		239.6				

(* Significant at the 5% level, Fcal 2,2 =19)

Table 4.6 ANOVA table for average hole cylindricity and out of roundness

4.4.4 Burr formation

Figure 4.55 shows the measured entrance and exit burr height for both the Ti and Al sections at test cessation in all tests. The burrs were typically larger at the exit position with a maximum of 0.27mm and 2.27mm compared to 0.24mm and 0.1mm at the hole entrance in the Ti and Al layers respectively. The smaller exit and entrance burrs at the Ti and Al sections respectively, were both due to the presence of the CFRP laminate, which acted to suppress/resist material flow at the interface. The prevailing burr morphology at the hole entrance and exit in the Ti and Al layers were uniform Type II burrs; however various types of exit burrs were observed in the Al layers including crown, transient and uniform burrs with and without caps as shown in Figure 4.56.

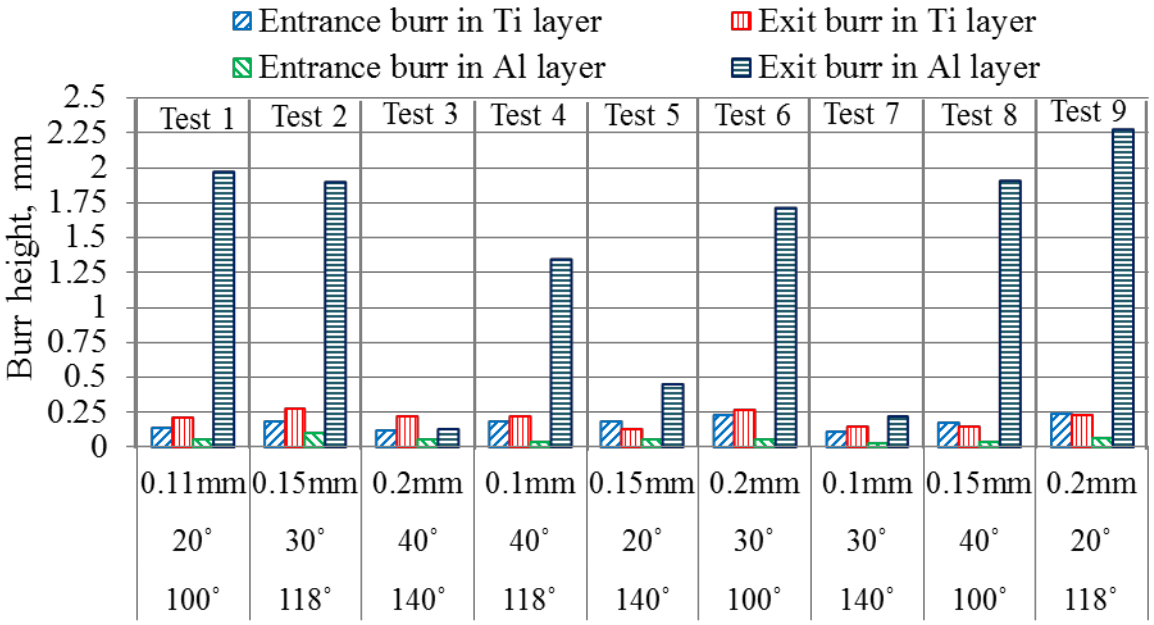


Figure 4.55 Maximum entrance and exit burr heights in Ti and Al layers

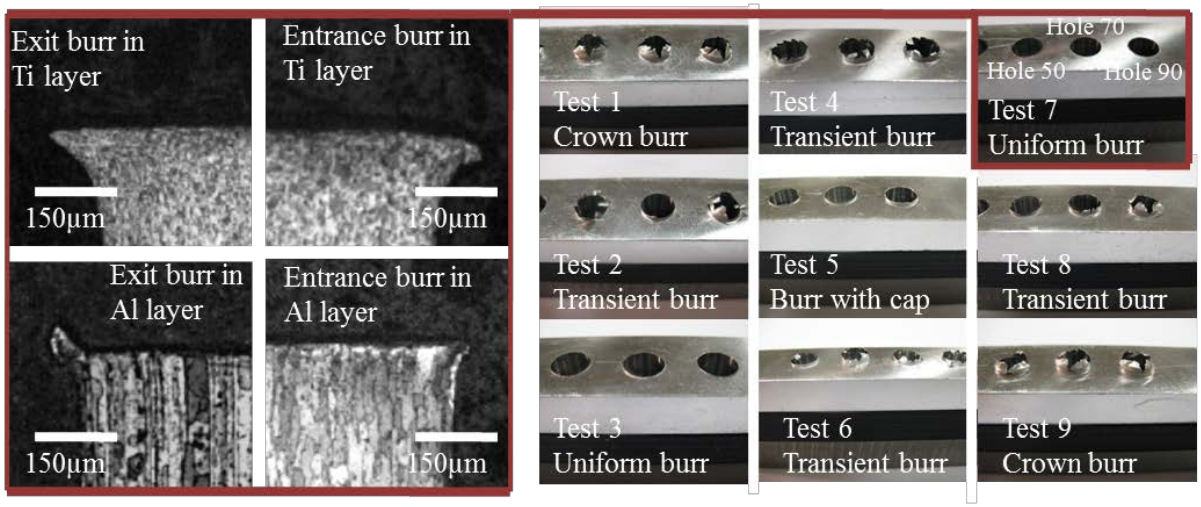


Figure 4.56 Exit burr form for hole 50, 70, 90 in Al layers

Figure 4.57 shows the main effects plots for entrance and exit burr height in the Ti and Al layers respectively. Although variation in chisel diameter and point angle appeared to have a moderate influence on hole entrance burr height in the Ti layer, the associated ANOVA calculations shown in Table 4.7 indicated that none of the factors were significant at the 5% level. Conversely, point angle was found to have a substantial effect on the exit burr size in the Al layer, with a PCR of 85.2%. The SEM micrographs of the burrs generated at the entrance and exit of the last hole drilled in the Ti and Al layers from Test 7 shown in Figure 4.56, also suggests that burr size was minimised when employing a drill with point geometry of 0.1mm chisel diameter, 140˚ point angle and 40˚ helix angle.

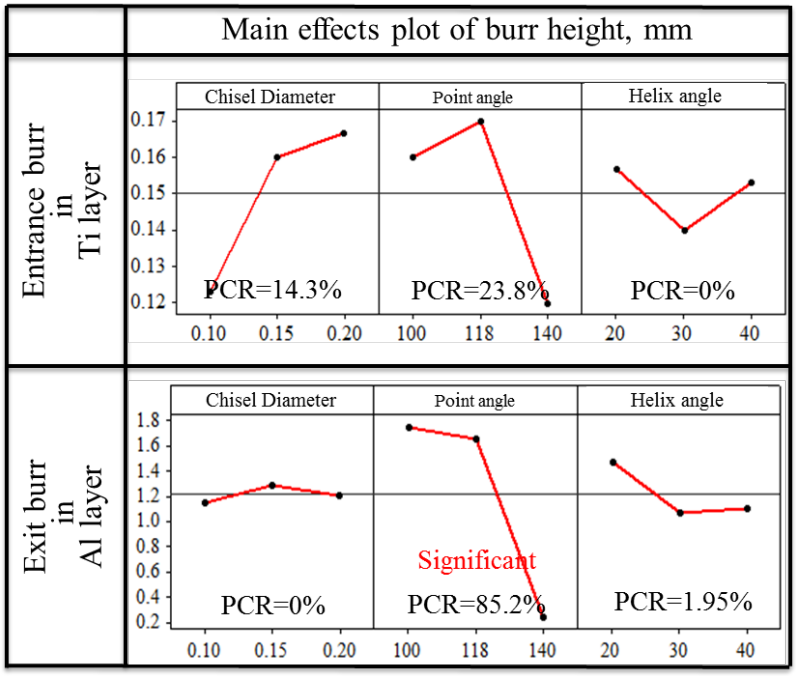


Figure 4.57 Main effects plot for burr height

Entrance burr height	Ti layer					
Source of variances	D.F.	Seq S.S.	M.S.	F	P	PCR
Chisel diameter	2	0.00327	0.00163	1.75	0.364	14.33%
Point angle	2	0.00420	0.00210	2.25	0.308	23.82%
Helix angle	2	0.00047	0.00023	0.25	0.800	0.00%
Residual	2	0.00187	0.00093			61.85%
Sum of square variances		0.00980				
Exit burr height	Al layer					
Source of variances	D.F.	Seq S.S.	M.S.	F	P	PCR
Chisel diameter	2	0.02816	0.01408	0.14	0.876	0.00%
Point angle	2	4.32416	2.16208	21.82*	0.044	85.19%
Helix angle	2	0.29269	0.14634	1.48	0.404	1.95%
Residual	2	0.19816	0.09908			12.86%
Sum of square variances		4.84316				

(* Significant at the 5% level, F cal 2,2 =19)

Table 4.7 ANOVA table of burr height in Ti and Al layers

The results generally show that drills with larger point and helix angles produced smaller burrs at both hole entrance and the exit positions, which was in line with research reported by Ko and Lee [171]. It was suggested that a smaller point angle exerted larger strains at the drill point regardless of thrust force and tool wear. As the drill advanced, the material failure zone was concentrated at the centre of the hole, which resulted in a crown burr as seen in Figure 4.56 (Test 9). With larger point angles, the strain is balanced between the centre and periphery of the hole leading to the formation of uniform burrs detailed in Figure 4.56 (Test 3 and Test 7).

4.4.5 Workpiece surface roughness and microhardness

Figure 4.58 presents the average surface roughness (Ra) in the Ti, CFRP and Al layers at the last hole drilled for all tests. In general, the roughness (Ra) in the metallic sections did not exceed 2µm Ra whilst a maximum of 13.55µm was recorded in the CFRP layers.

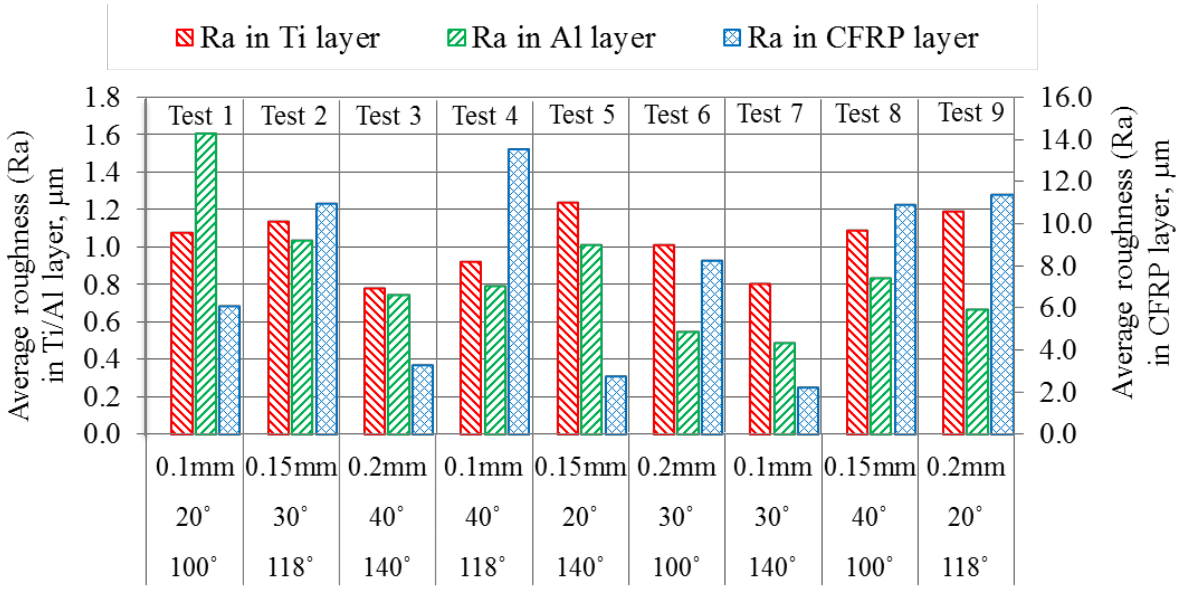


Figure 4.58 Average roughness in Ti, CFRP and Al layers

The ANOVA for workpiece surface roughness (Ra) in Table 4.8 showed that the helix angle was statistically significant at the 5% level with a PCR of 42.66% when drilling the Ti layer. In contrast, the point angle was the dominant factor influencing Ra in the CFRP section with a high PCR of 86.26%. However, none of the variables was significant with respect to hole surface roughness in the Al layers. Fundamentally, surface roughness when drilling is dominated by feed rate per revolution and nose radius at the intersection of the cutting lips and drill corner. The former determines the distance between peaks of the surface profile whereas the latter influences the amount of rubbing and plastic deformation on the machined surface. For drills having a high helix angle, the cutting mechanism and subsequent chip evacuation is generally more efficient, leading to a reduction in tool-workpiece rubbing and improvement in surface roughness. When considering tools with the highest helix angle of 40˚ in Test 3, Test 4 and Test 8, the drill in Test 3 with a point angle produced the lowest surface roughness (Ra) of 0.78µm in the Ti layer, compared to 0.92µm and 1.02µm obtained with those in Test 4 (118°) and Test 8 (100°) respectively. This was attributed to the combination of smallest cutting nose angle (110°) and rake angle (41.7°) at the peripheral corner, which increased rubbing between the drill peripheral corners and machined surface.

Surface roughness (Ra)	Ti layer					
Source of variances	D.F.	Seq S.S.	M.S.	F	P	PCR
Chisel diameter	2	0.07738	0.03869	16.06	0.059	33.86%
Point angle	2	0.03586	0.01793	7.44	0.118	14.49%
Helix angle	2	0.09624	0.04812	19.98*	0.048	42.66%
Residual	2	0.00482	0.00241			8.99%
Sum of square variances		0.21430				
Surface roughness (Ra)	CFRP layer					
Source of variances	D.F.	Seq S.S.	M.S.	F	P	PCR
Chisel diameter	2	1.34300	0.67100	0.34	0.747	0.00%
Point angle	2	130.38500	65.19200	32.81*	0.030	86.26%
Helix angle	2	10.84900	5.42500	2.73	0.268	4.69%
Residual	2	3.97300	1.98700			9.05%
Sum of square variances		146.55000				
Surface roughness (Ra)	A7050 layer					
Source of variances	D.F.	Seq S.S.	M.S.	F	P	PCR
Chisel diameter	2	0.01915	0.09580	0.54	0.649	0.00%
Point angle	2	0.09460	0.04730	0.27	0.789	0.00%
Helix angle	2	0.27260	0.13630	0.77	0.565	0.00%
Residual	2	0.35370	0.17680			100.00%
Sum of square variances		0.91240				

(* Significant at the 5% level, F cal 2,2 =19)

Table 4.8 ANOVA table of hole surface roughness (Ra) in Ti and Al layers

Figure 4.59 shows the typical hole surfaces in the Ti layer at the cessation of all tests. In Test 1 (100° point angle, 20° helix angle and 0.1mm chisel diameter), sporadic laps and adhesion of titanium chips was evident on the drilled surface. This was attributed to the tri-lobed form of the hole, which likely induced chatter and low frequency vibrations during drilling. Heavy scoring, feed marks and instances of chip rest/side flow or adhesion chips were observed in the majority of tests resulting in elevation of surface roughness values. Surfaces generated in Test 3 and Test 7 employing drills with a 140° point angle showed the least defects and lowest surface roughness level (<0.8µm Ra). This was probably due to the shorter cutting lip (from the larger point angle), which reduced the chatter and vibration as well as the increase in rubbing resulting from the smaller cutting nose angle (110°).

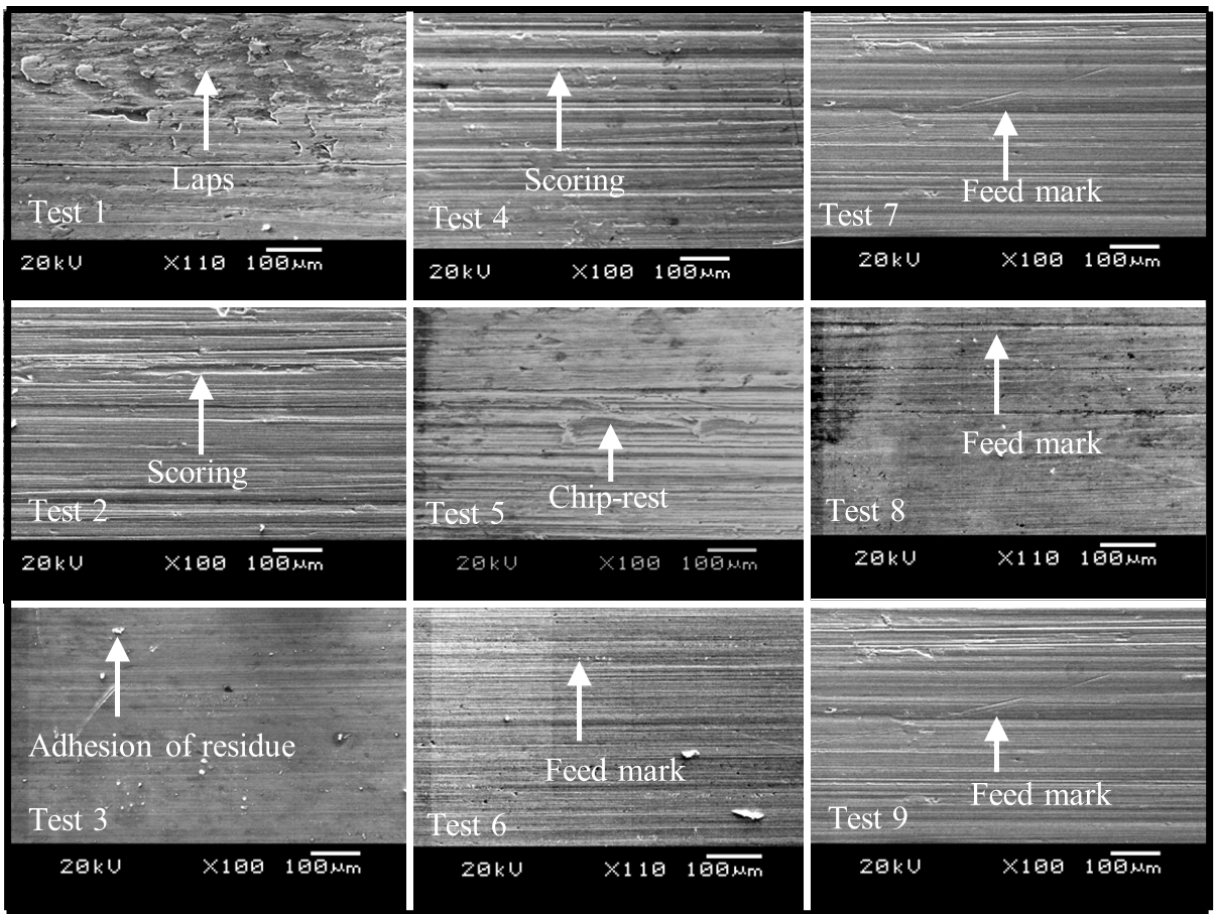


Figure 4.59 Micrographs of hole surface texture in Ti layers

When drilling CFRP materials, the cutting edge condition is a key factor affecting surface quality. Figure 4.60 shows SEM micrographs of the machined CFRP surfaces at hole 90 for all tests. Matrix cracking and fibre loss/pullout was prevalent in the majority of surfaces evaluated due to wear of the drills. Experiments involving tools with the largest point angle of 140° in Tests 3 and 7 exhibited minimum surface damage with matrix smearing seen as the principal defect. The results demonstrate the significant influence of point angle on surface roughness as indicated by the statistical analysis (ANOVA) discussed previously.

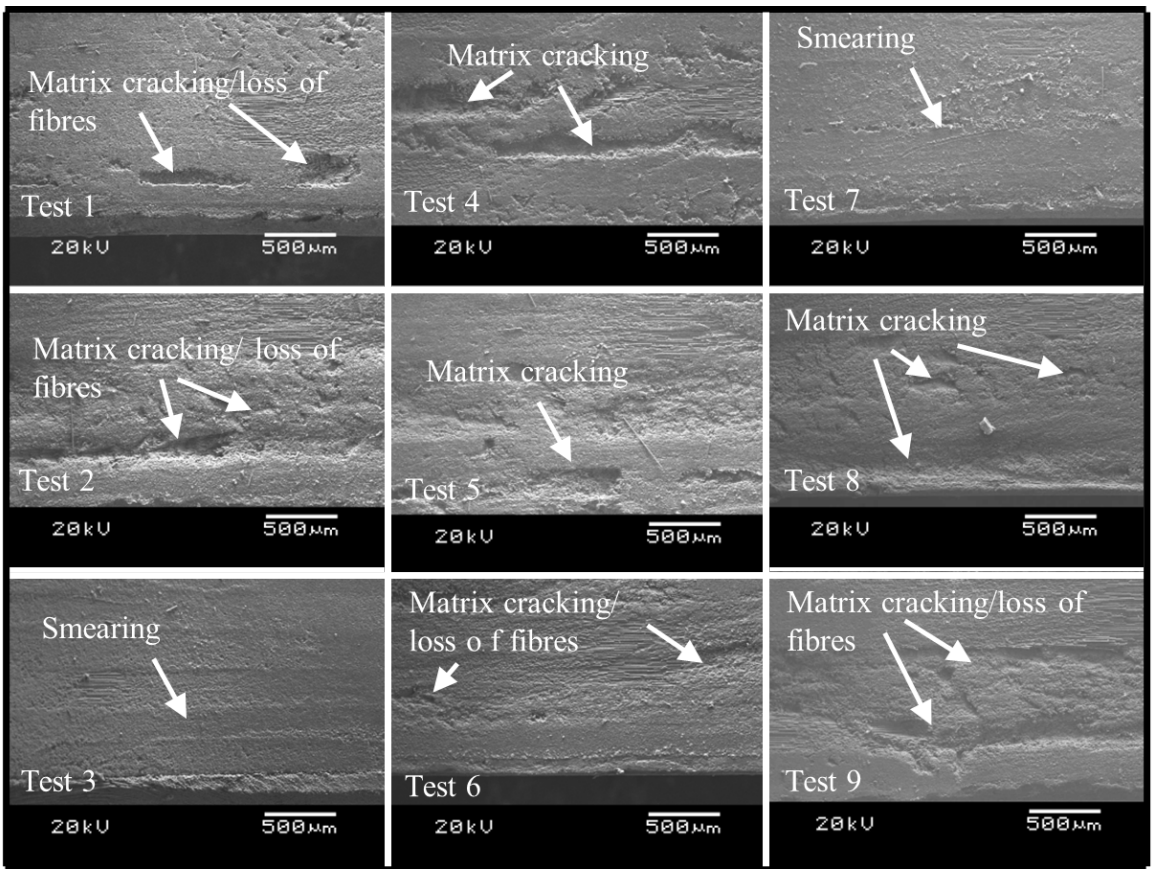


Figure 4.60 Micrographs of hole surface texture in CFRP layers

Although the ANOVA indicated that none of the factors were statistically significant with respect to hole surface roughness in the Al section, surfaces machined with drills having the highest point angle in Test 3 and 7 exhibited the least amount of flaws as observed from the SEM micrographs shown in Figure 4.61. In contrast, extensive workpiece adhesion together with the presence of laps and micro-cracks were evident in specimens from Tests 4, 8 and 9, although average surface roughness did not exceed ~0.9µm Ra as shown in Figure 4.58. The defects were most likely caused by fracture of the drill cutting lip prior to test cessation. In addition, heavy scoring/feed marks were apparent on workpiece surfaces from Tests 1, 2 and 5, which resulted in elevated roughness values ranging from ~1.0 - 1.6µm Ra.

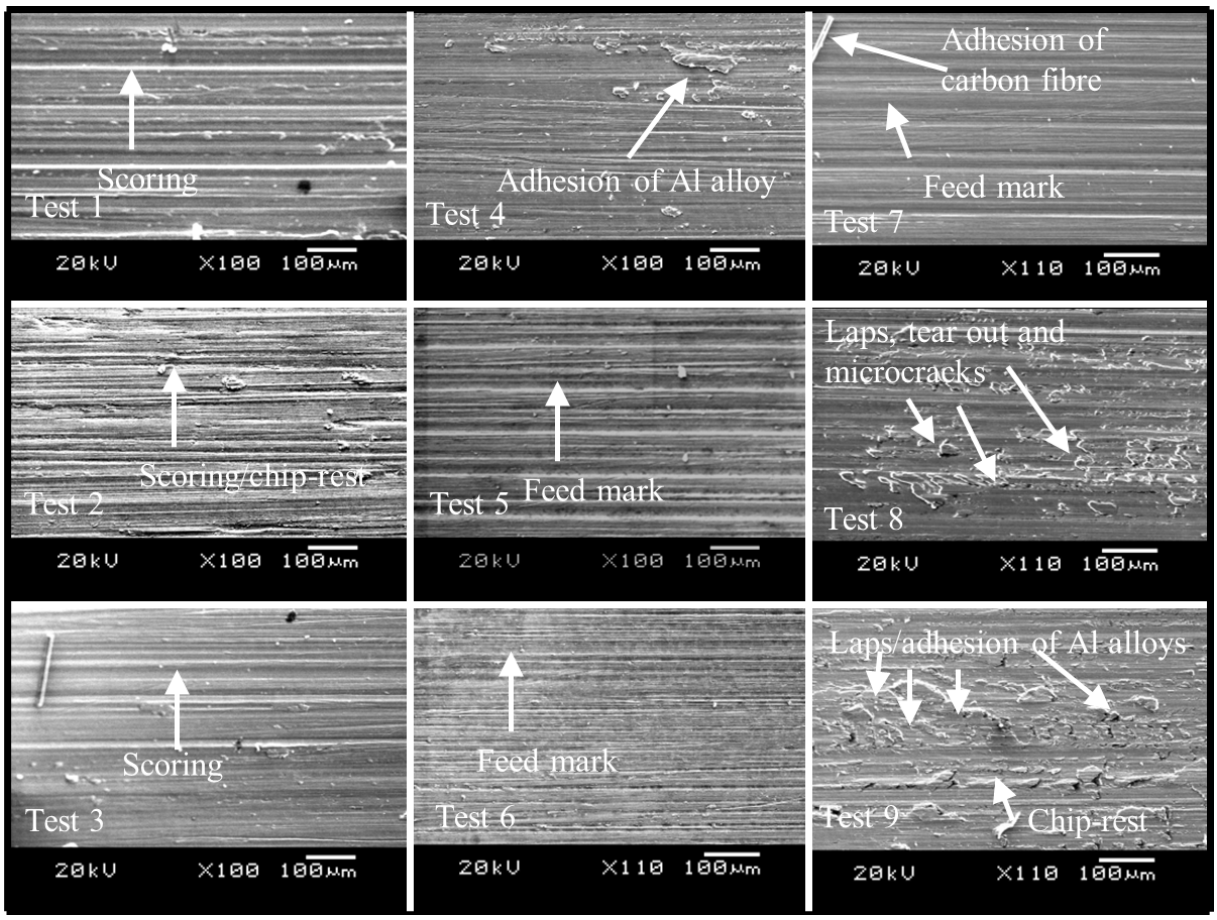


Figure 4.61 Micrographs of hole surface texture in Al layers

4.4.6 Subsurface alteration

Figure 4.62 shows the workpiece microstructure at the last hole machined in the Ti layers for all tests. Most of the samples evaluated showed no indication of microstructural alteration except for Test 6 and 8, which revealed plastically deformed layers extending to depths of ~55 and 75µm respectively. In addition, a thin white layer (~5.7µm) was also observed on the hole subsurface in the former. This was possibly due to chipping at the peripheral corners of the drills utilised in Tests 6 and 8, which increased the tendency for ploughing and straining of the material.

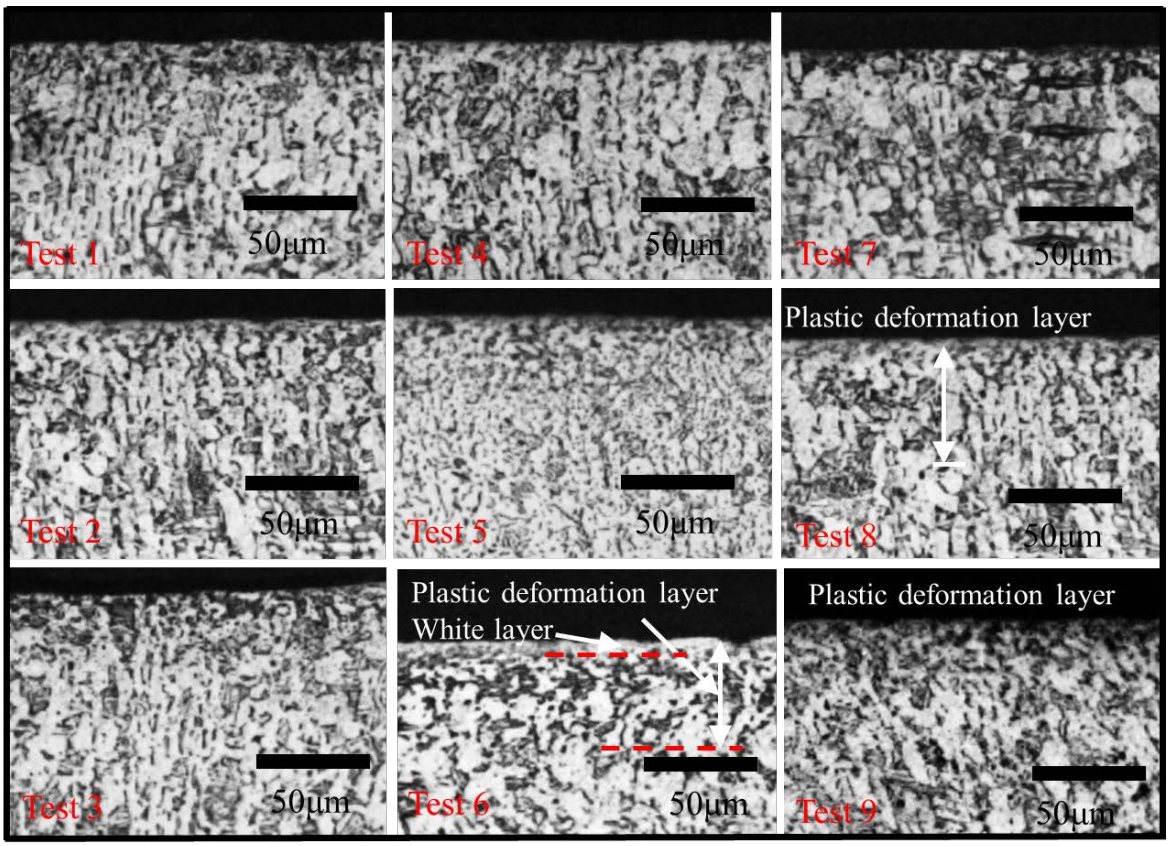


Figure 4.62 Micrographs of subsurface microstructure in Ti layers for all tests

Corresponding microhardness depth profiles of the cross-sectioned Ti holes are shown in Figure 4.63. The majority of samples displayed a 5-16% increase in microhardness over the bulk hardness within a 60µm region beneath the machined surface. The highest rise (~430$HK_{0.025}$) was observed in Test 8, which corresponds to the deformed microstructure seen in Figure 4.63 however, ANOVA calculations (not shown here) suggested that none of the variables had a significant effect on workpiece microhardness.

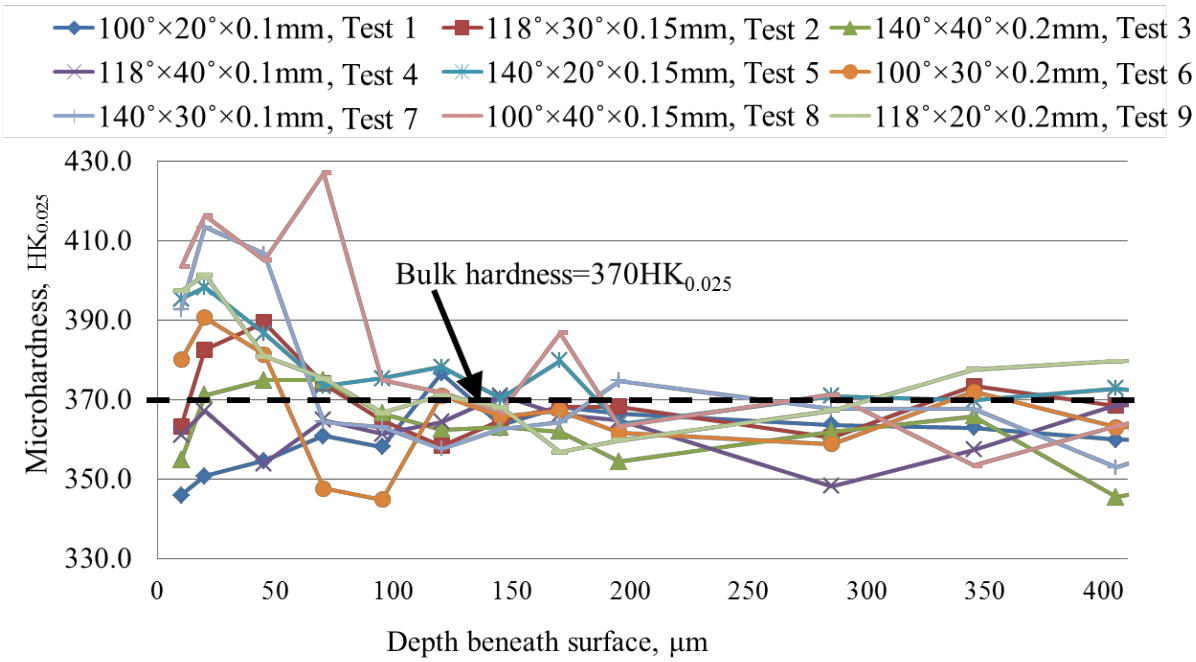


Figure 4.63 Microhardness depth profile measurement for all tests in Ti layer

Figure 4.64 shows the subsurface microstructure at the last hole in the aluminium layer for all tests. Typical elongated grains were evident in all specimens for Test 1, which showed evidence of deformed grain structure to a depth of ~20µm. This would appear to correlate with the microhardness depth profile data detailed in Figure 4.65, which shows that only Test 1 exhibited strain hardening at 10µm beneath the hole surface ($185HK_{0.025}$). All the other specimens exhibited an initial reduction in microhardness ranging from 5-30$HK_{0.025}$ below the bulk hardness value, with some tests showing a subsequent increase to a maximum of ~200$HK_{0.025}$ (Test 2 and Test 5).

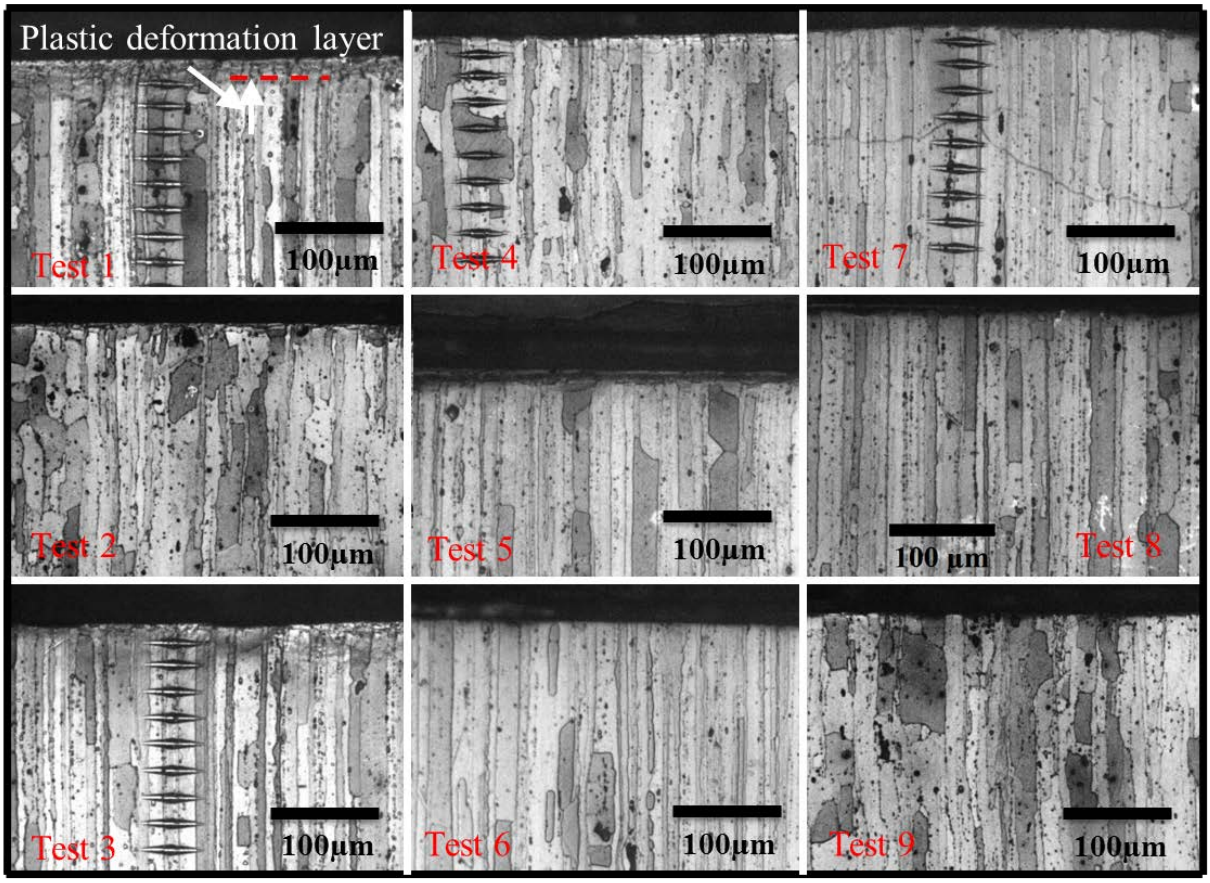


Figure 4.64 Micrographs of subsurface microstructure in Al layer for all tests

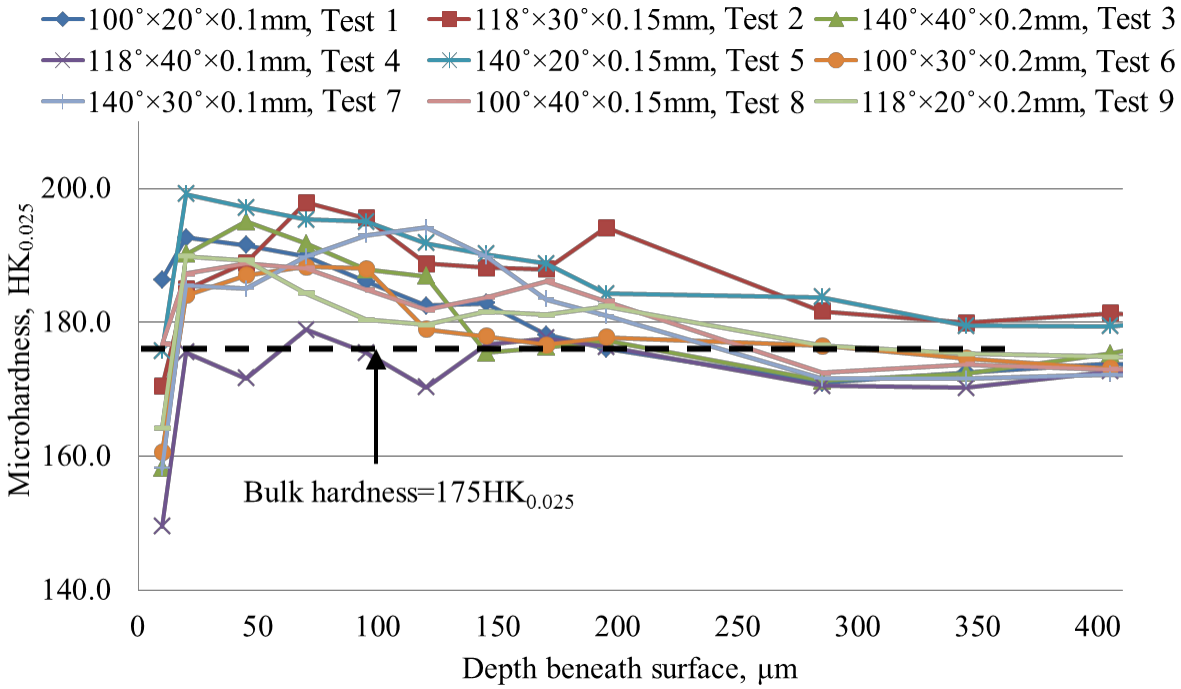


Figure 4.65 Microhardness depth profile measurement for all tests in Al layer

4.5 Phase 2A: Evaluation of diamond coated/novel PCD drills and feed rate at elevated cutting speed

4.5.1 Thrust force and torque

Figure 4.66 shows the thrust force measured at the first hole (new tools) for all tests when single shot drilling Ti/CFRP/Al stacks at a cutting speed of 36/144/144m/min. In general, thrust forces were observed to increase with feed rate irrespective of the drill employed. When using domed PCD drills under feed rates of 0.05mm/rev and 0.08mm/rev, the thrust force and torque in Ti layers were typically up to 25% and 17.8% lower respectively, than those produced by the CVD diamond coated drills. Similarly, the trend was mirrored in the CFRP layers with reductions in thrust force and torque of up to 41% and 18% when utilising the domed PCD tools. Conversely, thrust forces measured in the Al layers were 19-32% higher when employing the domed PCD drills whilst torque values showed only ~3% reduction, when compared against the CVD diamond tools.

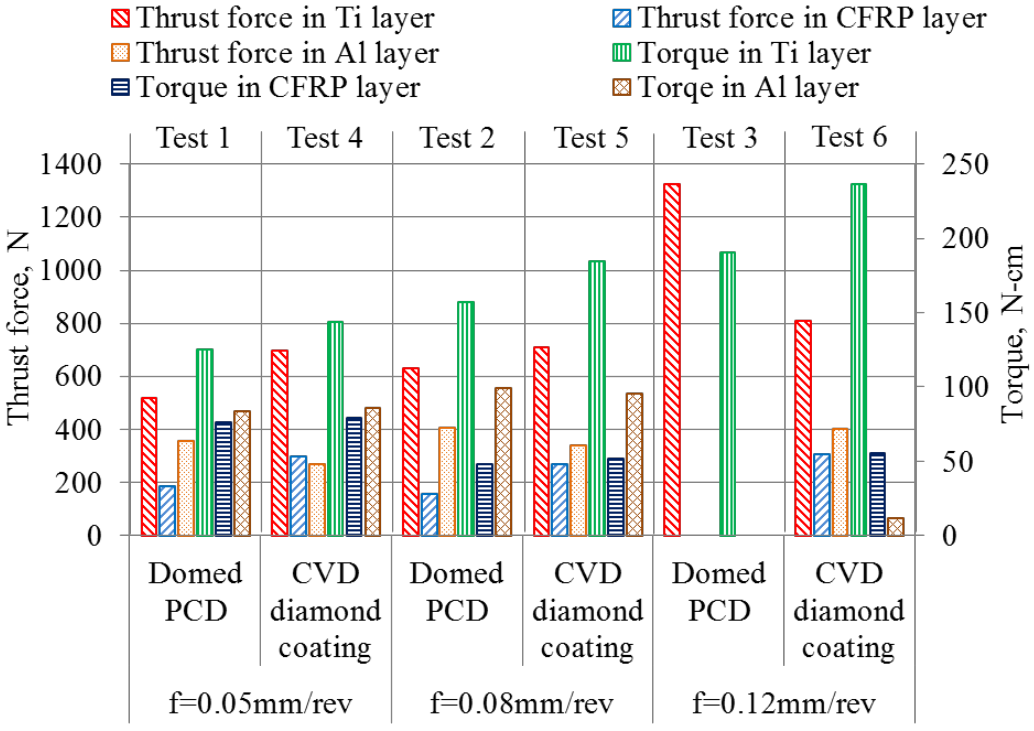


Figure 4.66 Thrust force and torque in the first hole for all tests

In addition to the superior hardness levels (8000-10000HV), the cutting edge radius of the domed PCD drills was over 4 times smaller (~5.95um) compared to the CVD diamond coated tools (24.32µm), which explains the lower thrust forces recorded when employing the former in the new condition, see Figure 4.67. Furthermore, the lower surface roughness (2.7µm Ra)

of domed PCD drills was also expected result in a lower coefficient of friction compared to the CVD diamond coating, which had a comparatively higher roughness of ~4µm Ra.

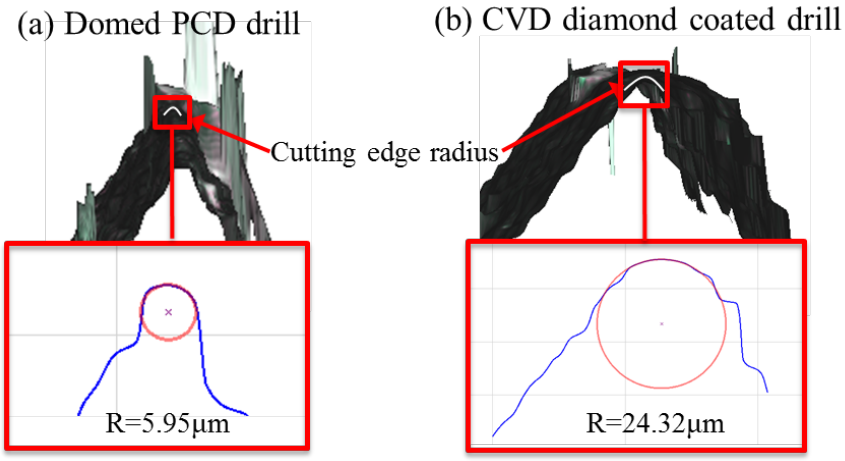


Figure 4.67 Scanning and measurement of cutting edge radius of new domed PCD and CVD diamond coated drills

4.5.2 Tool wear and tool life

Figure 4.68 shows the progression of tool wear to drill failure for all tests. The domed PCD drills utilised at low (0.05mm/rev) and intermediate (0.08mm/rev) feed rates both showed signs of tool fracture/macro chipping (primarily at the chisel edge and peripheral corners) after only 2 holes. Similarly, the test at 0.12mm/rev resulted in catastrophic failure of the drill at the shank after entering the Ti layer of the stack at the first hole; see Figure 4.69.

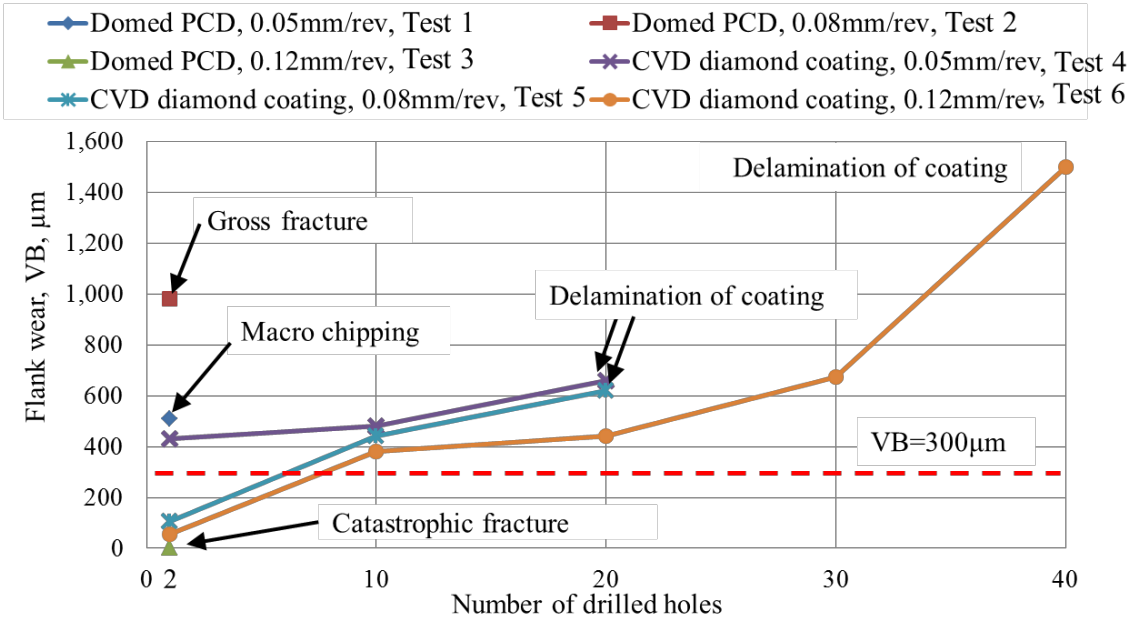


Figure 4.68 Progression of tool wear to fracture in all tests

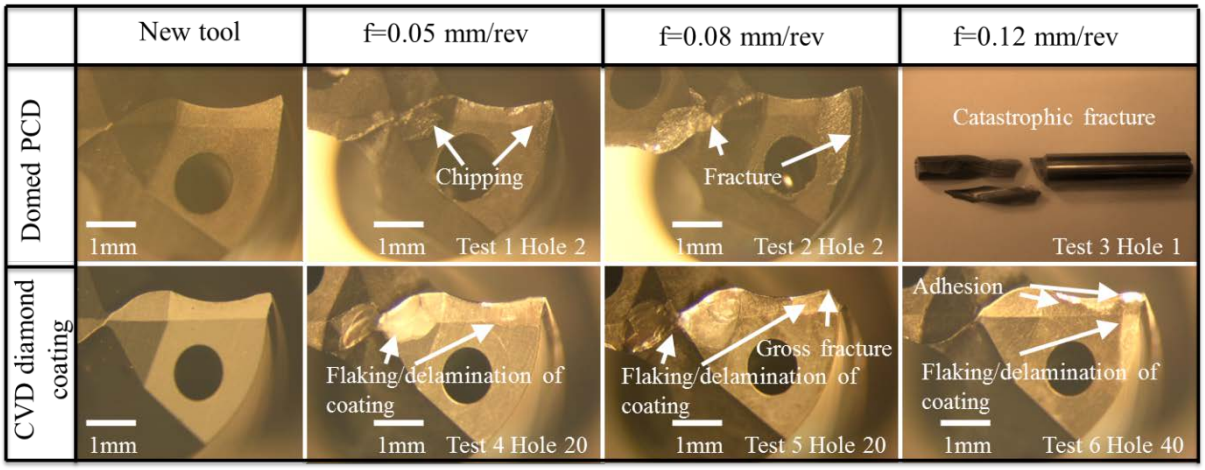


Figure 4.69 Micrographs of tool wear/fracture at the last hole for all tests

This was due to the relatively low fracture toughness of the PCD material (7.9MPa·$m^{1/2}$), with the point geometry employed thought to be inappropriate (two-stage design) to withstand the loads encountered particularly when drilling through the Ti segment. Conversely, the CVD diamond coated drills produced 20-40 holes before severe delamination of the coating and subsequent fracture of the carbide substrate necessitated the cessation of the trials. Following discussions with the industrial partners (Seco Tools and Element Six) regarding the unexpected poor performance of the domed PCD drills; several modified point geometries were designed to account for the inherent mechanical properties of PCD. Limited performance trials were subsequently undertaken using the modified drill designs on 2 layer CFRP/Al stacks, with the results detailed in Appendix 5.

4.5.2.1 Fracture pattern in domed PCD drills

The main failure modes observed on the domed PCD drills when operating at feed rates of 0.05 and 0.08mm/rev (Test 1 and Test 2) were micro and macro-chipping together with fracture along the cutting lips, which propagated from the chisel edge to the peripheral corner. This was thought to have been triggered by tensile stresses due to the resultant forces at the cutting edge [205]. Figure 4.70 shows SEM images of the worn drill in Test 1, which revealed signs of cracking at the chisel together with instances of workpiece adhesion in the immediate vicinity. Although the lead cutting lips near the chisel zone remained largely intact, micro-chipping encompassing an area of ~50μm×700μm with a depth of up to 30μm was evident. The growth of wear extending from micro-chipping to macro-chipping (area of 250×910μm and 70μm in depth) and gross fracture (500×250μm) at the peripheral corners was attributed to the increase in thrust forces and torque at hole 2.

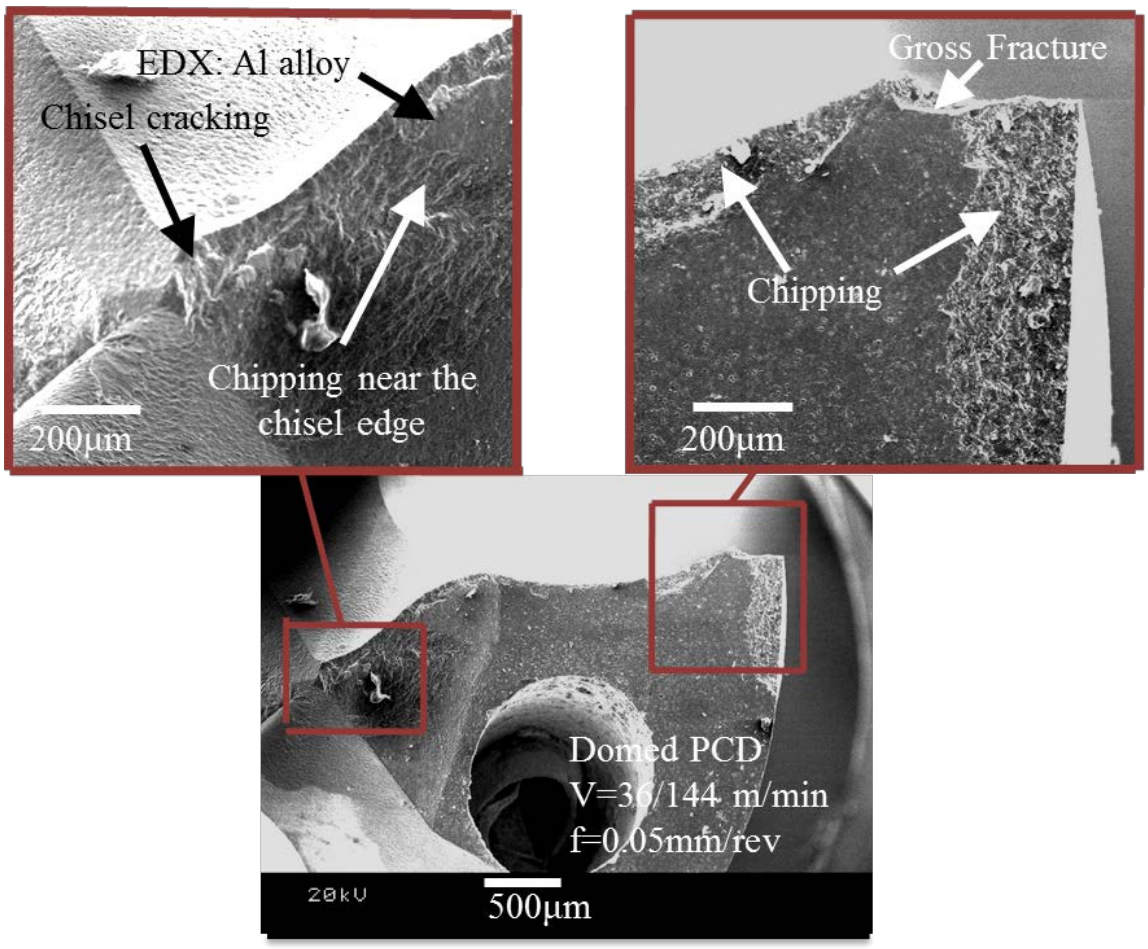


Figure 4.70 Micrograph of tool fractures at the cessation of Test 1

Figure 4.71 details SEM micrographs detailing drill failure at the chisel edge after 2 holes when feed rate was increased by 60% to 0.08mm/rev. On the lead cutting lips, macro chipping of the PCD covering almost the entire lead relief plane (500×1000µm area) was observed, which implied the presence of very high thrust forces acting on the lead relief plane before the cutting lips were fully engaged. This was likely due to thinning of the web on the rake face at the drill lead point, which tends to reduce the strength near the chisel zone. Similarly, the severe fracture of the drill corner was attributed to the relatively sharp geometry at the tool periphery, resulting in large stress concentrations upon contact with the workpiece material. When drilling at the highest feed rate of 0.12mm/rev, the drill experienced catastrophic failure at hole 1 after only advancing 0.86mm into the Ti layer.

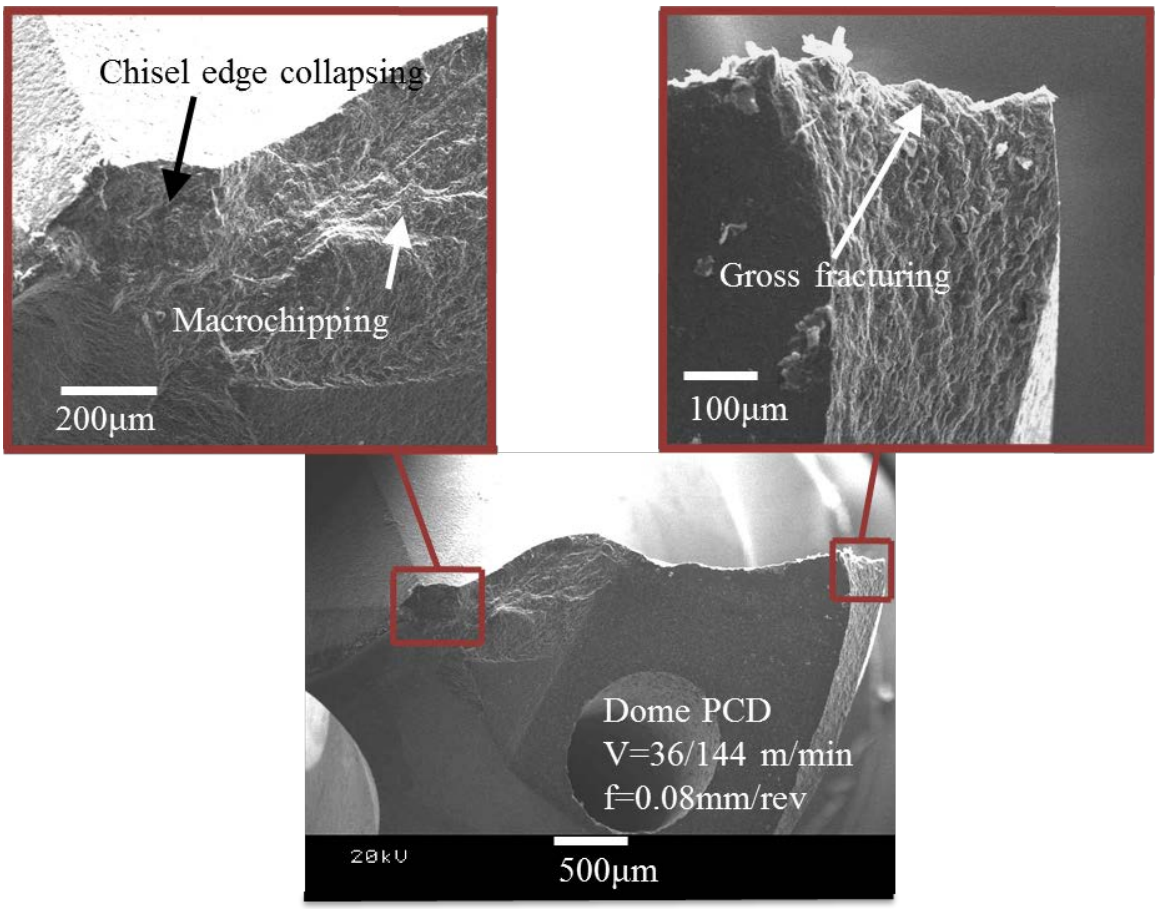


Figure 4.71 Micrograph of tool fractures at the cessation of Test 2

4.5.2.2 Failure pattern in CVD diamond coated drills

Figure 4.72 shows SEM micrographs of tool failure in Test 4 when drilling at a feed rate of 0.05mm/rev. Wear of the drill was dominated by severe delamination of the coating but was mainly confined to the chisel section and peripheral corner. This was partly due to the internal stress generated between the carbide substrate and coating during drilling due to their dissimilar stiffness modulus. Abrasion and wear of the exposed WC substrate was also observed with the test halted when the delamination area exceed ~1500x1500µm.

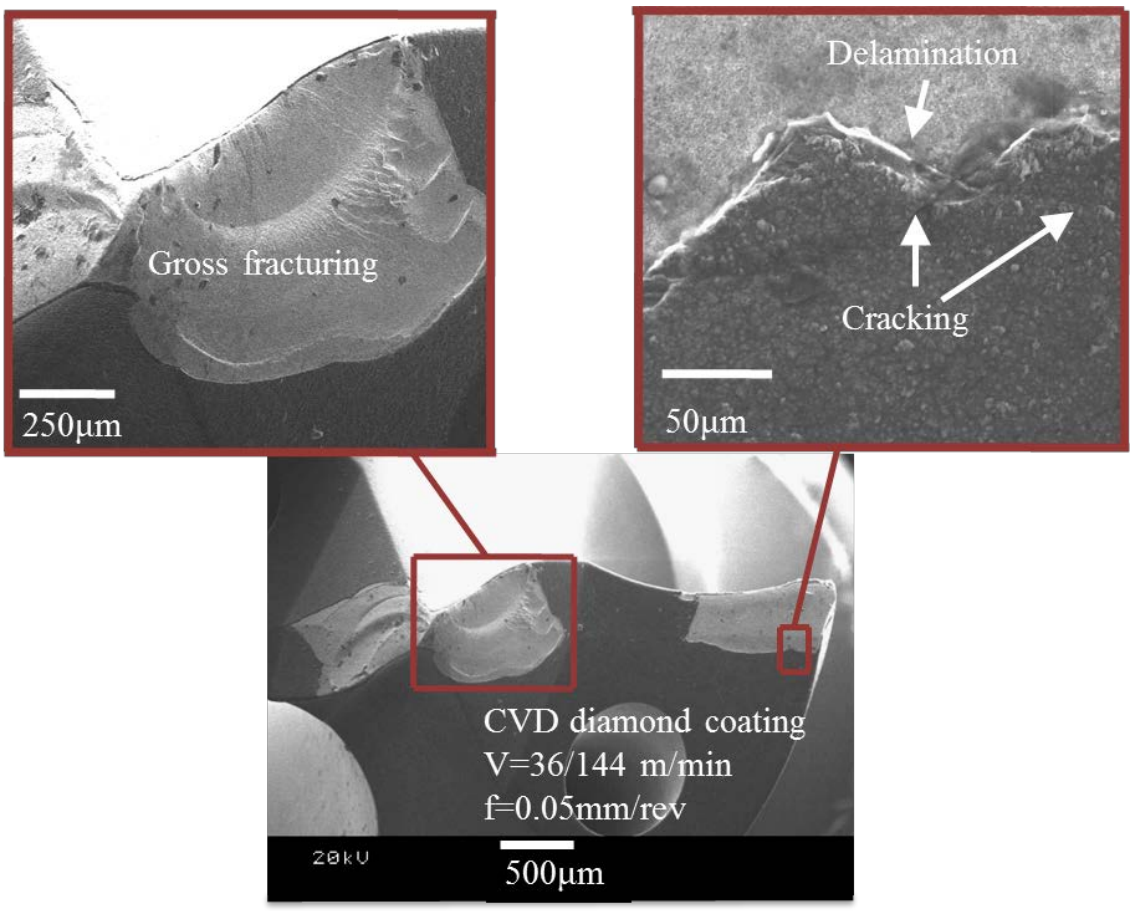


Figure 4.72 Micrograph of tool wear modes at the cessation of Test 4

Figure 4.73 details the SEM micrographs of the worn drill when feed rate was increased to 0.08mm/rev. While the wear pattern and location was similar to that observed in Test 4, adhesion of aluminium/BUE was evident in Test 5. Fracture of the drill corner occurred after 20 holes when the area of coating delamination extended beyond ~1500×1500µm.

Figure 4.74 presents the drill wear pattern at the cessation of Test 6, which surprisingly shows coating delamination only occurring around the drill corners, but propagating down the clearance face and cutting lips. Unlike Tests 4 and 5, no signs of wear were visible at the chisel edge when operating at a feed rate of 0.12mm/rev. This was most likely due to the reduced contact time as well as the greater distribution of load to the drill periphery.

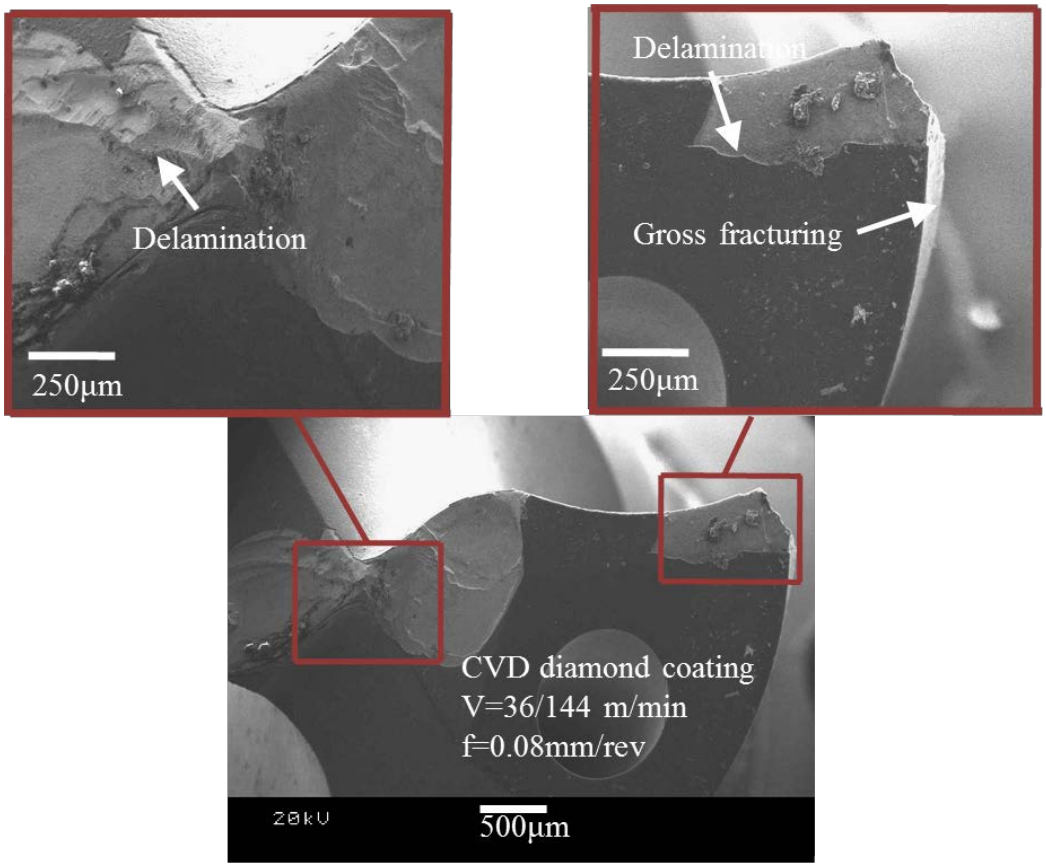


Figure 4.73 Micrograph of tool fractures at the cessation of Test 5

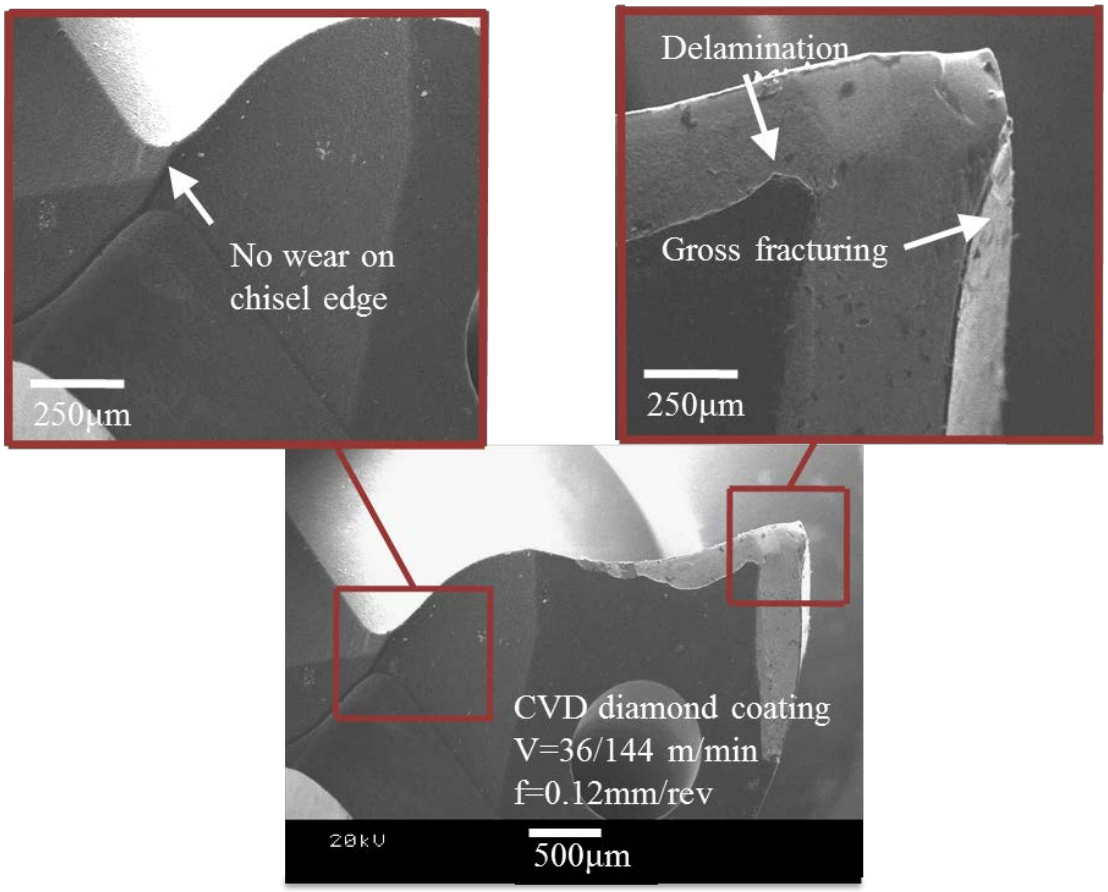


Figure 4.74 Micrograph of tool fracture at the cessation of the Test 6

4.5.3 Hole accuracy (diameter, out of roundness, and cylindricity)

Figure 4.75 shows results of the hole diameter measurement. Due to chipping along the cutting edge as well as the severe fracture at the chisel and corners of the cutting lips on the domed PCD drills, the hole diameter was up to 70µm larger than the nominal value as seen in Test 2. Conversely, despite severe coating delamination and fracture at the drill corners, the diameter of holes produced by the CVD diamond coated drills were all within 6.38±0.0375mm, which is within typical industrial tolerance. This was possibly due to the two-stage point design of the drill, which remained intact and provided improved stability /reduced run out similar to that observed in Section 4.3.3.

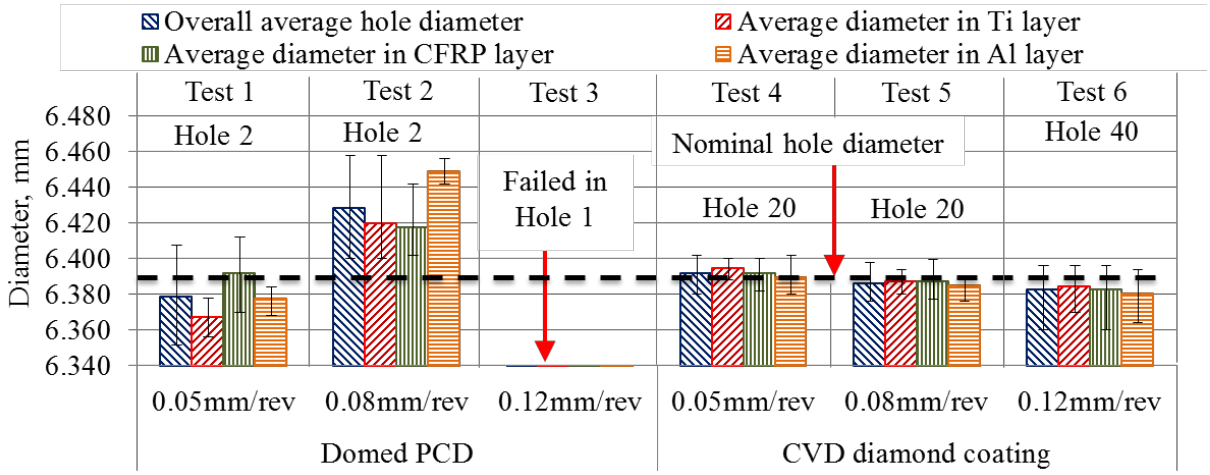


Figure 4.75 Average hole diameter over test duration

Figure 4.76 details the overall hole cylindricity and average out of roundness for all trials. Holes produced by the domed PCD drills showed high values of cylindricity (~125µm) and out of roundness (~48µm) particularly in the CFRP layer. This was attributed to the fractured cutting lip, which probably caused severe matrix/fibre pull out during drilling. Tests with the CVD diamond to relatively high out of roundness values in the CFRP and especially the Al section of the stack. This may have been due to re-deposited Al workpiece material on the surface of the hole.

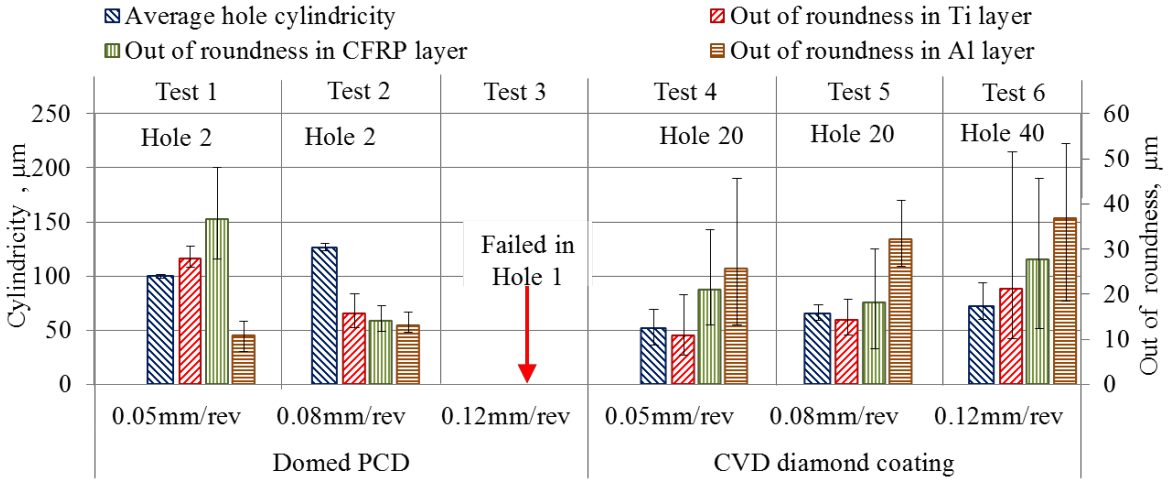


Figure 4.76 Average hole cylindricity and out of roundness over test duration

4.5.4 Burr formation

Figure 4.77 details the burr height measurement at the cessation of all tests. In general when employing CVD diamond coated drills, entrance burr height in both the titanium and aluminium layers decreased with increasing feed rate and the exit burr exhibiting similar results when the test duration lasted 40 holes. This was attributed to the higher feed rate, which reduced time for plastic deformation of the workpiece material and hence burr formation. Figure 4.78 shows the burr forms produced at hole 10 in Test 6 using a CVD diamond coated drill at a feed rate of 0.12mm/rev. The entrance burr in the titanium layer also shows an irregular protrusion, which indicates severe wear of the cutting lips, leading to wrinkled, extruded burr morphology.

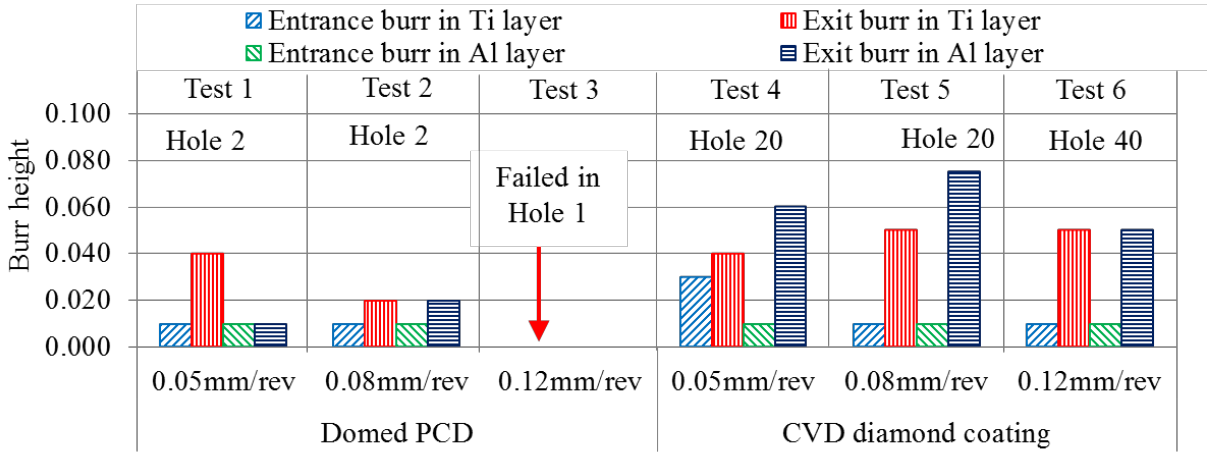


Figure 4.77 Burr height at the last hole in all tests

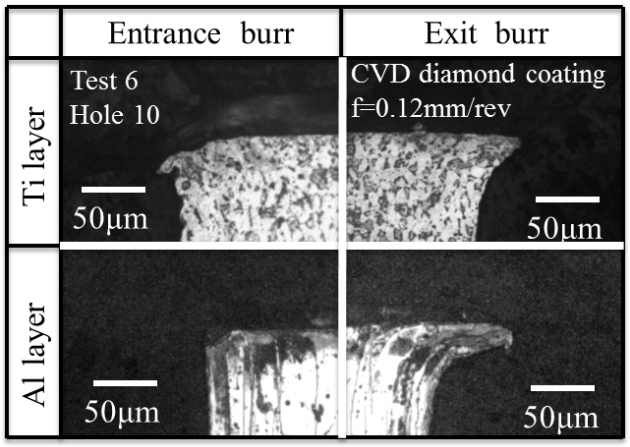


Figure 4.78 Burr at hole entry and exit in the Ti and Al layers at hole 10 in Test 6

4.5.5 Surface integrity (roughness and microhardness)

The highest hole surface roughness in the Ti, CFRP, and Al layers produced by the domed PCD drills was 2.26, 8.33 and 1.63μm Ra respectively, with both Tests 1(0.05mm/rev) and 2 (0.08mm/rev) producing only 2 holes prior to test cessation, see Figure 4.79. In contrast, surface roughness was superior when utilising the CVD diamond coated drills, with Ra not exceeding 0.84, 2.09 and 0.46μm in the Ti, CFRP and Al layers respectively, even after 20-40 holes as detailed in Figure 4.79.

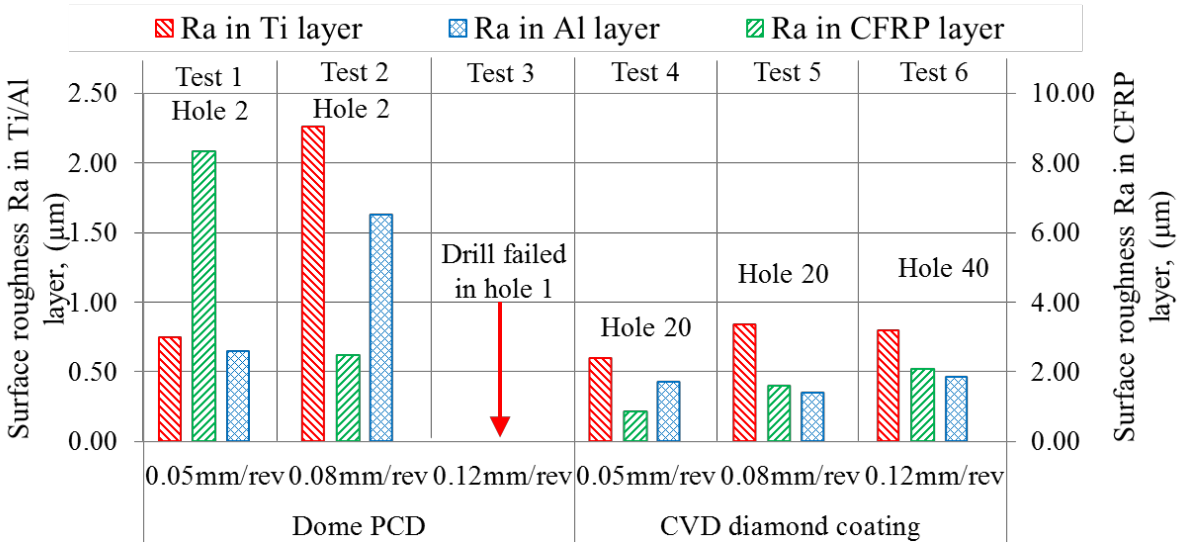


Figure 4.79 Hole surface roughness in each material layer at test cessation

The fracture pattern of the domed PCD drills was generally characterised by chipping along the cutting edge together with severe fracture at the chisel and corner sections as seen in Figure 4.70 and Figure 4.71, which accounts for the relatively high hole surface roughness recorded. Conversely, the CVD diamond coated drills typically suffered from

flaking/delamination of the coating at the chisel region as well as peripheral corners, see Figure 4.71 and Figure 4.73. Subsequent wear of the exposed WC substrate increased the tool edge radius, which likely led to the lower hole surface roughness produced. There were no clear trends detected in the workpiece surface roughness results with regard to varying feed rate when utilising the PCD drills, which was probably due to fracture of the corner edge. In terms of the CVD diamond coated tools, increasing feed rate generally resulted in higher Ra values, particularly in the Ti and CFRP layers. Figure 4.80(a) shows an SEM image and corresponding 3D topographic map (1.25×0.5mm scanned area) of the machined surface in the CFRP layer from Test 1. Grooves were observed at the 45° and 135° ply orientations due to gross fibre loss and matrix pull out, which was most likely caused by the high level of wear on the domed PCD drill. This also explains the adverse surface roughness values recorded in the CFRP layer previously shown in Figure 4.79. In contrast, using the CVD diamond coated drills revealed only minor smearing of the polymer resin and sporadic micro cracking with no signs of any wholesale material removal as seen in Figure 4.80(b).

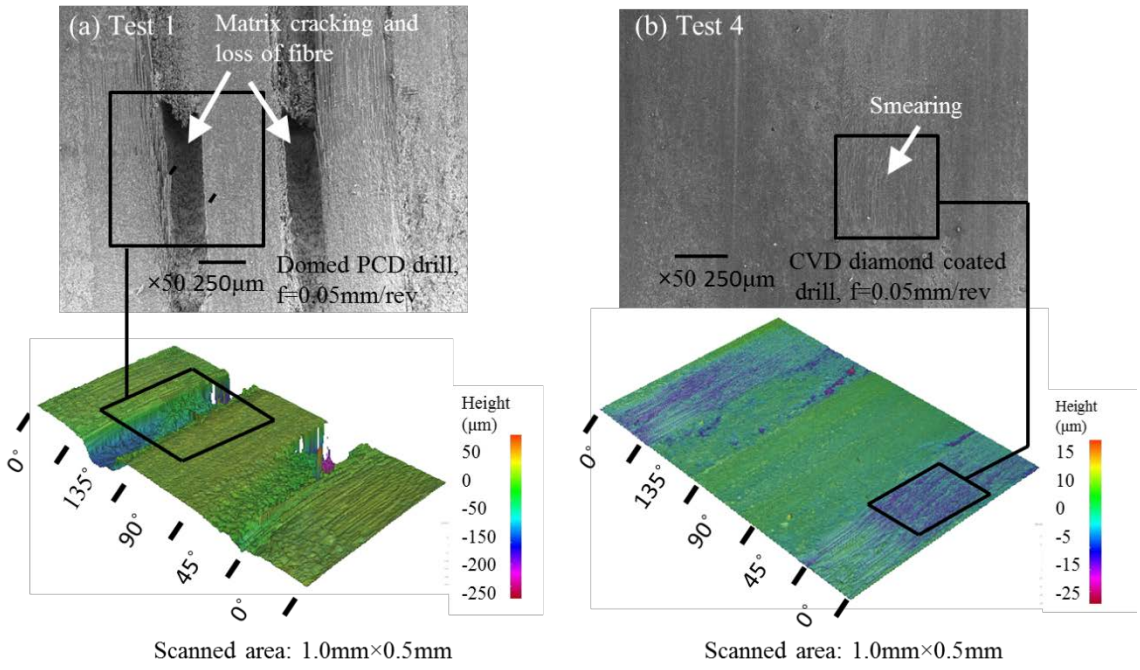


Figure 4.80 SEM micrographs and 3D topographic maps of CFRP hole surfaces in Test 1 and Test 4

Figure 4.81 details the micrograph of a cross-sectioned hole surface (Test 5) and microhardness depth profiles of the Ti layer for the last hole drilled in all experiments. There was no significant increase in microhardness observed in any of the tests, except for a spike rising to 393$HK_{0.025}$ (~12% above the bulk hardness) at ~170µm beneath the surface, when employing the domed PCD drill under a feed rate of 0.08mm/rev (Test 2). Conversely, when

using the CVD diamond coated drill under the same feed rate (Test 5), the corresponding cross-sectional micrograph of the machined Ti subsurface showed no appreciable change in workpiece microstructure, which was representative of results seen in the other trials. In addition, thrust forces measured in the Ti layer showed only a limited rise of ~15% as the feed rate was increased from 0.05 to 0.12mm/rev.

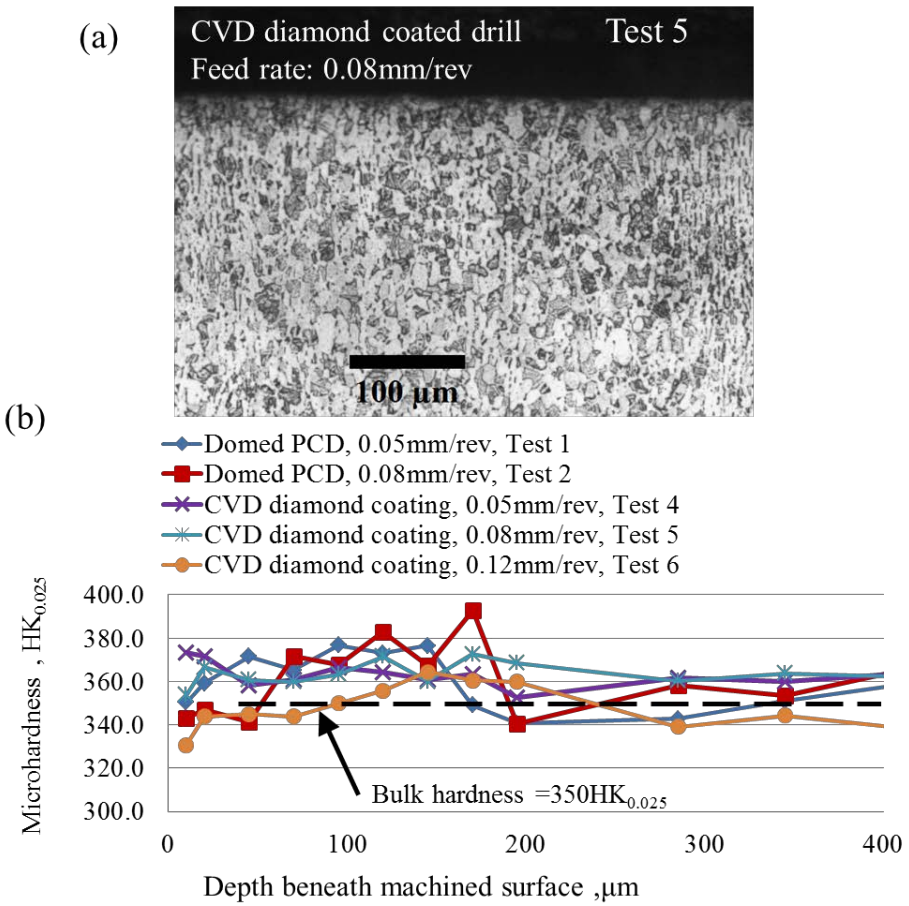


Figure 4.81 Cross-sectional micrograph and microhardness depth profile in Ti layers

Figure 4.82 shows an optical micrograph of a cross-sectioned hole surface in Test 2 and corresponding microhardness depth profile measurements in the Al layer for all tests. The results revealed no substantial changes in subsurface microhardness irrespective of variation in tool material and feed rate. Despite the relatively high levels of tool wear/coating delamination at test cessation, thrust forces and torque did not exceed ~410N and ~100N-cm respectively in any of the trials, with minimal discrepancy in the values recorded due to changes in test conditions. This suggests that neither strain hardening nor thermal softening were dominant mechanisms in affecting workpiece microhardness or microstructural alternations during the drilling operation.

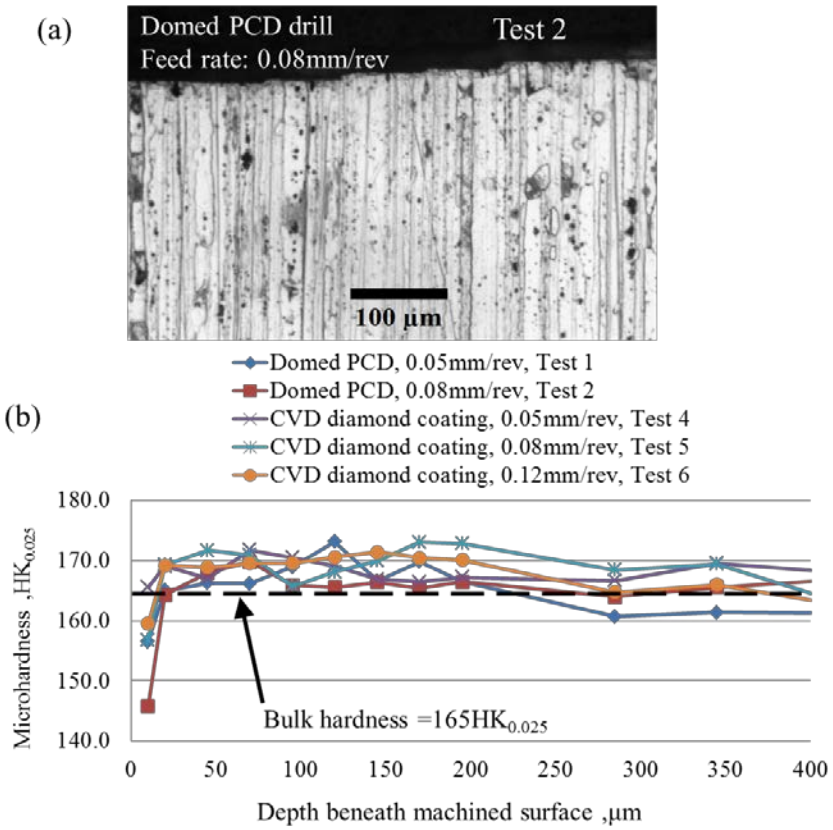


Figure 4.82 (a) Micrograph and (b) microhardness depth profile in Al layers

4.6 Phase 2B: Confirmation test and benchmarking of bespoke drill geometry

4.6.1 Performance of preferred drill geometry

A confirmation test was carried out to validate the preferred drill point design of 0.1mm chisel diameter, 140° point angle and 40° helix angle. This was determined based on the statistical analysis of all response measures (cutting force, tool wear, hole diameter, out of roundness, cylindricity, burr height and hole surface roughness) obtained from the experiments undertaken in Phase 1D (Section 4.4). Table 4.9 details the test results from the confirmation trial compared to the estimated optimum values calculated from the significant factors. The majority of the results produced from the test with the preferred drill design were within the statistical confidence interval, although the out of roundness and hole surface roughness in the CFRP layer was 30.5% and 31.29% higher than the estimated optimum value respectively. The former was possibly due to the inconsistent chip formation mechanism in CFRP, while the latter was somewhat unexpected as the associated ANOVA in Table 4.8 showed a relatively low residual error level of ~ 9%. Conversely, analysis of the hole surface roughness in the Al layer showed a high residual error of 100% as detailed in Section 4.4.5,

although the result from the confirmation test indicated a 46.9% reduction in surface roughness in the Al section. Surprisingly, hole cylindricity (48.03µm) was lower than the estimated optimum value (80.1µm) despite a comparatively high error level of ~56% as shown in the corresponding ANOVA (Table 4.6) in Section 4.4.3.

V= 30/120m/min, f= 0.08mm/rev, Pecking, at hole 90 in all tests		Preferred combination in Phase1D			Mean value	**Estimated optimum value**	C.I.	**Confirmation result**	Error (%)
		A (mm)	B (˚)	C (˚)					
Ti layer	Thrust force, N	0.1	140	40*	1327.1	**1051.05**	326.32	**1163**	↑10.6
	Torque, N-cm	0.1	140	40*	359.04	**317.60**	174.19	**332.60**	↑4.72
	Hole diameter, mm	0.1	140	20	6.36	**6.36**	0.01	**6.36**	↑0.03
	Out of roundness, µm	0.1	140*	40	18.00	**15.10**	1.79	**16.08**	↑6.49
	Entrance burr, mm	0.1	140*	30	0.20	**0.19**	0.13	**0.20**	↑5.26
	Roughness (Ra), µm	0.2	140	40*	1.05	**0.85**	0.21	**1.07**	↑25.9
CFRP layer	Thrust force, N	0.1	100	40*	479.33	**409.05**	105.13	**429.00**	↑4.88
	Torque, N-cm	0.2	140*	30	160.17	**143.86**	102.00	**79.8**	↓44.5
	Hole diameter, mm	0.2	140	40*	6.36	**6.36**	0.01	**6.35**	↓0.11
	Out of roundness, µm	0.1	140*	40	23.00	**18.60**	2.05	**24.42**	↑31.3
	Roughness (Ra), µm	0.1	140*	30	7.68	**2.72**	N/A	**3.55**	↑30.5
Al layer	Thrust force, N	0.1	140	40*	479.23	**408.10**	143.48	**475.00**	↑16.4
	Torque, N-cm	0.1	140	40	202.11	**143.66**	N/A	**179.60**	↑25.0
	Hole diameter, mm	0.2	118*	40	6.37	**6.37**	0.03	**6.34**	↓0.41
	Out of roundness, µm	0.2	100*	30	19.00	**12.95**	2.65	**10.62**	↓17.9
	Exit burr, mm	0.1	140*	30	0.06	**0.04**	N/A	**0.05**	↑25.0
	Roughness (Ra), µm	0.1	140	30	0.81	**0.81**	N/A	**0.43**	↓46.9
Overall stack	Tool wear, µm	0.2	118	40*	84	**77.5**	47.52	**91**	↑17.4
	Hole cylindricity, µm	0.2	140	40*	90	**80.1**	N/A	**48.03**	↓40.0

*: Significant at the 5 % level/high influence factor
A: chisel diameter; B: point angle; C: helix angle
C.I.: Confidence interval

Table 4.9 Validation of results produced using the bespoke design drill in Phase 1D

4.6.2 Comparison against uncoated, TiAlN/TiN coated and triple margin carbide drills

Table 4.10 lists the results of key response measures from Phase 1A and Phase 1B experiments carried out under a dual-level cutting speed of 30/120/120m/min, a feed rate of 0.08mm/rev and pecking strategy (2mm retraction after feeding 5mm). These were compared to the performance of the preferred drill geometry (0.1mm chisel diameter, 140° point angle, 40° helix angle) employed in Phase 1D trials. In general, the results indicated that the preferred drill generally outperformed the coated carbide (in Section 4.1), uncoated carbide (in Section 4.1) and triple margin (in Section 4.2) drills in 12, 18, and 13 out of the 19 response measures respectively.

V=30/120/120m/min, f=0.08mm/rev, pecking, at hole 90 in all tests		**Experimental results**			
		Preferred drill design	Phase 1A coated drill	Phase 1A uncoated drill	Phase 1B triple margin drill
Ti layer	Thrust force, N	1054.00	1751 (↑66%)	1660(↑57.5%)	2531(↑140%)
	Torque, N-cm	332.60	331(↓0.5%)	397(↑19.4%)	785.8(↑136%)
	Hole diameter, mm	6.36	6.355(↓0.1%)	6.383(↑0.4%)	6.352(↓0.1%)
	Out of roundness, μm	16.1	53(↑231%)	62(↑288%)	21.1(↑31.2%)
	Entrance burr, mm	0.20	0.28(↑40%)	0.36(↑80%)	0.21(↑5.0%)
	Roughness (Ra), μm	1.07	0.58(↓45.8%)	1.14(↑6.5%)	1.16(↑8.4%)
CFRP layer	Thrust force, N	429.00	717(↑67.3%)	732(↑70.6%)	922.7(↑115.1%)
	Torque, N-cm	79.8	117(↑46.6%)	397(↑397%)	322(↑303%)
	Hole diameter, mm	6.4	6.34(↓0.2%)	6.36(↑0.2%)	6.342(↓0.1%)
	Out of roundness, μm	24.42	53(↑117.6%)	29(↑18.1%)	18.7(↓23.4%)
	Roughness (Ra), μm	3.55	4.46(↑25.6%)	3.68(↑3.6%)	2.98(↓16.1%)
Al layer	Thrust force, N	475.00	553.4(↑17%)	591(↑24.4%)	927.8(↑95.3%)
	Torque, N-cm	179.60	129(↓27.9%)	183(↑1.8%)	251.2(↑39.9%)
	Hole diameter, mm	6.34	6.33(↓0.2%)	6.350(↑0.2%)	6.330(↓0.2%)
	Out of roundness, μm	10.6	22(↑107.8%)	25(↑138.1%)	20.5(↑93%)
	Exit burr, mm	0.05	0.17(↑240%)	0.14(↑180%)	0.68(↑1260%)
	Roughness (Ra), μm	0.43	0.25(↓41.9%)	0.36(↓16.3%)	0.39(↓9.3%)
Overall Stack	Tool wear, μm	91	207(↑128%)	115(↑26.4%)	240(↑163.7%)
	Hole cylindricity, μm	48.03	74.1(↑54.3%)	77.5(↑61.4%)	55.6(↑15.8%)

Table 4.10 Comparison of bespoke drill performance to results from Phase 1A/1B/1D

In comparison to the bespoke design drill, the coated tools utilised in Phase 1A showed a drop in torque by up to 27.9% in the aluminium layer. This was most likely due to the TiAlN/TiN coating providing increased resistance to abrasion wear at the drill peripheral corners, leading to a reduction in frictional contact as discussed previously in Section 4.1.1. Another significant advantage was the roughness produced in the titanium and aluminium layer by using coated tools despite minor differences in point geometry between the drills (the coated drill had a chisel diameter of 0.2mm and helix angle of 30°). The major performance improvement when employing the TiAlN/TiN multilayer coated drills was the considerable reduction in hole surface roughness within the metallic sections of the stack, which was attributed to the increased reaming effect caused by retraction of the coated tool during the pecking cycle (as discussed in Section 4.1.5). In contrast, the uncoated drills utilised in Phase 1A was inferior compared to the preferred point design in all of the responses evaluated except for a marginal reduction in hole surface roughness in the aluminium layer.

The triple margin drills tested in Phase 1B were found to provide holes with lower average out of roundness (23.4%) and surface roughness (16.1%) in the CFRP layer compared to the bespoke point geometry. This was due to the significantly greater contact between the triple margin tools and hole surface, thereby increasing the likelihood of a reaming/ploughing mechanism. Similarly, the influence was also evident in the Al layer, albeit with a smaller reduction in surface roughness (9.3%).

4.6.3 Comparison against diamond coated drills

Table 4.11 lists the mean test results from Phase 1C using DLC and CVD diamond coated drills under a dual-level cutting speed of 30/120/120m/min, a feed rate of 0.08mm/rev and a pecking drilling strategy (2mm retraction after feeding 5mm), compared to the preferred drill design (0.1mm chisel diameter, 140° point angle and 40° helix angle). When assessed against the DLC coated drill, the bespoke point design was superior in 13 out of the 19 response measures (the majority by a significant level), although the height of the stack entrance burr was ~75% smaller when using the former. This was attributed to the higher hardness (4000-6000HV) and low friction coefficient (~ 0.1) of the DLC coating, which provided greater wear resistance and hence more effective shearing action, particularly in the titanium layer. This reduced ploughing/impact extrusion at the peripheral corners leading to suppression of burr growth. In addition, torque in the aluminium layer was also lower by up to 10.4% when utilising the DLC coated drill compared to the bespoke geometry. This was primarily due to

the reduced tendency for Al workpiece adhesion and BUL/BUE formation on the DLC coated drills [23] compared to the uncoated bespoke design tool.

V=30/120/120m/min, f=0.08mm /rev, pecking, at hole 70 in all tests		**Experimental results**		
		Preferred drill design	Phase 1C DLC drill	Phase 1C CVD diamond coated drill
Ti layer	Thrust force, N	1054	1047 (↓0.66%)	917(↓13%)
	Torque, N-cm	309	459(↑48.5%)	254(↓17.8%)
	Hole diameter (normalised), mm	6.34(↓0.15%)	6.39(↑0.15%)	6.38(–)
	Out of roundness, µm	23.26	115(↑394%)	9.1(↓60.9%)
	Entrance burr, mm	0.20	0.05(↓75%)	0.06(↓70%)
	Roughness (Ra), µm	0.96	1.38(↑43.8%)	0.45(↓53.13%)
CFRP layer	Thrust force, N	391.9	466(↑18.9%)	375(↓4.31%)
	Torque, N-cm	85.14	294(↑245.3%)	114(↑33.90%)
	Hole diameter (normalised), mm	6.34 (↓0.15%)	6.38(–)	6.37 (↓0.15%)
	Out of roundness, µm	30.84	62.1(↑101.4%)	21(↓31.91%)
	Roughness (Ra), µm	4.71	0.53(↓88.8%)	2.95(↓37.37%)
Al layer	Thrust force, N	437	432(↓1.14%)	428(↓2.06%)
	Torque, N-cm	164	147(↓10.4%)	122(↓25.61%)
	Hole diameter (normalised), mm	6.33 (↓0.3%)	6.39(↑0.15%)	6.37(↓0.15%)
	Out of roundness, µm	11.86	33(↑178.3%)	25(↑110.79%)
	Exit burr, mm	0.05	0.32(↑540%)	0.08(↑60%)
	Roughness (Ra), µm	0.16	0.28(↑75%)	0.18(↑12.5%)
Overall stack	Tool wear, µm	66	127(↑92.42%)	97(↑46.97%)
	Hole cylindricity, µm	54.97	140(↑154.68%)	49.23(↓10.44%)

Table 4.11 Comparison of bespoke drill performance to results from Phase 1C/1D

In contrast, the CVD diamond coated tools outperformed the preferred drill design in 13 of the 19 output measures, in particular hole quality parameters (out of roundness and surface roughness) in the Ti and CFRP layers. Despite this however, tool wear in the former was more pronounced, which was ~47% higher than the bespoke drill. This was due to the severe flaking/delamination of the CVD diamond coating (and subsequent wear of the substrate) over a large area of the drill (discussed in Section 4.3.2). This most likely caused the larger exit burrs as well as the inferior hole out of roundness and surface roughness observed in the

Al layer. Furthermore, the higher wear levels promoted increased adhesion of the Al workpiece material together with formation of BUL/BUE.

4.7 Phase 3: Effect of cutting environment and feed rate

4.7.1 Cutting force

Figure 4.83 details the cutting temperature together with associated thrust force and torque signal traces measured over the final 4mm of the last hole (180) in the Ti layer when drilling under a cutting fluid pressure of 10 bar and feed rate of 0.08mm/rev (Test 1). Cutting temperature was observed to increase rapidly from 42 to ~ 351°C as the drill advanced further into the titanium layer following a peck cycle (6-10mm depth). The results suggests inadequate transport of cutting fluid to the shear zone even at 10 bar pressure and associated flow rate of 38 l/min, leading to build-up of heat in the workpiece material. This led to thermal softening of the Ti alloy, which was reflected in the corresponding reduction of thrust force from 1173 down to 739N, while torque similarly decreased from 377 to 341N-cm over same period. As the thermocouples were implanted at ~1.5mm from the cutting lips, the temperature at the tool-chip interface was estimated to be ~ 387°C, based on calculations using a one-dimensional solid conduction law, which is sufficient to trigger a deterioration in strength of Ti-6Al-4V [11].

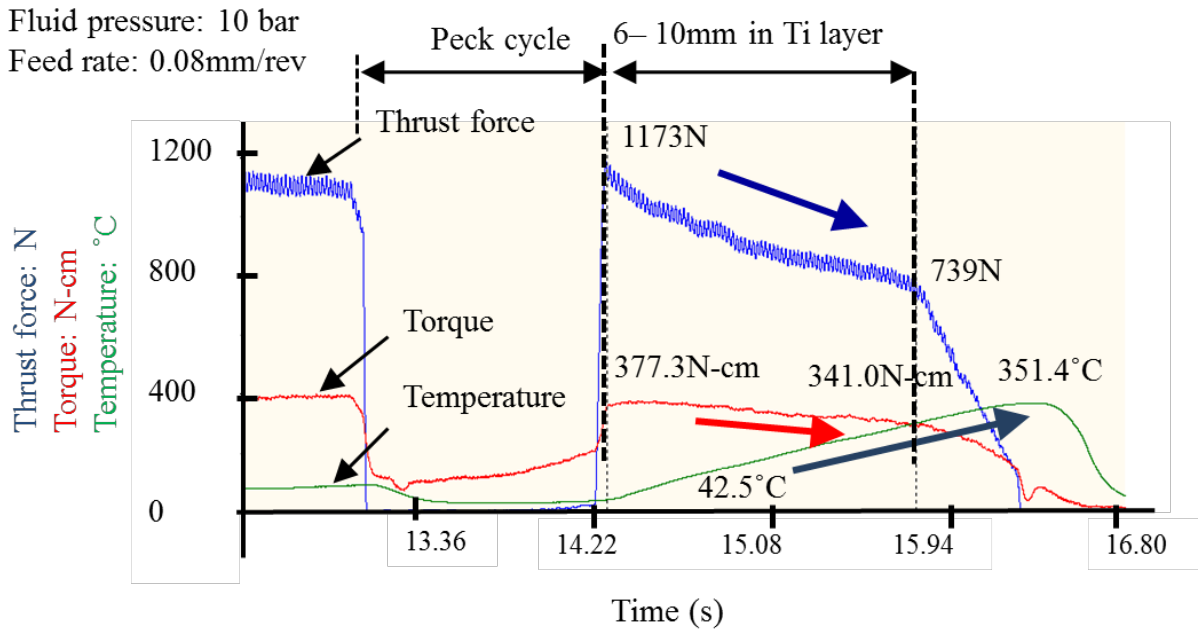


Figure 4.83 Thrust force, torque and temperature progression in Ti layer for last hole in Test 1

Figure 4.84 details the equivalent temperature, thrust force and torque traces measured at test cessation (hole 180) when drilling at 0.08mm/rev with 70 bar cutting fluid pressure under a higher flow rate of 58.8 l/min (Test 3). In contrast to results in Test 1, the variation in cutting temperature within the last 4mm of the Ti layer was minimal, which ranged from 18 to 46°C, with no sign of thermal softening detected as average thrust forces remained approximately constant/stable (1352-1393N) over the cutting duration. Additionally, friction between the drill and workpiece was also likely to have been reduced due to the improved delivery of cutting fluid/lubricant, leading to a decrease in torque levels (233-245N-cm) compared to Test 1.

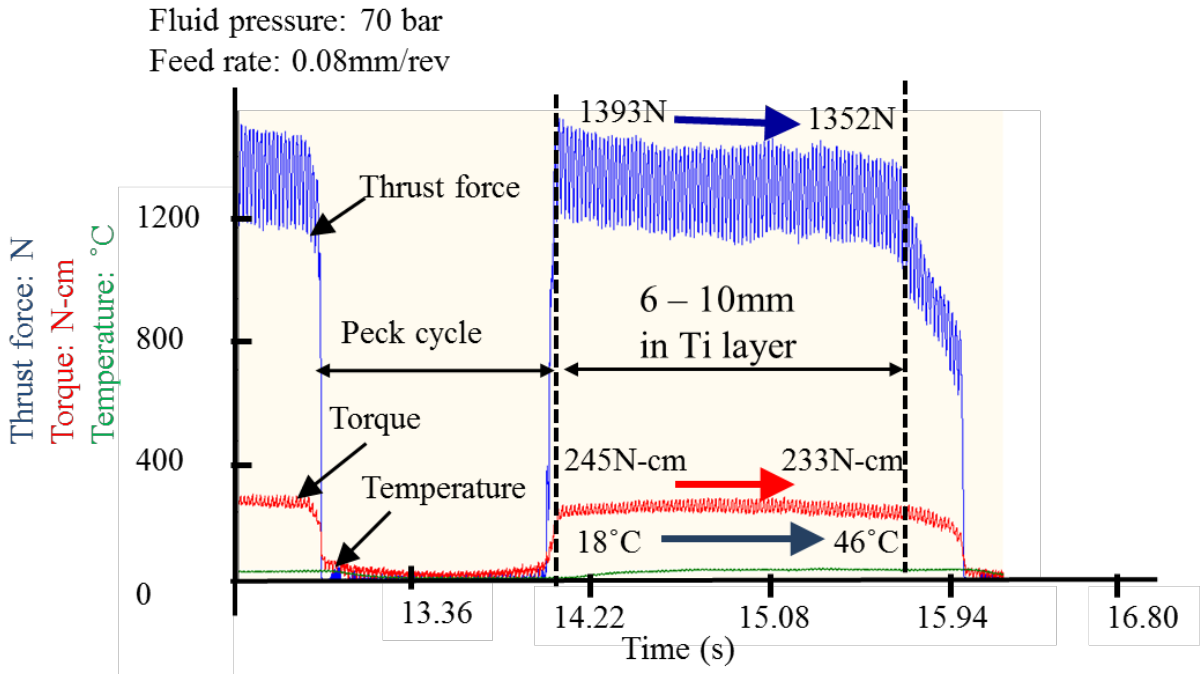


Figure 4.84 Thrust force, torque and temperature progression in Ti layer for last hole in Test 3

When machining dry under a feed rate of 0.08mm/rev (Test 6), the cutting temperature recorded in the Ti section was up to ~ 352°C after drilling only one hole, see Figure 4.85, which shows the evolution of temperature, thrust force and torque in the final 4mm of the workpiece. The rise in temperature coincided with a moderate reduction in thrust force from 428 to 362N, which suggests initiation of thermal softening in the material. Despite this, the relatively high temperatures caused rapid deterioration of the drill with maximum flank wear of 800µm, primarily due to coating delamination at the peripheral corner of the tool and hence necessitated cessation of the trial. This also explains the marginal increase in torque (82 to 91N-cm) observed in the final 4mm of the hole.

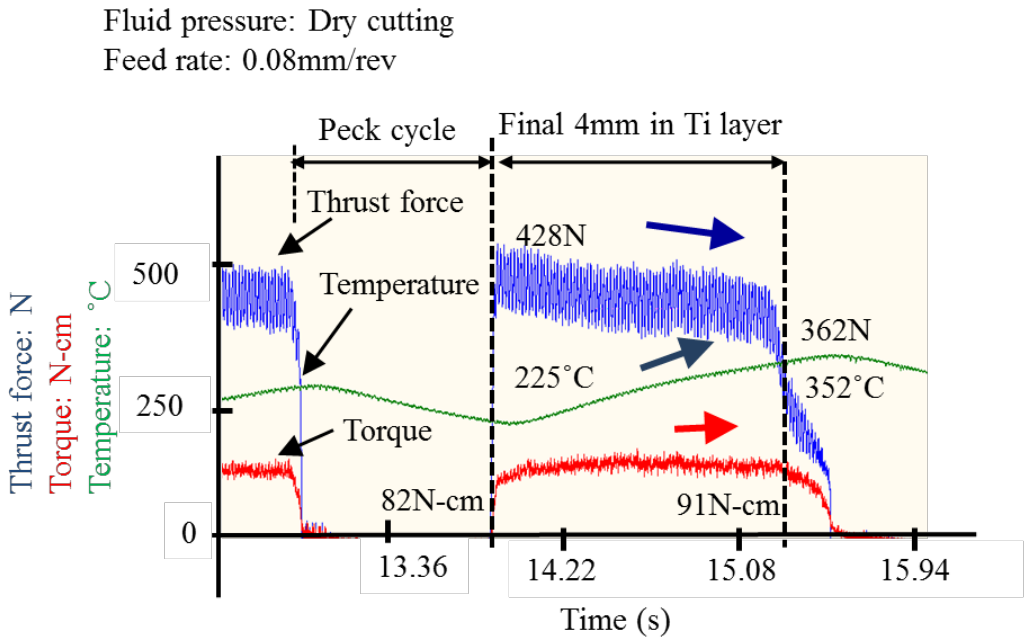


Figure 4.85 Thrust force, torque and temperature progression in Ti section for first hole in Test 6

Figure 4.86 details the measured thrust force, torque and corresponding cutting temperature in hole 180 when drilling through the CFRP layer (7mm thick) in Test 1 (fluid pressure of 10 bar and feed rate of 0.08mm/rev). A continuous rise in temperature was recorded from 23°C at the point of drill entry into the CFRP, up to 242°C upon exit of the tool from the workpiece. As with the Ti section, this implied low penetration of cutting fluid into the CFRP layer, leading to a drop in material strength/stiffness as evidenced by the corresponding reduction in average thrust force and torque from 376 to 124N and from 125 to 23.07N-cm respectively.

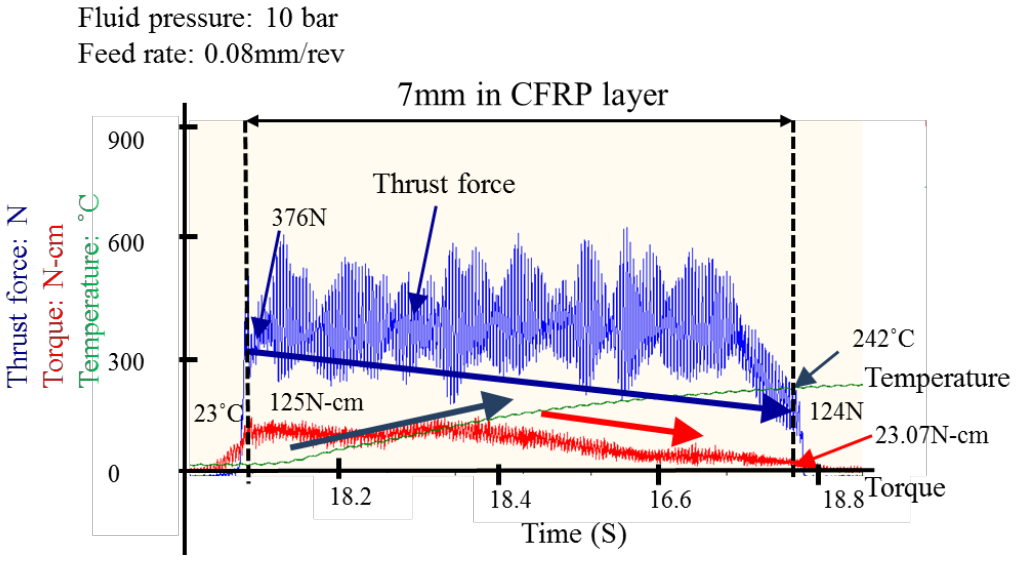


Figure 4.86 Thrust force, torque and temperature progression in CFRP layer for last hole in Test 1

Figure 4.87 shows the measured thrust forces, torque and corresponding cutting temperature for the last hole drilled in the Al layer in Test 1. Although exhibiting a gradual decreasing trend, the cutting temperature in the Al section remained elevated (even during the peck cycle) throughout the drilling operation, with only a 4% drop (207 to 198°C) observed in the final 5mm of the hole. The relatively slow rate of cooling further confirms the low volume of cutting fluid arriving at the bottom section of the stack under the applied machining environment (10 bar). The average thrust force and torque however remained approximately stable/constant over the distance machined, which suggests the absence of significant workpiece softening. This was possibly due in part to the comparatively high thermal conductivity of the aluminium alloy (154W/mK), which promoted rapid diffusion/dissipation of heat generated at the shear zone into the bulk material. Increasing the cutting fluid pressure to 35 and 70 bar in Tests 2 and 3 respectively yielded no significant differences in thrust force and torque responses (no apparent variation in values within a hole).

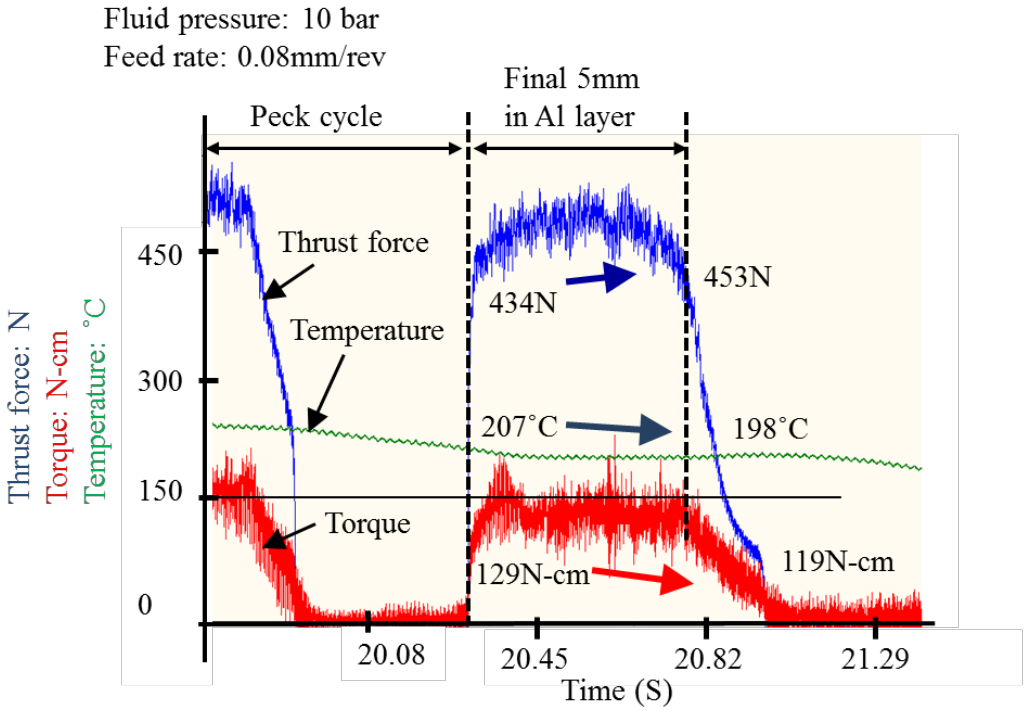


Figure 4.87 Thrust force, torque and temperature progression in Al layer for last hole in Test 1

Figure 4.88, Figure 4.89 and Figure 4.90 detail the progression of average thrust force and torque together with cutting temperature against the number of holes drilled in the titanium, CFRP and aluminium layers respectively, for all experiments. Both thrust forces and torque typically increased with the number of holes drilled due to the rise in tool wear. However,

when drilling at 0.08mm/rev, thrust forces in the Ti, CFRP and Al sections measured at the last hole were seen to increase by up to 22%, 22% and 13% respectively (from 1507, 626 and 638N), when operating with high pressure cutting fluid at 70 bar (Test 3) in comparison to 10 bar (Test 1). This was attributed to the deterioration in material strength as temperatures reached a maximum of ~ 351°C in the latter, as shown previously in Figure 4.83. Conversely, torque decreased by up to 54% when employing higher cutting fluid pressures.

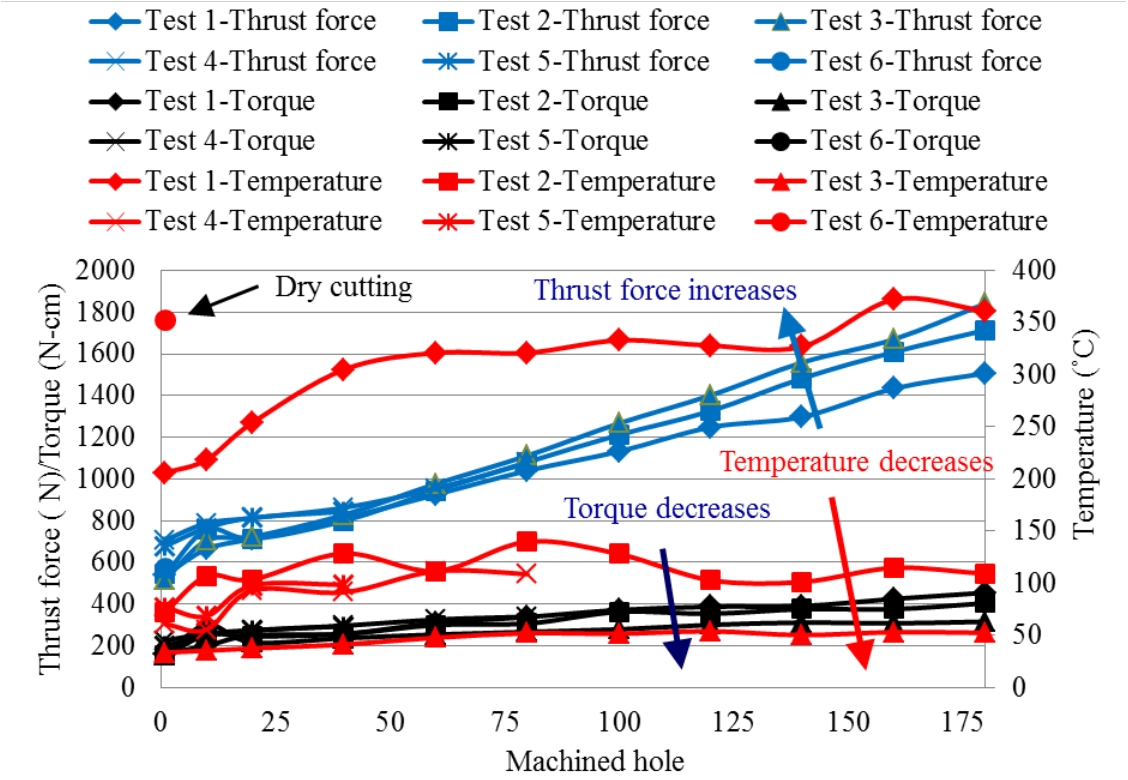


Figure 4.88 Progression of cutting force and temperature in the Ti layer for all tests

The efficiency of heat transfer/removal and lubrication is generally enhanced when applying cutting fluid at high pressures particularly for drilling operations, as it increases penetration into the shear zone as well as reducing tool-chip contact length, thereby reducing friction between the tool margin and machined surface [131]. When coolant is delivered through external jet nozzles, performance is also influenced by the direction of flow and location of cutting fluid impingement during the drilling process as well as the depth of hole machined. In the present work, the nozzles were fixed to the spindle and advanced together with tool feed, while the fluid jet was aimed towards the point geometry of the drill. The increase in cutting fluid pressure to 35 and 70 bar (Tests 2 and 3) from 10 bar (Test 1) when drilling at the lower feed rate of 0.08mm/rev was successful in improving the transport of

coolant into the titanium layer (10mm depth) at the top of the stack. This was evidenced by the significant reduction in cutting temperatures of up to ~ 70% and 86% respectively.

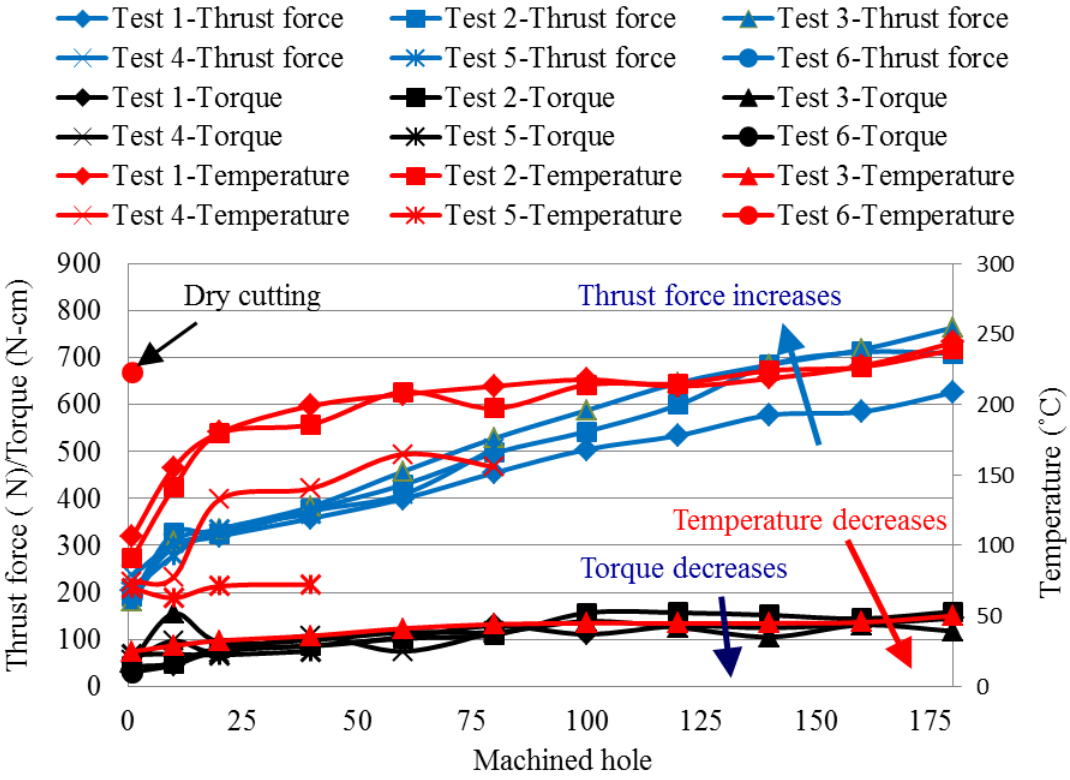


Figure 4.89 Progression of cutting forces and temperature in the CFRP layer for all tests

As the drill proceeded into the CFRP layer at a feed rate of 0.08mm/rev, the temperatures recorded were approximately equivalent when operating at 10 and 35 bar cutting fluid pressure, which was up to ~ 100°C even in the first hole and increased to a maximum of 242°C at test cessation (hole 180), see Figure 4.89. This suggests that similar to Test 1, a pump pressure of 35 bar in Test 2 was also inadequate in injecting sufficient cutting fluid deeper into the stack beyond the Ti plate, resulting in retardation of heat removal in the CFRP material. This was likely to have induced thermal damage in the polymer matrix (burning, melting, decomposition etc.) and causing severe weakening of the workpiece. In contrast, the application of coolant at 70 bar pressure in Test 3 managed to maintain temperatures in the CFRP below ~ 50°C throughout the experiment, which was comparable to results for the Ti layer. The associated maximum thrust force recorded at hole 180 was ~ 764N, which was understandably higher than values obtained in Tests 1 and 2. Nonetheless, the variation in cutting fluid pressure showed no appreciable influence on torque.

Similarly, for the Al layer at the bottom of the stack, cooling efficiency was poor when drilling at 10 and 35 bar due to low accessibility of cutting fluid into the hole, leading to a

rising trend in cutting temperatures from ~ 145°C in the first hole to ~ 242°C at test cessation, as illustrated in Figure 4.90. Corresponding thrust force was marginally higher at 671N in Test 2 (35 bar) compared to 638N in Test 1 (10 bar) after 180 holes, whilst the recorded torque was higher in the latter (224 vs. 188N-cm). Conversely, cutting temperatures while somewhat elevated (maximum of 137°C), remained relatively stable over the test duration when cutting fluid pressure was increased to 70 bar in Test 3, which was over 40% lower compared to results in Test 1 and 2 after drilling 180 holes. Consequently, the maximum thrust force rose to 723N whereas associated torque was lower by up to ~ 35% (145N-cm), probably due to superior lubrication from the increased volume of cutting fluid arriving at the Al section.

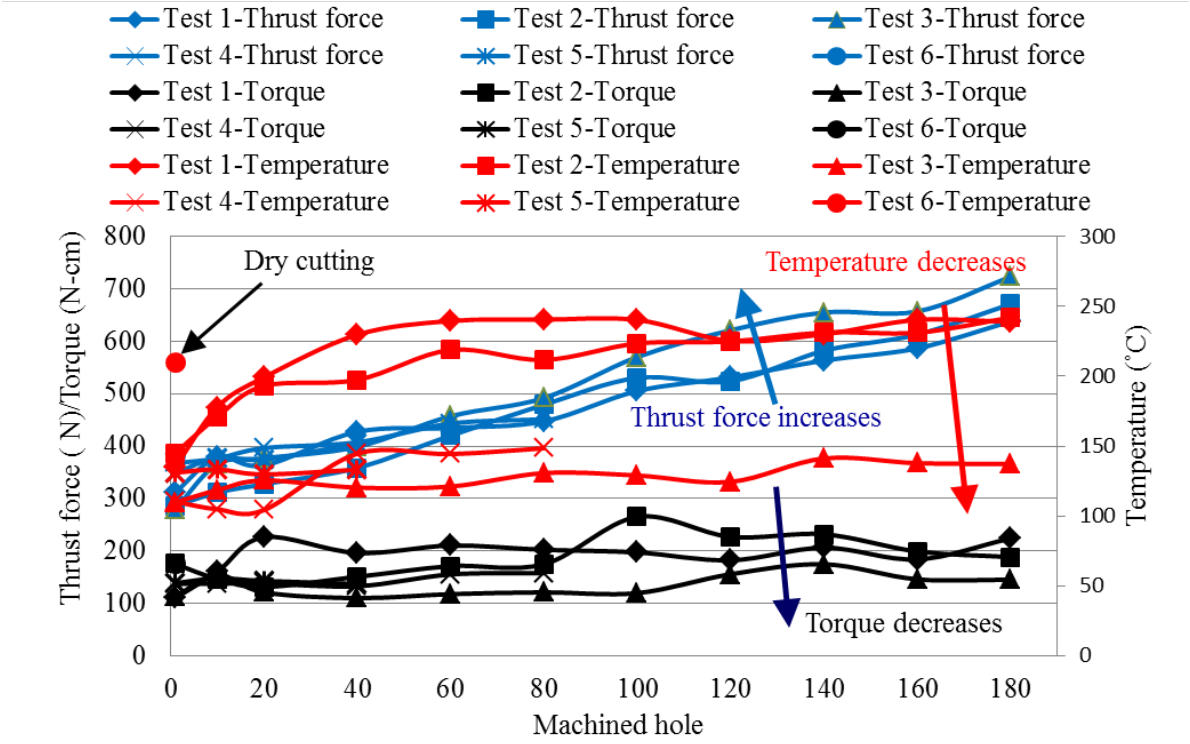


Figure 4.90 Progression of cutting force and temperature in Al layer for all tests

Raising the feed rate to 0.12mm/rev from 0.08mm/rev typically increased thrust forces by up to 36%, 31% and 24% in the Ti, CFRP and Al layers respectively for the first hole drilled, see Figure 4.88, Figure 4.89 and Figure 4.90. Similarly, torque levels rose by up to 49% in the Ti layer, 26% in the CFRP layer and 25% in the Al section. The influence of cutting fluid pressure on thrust forces when drilling at 0.12mm/rev however was negligible, with only a 2% discrepancy between Test 4 at 70 bar (843.8N) and Test 5 under 10 bar operation (862.7N) in the Ti layer after 30 holes, see Figure 4.88. Analogous trends were observed in

the CFRP and Al sections of the stack with torque results also exhibiting similar results. Unlike experiments at the lower feed rate of 0.08mm/rev, the effect of increasing fluid pressure (10 to 70 bar) on cutting temperature was less pronounced when drilling at 0.12mm/rev, particularly in the Ti and Al layers of the workpiece. This was possibly due to the shorter contact time between the drill and workpiece as well as greater deflection of cutting fluid when operating higher feed rates.

4.7.2 Tool wear and tool life

Figure 4.91 details the progression of flank wear against number of holes drilled in all tests. When drilling wet at 0.08mm/rev (Tests 1 – 3), all of the tools produced 180 holes without exceeding the flank wear criterion of 300µm, irrespective of the cutting fluid pressure applied. Tool life however declined considerably as feed rate increased to 0.12mm/rev, although the drill utilised in Test 4 together with 70 bar fluid pressure machined 80 holes compared to only ~ 30 holes when operating at 10 bar environment in Test 5. Rapid failure of the drill after only one hole was observer in Test 6 when drilling dry (flank wear over 800µm), with a maximum cutting temperature of ~ 352°C recorded as detailed in Section 4.7.1.

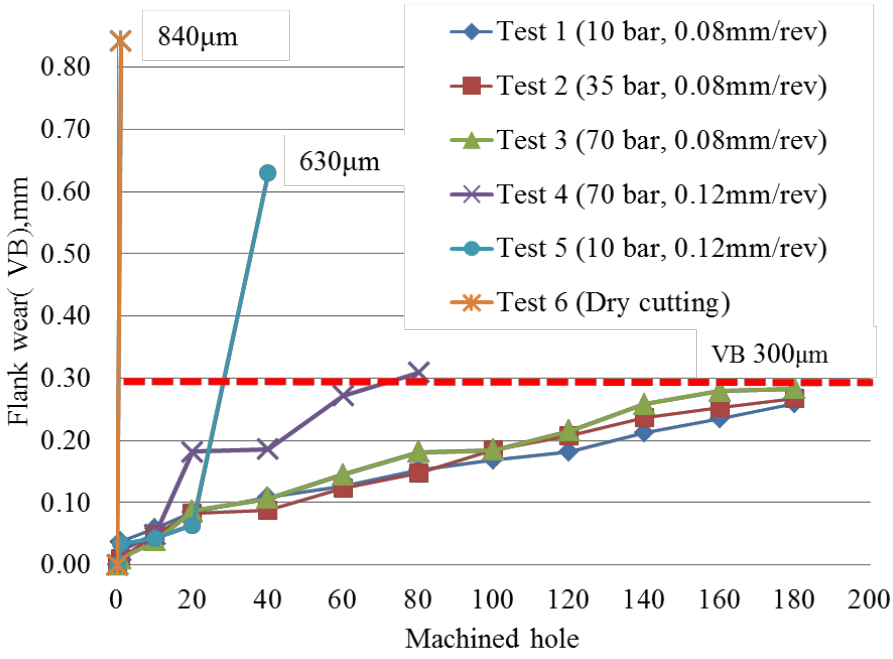


Figure 4.91 Progression of tool flank wear in all tests

Figure 4.92 shows micrographs of drill wear scars in Test 1 (0.08mm/rev feed rate and 10 bar fluid pressure) at different intervals of the trial. Sporadic signs of adhered aluminium workpiece material were observed after the first hole near the chisel edge, due to the lower cutting speed and effect of ploughing at this location. As cutting progressed, abrasion wear on the flank face was evident over the majority of the cutting lips and extending to the peripheral corners of the drill. The size of the abrasion wear scar as well as adhesion of Al alloy continued to grow steadily with increasing number of holes machined. At test cessation (180 holes), a substantial layer of adhered workpiece material was clearly visible along the entire length of the flute cutting edge, see Figure 4.92.

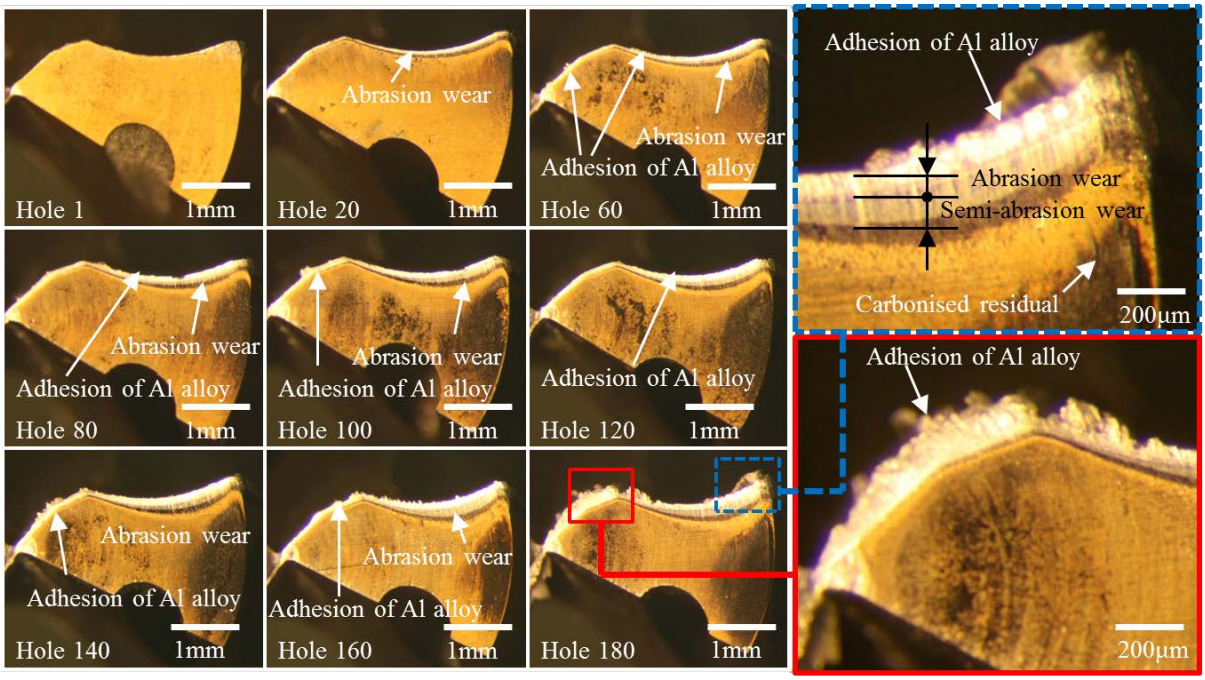


Figure 4.92 Micrographs of drill wear scar progression in Test 1

Further analysis of thrust force data recorded in the aluminium layer revealed a moderate rise between holes 140 to 180 in Figure 4.90, which could be attributed to the increasing adhesion of the workpiece material on the drill as shown in Figure 4.92. The adhered material/BUE near the chisel edge (bottom magnified image) was commonly observed as a protruding section normal to the rake face resulting from the low cutting speed and near 0° rake angle, which leads to ploughing at the tool-chip interface. Conversely, workpiece adhesion located at the cutting lips near the peripheral corner (top magnified image) developed due to the expected higher cutting temperatures.

Figure 4.93(a) and 4.93(b) detail the flank wear scars at test cessation when drilling at the higher feed rate (0.12mm/rev) and cutting fluid pressures of 70 and 10 bar in Tests 4 and 5 respectively. While tool life was higher in the former, both drills exhibited similar wear patterns with a combination of abrasion along the cutting lips and premature delamination of the coating at the peripheral corner. Similar coating delamination was also apparent in Test 6 after only one hole when machining dry at a lower feed rate of 0.08mm/rev, see Figure 4.93(c). This was most likely due to a combination of thermal and mechanical effects, derived from the dissimilar thermal expansion rates (6.5 and 5.6µm/K) and elastic moduli (515 and 580GPa) between the TiAlN/TiN coating layer and WC substrate. The exposed carbide substrate was more prone to adhesion of the Al workpiece material as highlighted from the SEM micrographs of the drill corners. The delamination wear pattern however was not present in any of the trials undertaken at 0.08rev/min (Tests 1 to 3).

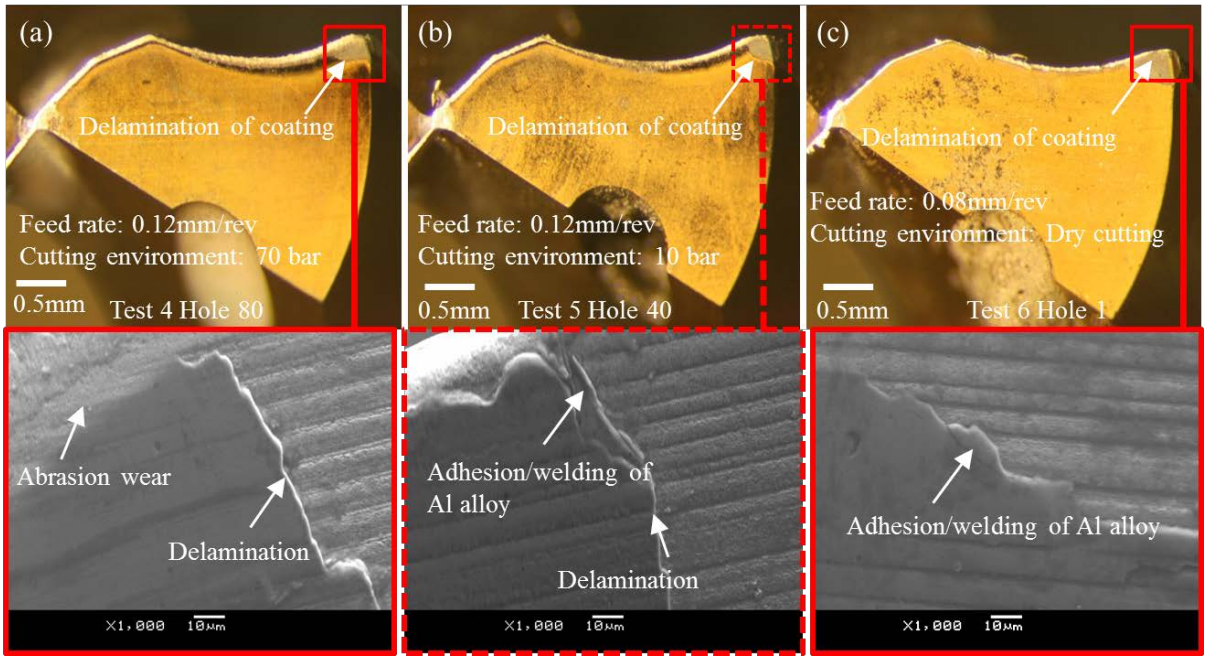


Figure 4.93 Optical and SEM micrographs of tool wear patterns after the last hole drilled in Tests 4, 5 and 6

4.7.3 Hole accuracy (diameter, out of roundness, and cylindricity)

Figure 4.94 details the average hole diameters in each layer as well as the overall stack measured over the drill life for all tests. The average hole diameter in the CFRP layer was typically larger compared to the Ti and Al sections when drilling with 0.08mm/rev feed rate under dry or low (10 bar) and intermediate (35 bar) pressure cutting fluid environments (Tests 1, 2 and 6). Additionally, the hole was oversized when machining dry in Test 6, which was most likely attributed to the rapid increase in cutting temperature leading to thermal expansion

of the workpiece materials and degradation of matrix material in CFRP. Hole diameter however was well within the upper and lower tolerance band (6.35 ± 0.04mm) when drilling using high pressure cutting fluid (70 bar) or at elevated feed rate of 0.12mm/rev, with relatively low spread of data/variation ranging between 6.32-6.37mm. In addition to lower anticipated thermal damage at high pressure fluid conditions, increasing feed rate also typically reduced the tendency for drill wander/eccentricity.

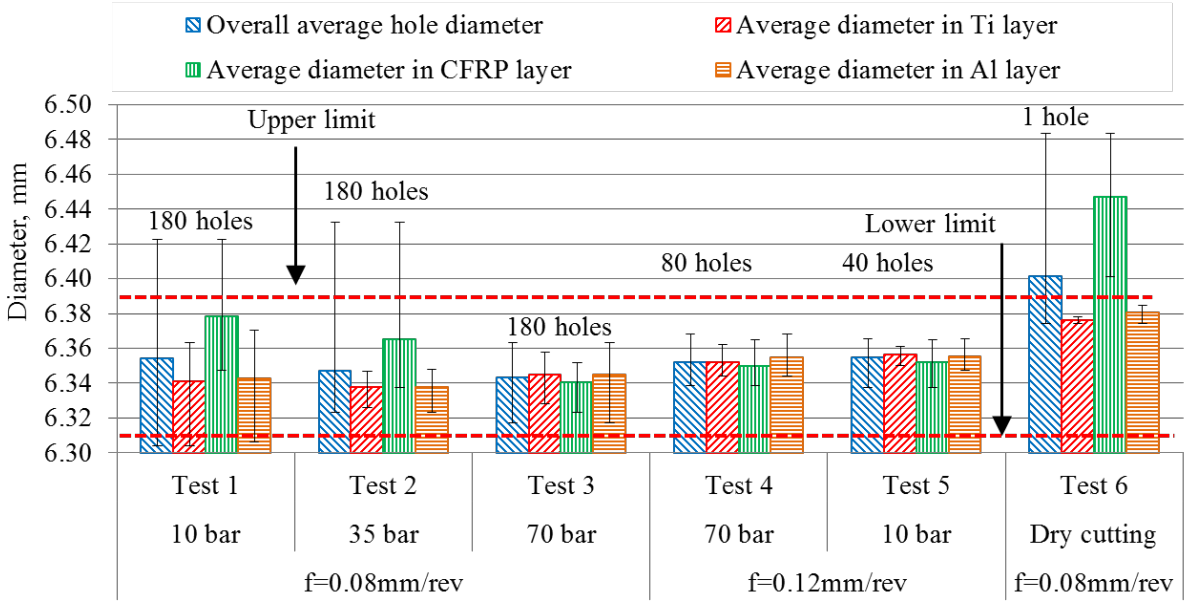


Figure 4.94 Average hole diameter over test duration in all experiments

Average hole cylindricity and the out of roundness in each material layer is outlined in Figure 4.95 for all trials. In general, the majority of hole form profiles produced in single-shot drilling of three-layer stacks exhibited bell-mouthing [83, 86], which is primarily influenced by tool wear. When drilling at a feed rate of 0.08mm/rev, the best hole cylindricity after 180 holes was obtained in Test 3 with an average of 104.4µm while corresponding out of roundness did not exceed 50µm in any of the material sections. Hole cylindricity improved by ~ 15% as feed rate was increased to 0.12mm/rev (Tests 4 and 5) compared to the results in Test 3, albeit with significantly lower tool life/number of holes drilled. Furthermore, the change in cutting fluid pressure however did not appear to have any substantial impact on average hole cylindricity and out of roundness, with the exception of the titanium layer. This was possibly due to the comparable wear modes/patterns at the drill periphery in Tests 4 and 5, thereby resulting in similar hole accuracies.

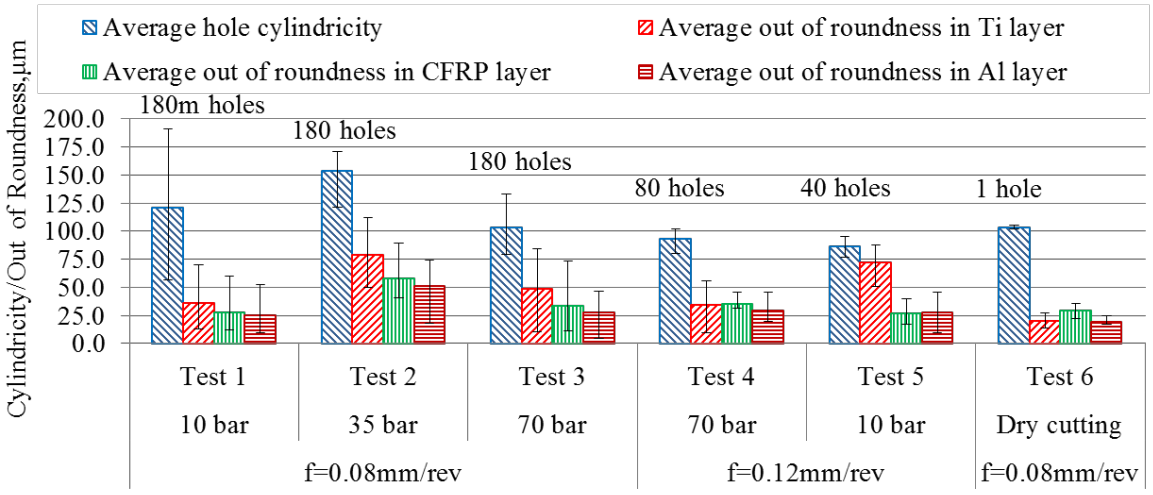


Figure 4.95 Average hole cylindricity and out of roundness over test duration in all experiments

4.7.4 Burr formation

Figure 4.96 details the progression of burr height measured at the hole entrance location of titanium layers over the duration of each trial. The largest burr height measured at hole entrance was 0.14mm after 180 holes when drilling at 0.08mm/rev feed rate and employing 70 bar cutting fluid pressure in Test 3.

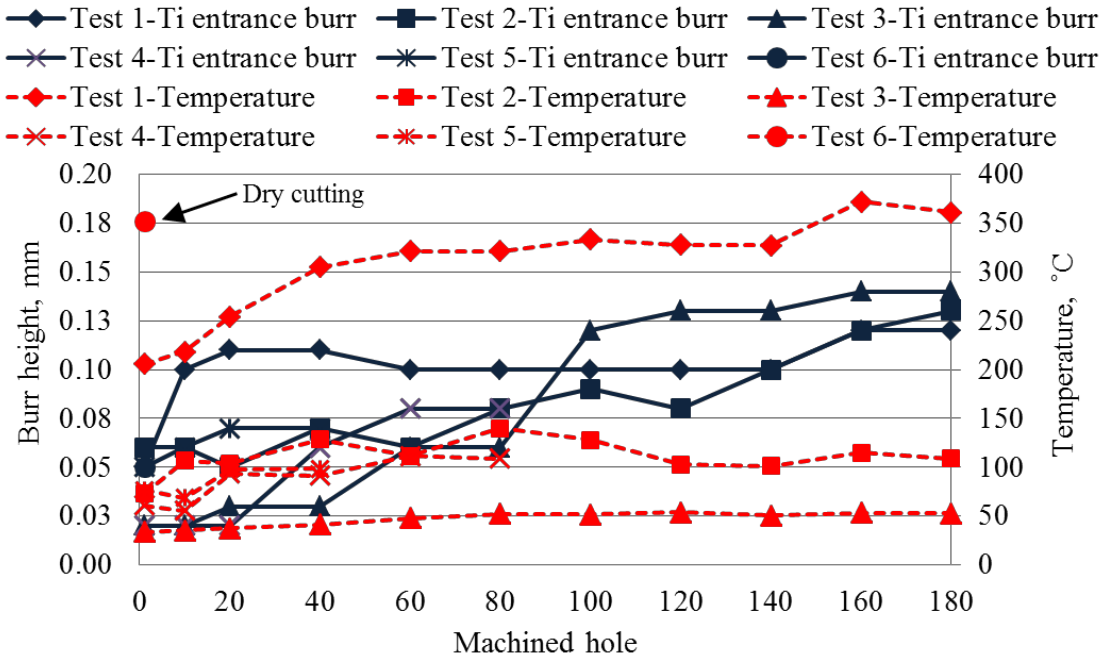


Figure 4.96 Progression of entrance burr height in the Ti layer for all tests

When drilling under lower cutting fluid pressure of 10 bar in Test 1, burr height increased up to ~0.11mm after 80 holes due to the greater material plasticity at high temperatures (~325°C). In contrast, when cutting fluid pressure was increased to 70 bar in Test 3, the burr height reduced to 0.07mm after 80 holes due to improved supply of cutting fluid and lower temperatures. However, a steep rise in entrance burr height to 0.12mm was observed in hole 100, with subsequent increments to a maximum 0.14mm at hole 160. Despite the cutting temperature in Test 3 remaining low (maximum of ~ 50°C) throughout the experiment (Figure 4.88), the formation of larger burrs during the latter part of the experiment was most likely due to the somewhat increasing tool wear rate after hole 100, see Figure 4.91. Larger burrs were also obtained as feed rate was increased to 0.12mm/rev in Test 4 compared to results from Test 1 at 0.08mm/rev.

Figure 4.97 details the progression of exit burr height in the aluminium layers for all tests. The trials conducted at a feed rate of 0.08mm/rev with cutting fluid pressures varying from 10 to 70 bar (Tests 1 to 3) showed that there was a strong correlation between burr height the cutting temperature. Burr size was typically stable at ~ 0.06mm in Test 3 involving high pressure fluid of 70 with comparatively lower cutting temperatures of ~137.3°C recorded. In contrast, burr height increased to a maximum of ~0.12mm in Tests 1 and 2, which were performed at lower cutting fluid pressures leading to elevated temperatures (up to ~242°C) and higher deformation of the workpiece. Research involving forming operations by Abedrabbo et al. [206] suggested that the plasticity of aluminium alloy increased with the working temperature, with strains up to 0.42 recorded at 260°C, which was twice that when performed at room temperature (25°C). The influence of temperature on burr formation was particularly pronounced in Test 6 when drilling dry, with the resultant burr height measuring 0.22mm after the first hole with a corresponding cutting temperature of 210°C.

When feed rate increased to 0.12mm/rev using 70 bar cutting fluid pressure in Test 4, the burr height within the first 40 holes was smaller in comparison to when drilling at 0.08mm/rev feed rate. This was due to the shorter tool-workpiece contact time in the former, which hindered material stretching and pivoting at the exit location; resulting in the reduction of burr growth [174]. However, after hole 40, the higher feed rate (0.12mm/rev) produced ~60% larger burr height (0.08mm) due to the increase of tool wear and corresponding cutting temperature from 104 to 144°C.

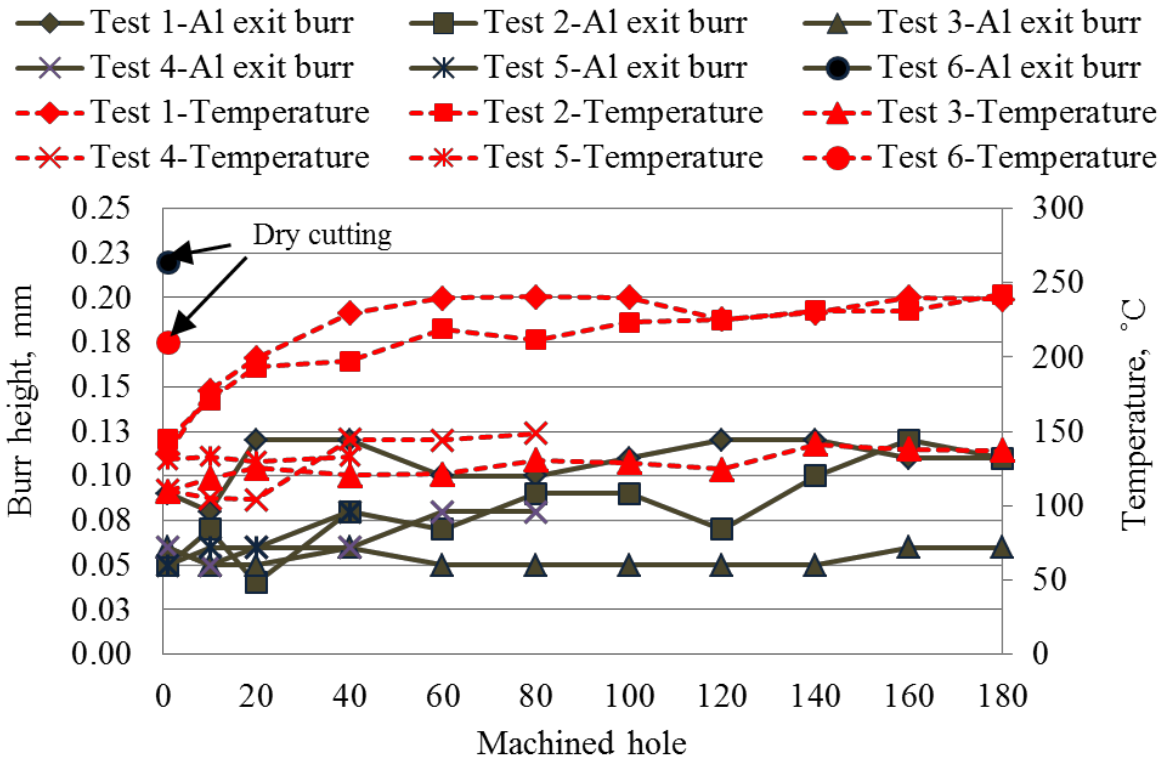


Figure 4.97 Progression of exit burr height in Al layer for all tests

4.7.5 Hole surface roughness

Figure 4.98 presents results of average hole surface roughness (Ra) for each material layer in all tests. Average hole surface roughness in the titanium and aluminium layers were comparable in all tests performed wet (Tests 1 to 5) and ranged between 0.6 and 0.85µm Ra. Additionally, none of the individual measurements exceeded 1.4µm Ra irrespective of feed rate and fluid pressure, which was within the typical industrial requirements of 1.6µm Ra for metallic materials. Corresponding roughness levels in the CFRP sections however were up to 10 fold higher (~14µm Ra), but with average values decreasing as cutting fluid pressure increased when drilling at 0.08mm/rev (Tests 1 to 3). This was due to the greater levels of matrix degradation and fibre pullout on hole surfaces machined with lower fluid pressures (higher temperatures), resulting in increased cavities particularly in the 135° and 45° plies, see 3D topographic scan in Figure 4.99.

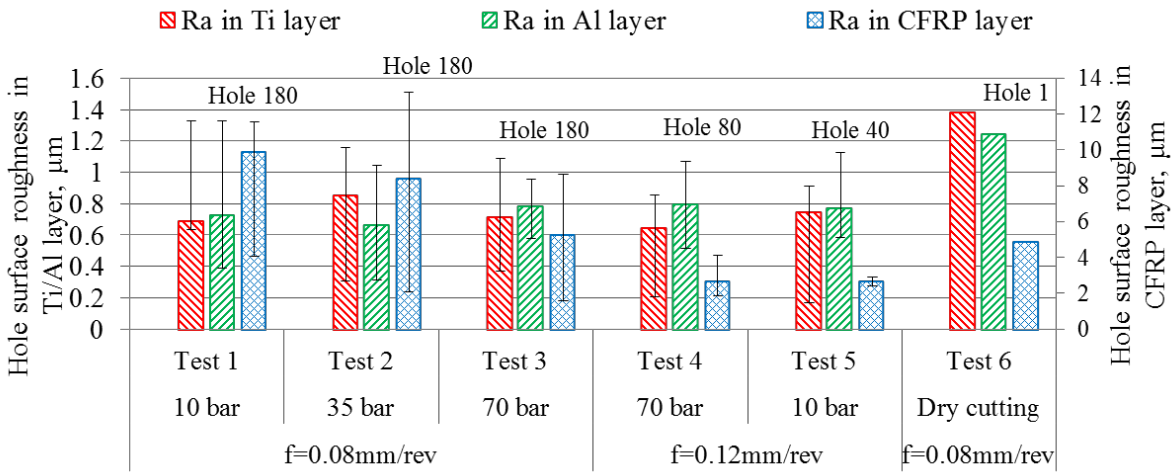


Figure 4.98 Average hole surface roughness (Ra) in Ti, CFRP and Al layers

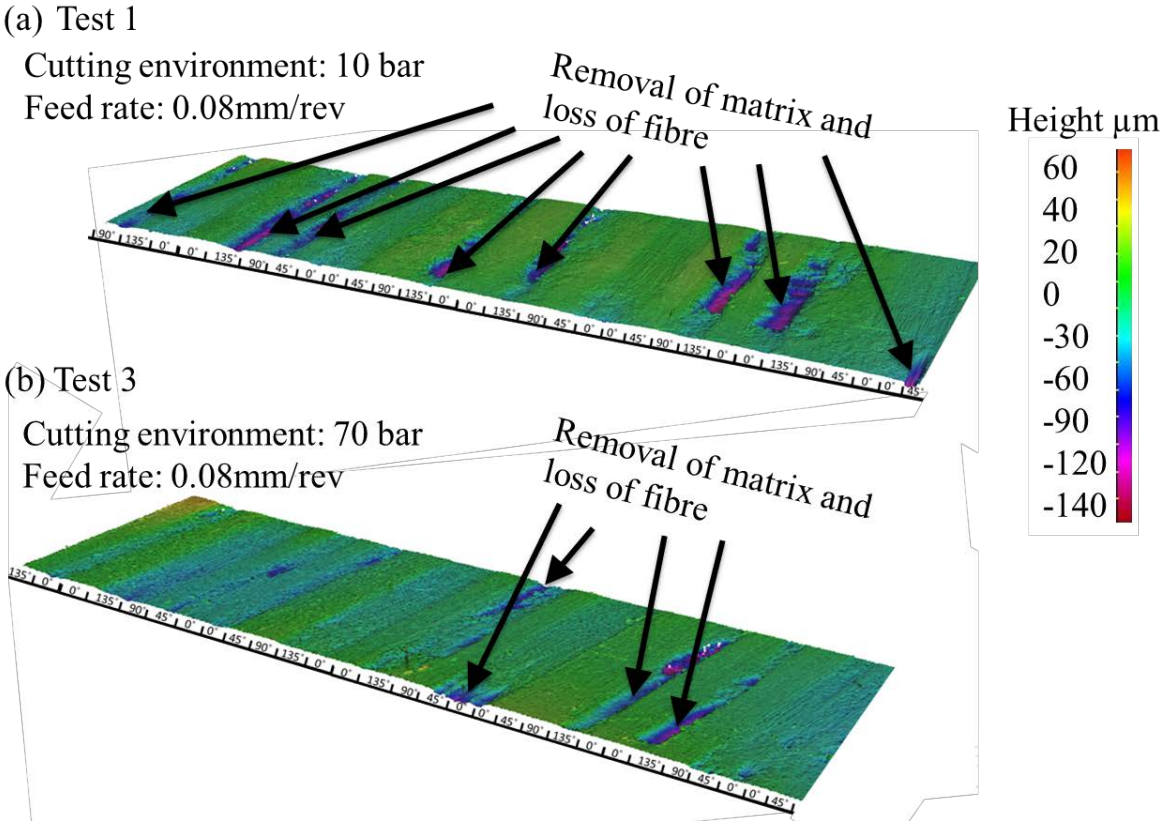


Figure 4.99 Three dimensional surface topography scan of hole surface in CFRP layer from (a) Test 1 and (b) Test 3

When feed rate increased to 0.12mm/rev, average hole surface roughness in the CFRP layer improved to < 3.0µm Ra with a relatively narrow spread of results in both trials involving low and high pressure cutting fluid. The superior surface roughness was attributed to the comparatively low levels of wear at the drill corners prior to tool failure from coating delamination/flaking. Conversely, measured surface roughness was 1.40, 5.70 and 1.23µm Ra in the Ti, CFRP and Al layers respectively after only one hole when drilling dry in Test 6.

4.7.6 Subsurface workpiece microstructure and microhardness

Figure 4.100 shows micrographs of workpiece subsurface microstructure for the last hole drilled in the Ti layer for all tests. None of the samples evaluated exhibited any signs of material phase variation or plastic deformation with the exception of Test 3, where a layer of bent grains was observed extending up to 70µm beneath the hole surface. This was most likely due to the highest thrust forces generated (~1850N) when drilling with 70 bar cutting fluid (low cutting temperatures) as detailed previously in Figure 4.88.

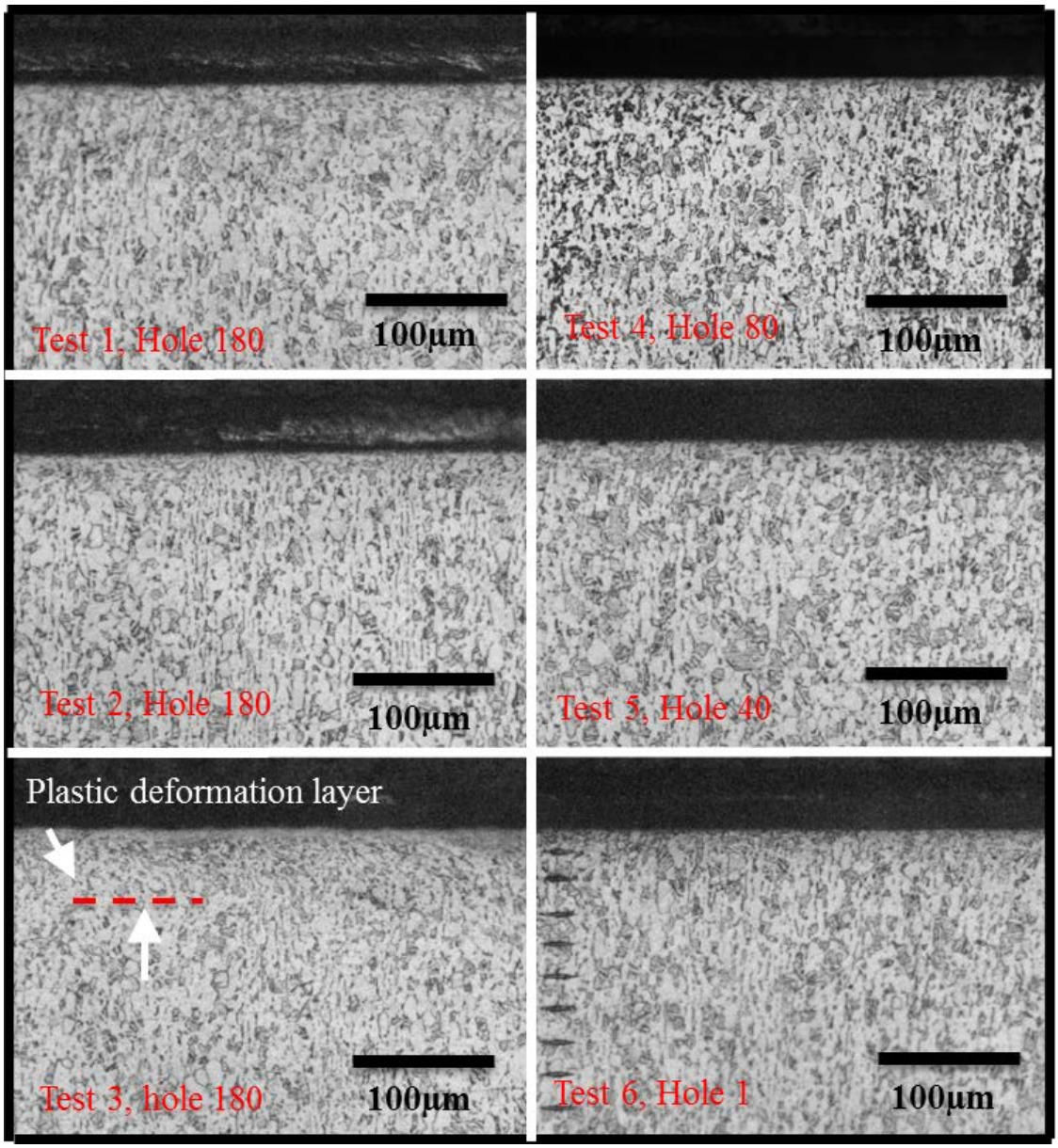


Figure 4.100 Micrographs of microstructure alteration in Ti layer at the last hole

Figure 101 shows images of machined surfaces in the CFRP layer (area of 1mm×2mm) obtained using an Alicona system with vertical and lateral resolutions of 563nm and 3.91µm

respectively at the last hole drilled for each test. Except for Test 6, all of the scanned surfaces revealed clear evidence of matrix/fibre removal and delamination, albeit at different degrees of severity depending on the operating conditions. The highest level of damage was seen in Test 1 due to the elevated cutting temperature of 244°C generated while the holes in Test 3 yielded better surface quality due to the considerably lower temperature of ~ 50°C. Although not shown here, matrix cracking was also apparent up to depths of ~6µm and ~9µm when feed rate was increased by 50% in Test 4 and Test 5 respectively.

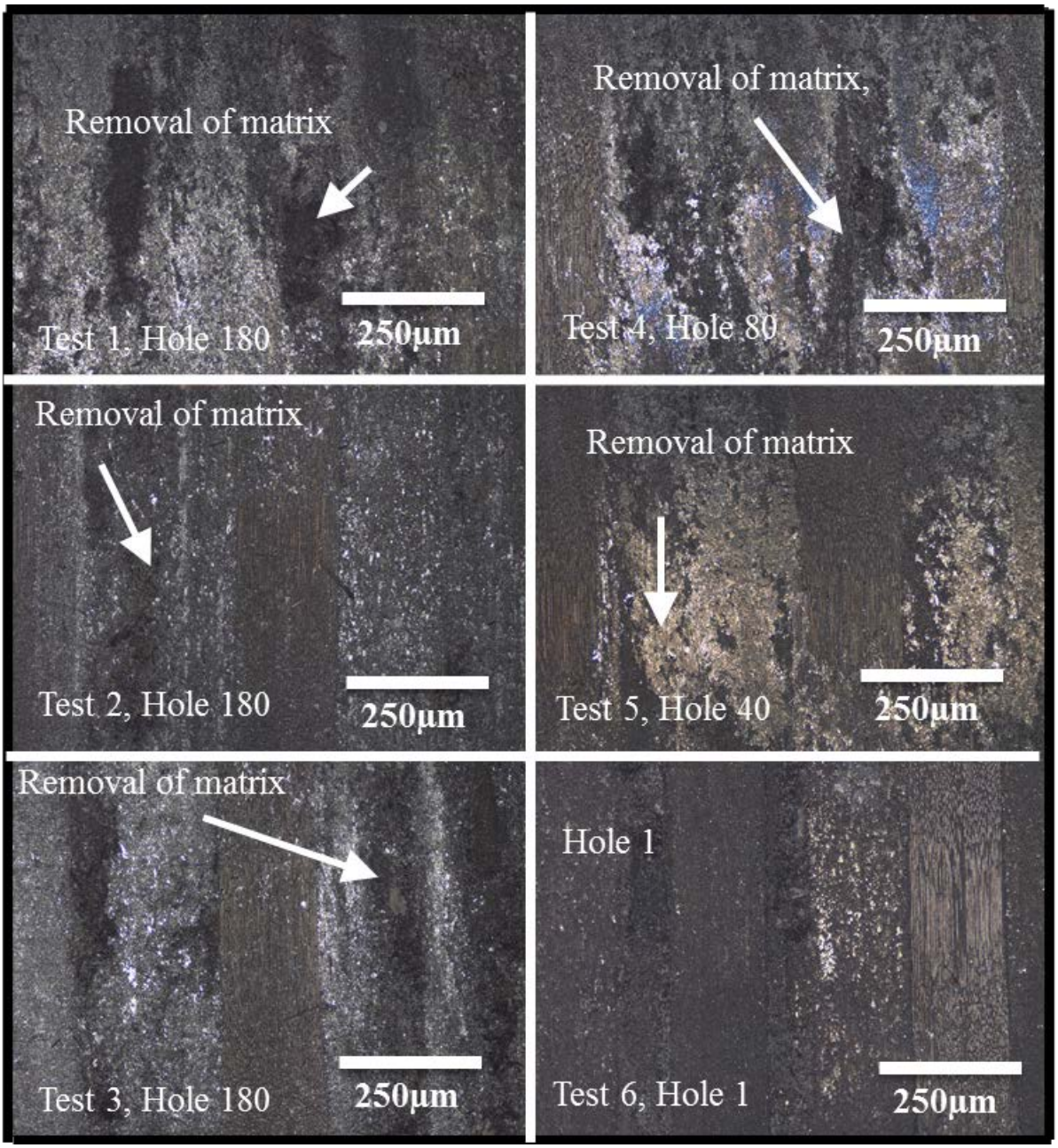


Figure 4.101 Micrographs of surface texture in CFRP layer at the last hole

Figure 4.102 details cross-sectional optical micrographs of subsurface microstructures at the last hole drilled in the Al layer for all tests. As with results in the Ti layer, only the hole produced in Test 3 at 70 bar fluid pressure and a feed rate of 0.08mm/rev revealed signs of deformed microstructure to a depth of ~50µm. This was also attributed to the high thrust force of 723N due to the lower cutting temperatures generated, see Figure 4.90.

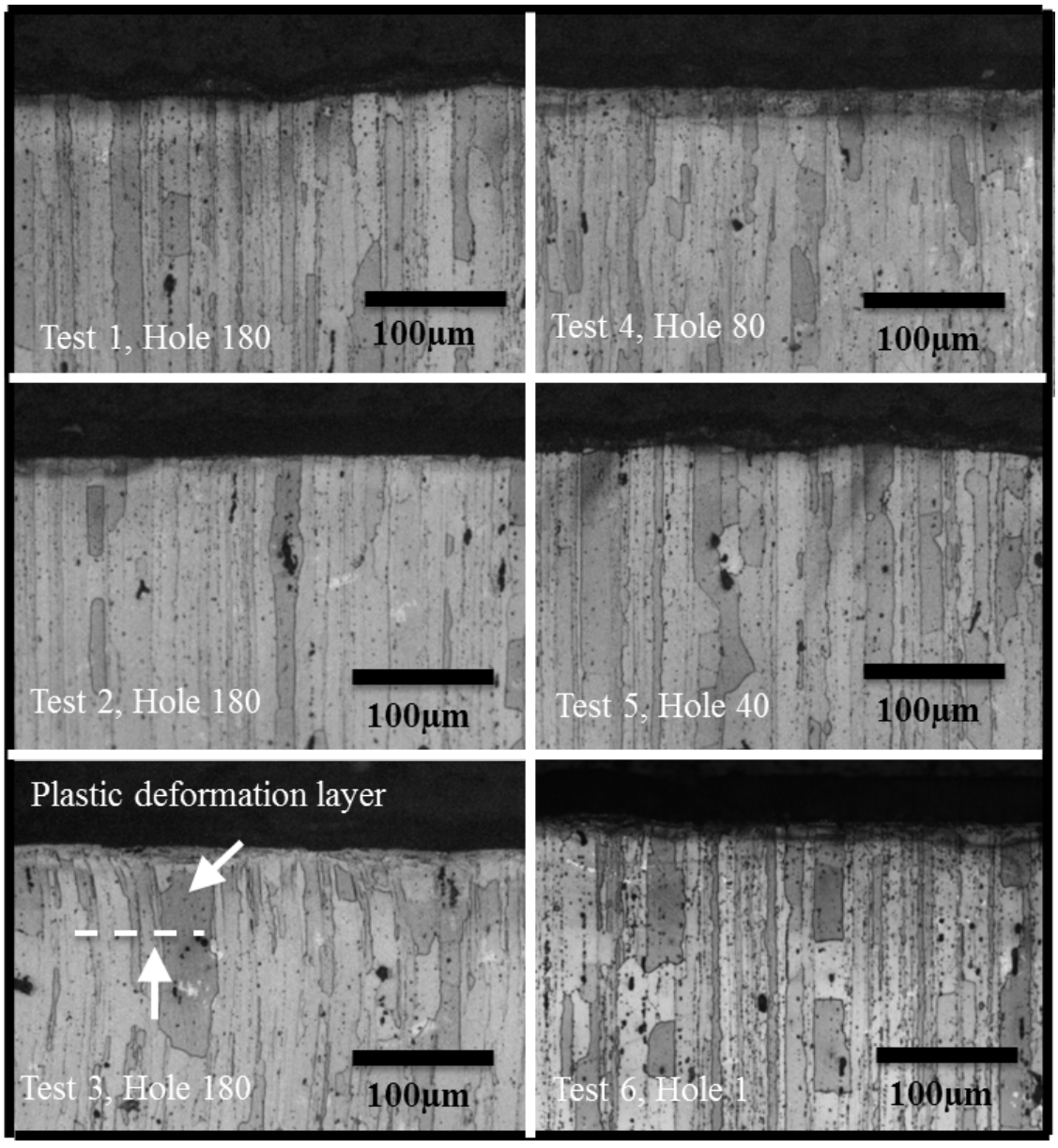


Figure 4.102 Micrographs of subsurface microstructure in Al layer at the last hole

Figure 4.103 details the microhardness depth profiles measured for the last hole drilled in the Ti layer for all tests. A reduction in workpiece microhardness of up to 29% ($240.73HK_{0.025}$) below the bulk material hardness ($340HK_{0.025}$) was observed in Test 1, which confirms the occurrence of thermal softening to a depth of ~150µm. This was due to the high

temperatures generated (352°C) resulting from the poor transport of fluid to the cutting zone at 10 bar pressure. In contrast, a hardened region of up to ~360 and 375.73HK$_{0.025}$ extending to a depth of ~ 80µm beneath the hole surface was seen in Tests 2 and 3 respectively. The relatively lower temperatures when drilling with intermediate and high pressure cutting fluid meant that workpiece strain hardening was dominant, which correlates with the deformed microstructure seen in Figure 4.100. When feed rate was increased to 0.12mm/rev in Tests 4 and 5, no major change in workpiece microhardness was apparent, except for marginal softening in the latter. Similarly, workpiece microhardness remained unchanged when drilling dry, although the trial was halted after only one hole due to premature failure of the cutting tool.

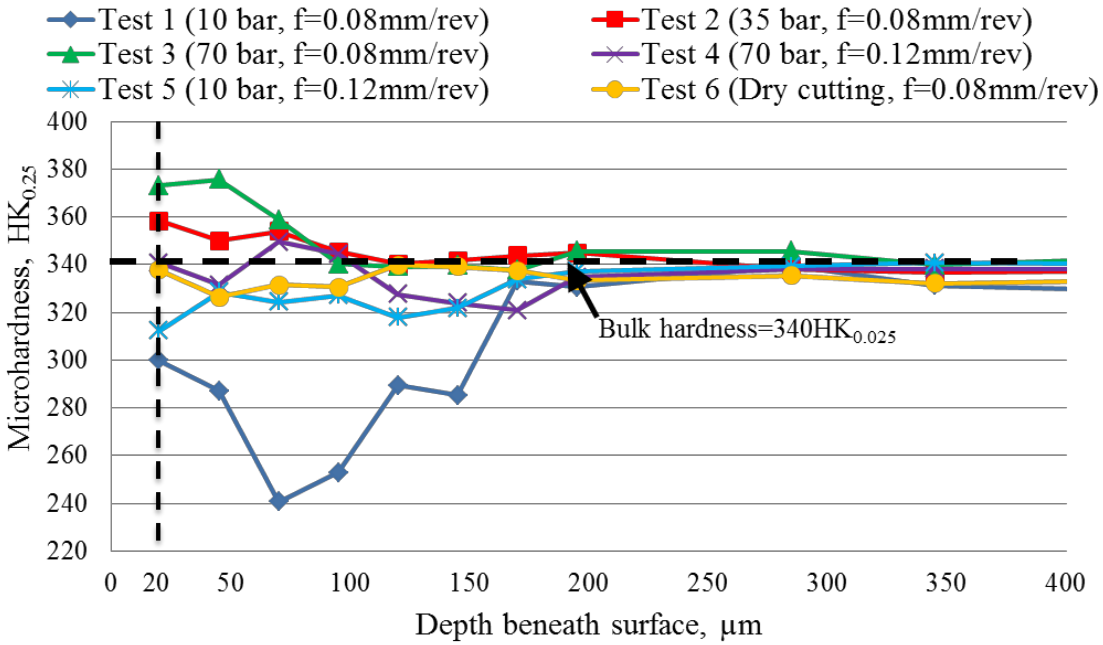


Figure 4.103 Microhardness depth profile measurement for the last hole drilled in the Ti layer for all tests

The microhardness depth profiles measured at the last hole in the Al layer for all tests are shown in Figure 4.104. When drilling at a feed rate of 0.08mm/rev and cutting fluid pressure of 10 bar (Test 1), the elevated temperature (~242°C) most likely resulted in the ~ 10% drop in microhardness (~152HK$_{0.025}$) near the surface of the hole. Conversely, when drilling at cutting fluid pressure of 70 bar, the hole subsurface microhardness showed no appreciable difference compared to the bulk hardness value. This was attributed to the lower cutting temperatures (~137.3°C) produced in the shear zone, which minimised workpiece thermal softening. When operating with the higher feed rate of 0.12mm/rev in Tests 4 and 5, a minor

increase in microhardness (up to 15$HK_{0.025}$ above bulk hardness) was detected. This was attributed to the increased feed rate yielding higher thrust forces (405 – 451N) coupled with relatively low cutting temperatures (maximum of ~ 133 - 149°C).

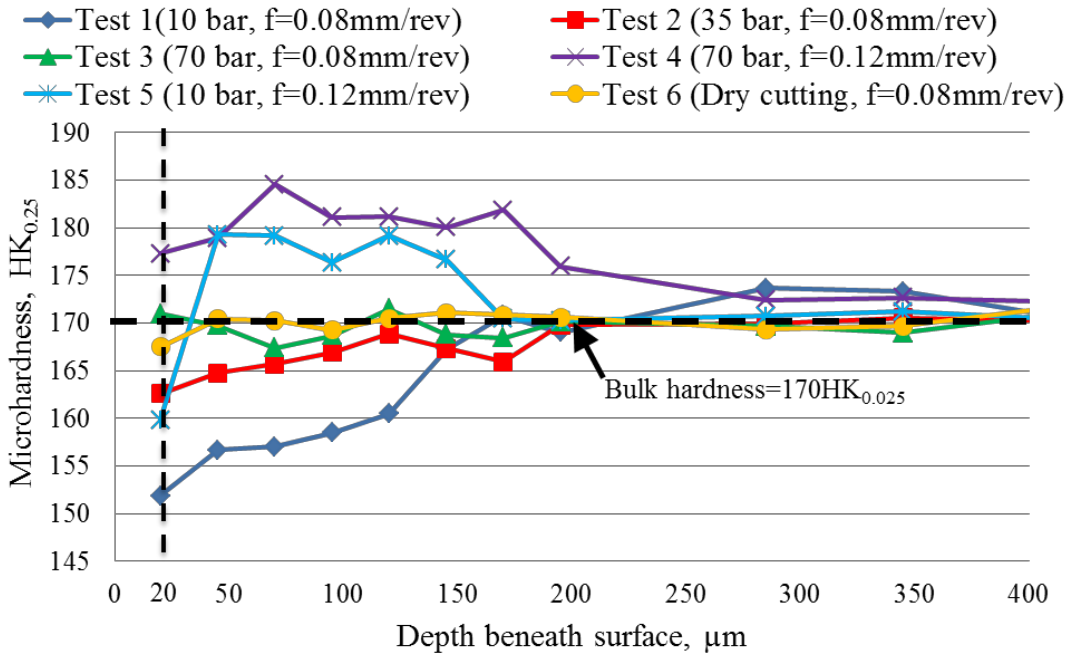


Figure 4.104 Microhardness depth profile measurement for the last hole drilled in the Al layer for all tests

5 CONCLUSIONS

5.1 Literature review

- The recommended cutting conditions for single-shot drilling of Ti/CFRP/Al stacks are a cutting speed range of 15-30m/min and feed rate of 0.05-0.08mm/rev when using K10-20 carbide drills. Alternative solutions include WC with higher cobalt content (K30-K40) at increased feed rates (0.08-0.12mm/rev) together with a carbon based coating (e.g. DLC/CVD diamond coatings), which generally forms a protective layer of TiC during machining to prevent solution/diffusion wear.
- Drilling of structural aluminium alloys can be performed at cutting speeds and feed rates of up to ~200m/min and ~0.10mm/rev respectively using PCD tools, with minimal BUL/BUE even in the dry condition. Alternatively, the use of diamond coated (DLC/CVD-diamond) WC drills is capable of producing comparable performance at lower cost.
- When drilling CFRP laminates, PCD is recommended due to its superior abrasion resistance and edge geometry, although WC is still the predominant tool material employed due to cost restrictions.
- A dual stage cutting speed (30/120/120m/min) with a feed rate of 0.05mm/rev is recommended in order to achieve acceptable hole quality and surface integrity when single-shot drilling Ti/CFRP/Al stacks.
- There is currently limited published data relating to the influence of drill geometry parameters when single-shot drilling multilayer metallic-composite stacks.

5.2 Experimental work

5.2.1 Effect of tool material, feed rate and drilling strategy

- Uncoated carbide drills showed longer tool life (by up to 90 holes) compared to equivalent coated tools irrespective of the feed rate and pecking strategy employed, with flank wear < 0.3mm even after 180 holes, which was partially attributed to the lower cutting edge radius in the former (sharper).
- Drilling at the higher feed of 0.08mm/rev produced lower thrust forces due to the increase in effective rake angle.
- Increasing feed rate was seen to suppress burr formation at the hole exit due to greater shearing rather than material deformation.

- Coated tools produced superior hole diameter accuracy due to lower wear rates at the drill peripheral corners.
- Coated carbide tools produced lower cylindricity because of the larger radius at the chisel edge, providing better drill centring and restricting ‘walking’ during machining, thereby minimising tri-lobed hole profiles.
- Use of a pecking strategy reduced the maximum roughness in the CFRP layer due to greater rubbing action during tool retraction. In contrast, roughness in the Ti layer deteriorated when employing a peck cycle possibly resulting from drill chatter/vibration.
- Drilling with pecking typically resulted in a hardened layer extending to ~100µm beneath the hole surface in the Ti layer.

5.2.2 Influence of margin design, feed rate and drilling strategy

- Thrust force and torque typically increased by a maximum of 67 and 160% respectively when drilling Ti-6Al-4V/CFRP/A7050 stacks using triple margin tools. This was mainly due to the increased frictional contact between the tool and workpiece surface.
- Feed rate was significant factor with respect to tool life, while the effects of margin design and drilling strategy were minimal. Reducing feed rate and drilling without pecking resulted in a minor increase in tool wear.
- Margin design had a significant influence on hole diameter, regardless of feed rate and drilling strategy. Triple-margin drills produced smaller diameters due to the reduction in vibration resulting from increased contact with the machined surface.
- Burr height at the hole entrance (titanium) and exit (aluminium) of the stack workpieces increased by up to ~430% when utilising triple margin drills, due to the greater contact between tool and machined surface.
- Hole surface roughness in the metallic layers of the stack were typically 2 to 3 times higher when utilising triple margin drills in comparison to the conventional single margin geometry. This trend however was reversed in the CFRP section due to the greater levels of matrix smearing and lower incidence of uncut fibres when employing the former drill design.

5.2.3 Hole quality and failure modes of diamond coated tools

- Wear of the DLC coated drills at a feed rate of 0.08mm/rev was initially dominated by abrasion, with increasing levels of workpiece adhesion and micro chipping evident as machining progressed. Tool failure occurred in the form of drill corner fracture due to

attrition from the repeated cycle of adhered material build up and removal, resulting in plucking of the coating and weakening of the substrate material.

- The primary wear mode of the CVD diamond coated drill at 0.08mm/rev was premature flaking/delamination of the coating, particularly in the vicinity of the chisel section, which finally resulted in fracture after 70 holes. This was most likely due to the double point design, which concentrated the thrust forces over a relatively small area.
- Both thrust force and torque in the titanium layer increased significantly when machining at the higher feed rate of 0.15mm/rev using the DLC coated drill, with values of ~2500N and 725N-cm recorded after 70 holes. This was ~150% and 60% higher than corresponding levels at 0.08mm/rev respectively.
- The failure mechanism of the DLC coated drill when operating at 0.15mm/rev was brittle fracture due to a low cycle fatigue condition. This was most likely induced by the large variation in thrust forces (up to ~1000N) acting on the drill as it moved through the titanium and CFRP/Al layers of the stack.
- Despite severe flaking/chipping, the CVD diamond coated drill produced superior hole quality coupled with reduced burring compared to the DLC coated tools due to the two stage point design and lower geometrical damage at the peripheral corner.

5.2.4 Effect of drill point geometry

- When using drills with 140° point angle, 30° helix angle and thinned web to a chisel diameter of 0.1mm, the measured thrust force and torque were reduced to 1156N (27%) and 318N-cm (16%) in comparison with a standard drill having a 0.35mm chisel edge. The reduction in cutting force can be attributed to the more effective cutting action alongside the chisel zone via the thinned chisel, positive rake angle and larger space for chip evacuation.
- At the chisel zone, built-up edge (BUE) developed through adhesion of workpiece material due to the low cutting speed.
- The preferred operating parameters for minimum burr height in the aluminium layer was a chisel diameter 0.1mm, a point angle of 140° (PCR of 85.2%) and a helix angle of 30°/40°, since the larger point angle resulted in smaller strains at the periphery.
- A larger helix angle (40°) increased hole diameters in the titanium layer (PCR of 60.8%) however, in the CFRP layer, a smaller helix angle (20°) led to larger diameter holes with a PCR of 50.1%. Increasing helix angle generally reduces tool rigidity leading to possible vibration and enlarged hole diameters in the Ti layer. Conversely, the high thrust forces

may have caused fuzzing / exposed uncut fibres, leading to smaller diameters in the CFRP layer.

- None of the drill geometry variables was statistical significant with respect to cylindricity and out of roundness. However, the preferred factor levels were a point angle of 140°, helix angle of 30° and chisel diameter of 0.1mm, which minimised hole cylindricity (52µm) and out of roundness (24, 30 and 27µm in the titanium, CFRP and aluminium respectively).
- Drills with a high helix angle (40°) produced lower surface roughness values in the titanium layer with the factor statistically significant and having a PCR of 42.7%. In contrast, increasing point angle (140°) had a significant influence on reducing surface roughness values in the CFRP layer with a corresponding PCR of 86.3%.

5.2.5 Evaluation of diamond coated/novel PCD drills and feed rate at elevated cutting speed

- Thrust forces were 22-25% and 37-41% lower in the titanium and CFRP layer respectively for the first hole when employing domed PCD drills compared to CVD diamond coated carbide tools while corresponding torque was similarly 15.2% and 17.8% lower.
- The fracture modes of the domed PCD drills were micro-chipping at the chisel zone as well as gross fracture at the peripheral corner.
- The fracture mode of the CVD diamond coated drills was cyclic flaking/delamination of the coating at the cutting lips coupled with adhesion/BUE, which resulted in unbalanced forces on the cutting lips leading to premature fracture of the chisel edge and peripheral corner.
- When operating at high feed rate (0.12mm/rev), the CVD diamond coated drills exhibited lower levels of flaking and delamination in comparison when drilling at 0.05mm/rev and 0.08mm/rev.
- Tests carried out using the domed PCD drills generally produced greater hole surface roughness compared to the CVD diamond coated tools. This was due to premature micro/macro fracture at the peripheral corners in the former, while the primary wear mode of the latter was flaking/delamination of the coating.
- The relatively poor tool life of the PCD drills was attributed to the tool geometry/design employed, which was inappropriate particularly for the drilling of titanium alloys.
- No significant changes in workpiece microhardness (Ti and Al layers) were observed at test cessation, irrespective of the tool material or feed rate employed. Similarly, no subsurface microstructural modification or damage was apparent in any of the metallic samples evaluated.

- Surface defects in the form of grooves due to fibre loss and matrix cracking were evident particularly on the 45° and 135° direction plies of the CFRP layers when drilling with the domed PCD tools. In contrast, tests involving the CVD diamond coated drills caused only minor matrix smearing with some evidence of micro cracking on the workpiece surface.

5.2.6 Confirmation test and benchmarking of bespoke drill geometry

- The bespoke drill geometry outperformed the coated carbide (Section 4.1), uncoated carbide (Section 4.1) and triple margin drills (in Section 4.2) in 12, 18 and 13 of the 19 measures analysed, including thrust force, torque, tool wear, hole diameter, out of roundness, hole cylindricity, burr height and surface roughness.
- When compared to the DLC drill, the optimum designed drill was superior in 13 of the 19 responses, except for the thrust force and entrance burr in the Ti layer, hole surface roughness in the CFRP layer as well as thrust force and torque in the Al layer.
- When compared to CVD diamond coated drills, the optimum designed drills showed limited benefits, with improvements in only 5 of the response measures (out of 19), which included torque in the CFRP layer, out of roundness, exit burr and hole surface roughness in the Al layer together with overall tool wear.

5.2.7 Effect of cutting environment and feed rate

- When drilling with 10 bar cutting fluid pressure at a feed rate of 0.08mm/rev, a significant increase in temperature was observed in the Ti layer (up to ~300°C in hole 180) over the last 4mm of the workpiece. A corresponding reduction in thrust force (37%) was also evident, suggesting the presence of thermal softening.
- Minimal variation in cutting temperature and thrust forces in the Ti layer were observed (within each hole) when operating at 70 bar pressure, indicating an improvement in cooling efficiency.
- Operating with high cutting fluid pressure (70 bar) and a feed rate of 0.08mm/rev led to the best results with respect to hole diameter (6.32-6.36mm), hole cylindricity (104.4µm) and out of roundness (Ti: 48.7µm, CFRP: 33.8µm, Al: 27.9µm).
- Cutting fluid pressures (10-70 bar) did not have any significant influence on the average hole surface roughness (0.70-0.85µm Ra) in the metallic layers, however surface roughness in the CFRP layer generally improved when drilling with high pressure cutting fluid environment (70 bar).

- Subsurface analysis showed a decrease in microhardness of up to 29% and 10% in the Ti and Al layers respectively when operating at 10 bar fluid pressure. Conversely, up to 11% increase in hardness was observed in the Ti layer when drilling under 70 bar cutting fluid pressure, while negligible variation was detected in the Al layer.

5.3 Overall conclusions and recommended operating conditions

5.3.1 Tool material, coating and point geometry

The suggested tool material for single-shot drilling of Ti/CFRP/Al stacks is submicron tungsten carbide (K30-K40) with 10% Co binder (K30-K40) coated with TiAlN/TiN. The recommended point geometry is a point angle 140°, helix angle of 40° and chisel diameter of 0.1mm.

5.3.2 Operating parameters

The preferred operating parameters is a cutting speed of 30/120/120m/min for a Ti/CFRP/Al stack arrangement with a constant feed rate of 0.08mm/rev.

5.3.3 Cutting environment

The recommended cutting environment is wet at a pressure of 70 bar, preferably via through-tool coolant supply.

6 RECOMMENDATIONS FOR FUTURE WORK

A list of publications stemming from the project is detailed in Appendix 6; however, a number of issues have been identified which warrants further investigation. These include:

- Evaluation of diamond coated and domed PCD drills with the preferred drill geometry when drilling Ti/CFRP/Al stacks.
- Finite element simulation of single shot drilling of multilayer metallic composite stacks using different tool material/geometry.
- Temperature measurement when drilling Ti/CFRP/Al stacks with through tool cutting fluid application.

REFERENCES

1. Ezugwu, E.O. and Wang, Z.M., Titanium alloys and their machinability--a review. Journal of Materials Processing Technology, 1997. 68(3): p. 262-274.
2. Yamada, M., An overview on the development of titanium alloys for non-aerospace application in Japan. Materials Science and Engineering: A, 1996. 213(1-2): p. 8-15.
3. Boyer, R., Welsch, G., and Collings, E.W., Materials properties handbook: titanium alloys. 1994, Material Park, OH: ASM International
4. Leyens, C. and Peters, M., eds. Titanium and titanium alloys. 2003, Wiley-VCH: Weinheim.
5. Boyer, R.R., An overview on the use of titanium in the aerospace industry. Materials Science and Engineering, 1996. A213: p. 103-114.
6. Nabhani, F., Machining of aero titanium alloys. Robotics and Computer Ietegrated Manufacturing 2001. 17: p. 99-106.
7. Donachie, M.J., Titanium : A Technical Guide. 1988, Material Park, OH: ASM international
8. Ezugwu, E.O., Key improvements in the machining of difficult-to-cut aerospace superalloys. International Journal of Machine Tools and Manufacture, 2005. 45(12-13): p. 1353-1367.
9. Zoya, Z.A. and Krishnamurthy, R., The performance of CBN tools in the machining of titanium alloys. Journal of Materials Processing Technology, 2000. 100(1-3): p. 80-86.
10. Narutaki, N., Murakoshi, A., Motonishi, S., and Takeyama, H., Study on Machining of Titanium Alloys. CIRP Annals - Manufacturing Technology, 1983. 32(1): p. 65-69.
11. Karpat, Y., Temperature dependent flow softening of titanium alloy Ti6Al4V: An investigation using finite element simulation of machining. Journal of Materials Processing Technology, 2011. 211(4): p. 737-749.
12. Hartung, P.D., Kramer, B.M., and von Turkovich, B.F., Tool Wear in Titanium Machining. CIRP Annals - Manufacturing Technology, 1982. 31(1): p. 75-80.
13. Komanduri, R. and Von Turkovich, B.F., New observations on the mechanism of chip formation when machining titanium alloys. Wear, 1981. 69(2): p. 179-188.
14. Trent, E. and Wright, P., Metal cutting. 4th ed. 2000, Woburn: Butterworth-Heinemann. 446.
15. Shaw, M.C., Metal cutting principles. 2nd ed. 2005, New York: Oxford University Press, Inc. 651.
16. Shaw, M.C. and Vyas, A., Chip Formation in the Machining of Hardened Steel. CIRP Annals - Manufacturing Technology, 1993. 42(1): p. 29-33.
17. Degarmo, E.P., Black, J., and Kohser, R.A., Materials and processes in manufacturing. 9th ed. 2003, Hoboken: John Wiely & Sons,Inc
18. Anon, Metal reference book 3rd ed, ed. Bauccio, M. 1993, USA: ASM international.
19. Williams, J.C. and Starke, E.A., Progress in structural materials for aerospace systems. Acta Materialia, 2003. 51(19): p. 5775-5799.
20. Polmear, I., Light alloys: Metallurgy of the light metals. 3rd ed. 1995, London: Arnold, Holder Headline PLC.
21. König, W. and Erinski, D., Machining and Machinability of Aluminium Cast Alloys. CIRP Annals - Manufacturing Technology, 1983. 32(2): p. 535-540.
22. Nouari, M., List, G., Girot, F., and Coupard, D., Experimental analysis and optimisation of tool wear in dry machining of aluminium alloys. Wear, 2003. 255(7–12): p. 1359-1368.

23. Sánchez, J.M., Rubio, E., Álvarez, M., Sebastián, M.A., and Marcos, M., Microstructural characterisation of material adhered over cutting tool in the dry machining of aerospace aluminium alloys. Journal of Materials Processing Technology, 2005. 164–165(0): p. 911-918.
24. Fukui, H., Okida, J., Omori, N., Moriguchi, H., and Tsuda, K., Cutting performance of DLC coated tools in dry machining aluminum alloys. Surface and Coatings Technology, 2004. 187(1): p. 70-76.
25. Lequeu, P., Lassince, P., and Warner, T., Aluminium alloy development for the airbus A380-Part 1. Advanced materials and processs, 2007: p. 33-35.
26. Lequeu, P., Lassince, P., and Warner, T., Aluminium alloy development for the airbus A380-Part 2. Advanced materials and processes, 2007: p. 41-44.
27. Miller, F.P., Vandome, A.F., and McBrewster, J., Carbon fiber-reinforced polymer. 2009: Alphascript Publishing.
28. Gill, R.M., Carbon fibres in composite materials. Engineering, Chemistry, ed. R.M. Ogorkiewicz, P.D.R. 1972: Iliffe Books.
29. Soutis, C., Carbon fiber reinforced plastics in aircraft construction. Materials Science & Engineering, 2005. 412(1-2): p. p. 171-176
30. Vijayaraghavan, A. Drilling of fiber-reinforced plastics-tool modeling and defect prediction. 2006; Available from: www.cs.berkeley,edu/~sequin/CS285/PAPERS/ Athulan-Masters.pdf.
31. Peters, S.T., Introduction, composite basics and road map. Handbook of composites 1998, London: Chapman & Hall.
32. Sheikh-Ahmad, J.Y., Machining of polymer composites. 2009: Springer Science+Business Media.
33. Astrom, B.T., Manufacturing of polymer composites. 1997, London: Chapman & Hall.
34. Mallick, P.K., Fiber reinforced composites- material, manufacturing and design. 2007, New York: CRC Press.
35. Watt, W., Carbon work at the Royal Aircraft Establishment. Carbon, 1972. 10(2): p. 121-143.
36. Morgan, P., Carbon fibers and their composites. 2005, London: CRC press.
37. Chen, J.C. and Harrison, I.R., Modification of polyacrylonitrile (PAN) carbon fiber precursor via post-spinning plasticization and stretching in dimethyl formamide (DMF). Carbon, 2002. 40(1): p. 25-45.
38. The Japan Carbon Fibre Association. Types of carbon fibre products and their special features. 2010; Available from: http://www.carbonfiber.gr.jp/english/transo/02.html.
39. Wang, D.H., Ramulu, M., and Arola, D., Orthogonal cutting mechanisms of graphite/epoxy composite. Part I: unidirectional laminate. International Journal of Machine Tools and Manufacture, 1995. 35(12): p. 1623-1638.
40. Wang, D.H., Ramulu, M., and Arola, D., Orthogonal cutting mechanisms of graphite/epoxy composite. Part II: multi-directional laminate. International Journal of Machine Tools and Manufacture, 1995. 35(12): p. 1639-1648.
41. Wang, X.M. and Zhang, L.C., An experimental investigation into the orthogonal cutting of unidirectional fibre reinforced plastics. International Journal of Machine Tools and Manufacture, 2003. 43(10): p. 1015-1022.
42. Arola, D., Ramulu, M., and Wang, D.H., Chip formation in orthogonal trimming of graphite/epoxy composite. Composites Part A: Applied Science and Manufacturing, 1996. 27(2): p. 121-133.
43. Rawat, S. and Attia, H., Wear mechanisms and tool life management of WC–Co drills during dry high speed drilling of woven carbon fibre composites. Wear, 2009. 267(5–8): p. 1022-1030.

44. Chen, W.-C., Some experimental investigations in the drilling of carbon fiber-reinforced plastic (CFRP) composite laminates. International Journal of Machine Tools and Manufacture, 1997. 37(8): p. 1097-1108.
45. König, W. and Graß, P., Quality Definition and Assessment in Drilling of Fibre Reinforced Thermosets. CIRP Annals - Manufacturing Technology, 1989. 38(1): p. 119-124.
46. Koplev, A., Lystrup, A., and Vorm, T., The cutting process, chips, and cutting forces in machining CFRP. Composites, 1983. 14(4): p. 371-376.
47. Hocheng, H. and Puw, H.Y., On drilling characteristics of fiber-reinforced thermoset and thermoplastics. International Journal of Machine Tools and Manufacture, 1992. 32(4): p. 583-592.
48. Hocheng, H. and Tsao, C.C., Comprehensive analysis of delamination in drilling of composite materials with various drill bits. Journal of Materials Processing Technology, 2003. 140(1-3): p. 335-339.
49. Hocheng, H. and Tsao, C.C., The path towards delamination-free drilling of composite materials. Journal of Materials Processing Technology, 2005. 167(2-3): p. 251-264.
50. Peters, S.T., Overview of composite materials. Handbook of composite. 1998: Chapman & Hall
51. Bhatnagar, N., Ramakrishnan, N., Naik, N.K., and Komanduri, R., On the machining of fiber reinforced plastic (FRP) composite laminates. International Journal of Machine Tools and Manufacture, 1995. 35(5): p. 701-716.
52. El-Sonbaty, I., Khashaba, U.A., and Machaly, T., Factors affecting the machinability of GFR/epoxy composites. Composite Structures. 63(3-4): p. 329-338.
53. Lin, S.C. and Chen, I.K., Drilling carbon fiber-reinforced composite material at high speed. Wear, 1996. 194(1-2): p. 156-162.
54. Arul, S., Vijayaraghavan, L., Malhotra, S.K., and Krishnamurthy, R., The effect of vibratory drilling on hole quality in polymeric composites. International Journal of Machine Tools and Manufacture, 2006. 46(3-4): p. 252-259.
55. Campos Rubio, J.C., Abrão, A.M., Eustáquio Faria, P., Correia, A.E., and Davim, J.P., Delamination in High Speed Drilling of Carbon Fiber Reinforced Plastic (CFRP). Journal of Composite Materials, 2008. 42(15): p. 1523-1532.
56. Khashaba, U.A., Delamination in drilling GFR-thermoset composites. Composite Structures. 63(3-4): p. 313-327.
57. Durão, L.M.P., Gonçalves, D.J.S., Tavares, J.M.R.S., de Albuquerque, V.H.C., Aguiar Vieira, A., and Torres Marques, A., Drilling tool geometry evaluation for reinforced composite laminates. Composite Structures, 2010. 92(7): p. 1545-1550.
58. Faraz, A., Biermann, D., and Weinert, K., Cutting edge rounding: An innovative tool wear criterion in drilling CFRP composite laminates. International Journal of Machine Tools and Manufacture, 2009. 49(15): p. 1185-1196.
59. Poutord, A., Rossi, F., Poulachon, G., M'Saoubi, R., and Abrivard, G., Local Approach of Wear in Drilling Ti6Al4V/CFRP for Stack Modelling. Procedia CIRP, 2013. 8(0): p. 315-320.
60. Park, K.-H., Beal, A., Kim, D., Kwon, P., and Lantrip, J., Tool wear in drilling of composite/titanium stacks using carbide and polycrystalline diamond tools. Wear, 2011. 271(11-12): p. 2826-2835.
61. Burianek, D.A. and Spearing, S.M., Fatigue damage in titanium-graphite hybrid laminates. Composites Science and Technology, 2002. 62(5): p. 607-617.
62. Carvajal, R., González-R, P.L., and Lozano, S., Research study of factors affecting difference between hole diameters in hybrid metal-composite drilling. Proceedings of the Institution of Mechanical Engineers, Part B: Journal of Engineering Manufacture, 2011. 225(7): p. 991-1000.

63. Denkena, B., Boehnke, D., and Dege, J.H., Helical milling of CFRP-titanium layer compounds. CIRP Journal of Manufacturing Science and Technology, 2008. 1(2): p. 64-69.
64. Zitoune, R., Krishnaraj, V., and Collombet, F., Study of drilling of composite material and aluminium stack. Composite Structures, 2010. 92(5): p. 1246-1255.
65. Zitoune, R., Krishnaraj, V., Sofiane Almabouacif, B., Collombet, F., Sima, M., and Jolin, A., Influence of machining parameters and new nano-coated tool on drilling performance of CFRP/Aluminium sandwich. Composites Part B: Engineering, 2012. 43(3): p. 1480-1488.
66. Garrick, R., Drilling Advanced Aircraft Structures with PCD (Poly-Crystalline Diamond) Drills. ASE international, 2007.
67. Kim, D. and Ramulu, M., Drilling process optimization for graphite/bismaleimide-titanium alloy stacks. Composite Structures, 2004. 63(1): p. 101-114.
68. Ramulu, M., Branson, T., and Kim, D., A study on the drilling of composite and titanium stacks. Composite Structures, 2001. 54(1): p. 67-77.
69. Brinksmeier, E. and Janssen, R., Drilling of Multi-Layer Composite Materials consisting of Carbon Fiber Reinforced Plastics (CFRP), Titanium and Aluminum Alloys. CIRP Annals - Manufacturing Technology, 2002. 51(1): p. 87-90.
70. Shyha, I.S., Soo, S.L., Aspinwall, D.K., Bradley, S., Perry, R., Harden, P., and Dawson, S., Hole quality assessment following drilling of metallic-composite stacks. International Journal of Machine Tools and Manufacture, 2011. 51(7–8): p. 569-578.
71. Zheng, L., Wang, C., Yang, L., Song, Y., and Fu, L., Characteristics of chip formation in the micro-drilling of multi-material sheets. International Journal of Machine Tools and Manufacture, 2012. 52(1): p. 40-49.
72. Watson, A.R., Geometry of drill elements. International Journal of Machine Tool Design and Research, 1985. 25(3): p. 209-227.
73. Armarego, E.J.A. and Cheng, C.Y., Drilling with flat rake face and conventional twist drills--I. Theoretical investigation. International Journal of Machine Tool Design and Research, 1972. 12(1): p. 17-35.
74. Bhattacharyya, A., Metal cutting theory AND PRACTICE. 1984, Kolkata: New central book agency.
75. Merchant, M.E., Mechanics of the Metal Cutting Process. I. Orthogonal Cutting and a Type 2 Chip. Journal of Applied Physics, 1945. 16(5): p. 267-275.
76. Watson, A.R., Drilling model for cutting lip and chisel edge and comparison of experimental and predicted results. I -- initial cutting lip model. International Journal of Machine Tool Design and Research, 1985. 25(4): p. 347-365.
77. Standard, B., B.S. 328, in Part 1. 1959.
78. El-Hofy, H., Fundmentals of machining process: conventional and nonconventional process. 2006, Boca Raton: Taylor & Francis Group, LLC.
79. Moufki, A., Molinari, A., and Dudzinski, D., Modelling of orthogonal cutting with a temperature dependent friction law. Journal of the Mechanics and Physics of Solids, 1998. 46(10): p. 2103-2138.
80. F.A.A., Boeing 787 Dreamliner composite profile. 2014, http://www.airporttech.tc.faa.gov//safety/bagot2.asp.
81. Stephan, P.M., Hay, R.A., and Dean, C.D., The new diamond technology and its application in cutting tools. Diamond and Related Materials, 1992. 1(5-6): p. 710-716.
82. Liu, H. and Dandy, D.S., Diamond CVD Techniques, in Diamond Chemical Vapor Deposition. 1996, William Andrew Publishing: Park Ridge, NJ. p. 14-45.
83. Kuo, C.L., Soo, S.L., Aspinwall, D.K, Bradley, S., Thomas, W., M'Saoubi, R., Pearson, D., and Leahy, W., Tool wear and hole quality when single shot drilling of metallic-composite stacks with diamond coated tools Proceedings of the Institution of

Mechanical Engineers, Part B: Journal of Engineering Manufacture, 2014, 228(10): p. 1314-1322.
84. Ema, S., Fujii, H., and Marui, E., Cutting performance of drills with three cutting edges (effects of chisel edge shapes on the cutting performance). International Journal of Machine Tools and Manufacture, 1991. 31(3): p. 361-369.
85. Piquet, R., Ferret, B., Lachaud, F., and Swider, P., Experimental analysis of drilling damage in thin carbon/epoxy plate using special drills. Composites Part A: Applied Science and Manufacturing, 2000. 31(10): p. 1107-1115.
86. Kuo, C.L., Soo, S.L., Aspinwall, D.K., Bradley, S., Thomas, W., M'Saoubi, R., Pearson, D., and Leahy, W., The influence of tool geometry, feed rate and machining strategy on hole surface integrity following single-shot drilling of 3 layer metallic-composite stacks, in Proceedings of the 30th International Manufacturing Conference, (Byrne, G., Mullany, B., Connolly, P., Ahearne, E., and Green, N., Eds.), 2013, University College Dublin: Dublin. p. 104-113.
87. Aspinwall, D.K., Cutting tool material-1/2/3/4. 2008, School of Manufacturing and Mechanical Engineering, University of Birmingham.
88. Mills, B., Recent developments in cutting tool materials. Journal of Materials Processing Technology, 1996. 56(1-4): p. 16-23.
89. Aspinwall, D. and Dewes, R., New developments in cutting tools. 2004, School of Manufacturing and Mechanical Engineering, University of Birmingham.
90. Heath, P.J., Developments in applications of PCD tooling. Journal of Materials Processing Technology, 2001. 116(1): p. 31-38.
91. Nordberg, P. and Pearson, D., Industrial communication. 2013, Seco Tools AB.
92. Oles, E.J., Inspektor, A., and Bauer, C.E., The new diamond-coated carbide cutting tools. Diamond and Related Materials, 1996. 5(6-8): p. 617-624.
93. Haubner, R., Schubert, W.D., and Lux, B., Interactions of hard metal substrates during diamond deposition. International Journal of Refractory Metals and Hard Materials, 1998. 16(3): p. 177-185.
94. Saito, H., Iwabuchi, A., and Shimizu, T., Effects of Co content and WC grain size on wear of WC cemented carbide. Wear, 2006. 261(2): p. 126-132.
95. Miess, D. and Rai, G., Fracture toughness and thermal resistance of polycrystalline diamond compacts. Materials Science and Engineering: A, 1996. 209(1–2): p. 270-276.
96. Zeren, M. and Karagöz, Ş., Sintering of polycrystalline diamond cutting tools. Materials & Design, 2007. 28(3): p. 1055-1058.
97. Werner, G. and Renter, M., Grindability of PCD. Industrial Diamond Review, 1989.
98. Ramulu, M.F., Garbini, J.L., Jorgensen, J.E., Machining of Graphite/Epoxy Composite Materials with Polycrystalline Diamond (PCD) Tools. Journal of Engineering Materials and Technology, Transactions of the ASME, 1991. 113: p. 430-436.
99. Thoe, T.B., Aspinwall, D.K., Wise, M.L.H., and Oxley, I.A., Polycrystalline diamond edge quality and and surface integrity following electrical discharge grinding. Journal of Materials Processing Technology, 1996. 56(1-4): p. 773-785.
100. Dold, C., Henerichs, M., Bochmann, L., and Wegener, K., Comparison of Ground and Laser Machined Polycrystalline Diamond (PCD) Tools in Cutting Carbon Fiber Reinforced Plastics (CFRP) for Aircraft Structures. Procedia CIRP, 2012. 1: p. 178-183.
101. Prengel, H.G., Pfouts, W.R., and Santhanam, A.T., State of the art in hard coatings for carbide cutting tools. Surface and Coatings Technology, 1998. 102(3): p. 183-190.
102. Kalss, W., Reiter, A., Derflinger, V., Gey, C., and Endrino, J.L., Modern coatings in high performance cutting applications. International Journal of Refractory Metals and Hard Materials, 2006. 24(5): p. 399-404.

103. Fox, V., Jones, A., Renevier, N.M., and Teer, D.G., Hard lubricating coatings for cutting and forming tools and mechanical components. Surface and Coatings Technology, 2000. 125(1-3): p. 347-353.
104. Murakawa, M. and Takeuchi, S., Mechanical applications of thin and thick diamond films. Surface and Coatings Technology, 1991. 49(1-3): p. 359-364.
105. Kloke, F., Manufacturing process 1, cutting. RWTH ed. 2011: Spring Heidelberg Dordrecht London New York.
106. Meng, X.M., Tang, W.Z., Hei, L.F., Li, C.M., Askari, S.J., Chen, G.C., and Lu, F.X., Application of CVD nanocrystalline diamond films to cemented carbide drills. International Journal of Refractory Metals and Hard Materials, 2008. 26(5): p. 485-490.
107. Gäbler, J., Schäfer, L., and Westermann, H., Chemical vapour deposition diamond coated microtools for grinding, milling and drilling. Diamond and Related Materials. 9(3-6): p. 921-924.
108. Haubner, R. and Lux, B., On the formation of diamond coatings on WC/Co hard metal tools. International Journal of Refractory Metals and Hard Materials, 1996. 14(1-3): p. 111-118.
109. Konstanty, J., Diamond tool design and composition, in Powder Metallurgy Diamond Tools. 2005, Elsevier Science: Amsterdam. p. 39-68.
110. Jiang, J. and Arnell, R.D., The effect of substrate surface roughness on the wear of DLC coatings. Wear, 2000. 239(1): p. 1-9.
111. Vandevelde, T.C.S., Vandierendonck, K., Van Stappen, M., Du Mong, W., and Perremans, P., Cutting applications of DLC, hard carbon and diamond films. Surface and Coatings Technology, 1999. 113(1-2): p. 80-85.
112. Hanyu, H., Kamiya, S., Murakami, Y., and Kondoh, Y., The improvement of cutting performance in semi-dry condition by the combination of DLC coating and CVD smooth surface diamond coating. Surface and Coatings Technology, 2005. 200(1-4): p. 1137-1141.
113. Taylor, F.W., On the art of cutting metals. American society of mechanical engineers , Metal-cutting, 1907: p. 248.
114. Masuda, M., Kuroshima, Y., and Chujo, Y., Failure of tungsten carbide-cobalt alloy tools in machining of carbon materials. Wear, 1993. 169(2): p. 135-140.
115. ISO, 3685 : 1993 Tool-life testing with single-point turning tools. 1993.
116. Engqvist, H. and Axén, N., Abrasion of cemented carbides by small grits. Tribology International, 1999. 32(9): p. 527-534.
117. Gee, M.G., Gant, A., and Roebuck, B., Wear mechanisms in abrasion and erosion of WC/Co and related hardmetals. Wear, 2007. 263(1-6): p. 137-148.
118. Arsecularatne, J.A., Zhang, L.C., and Montross, C., Wear and tool life of tungsten carbide, PCBN and PCD cutting tools. International Journal of Machine Tools and Manufacture, 2006. 46(5): p. 482-491.
119. Cantero, J.L., Tardío, M.M., Canteli, J.A., Marcos, M., and Miguélez, M.H., Dry drilling of alloy Ti-6Al-4V. International Journal of Machine Tools and Manufacture, 2005. 45(11): p. 1246-1255.
120. König, W. and Neises, A., Wear mechanisms of ultrahard, non-metallic cutting materials. Wear, 1993. 162-164(Part 1): p. 12-21.
121. Jianxin, D., Hui, Z., Ze, W., and Aihua, L., Friction and wear behavior of polycrystalline diamond at temperatures up to 700 °C. International Journal of Refractory Metals and Hard Materials. In Press, Corrected Proof.
122. Schouwenaars, R., Jacobo, V.H., and Ortiz, A., Transition from normal to severe wear in PCD during high-speed cutting of a ductile material. International Journal of Refractory Metals and Hard Materials, 2009. 27(2): p. 403-408.

123. Kovacevic, R., Cherukuthota, C., and Mazurkiewicz, M., High pressure waterjet cooling/lubrication to improve machining efficiency in milling. International Journal of Machine Tools and Manufacture, 1995. 35(10): p. 1459-1473.
124. Machado, A.R. and Wallbank, J., The effect of extremely low lubricant volumes in machining. Wear, 1997. 210(1-2): p. 76-82.
125. Byrne, G., Dornfeld, D., and Denkena, B., Advancing Cutting Technology. CIRP Annals - Manufacturing Technology, 2003. 52(2): p. 483-507.
126. Hong, S.Y. and Ding, Y., Cooling approaches and cutting temperatures in cryogenic machining of Ti-6Al-4V. International Journal of Machine Tools and Manufacture, 2001. 41(10): p. 1417-1437.
127. Haan, D.M., Batzer, S.A., Olson, W.W., and Sutherland, J.W., An experimental study of cutting fluid effects in drilling. Journal of Materials Processing Technology, 1997. 71(2): p. 305-313.
128. Palanisamy, S., McDonald, S.D., and Dargusch, M.S., Effects of coolant pressure on chip formation while turning Ti6Al4V alloy. International Journal of Machine Tools and Manufacture, 2009. 49(9): p. 739-743.
129. López de Lacalle, L.N., Pérez-Bilbatua, J., Sánchez, J.A., Llorente, J.I., Gutiérrez, A., and Albóniga, J., Using High Pressure Coolant in the Drilling and Turning of Low Machinability Alloys. The International Journal of Advanced Manufacturing Technology, 2000. 16(2): p. 85-91.
130. Nandy, A.K., Gowrishankar, M.C., and Paul, S., Some studies on high-pressure cooling in turning of Ti-6Al-4V. International Journal of Machine Tools and Manufacture, 2009. 49(2): p. 182-198.
131. Machado, A.R., Wallbank, J., Pashby, I.R., and Ezugwu, E.O., Tool performance and chip control when machining Ti6Al4V and Inconel 901 using high pressure coolant supply. Machining Science and Technology, 1998. 2(1): p. 1-12.
132. Field, M. and Kahles, J., Review of surface integrity of machined components. CIRP Annals - Manufacturing Technology, 1971. 20/2: p. 153-163.
133. Jahanmir, S., Ramulu, M., and Koshy, P., Machining of ceramics and composites. 1999, New York: Markcel Dekker, Inc.
134. Griffiths, B., Manufacturing surface technology. 2001, Penton Press: London.
135. Field, M., Kahles, J.F., and Cammett, J.T., Review of measuring methods for surface integrity Annal of CIRP, 1972. 21: p. 219-239.
136. Davim, J.P., Surface integrity in machining. 2010, New York: Springer-Verlag London limited 2010.
137. Ulutan, D. and Ozel, T., Machining induced surface integrity in titanium and nickel alloys: A review. International Journal of Machine Tools and Manufacture, 2011. 51(3): p. 250-280.
138. Enemuoh, E.U., El-Gizawy, A.S., and Chukwujekwu Okafor, A., An approach for development of damage-free drilling of carbon fiber reinforced thermosets. International Journal of Machine Tools and Manufacture, 2001. 41(12): p. 1795-1814.
139. Tsao, C.C. and Hocheng, H., Computerized tomography and C-Scan for measuring delamination in the drilling of composite materials using various drills. International Journal of Machine Tools and Manufacture, 2005. 45(11): p. 1282-1287.
140. Babu, P.R. and Pradhan, B., Effect of damage levels and curing stresses on delamination growth behaviour emanating from circular holes in laminated FRP composites. Composites Part A: Applied Science and Manufacturing, 2007. 38(12): p. 2412-2421.
141. Babu, P.R. and Pradhan, B., Thermoelastic effects on mixed-mode delamination growth emanating from circular holes in laminated FRP composites. Composite Structures, 2008. 82(1): p. 50-60.

142. Stout, K.J., King, T.G., and Whitehouse, D.J., Analytical techniques in surface topography and their application to a running-in experiment. Wear, 1977. 43(1): p. 99-115.
143. Zipin, R.B., The analysis of profile strata for surface texture specification. Applications of Surface Science, 1983. 15(1-4): p. 334-358.
144. Whitehouse, D., Identification and separation of surface features, in Surfaces and Their Measurement. 2002, Kogan Page Science: Oxford. p. 16-47.
145. Smith, G.T., Industrial metrology. 2002, London: Springer-Verlag London Limited 2002.
146. Zipin, R.B., The height sensitive surface roughness parameters. Applications of Surface Science, 1981. 9(1-4): p. 266-287.
147. Peters, J., Bryan, J.B., Estler, W.T., Evans, C., Kunzmann, H., Lucca, D.A., Sartori, S., Sato, H., Thwaite, E.G., Vanherck, P., Hocken, R.J., Peklenik, J., Pfeifer, T., Trumpold, H., and Vorburger, T.V., Contribution of CIRP to the Development of Metrology and Surface Quality Evaluation during the last fifty years. CIRP Annals - Manufacturing Technology, 2001. 50(2): p. 471-488.
148. ISO, Geometrical Product Specifications (GPS) -surface texture : Profile method: Surface having stratified functional properties-Part 2: Height Characterization using the linear material ratio curve. 1997.
149. Ramulu, M., Wern, C.W., and Garbini, J.L., Effect of fibre direction on surface roughness measurements of machined graphite/epoxy composite. Composites Manufacturing, 1993. 4(1): p. 39-51.
150. Brinksmeier, E., Cammett, J.T., König, W., Leskovar, P., Peters, J., and Tönshoff, H.K., Residual Stresses -- Measurement and Causes in Machining Processes. CIRP Annals - Manufacturing Technology, 1982. 31(2): p. 491-510.
151. Grzesik, W., Cutting Vibrations, in Advanced Machining Processes of Metallic Materials. 2008, Elsevier: Amsterdam. p. 115-125.
152. Grzesik, W., Heat in Metal Cutting, in Advanced Machining Processes of Metallic Materials. 2008, Elsevier: Amsterdam. p. 127-140.
153. Postlethwaite, S.R., Ford, D.G., and Morton, D., Dynamic calibration of CNC machine tools. International Journal of Machine Tools and Manufacture, 1997. 37(3): p. 287-294.
154. Galloway, D., Some experiments on the influence of various factors on drill performance. Trans. ASME, 1957. 79: p. 191-231.
155. Astakov, V.P., Geometry of single-point turning tools and drills. 2010, London: Springer-Verlag.
156. Franke, V., Drilling of long fiber reinforced thermoplastics--Influence of the cutting edge on the machining results. CIRP Annals - Manufacturing Technology, 2011. 60(1): p. 65-68.
157. de Morais, A.B., de Moura, M.F., Marques, A.T., and de Castro, P.T., Mode-I interlaminar fracture of carbon/epoxy cross-ply composites. Composites Science and Technology, 2002. 62(5): p. 679-686.
158. Arul, S., Vijayaraghavan, L., and Malhotra, S.K., Online monitoring of acoustic emission for quality control in drilling of polymeric composites. Journal of Materials Processing Technology, 2007. 185(1-3): p. 184-190.
159. Marques, A.T., Durão, L.M., Magalhães, A.G., Silva, J.F., and Tavares, J.M.R.S., Delamination analysis of carbon fibre reinforced laminates: Evaluation of a special step drill. Composites Science and Technology, 2009. 69(14): p. 2376-2382.
160. Davim, J.P., Rubio, J.C., and Abrao, A.M., A novel approach based on digital image analysis to evaluate the delamination factor after drilling composite laminates. Composites Science and Technology, 2007. 67(9): p. 1939-1945.

161. Abrão, A.M., Faria, P.E., Rubio, J.C.C., Reis, P., and Davim, J.P., Drilling of fiber reinforced plastics: A review. Journal of Materials Processing Technology, 2007. 186(1-3): p. 1-7.
162. Ko, S.L., Chang, J.E., and Yang, G.E., Burr minimizing scheme in drilling. Journal of Materials Processing Technology, 2003. 140(1-3): p. 237-242.
163. Aurich, J.C., Dornfeld, D., Arrazola, P.J., Franke, V., Leitz, L., and Min, S., Burrs--Analysis, control and removal. CIRP Annals - Manufacturing Technology, 2009. 58(2): p. 519-542.
164. Dornfeld, D.A., Kim, J.S., Dechow, H., Hewson, J., and Chen, L.J., Drilling Burr Formation in Titanium Alloy, Ti-6AI-4V. CIRP Annals - Manufacturing Technology, 1999. 48(1): p. 73-76.
165. Gillespie, L.K. and Blotter, P.T., Formation and properties of machining burrs. ASME Transactions, Journal of Engineering for Industry, 1976. 98(1): p. 66-74.
166. ISO, 3175:2000, in technical drawings-Edges of undefined shape-Vocabulary and indications. 2000.
167. Kim, J., Min, S., and Dornfeld, D.A., Optimization and control of drilling burr formation of AISI 304L and AISI 4118 based on drilling burr control charts. International Journal of Machine Tools and Manufacture, 2001. 41(7): p. 923-936.
168. Min, S. and Dornfeld, D.A., Current advanced research projects in burr formation and deburring. The Association for Manufacturing Technology (electronic article), 2004.
169. Nakao, Y. and Watanabe, Y., Measurements and Evaluations of Drilling Burr Profile. Proceedings of the Institution of Mechanical Engineers, Part B: Journal of Engineering Manufacture, 2006. 220(4): p. 513-523.
170. Hashimura, M., Hassamontr, J., and Dornfeld, D.A., Effect of In-Plane Exit Angle and Rake Angles on Burr Height and Thickness in Face Milling Operation. Journal of Manufacturing Science and Engineering, 1999. 121(1): p. 13-19.
171. Ko, S.L. and Lee, J.K., Analysis of burr formation in drilling with a new-concept drill. Journal of Materials Processing Technology, 2001. 113(1-3): p. 392-398.
172. Vijayaraghavan, A. and Dornfeld, D. Challenges in Modeling Machining of Multilayer Materials. Proceedings of the 8th CIRP Workshop on Modeling of Machining,Chemnitz University , Chemnitz, Germany.
173. Gillespie, L.K., Deburring precision miniature parts. Precision Engineering, 1979. 1(4): p. 189-198.
174. Ko, S.L., Chang, J.E., and Kalpakjian, S., Development of Drill Geometry for Burr Minimization In Drilling. CIRP Annals - Manufacturing Technology, 2003. 52(1): p. 45-48.
175. Gillespie, L.K., Third international deburring and surface conditioning conference: 23-25 October 1979, Cincinnati, USA. Precision Engineering, 1980. 2(2): p. 116-116.
176. Stein, J.M. and Dornfeld, D.A., Burr Formation in Drilling Miniature Holes. CIRP Annals - Manufacturing Technology, 1997. 46(1): p. 63-66.
177. Min, S., Dornfeld, D., and Nakao, Y., Influence of Exit Surface Angle on Drilling Burr Formation. Transaction of the ASME Journal of Manufacturing Science and Engineering 2003. 125(4): p. 7.
178. Brehl, D.E. and Dow, T.A., Review of vibration-assisted machining. Precision Engineering, 2008. 32(3): p. 153-172.
179. Pujana, J., Rivero, A., Celaya, A., and López de Lacalle, L.N., Analysis of ultrasonic-assisted drilling of Ti6Al4V. International Journal of Machine Tools and Manufacture, 2009. 49(6): p. 500-508.
180. Chang, S.S.F. and Bone, G.M., Burr height model for vibration assisted drilling of aluminum 6061-T6. Precision Engineering, 2010. 34(3): p. 369-375.

181. Davies, M.A., Ueda, T., M'Saoubi, R., Mullany, B., and Cooke, A.L., On The Measurement of Temperature in Material Removal Processes. CIRP Annals - Manufacturing Technology, 2007. 56(2): p. 581-604.
182. Agapiou, J.S. and DeVries, M.F., On the determination of thermal phenomena during drilling—Part I. Analytical models of twist drill temperature distributions. International Journal of Machine Tools and Manufacture, 1990. 30(2): p. 203-215.
183. Bono, M. and Ni, J., The location of the maximum temperature on the cutting edges of a drill. International Journal of Machine Tools and Manufacture, 2006. 46(7–8): p. 901-907.
184. Ueda, T., Nozaki, R., and Hosokawa, A., Temperature Measurement of Cutting Edge in Drilling -Effect of Oil Mist. CIRP Annals - Manufacturing Technology, 2007. 56(1): p. 93-96.
185. Le Coz, G., Marinescu, M., Devillez, A., Dudzinski, D., and Velnom, L., Measuring temperature of rotating cutting tools: Application to MQL drilling and dry milling of aerospace alloys. Applied Thermal Engineering, 2012. 36(0): p. 434-441.
186. Zeilmann, R.P. and Weingaertner, W.L., Analysis of temperature during drilling of Ti6Al4V with minimal quantity of lubricant. Journal of Materials Processing Technology, 2006. 179(1-3): p. 124-127.
187. Li, R. and Shih, A.J., Spiral point drill temperature and stress in high-throughput drilling of titanium. International Journal of Machine Tools and Manufacture, 2007. 47(12–13): p. 2005-2017.
188. Li, R., Riester, L., Watkins, T.R., Blau, P.J., and Shih, A.J., Metallurgical analysis and nanoindentation characterization of Ti-6Al-4V workpiece and chips in high-throughput drilling. Materials Science and Engineering: A, 2008. 472(1-2): p. 115-124.
189. Weinert, K. and Kempmann, C., Cutting temperature and their effects on the machining behaviour in drilling reinforced plastic composites. Advanced Engineering Materials, 2004. 6: p. 684-689.
190. Kalidas, S., DeVor, R.E., and Kapoor, S.G., Experimental investigation of the effect of drill coatings on hole quality under dry and wet drilling conditions. Surface and Coatings Technology, 2001. 148(2–3): p. 117-128.
191. Bağci, E. and Ozcelik, B., Investigation of the effect of drilling conditions on the twist drill temperature during step-by-step and continuous dry drilling. Materials & Design, 2006. 27(6): p. 446-454.
192. Aspinwall, E., Introduction to experimental design (Handout). 2009, School of Manufacturing and Mechanical Engineering, University of Birmingham.
193. Shyha, I.S., Aspinwall, D.K., Soo, S.L., and Bradley, S., Drill geometry and operating effects when cutting small diameter holes in CFRP. International Journal of Machine Tools and Manufacture, 2009. 49(12-13): p. 1008-1014.
194. Ross, P.J., Taguchi techniques for quality engineering. 2 ed. 1996, New York: McGraw-Hill.
195. Aspinwall, E., Taguchi methods and factional factorial designs. 2009, School of Manufacturing and Mechanical Engineering, University of Birmingham.
196. Aspinwall, E., Analysing data from orthogonal arrays (Handout). 2009, School of Manufacturing and Mechanical Engineering, University of Birmingham.
197. MIL-T-9046J, Military specification: titanium and titanium alloy, sheet, strip and plate. 1983: Department of Defence, USA.
198. Shyha, I., Drilling of carbon fibre reinforced plastic composites, in Mechanical School 2010, University of Birmingham: Birmingham.
199. Holemaking: Catalogue & technical Guide. 2013, Seco Tools.
200. Bermingham, M.J., Kirsch, J., Sun, S., Palanisamy, S., and Dargusch, M.S., New observations on tool life, cutting forces and chip morphology in cryogenic machining

Ti-6Al-4V. International Journal of Machine Tools and Manufacture, 2011. 51(6): p. 500-511.
201. Jawahir, I.S., The chip control factor in machinability assessments: Recent trends. Journal of Mechanical Working Technology, 1988. 17(0): p. 213-224.
202. Jawahir, I.S. and van Luttervelt, C.A., Recent Developments in Chip Control Research and Applications. CIRP Annals - Manufacturing Technology, 1993. 42(2): p. 659-693.
203. Hull, D., Fractography: Observing, measuring, and interpreting fracture surface topography. 1999, Cambridge: Cambridge University Press.
204. Guo, Y.B. and Dornfeld, D.A., Finite element modeling of burr formation process in drilling of 304 stainless steel. Trans ASME: Journal of manufacturing science and engineering 2000. 122: p. 612-620.
205. Tze-Pin, L., Hood, M., Cooper, G.A., and Xiaohong, L., Wear and failure mechanisms of polycrystalline diamond compact bits. Wear, 1992. 156(1): p. 133-150.
206. Abedrabbo, N., Pourboghrat, F., and Carsley, J., Forming of aluminum alloys at elevated temperatures – Part 2: Numerical modeling and experimental verification. International Journal of Plasticity, 2006. 22(2): p. 342-373.

APPENDIX 1

Contact details of industrial collaborators

This project was carried out in collaboration with industrial sponsors including GKN Aerospace Service Ltd., Seco Tools (UK) Ltd. and Element Six Ltd. The contact details from these collaborators during the project development and thesis writing are as followings,

Collaborator contact details	Contributions
Mr. Will Thomas/Mr. Mark Raymond GKN Aerospace Services Ltd., Composites Research Centre, Whippingham Road, East Cowes, Isle of Wight, PO32 6LR, UK.	• Funding: £42,000 • Workpiece material (Titanium/CFRP/Aluminium stacks) • Technical expertise
Mr. David Pearson Seco Tools (UK) Ltd, Springfield Business Park, Alcester, B49 6PU, UK Mr. Par Nordberg Seco Tools AB, SE-737 82, Fagersta, Sweden.	• Funding: £6000 • Cutting tools • Technical expertise
Dr. Wayne Leahy Element Six Ltd., Global Innovation Centre, Harwell, Oxford, OX11 0QR, UK	• Funding: £6000 • PCD diamond • Technical expertise

APPENDIX 2

CNC machining programme for Phase 1/2/3 experimental work

P600 (drilling in plate workpiece material, shifting +10.0mm in X direction)

```
G21;(metric)
G54 G90 G0 X0. Y0.;
G43 H10 Z40.;
M01;
G0 Z15. S1504 M03;

M98 P601 L10;
M98 P602;
G90 G0 X10.;

M98 P601 L10;
M98 P602;
G90 G0 X20.;

M98 P601 L10;
M98 P602;
G90 G0 X30.;

M98 P601 L10;
M98 P602;
G90 G0 X40.;

M98 P601 L10;
M98 P602;
G90 G0 X50.;

M98 P601 L10;
M98 P602;
G90 G0 X60.;

M98 P601 L10;
M98 P602;
G90 G0 X70.;

M98 P601 L10;
M98 P602;
G90 G0 X80.;

M98 P601 L10;
M98 P602;
G90 G0 X90.;
```

P601 (Drilling 30mm in depth, and shifting -10.0mm in Y direction)

```
G90 G0 Z10. S1504 M03
G01 Z3. F75.2
M01
G91 G1 Z-15. F75.2
S4012
G91 G1 Z-10. F200.6
S6018
G91 G1 Z-10. F300.9
G90 Z10.
Y-10.
M99
```

P602 (Drilling 30mm in depth in strip workpiece material)

```
G21;
G54 G90 X0. Y0.;
G43 H10 Z10. F1000.;
M01;

G0 Z15. S1504 M03;
G01 Z-12. F200.6;
S4012;
G01 Z-22. F200.6;
S6018;
G01 Z-32. F300.9;
G01 Z50.;
M30;
M99;
```

APPENDIX 3

Tool wear	Ti/CFRP/Al stack					
Source of variances	D.F.	Seq S.S.	M.S.	F	P	PCR
Tool material	1	0.028203	0.028203	81.19*	0.001	78.4%
Feed rate	1	0.005050	0.005050	14.54*	0.019	13.2%
Drilling strategy	1	0.000861	0.000861	2.48	0.190	1.4%
Residual	4	0.001389	0.000347			7%
Sum of square variances	7	0.035504				

(* Significant at the 5% level, $F_{cal\ 1,4}$ =7.71)

Table A3-1 ANOVA table for tool wear in Phase1A experiment

Diameter	Ti layer					
Source of variances	D.F.	Seq S.S.	M.S.	F	P	PCR
Tool material	1	0.0005595	0.0005595	33.51*	0.004	64.5%
Feed rate	1	0.0000521	0.0000521	3.12	0.152	4.2%
Drilling strategy	1	0.0001626	0.0001626	9.74*	0.036	17.3%
Residual	4	0.0000668	0.0000167			14%
Sum of square variances	7	0.0008409				
Diameter	CFRP layer					
Source of variances	D.F.	Seq S.S.	M.S.	F	P	PCR
Tool material	1	0.0003044	0.0003044	32.72*	0.055	57.5%
Feed rate	1	0.0001688	0.0001688	18.15*	0.099	31.0%
Drilling strategy	1	0.0000026	0.0000026	0.28	0.900	0%
Residual	4	0.0000372	0.0000093			11.5%
Sum of square variances	7	0.0005130				
Diameter	Al layer					
Source of variances	D.F.	Seq S.S.	M.S.	F	P	PCR
Tool material	1	0.0001761	0.0001761	2.78	0.171	21.0%
Feed rate	1	0.0000971	0.0000971	1.53	0.283	18.2%
Drilling strategy	1	0.0000095	0.0000095	0.15	0.718	6.3%
Residual	4	0.0002532	0.0000633			54.5%
Sum of square variances	7	0.0005360				

(* Significant at the 5% level, $F_{cal\ 1,4}$ =7.71)

Table A3-2 ANOVA table for diameter in Phase1A experiment

Cylindricity	Ti/CFRP/Al stack					
Source of variances	D.F.	Seq S.S.	M.S.	F	P	PCR
Tool material	1	895.9	895.9	1.80	0.128	10.5%
Feed rate	1	1112.8	1112.8	2.23	0.201	16.3%
Drilling strategy	1	841.2	841.2	1.69	0.213	9.1%
Residual	4	1917.3	497.33			64.1%
Sum of square variances		3767.2				
Out of roundness			Ti layer			
Source of variances	D.F.	Seq S.S.	M.S.	F	P	PCR
Tool material	1	1699.6	1699.6	8.87*	0.041	41.8%
Feed rate	1	1371.2	1371.2	7.16	0.055	32.7%
Drilling strategy	1	511.7	511.7	2.67	0.178	8.9%
Residual	4	766.2	191.5			16.6%
Sum of square variances		3601.2				
Out of roundness			CFRP layer			
Source of variances	D.F.	Seq S.S.	M.S.	F	P	PCR
Tool material	1	1378.9	1378.9	3.66	0.128	22.9%
Feed rate	1	931.7	931.7	2.47	0.191	12.6%
Drilling strategy	1	558.9	558.9	1.48	0.290	4.16%
Residual	4	1507.1	376.8			60.34
Sum of square variances		4376.6				
Out of roundness			Al layer			
Source of variances	D.F.	Seq S.S.	M.S.	F	P	PCR
Tool material	1	267.2	267.2	1.79	0.251	0.00%
Feed rate	1	740.4	740.4	4.97	0.090	7.57%
Drilling strategy	1	306.2	306.2	2.06	0.225	0%
Residual	4	595.8	595.8			92.43%
Sum of square variances		1909.55				

(* Significant at the 5% level, $F_{cal\ 1,4}$ =7.71)

Table A3-3 ANOVA table for burr height in Phase1A experiment

Entrance burr height	Ti layer					
Source of variances	D.F.	Seq S.S.	M.S.	F	P	PCR
Tool material	1	0.002450	0.002450	1.06	0.362	0.3%
Feed rate	1	0.005000	0.005000	2.16	0.215	6.2%
Drilling strategy	1	0.026450	0.026450	11.44*	0.028	55.9%
Residual	4	0.009250	0.002312			37.6%
Sum of square variances	7	0.04315				
Exit burr height			Al layer			
Source of variances	D.F.	Seq S.S.	M.S.	F	P	PCR
Tool material	1	0.0002000	0.0002000	0.42	0.552	0%
Feed rate	1	0.0018000	0.0018000	3.79	0.123	30.4%
Drilling strategy	1	0.0004500	0.0004500	0.95	0.386	32.7%
Residual	4	0.0019000	0.0004750			36.9%
Sum of square variances	7	0.0043500				

(* Significant at the 5% level, $F_{cal\ 1,4}$ =7.71)

Table A3-4 ANOVA table for burr height in Phase1A experiment

Rt	Ti layer					
Source of variances	D.F.	Seq S.S.	M.S.	F	P	PCR
Tool material	1	2.055	2.055	1.06	0.361	0.42%
Feed rate	1	0.582	0.582	0.30	0.613	0%
Drilling strategy	1	17.122	17.122	8.83*	0.041	55.2%
Residual	4	7.754	1.939			44.38%
Sum of square variances	7	27.514				

Rt	CFRP layer					
Source of variances	D.F.	Seq S.S.	M.S.	F	P	PCR
Tool material	1	20.97	20.97	0.42	0.551	0%
Feed rate	1	22.40	22.40	0.45	0.538	0%
Drilling strategy	1	63.36	63.36	1.28	0.321	4.5%
Residual	4	198.16	49.54			95.5%
Sum of square variances	7	304.90				

Rt	Al layer					
Source of variances	D.F.	Seq S.S.	M.S.	F	P	PCR
Tool material	1	0.9429	0.9429	1.40	0.303	6.5%
Feed rate	1	0.3067	0.3067	0.45	0.537	0%
Drilling strategy	1	0.1220	0.1220	0.18	0.693	0%
Residual	4	2.7036	0.6759			93.5%
Sum of square variances	7	4.0752				

(* Significant at the 5% level, $F_{cal\ 1,4}$ =7.71)

Table A3-5 ANOVA table for peak-to-valley roughness (Rt) in Phase1A experiment

APPENDIX 4

Diameter	Ti6Al4V layer					
Source of variances	D.F.	Seq S.S.	M.S.	F	P	PCR
Margin design	1	0.00047	0.00047	29.5*	0.006	73.21%
Feed rate	1	0.00001	0.00001	0.71	0.446	0.00%
Drilling strategy	1	0.00002	0.00002	1.36	0.308	0.00%
Residual	4	0.00560	0.00006			26.78%
Sums of square variances		0.00056				

Diameter	CFRP layer					
Source of variances	D.F.	Seq S.S.	M.S.	F	P	PCR
Margin design	1	0.00106	0.00106	61.09*	0.001	87.39%
Feed rate	1	0.00006	0.00006	5.07	0.087	3.37%
Drilling strategy	1	0.00000	0.00000	0.13	0.739	0.00%
Residual	4	0.00006	0.00002			9.24%
Sums of square variances		0.00119				

Diameter	Al7050 layer					
Source of variances	D.F.	Seq S.S.	M.S.	F	P	PCR
Margin design	1	0.00123	0.00123	51.71*	0.002	89.62%
Feed rate	1	0.00000	0.00000	0.00	0.976	0.00%
Drilling strategy	1	0.00003	0.00003	1.20	0.335	0.74%
Residual	4	0.00010	0.00002			9.64%
Sums of square variances		0.00135				

(* Significant at the 5% level, $F_{cal\ 1,4}$ =7.71)

Table A4-1 ANOVA table for diameter in Phase1B experiment

Cylindricity	Ti/CFRP/Al stack					
Source of variances	D.F.	Seq S.S.	M.S.	F	P	PCR
Margin design	1	334.5	334.5	1.07	0.360	0.67%
Feed rate	1	324.5	324.5	1.04	0.366	0.36%
Drilling strategy	1	1324.8	1324.8	4.23	0.109	31.28%
Residual	4	1251.4	312.8			67.69%
Sums of Squares		3235.3				
Out of roundness	Ti layer					
Source of variances	D.F.	Seq S.S.	M.S.	F	P	PCR
Margin design	1	3486.0	3486.0	144.14*	0.000	96.13%
Feed rate	1	1.7	1.7	0.07	0.801	0.00%
Drilling strategy	1	16.7	16.7	0.69	0.453	0.00%
Residual	4	96.7	24.2			3.87%
Sums of Squares		3601.2				
Out of roundness	CFRP layer					
Source of variances	D.F.	Seq S.S.	M.S.	F	P	PCR
Margin design	1	1048.26	1048.26	13.79*	0.021	70.04%
Feed rate	1	0.86	0.86	0.01	0.920	0.00%
Drilling strategy	1	35.01	35.01	0.46	0.535	0.00%
Residual	4	303.98	75.99			29.96%
Sums of Squares		1388.11				
Out of roundness	Al layer					
Source of variances	D.F.	Seq S.S.	M.S.	F	P	PCR
Margin design	1	2.5	2.5	0.01	0.916	0.00%
Feed rate	1	455.3	455.3	2.27	0.207	16.32%
Drilling strategy	1	298.5	298.5	1.49	0.290	6.26%
Residual	4	803.2	200.8			77.42%
Sums of Squares		1559.5				

(* Significant at the 5% level, $F_{cal\ 1,4}$ =7.71)

Table A4-2 ANOVA table for cylindricity/out of roundness in Phase1B experiment

Entrance burr height	Ti layer					
Source of variances	D.F.	Seq S.S.	M.S.	F	P	PCR
Margin design	1	0.04651	0.04651	82.69*	0.001	90.12%
Feed rate	1	0.00011	0.00011	0.20	0.676	0.00%
Drilling strategy	1	0.00211	0.00211	3.76	0.125	3.04%
Residual	4	0.00225	0.00056			6.84%
Sums of square variances		0.05099				

Exit burr height	Al layer					
Source of variances	D.F.	Seq S.S.	M.S.	F	P	PCR
Margin design	1	0.39161	0.39161	45.21*	0.003	80.45%
Feed rate	1	0.00011	0.00011	0.01	0.915	0.00%
Drilling strategy	1	0.04961	0.04961	5.73	0.075	8.60%
Residual	4	0.03465	0.00866			10.95%
Sums of square variances		0.47599				

(* Significant at the 5% level, $F_{cal\ 1,4}$ =7.71)

Table A4-3 ANOVA table for burr height in Phase1B experiment

APPENDIX 5

DRILLING OF Ti/CFRP/Al MULTILAYER STACK MATERIAL USING MODIFIED DOMED PCD DRILLS

Date: Saturday, 22 Feb 2013

Collaborators : GKN Aerospace
Seco Tools
Element Six

1. Aim and scope

The aim of this test is to validate the effectiveness of the modifications on the point geometry of the domed PCD drills (following results from Phase 2A) in extending tool life and improving hole surface quality while drilling of 2 layer CFRP/Al stacks.

2. Experimental work

Workpiece materials used in this test were two layer metallic-composite stacks comprising 10 mm thick aluminium alloy and 10 mm thick CFRP laminates in the form of plates measuring 120×120×20 mm and strips with a width of 17mm, see Figure 6-1(a). The age strengthened A7050-T7651 aluminium alloy had an elastic modulus of 72 GPa and the CFRP (ACG MTM44-1/HTS-268-12K, Vf=56%) laminates consisted of 36 unidirectional prepregs (individual ply thickness of 0.30 mm) which were laid up according to an orientation of $[45^{\circ}/0^{\circ}/135^{\circ}/90^{\circ}/45^{\circ}/0^{\circ}]_{3s}$ resulting in a tensile strength of 1200MPa and modulus of 145GPa. The plates were employed for mainstream tool life/wear testing and were bonded together using a cured adhesive film (3M AF163) having an ultimate tensile strength and shear modulus of 48MPa and 439.1GPa respectively. In contrast the strip specimens were held together using M6 socket screws and were used for cutting force evaluation and subsequent hole quality analysis. The drills evaluated were of a ‘domed’ polycrystalline (PCD) design, which was fabricated with a solid domed cylindrical PCD blank and brazed onto a WC shank. The drills had three different geometries of 120˚×186˚, 120˚×159˚ 120˚×169˚point angle (two-stage design), a 30˚ helix angle and 14˚ relief angle with a fixed diameter of 6.36mm as seen in Figure 6-1(b). All experiments were undertaken on a Matsuura FX-5 CNC machining centre with a maximum spindle rotational speed of 20,000rpm rated at 15kW, see Fig. 6-1(c) for the test setup. Trials were performed wet involving a water-miscible emulsion with a 7-8% volume solution of mineral oil, which was delivered via external coolant nozzles at a fixed pressure of 70 bar and flow rate of 58.8 l/min and a preliminary test using dry cutting**.**

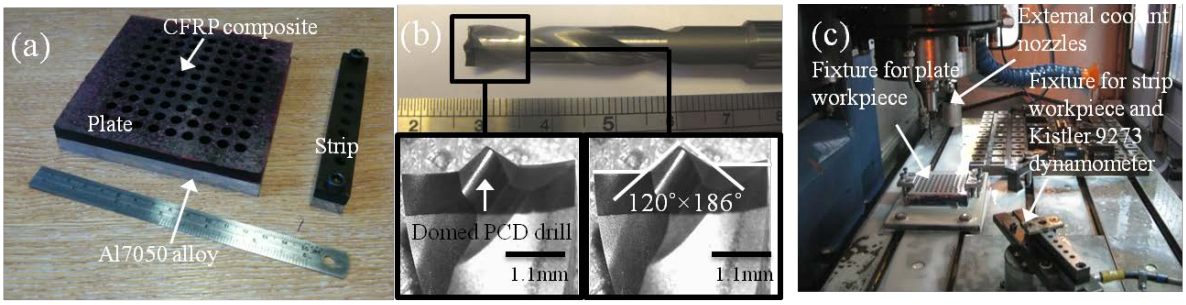


Figure A5-1 Plate and strip stack workpiece material

3. Test procedure

Three tests were employed involving point geometry at 3 levels,

- E geometry: 120˚×186˚
- D geometry: 120˚×169˚
- F geometry: 120˚×159˚

Cutting conditions were a constant feed rate of 0.05mm/rev (500m/min) and constant cutting speed of 200m/min. The tests were halted after drilling 100 holes due to the limited workpiece material.

4. Test results

4.1 E geometry

The tool failed at hole 2 under a **c**utting speed of 200m/min and a feed rate of 0.05mm/rev when machining dry cutting due to debrazing between the PCD drill part and carbide shank as seen in Figure 6-2.

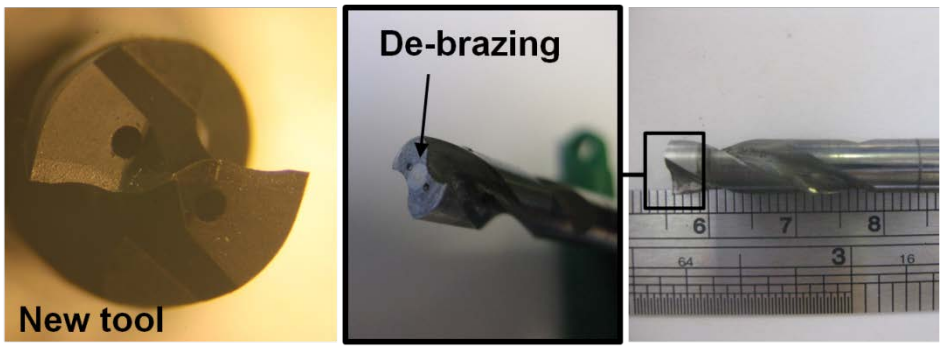


Figure A5-2 Micrograph of new and failed tools using E geometry design

4.2 D geometry

Figure 6-3 shows the tool wear progression. Flank wear was up to ~30μm after 100 holes. Burr height at hole 100 measured at the exit in the Al layer was 0.07mm.

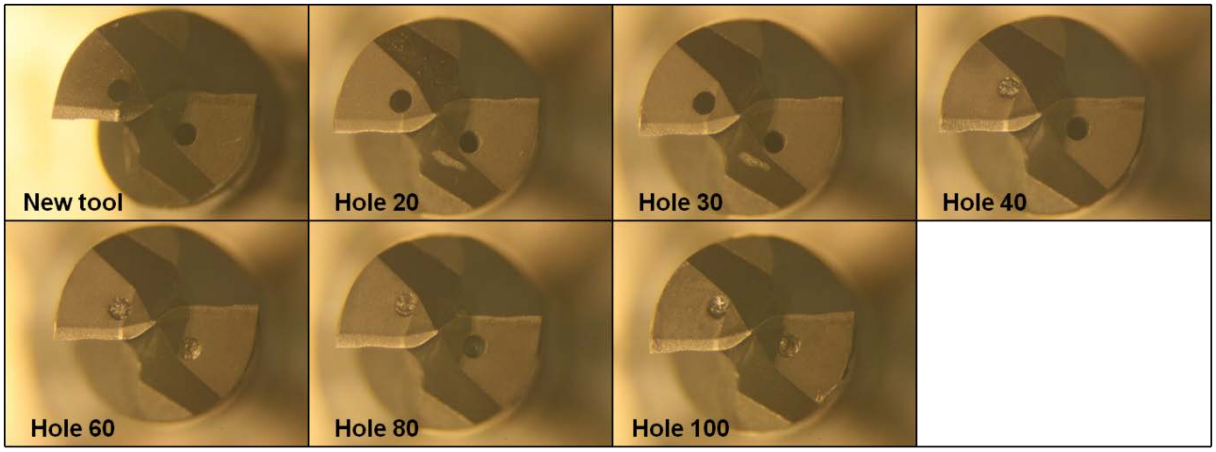


Figure A5-3 Micrograph of tool wear using D geometry of modified drills

4.3 F geometry

Figure 4 shows the micrographs of the tool wear progression for the test involving the F geometry tool. Chipping (~95μm) after drilling 20 holes was observed at the lead cutting lip. Despite this, burr height measured at Hole 100 was 0.08mm at the exit location of the Al layer.

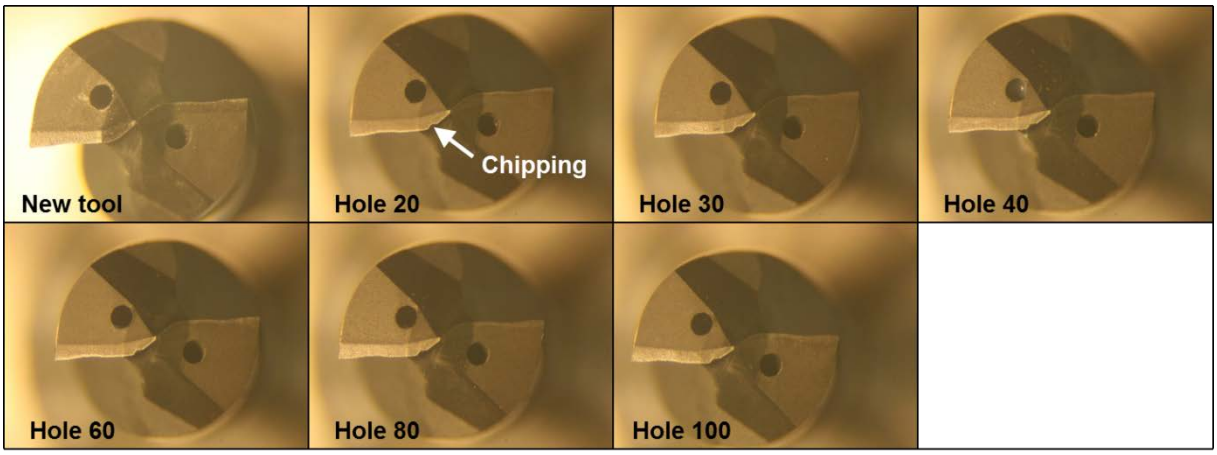


Figure A5-4 Micrograph the tool wear in F geometry of modified drills

5. Conclusions

Based on test results, the modified D geometry produced the lowest flank wear and the smallest burr height. Thus, it is recommended that the D geometry should replace the current 120˚×180˚ point design for future evaluation of domed PCD drill performance when drilling multilayer metallic-composite stack materials.

APPENDIX 6

List of publications

Papers accepted and published

- **C.L. Kuo**, S.L. Soo, D.K. Aspinwall, S. Bradley, W. Thomas, R. M'Saoubi, D. Pearson and W. Leahy. 2013. The influence of tool geometry, feed rate and machining strategy on hole surface integrity following single-shot drilling of 3 layer metallic composite stacks, Proceedings of the 30th International Manufacturing Conference (IMC30), University College Dublin, Ireland, 3-4 September, p.104-113.
- **C.L. Kuo**, S.L. Soo, D.K. Aspinwall, S. Bradley, W. Thomas, R. M'Saoubi, D. Pearson and W. Leahy. 2014. Tool wear and hole quality when single shot drilling of metallic-composite stacks with diamond coated tools. Proceedings of the Institution of Mechanical Engineers, Part B: Journal of Engineering Manufacture, 228(10), 1314-1322.
- **C.L. Kuo**, S.L Soo, D.K. Aspinwall, S. Bradley, W. Thomas, R. M'Saoubi, D. Pearson and W. Leahy. 2013. The effect of cutting speed and feed rate on hole surface integrity in single-shot drilling of metallic-composite stacks. Procedia CIRP, 13, 405-410.

Papers under preparation

- C.L. Kuo, S.L. Soo, D.K. Aspinwall, S. Bradley, W. Thomas, R. M'Saoubi, D. Pearson and W. Leahy. A study of hole accuracy and surface integrity in one-shot drilling of multilayer composite stacks using uncoated/TiAlN-TiN coated carbide drills (1st draft completed)
- C.L. Kuo, S.L. Soo, D.K. Aspinwall, S. Bradley, W. Thomas, R. M'Saoubi, D. Pearson and W. Leahy. The effect of point design to hole accuracy and surface integrity in drilling of multilayer composite stacks (1st draft completed)
- C.L. Kuo, S.L. Soo, D.K. Aspinwall, S. Bradley, W. Thomas, R. M'Saoubi, D. Pearson and W. Leahy. A study on the performance of multi-margin coated carbide drills in one-shot drilling of metallic/composite stack materials (1st draft completed)
- C.L. Kuo, S.L. Soo, D.K. Aspinwall, S. Bradley, W. Thomas, R. M'Saoubi, D. Pearson and W. Leahy. The cutting force, tool wear and fracture mode following one-shot drilling of metallic-composite stacks using diamond tools (1st draft completed)
- C.L. Kuo, S.L. Soo, D.K. Aspinwall, S. Bradley, W. Thomas, R. M'Saoubi, D. Pearson and W. Leahy. The thermal effect to the hole accuracy and surface integrity in drilling of metallic/composite stacks (1st draft completed)